COMPUTATIONAL AND EXPERIMENTAL INVESTIGATION OF SEISMIC STRUCTURAL FUSE SHAPES FOR STRUCTURAL SYSTEMS

Trai Ngoc Nguyen

Dissertation submitted to the Faculty of the Virginia Polytechnic Institute and State University in partial fulfillment of the requirements for the degree of

Doctor of Philosophy

in

Civil Engineering

Matthew R. Eatherton, Chair

Roberto T. Leon

Ioannis Koutromanos

Judy Liu

August 12, 2022

Blacksburg, Virginia

Keywords: Structural Fuse, Hysteretic Damper, Seismic Energy Dissipation, Seismic Behavior

COMPUTATIONAL AND EXPERIMENTAL INVESTIGATION OF SEISMIC STRUCTURAL FUSE SHAPES FOR STRUCTURAL SYSTEMS

Trai Ngoc Nguyen

ABSTRACT

Structural fuses are ductile elements of a structure that are designed to yield and protect the surrounding members from damage, and then be replaceable after a major seismic event. A promising type of seismic structural fuse consists of a steel plate with engineered cutouts leaving a configuration of shear-acting links remaining. There have been several studies on various cutout patterns for shear-acting structural fuses including butterfly-shaped links, hourglass-shaped links, elliptical holes, and link shapes obtained from topology optimization. In most cases, the links are designed to undergo flexural yielding as it is believed to exhibit more ductility than other limit states. However, computational and experimental studies on the shear yielding limit state are limited. Additionally, the transition between shear dominated and flexural dominated limit states has not been previously investigated. Hence, a systematic and thorough study on the different limit states of these structural fuse shapes is necessary to provide better understanding on the structural behavior of each shape and accurately predict the controlling limit state during a seismic event. In addition, a previous study recognized that delaying shear buckling while promoting yielding is a way to improve the seismic performance of shear-acting structural fuses. However, the resulting new topologies were not experimentally validated. Furthermore, the computational study revealed

that large localized plastic strain is one major challenge for these optimized configurations which might lead to potential for fracture.

With the goals of filling the gaps in previous research, a computational and experimental program was conducted to (1) understand seismic performance of five structural fuse shapes, (2) develop a new ductile structural fuse shape with both buckling and fracture resistance, and (3) create design guidelines for practical design. This study consisted of the following parts (a) Creation of a new structural fuse shape called the Tied Butterfly Shape, (b) An experimental program with 20 specimens categorized into five groups including the shape created using topology optimization to resist buckling, the new shape called Tied Butterfly Shape, the butterfly shape, the hourglass shape and the elliptical holes, (c) Use of finite element models to better understand and interpret test data, (d) Two computational parametric studies conducted to investigate the effect of geometrical parameters on structural behavior of the optimized shape and Tied Butterfly Shape, (e) Development of design recommendations for each structural fuse shape.

The computational and experimental results reported in this dissertation demonstrate that these structural fuse shapes are capable of improving the seismic performance of buildings. The presented design recommendations allow designers and researchers to continue exploring these structural fuse shapes.

COMPUTATIONAL AND EXPERIMENTAL INVESTIGATION OF SEISMIC STRUCTURAL FUSE SHAPES FOR STRUCTURAL SYSTEMS

Trai Ngoc Nguyen

GENERAL AUDIENCE ABSTRACT

Structural fuses are ductile elements of a structure that are designed to yield and protect the surrounding members from damage, and then be replaceable after a major seismic event. Several studies on various cutout patterns for shear-acting structural fuses including butterfly-shaped links, hourglass-shaped links, elliptical holes, and link shapes obtained from topology optimization, reported that they offer several advantages for use in structural systems. Nevertheless, systematic studies on key limit states of these structural fuse shapes are limited. In addition, some analytical results have not been validated by experiments.

The research work provides a comprehensive study on these structural fuse shapes. First, generalized design equations are derived using plastic mechanism analysis and key limit states of these structural fuse shapes are investigated. Second, an experimental program was conducted to further understand the cyclic behavior of these shapes associated with each limit state (i.e flexural yielding, shear yielding, lateral torsional buckling, transition between the flexural and shear yielding limit states). Then, nonlinear finite element modeling was implemented to validate against experimental results and provide better understanding of the behavior of the specimens which is not obvious during the test. Lastly, design recommendations are developed for each structural fuse shape.

ACKNOWLEDGEMENTS

I would like to express my profound gratitude to my advisor Dr. Matthew R. Eatherton for giving me the opportunity to be part of this project and the mentorship over the past four years. I am inspired by the high standards that he sets for himself and those around him. His dedication towards research have made me a better engineer, and a person. I have thoroughly enjoyed working with him and feel like I have learned a lot. I would also like to express gratitude to my committee member Dr. Roberto T. Leon, Dr. Ioannis Kotroumanos, Dr. Judy Liu for their advice and counsel.

I am also grateful for the assistance in preparation and constructions of my tests from students and technicians at the Thomas M Murray Structures Laboratory at Virginia Tech including David Mokarem, Brett Farmer, Garret Blankership, Samuel Sherry, etc.

Finally, I would like to thank my parents for their care and love throughout my life and education. Special acknowledgement goes to my Mom and I can honestly say that without her love I would not have gone this far.

This material is based upon the work supported by the National Science Foundation under Grant No. CMMI-1453960. In-kind funding was provided by AISC and INFRA-METALS. Any opinions, finding, and conclusions or recommendations expressed in this material are those of the authors and do not necessarily reflects the views of the National Science Foundation or other sponsors.

TABLE OF CONTENTS

1. INTRODUCTION

1.1 Overview of Structural Fuses

During seismic events, a large amount of seismic energy is transferred to structures, resulting in inelastic stresses and deformations within components of building structural systems. Therefore, earthquakes can cause significant damage to structures which may cause collapse, loss of life and high cost for repairs. The ability of a system to undergo inelastic deformations without significant loss of strength or stiffness (i.e., ductility) can significantly improve seismic performance of structures. One design approach to achieve the objective of repairable ductile energy dissipation is to concentrate inelastic deformations and seismic damage in sacrificial structural elements called structural fuses while limiting forces and inelastic deformations in the rest of the structure. The seismic structural fuses are designed to deform and dissipate the earthquake energy, thereby confining the damage. In addition, structural fuses enhance the repairability of structural systems since these critical elements are designed to be replaceable. If used with self-centering systems or a flexible elastic lateral force resisting system, the structure would return to its original un-deformed configuration with approximately zero residual drifts, further facilitating repair.

Structural fuses can be categorized into three groups including axial acting, flexural acting and shear acting. Axial acting structural fuses such as buckling restrained braces, which are composed of a ductile steel core fully braced within a grouted casing, are designed to yield in both tension and compression, thus dissipating seismic energy (e.g Clark et al. 1999) and if detailed properly, may be replaceable after an earthquake. Flexural acting structural fuses dissipate energy through the development of plastic flexural hinges such as triangular added damping and stiffness (TADAS) devices (e.g Tsai et al. 1993) and added damping and stiffness (ADAS) flexural beam

damper (e.g Bergman and Goel 1987). For shear acting structural fuses, components undergo inelastic shear deformations during extreme loading. An example of a shear acting structural fuse is the butterfly-shaped shear fuses (Ma et al. 2010, Farzampour and Eatherton 2019).

This work will focus on shear-acting structural fuses. More specifically, structural behavior of different shear-acting structural fuse shapes is investigated to explore the design space for these shapes, followed by design recommendation for each shape.

1.2 Research Motivation

Structural fuses can be used in seismic force resisting systems as they provide several advantages over conventional design approaches such as (1) they act as sacrificial elements to concentrate inelastic deformations, thus minimizing damage on main structural components (2) replaceability facilitates faster and more economical post-earthquake repair, (3) structural fuses can be implemented with different shapes, providing more design variables to separately tune strength, stiffness and ductility, (4) some cutout patterns have been shown to produce more deformation capacity compared to conventional options (e.g Ma et al. 2010).

There have been several cutout patterns that have been proposed for shear-acting structural fuses, for instance, steel slit panel with series of straight links (e.g Hitaka and Matsui 2003, Cortes and Liu 2011), butterfly-shaped links (e.g Ma et al. 2010, Farzampour and Eatherton 2019), hourglass-shaped links (e.g Lee et al. 2015, Lee et al 2014), ring-shaped steel plate shear wall (e.g Phillips and Eatherton 2018, Egorova et al. 2014), and steel plate shear wall with elliptical holes (e.g Vian et al. 2009).

The butterfly-shaped link was first tested by Kobori et al. (1992) (referred as honeycomb dampers in the literature). Since then, there have been several studies on butterfly-shaped link (e.g Teruna et al. 2015, Ma et al. 2010, Farzampour and Eatherton 2019). Shear strength equations

were also derived using plastic mechanism analysis and assuming flexural hinges (e.g. Ma et al. 2010). These equations typically neglect the effect of shear stress and do not give limits as to when shear yielding will control. Also, the transition between limit states of shear yielding and flexural yielding was not studied. Furthermore, experimental studies on different limit states with butterfly-shaped links are limited. Along the same lines, since the lateral torsional buckling (LTB) limit state has been considered advantageous for use with self-centering systems as strength degradation due to buckling means less resistance against restoring force (Eatherton et al. 2014), this limit state was also studied by several researchers. For example, Plaut and Eatherton (2017) analyzed lateral torsional buckling of tapered beams with rectangular cross-section. Farzampour and Eatherton (2019) derived shear strength of butterfly-shaped links associated with LTB limit state by solving governing differential equation and assuming elastic material behavior. However, these equations for LTB have not been validated by experiments.

Recently, new structural fuse configurations that have been examined are structural fuses with elliptical openings and hourglass-shaped links (e.g Lee et al. 2015, Lee et al. 2014, Aschheim and Halterman 2002, Koppal and Eatherton 2013). Lee et al. (2015) also conducted an experimental study on several hourglass-shaped links (referred as non-uniform steel strip dampers in the literature). However, the focus was on the flexural yielding limit state of the links. Prediction equations for strength and stiffness were derived assuming plastic flexural hinges (Lee et al. 2015). Nevertheless, generalized prediction equations for shear strength are not expressed in closed form equations making them difficult for use in practical design. For structural fuses with elliptical holes, there are very limited studies on this configuration and no prediction equations or limit states have been studied. None of these studies investigated the transition between shear and flexural yielding limit states.

In addition, shape optimization has been implemented to improve the seismic performance of shear-acting structural fuses. For instance, equivalent plastic strain was minimized to improve cyclic performance of shear panel dampers resulting in an 82% reduction of maximum cumulative equivalent plastic strain (Liu and Shimoda 2013). Also, Ghabraie et al. (2010) attempted to maximize dissipated plastic energy, resulting in an optimized topology that was capable of improving energy dissipation capacity by up to 96%.

A recent study by Avecillas and Eatherton (2020) recognized that resisting shear buckling while promoting yielding is a way to improve the buckling resistance of shear-acting structural fuses. It was reported that the optimized topologies are capable of delaying buckling when subjected to a cyclic displacement pattern up to 9% shear angle. However, the computational results revealed that large localized plastic strain is one of the challenges for new optimized topologies, thus causing concerns about early fracture and low levels of hysteretic energy dissipation.

From the discussions above, further computational and experimental studies are necessary for the following purposes:

1. For previously proposed structural fuse shapes (i.e butterfly shape, hourglass-shaped link and elliptical hole), research is required to better understand the structural behavior associated with each limit state and accurately predict the controlling limit state of each shape.

2. For recently developed buckling-resistant optimized topologies, it is necessary to experimentally validate the buckling resistance and explore the design space and performance for this new set of topologies.

There is a need to develop new structural fuse configurations that are capable of both resisting buckling and delaying fracture.

1.3 Overview and Research Objectives

This research aims to computationally and experimentally investigate five structural fuse configurations. First, structural fuse shapes resulting from topology optimization developed by Avecillas and Eatherton (2019) are studied to bridge the gap between topology optimization and practical seismic design. Second, as those optimized configurations are prone to brittle fracture, a new configuration is developed with the purpose of promoting both buckling resistance and fracture resistance of the structural fuse. Third, other structural fuse shapes including butterfly-shaped, hourglass shaped, structural fuses with elliptical holes and straight link are investigated to provide a better understanding of their seismic performance.

The major research objectives of this work are summarized as follows:

1. Develop design guidelines for the topologies optimized by Avecillas and Eatherton (2019) to resist buckling. This includes converting an optimized topology into a set of design parameters, the derivation of design equations, and creating an understanding of how design parameters affect the structural behavior of the structural fuse.

2. Create a new structural fuse shape, called Tied-Butterfly Shape, that draws on the topologies optimized to resist buckling and the butterfly-shaped link that has been shown to resist fracture. Design strategies are then developed for this Tied-Butterfly Shape.

3. Fill in the knowledge gaps for the previously studied butterfly-shaped link structural fuse shape. Experimentally validate theories related to lateral torsional buckling studied by Farzampour and Eatherton (2019) and the transition between the limit states of shear yielding and flexure yielding.

4. Derive and validate governing equations for two previously proposed structural fuse shapes, the hourglass links and elliptical holes. Understand how these structural fuse shapes perform compared to other shapes.

5. Develop experimentally validated design guidelines for all structural fuse shapes (shapes created using topology optimization to resist buckling, tied butterfly shape, butterfly-shaped link, hourglass links and elliptical hole). The straight link was included for the purposes of comparison.

To achieve the above objectives, the scope of this research is listed as follows:

1. A new shape called Tied Butterfly Shape was developed and investigated. This shape is expected to inherit the advantages of the butterfly-shaped link (good fracture resistance) and link shape obtained from topology optimization (good buckling resistance).

2. An experimental program was conducted including 20 specimens to validate theories and evaluate cyclic performance of five structural fuse shapes. Overall dimensions of specimens are approximately 762 mm x 711 mm and these specimens are subjected to cyclic shear displacement histories up to failure. Table 1.1 provides a summary of tested specimens.

3. Two computational finite element parametric studies on the shape created using topology optimization to resist buckling and the new shape called Tied Butterfly Shape were conducted to provide better understanding of effect of the geometrical parameters on seismic performance of these two shapes. Fully integrated 8-node solid elements with 5 elements through the thickness and nonlinear isotropic hardening and kinematic hardening constitutive model are used for modeling.

4. Generalized design equations were derived using plastic mechanism analysis to understand the structural behavior of all structural fuse shapes.

5. Nonlinear finite element modeling of each specimen was implemented to (1) validate against experimental results, (2) provide better understanding of the behavior of the specimen which is not obvious during the test.

Table 1.1 Test Matrix

Specimen Name	Group	Plate Thickness (mm)	Purposes
OPT1	Shapes obtained from topology optimization to resist bucking	25.4	Validate buckling resistance of the shape
OPT2		25.4	Evaluate buckling resistance and fracture resistance of this shape compared to OPT1
TBF1	Tied Butterfly Shape	25.4	Evaluate buckling and fracture resistance of this shape
TBF2		25.4	Examine overall performance of this shape compared to TBF1
TBF3		25.4	Study the ability of using multiple tied butterfly shapes.
BF1	Butterfly Shaped Link	25.4	Study flexural dominated limit state
BF2		25.4	Study shear dominated limit state
BF3		25.4	Study transition limit state between shear dominated and flexural dominated
BF4		25.4	Investigate flexural dominated behavior of the shape with plastic hinges move toward ends of the links
BF5		25.4	Investigate flexural dominated behavior of the shape with plastic hinges move toward the reduced sections of links
BF6		6.4	Examine elastic lateral torsional buckling
BF7		7.9	Examine inelastic lateral torsional buckling
BF8		9.5	
HG1	Hourglass-Shaped Link	25.4	Validate flexural controlled behavior of the shape
HG2		25.4	Validate shear controlled behavior of the shape
HG3		25.4	Validate transition behavior between shear controlled and flexural controlled of the shape
EL1	Elliptical Holes	25.4	Validate flexural controlled behavior of the shape
EL2		25.4	Validate shear controlled behavior of the shape
EL3		25.4	Validate transition behavior between shear controlled and flexural controlled of the shape
STL	Conventional Shape	25.4	Baseline specimen for the purposes of comparison to other shapes

1.4 Organization of this Dissertation

This dissertation is organized into manuscript format consisting of 7 Chapters and an Appendix. There are four journal articles contained in Chapter 3 through Chapter 6 which are organized around specific structural fuse shapes. Each chapter is briefly described as follows:

1. Chapter 1 introduces the concept of structural fuses and challenges associated with available links. This chapter highlights motivation and objectives of this research.
2. Chapter 2 provides literature review about previously investigated shear-acting structural fuse shapes consisting of butterfly shaped links, hourglass shaped link, optimized topologies, etc. This includes possible implementation of each structural fuse shape in practice.
3. Chapter 3 presents a computational study and experimental investigation on structural fuse shapes optimized to resist buckling by Avecillas and Eatherton (2020). This includes a computational parametric study, experimental program and computational modeling of the shapes.
4. Chapter 4 analytically develops a new shape, called the Tied Butterfly Shape, to provide better buckling and fracture resistance. A computational parametric study is used to evaluate the effect of geometrical parameters on this new shape, thus creating design guidelines for this shape. An experimental program is conducted to investigate the seismic performance of the tied butterfly shape.
5. Chapter 5 focuses on an experimental study of butterfly-shaped links and key limit states of this shape including shear yielding, flexural yielding, and lateral torsional buckling.

6. Chapter 6 develops generalized design equations for structural fuses with hourglass-shaped links and elliptical holes. This includes the experimental program to provide understanding of the cyclic behavior of these shapes associated with different limit states.
7. Chapter 7 summarizes results obtained from this research and recommendations for future research.

2. LITERATURE REVIEW

2.1 Conventional Lateral Force Resisting System with Shear-Acting Ductile Mechanism

There are typically two approaches to design seismic force resisting systems that rely on ductile elements subjected to shear deformations. The first methodology is shear buckling with tension field action developed along the diagonal used in conventional steel plate shear walls (SPSW). The second approach is shear yielding, such as used in link beam of eccentrically braced frames (EBF).

2.1.1 Steel Plate Shear Wall with Solid Web Plate

The SPSW system consists of thin vertical web plates or infill plates connected to surrounding beams and columns, namely horizontal boundary elements (HBE) and vertical boundary elements (VBE), respectively. HBE and VBE should have sufficient stiffness so that yielding along the tension diagonal of the web plate can be fully developed in the web plates. Moment resisting connections are typically used in SPSW system. Lateral loads are resisted by infill web plates with compression stresses are near zero after shear buckling and tension principal stresses oriented at approximately 45^0 to the direction of the load which is referred to tension field action mechanism of the web plates. The development of tension field action provides additional strength to the web plates after buckling referred as post-buckling strength. This mechanism has been found in aerospace engineering by Wagner in 1931, It was then applied into plate girder design (Basler 1961). Tension field action mechanism has been investigated and developed (Thorburn et al. 1983, Timler and Kulak 1983, Berman and Bruneau 2007).

SPSW system offers several advantages. First, SPSW system allows for less structural wall thickness compared to that of reinforced concrete shear walls. An illustration is a study performed for The Century project (San Francisco, California, USA). It was reported that an average SPSW

thickness, including furring of 18 inches was used compared to average thickness of 28 inches for reinforced concrete shear wall resulting in savings of approximately 2% in gross square footage (Seilie and Hooper 2005). In addition, structures using SPSW systems have less building weight compared to buildings designed with reinforced concrete shear walls. This leads to a reduction of foundation loads due to gravity and seismic loads.

Despite several advantages of SPSW systems, they are not widely used because of their own set of challenges due to thin web plates. More specifically, they can buckle under relatively small story drift ratio, leading to pinched hysteretic behavior and low level of energy dissipation as shown in Figure 2.1 below. Additionally, as SPSW systems do not provide much stiffness or energy dissipation during load reversals, moment connections between beams and columns are required by the U.S building code which leads to higher cost of structures. Furthermore, web plate thickness is the only independent design parameter and that does not allow flexibility to separately adjust strength, stiffness, buckling load or system ductility. In order to increase buckling resistance, thicker web plates are used. However, this adds load demand on HBE and VBE, leading to bigger cross sections and higher cost. Berman (2011) showed that the columns in a typical configuration of an example three story SPSW building were W14x398. To reduce column demands in SPSWs researchers have investigated the use of low yield point steels for the infills, reduced beam sections at beam-to-column connections, and strategic placement of holes in the infill panels (Vian et al. 2009, Koppal and Eatherton 2013).

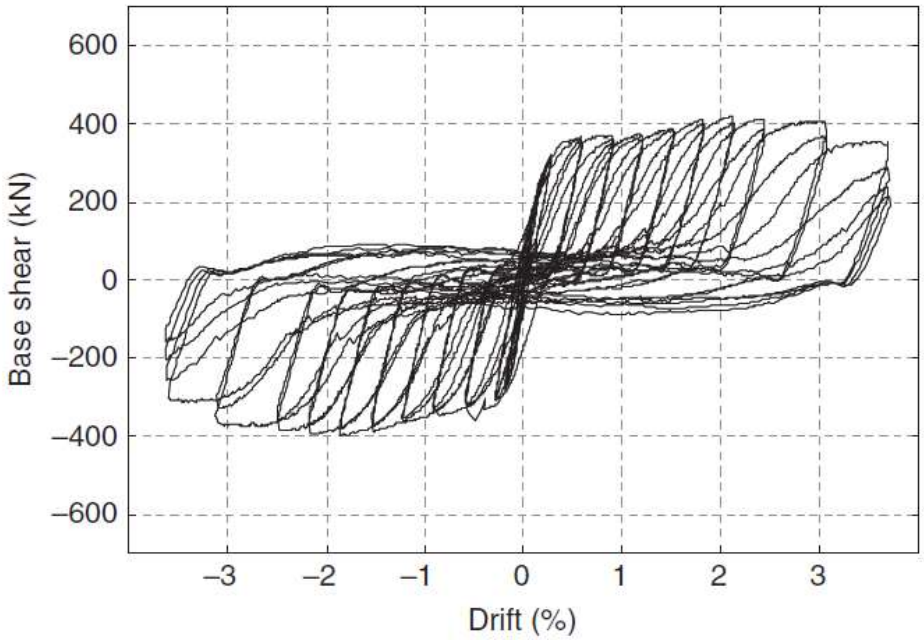

Figure 2.1. Hysteretic behavior of the web plate (from Berman and Bruneau 2003b)

2.1.2 Eccentrically Braced Frame (EBF)

Although moment resisting frames provide a high ductility capacity resulting in high level of energy dissipation, they provide low lateral stiffness capacity. On the other hand, concentrically braced frames (CBF) provide high level of lateral stiffness and low ductility capacity. EBF systems integrate the advantages of both systems into a single structural system. This EBF system originated from Japan in 1970s (Fujimoto et al., 1972, Tanabashi et al., 1974) with the aim of achieving a structure with high lateral stiffness as well as high energy dissipation capacity during earthquake events

This type of framing system typically dissipates seismic energy by either shear yielding or flexural yielding of a critical beam segment called “link”. More specifically, axial forces induced in the braces transferred to either to a column or another brace through shear and bending in a small segment of the beam referred as “link”. The length of a link segment *e* is one of the key

parameters that controls the stiffness, strength, ductility, and behavior of an EBF system. The link length ratio, $\rho = e / (M_p / V_p)$, where M_p and V_p are the plastic moment and plastic shear capacities of the link, provides a convenient measure for the yield behavior. While shear yielding of the web is found to be predominant for short links, in long links, flexural yielding controls the behavior of the link segment. An intermediate link however would experience a combination of both shear and flexural yielding. The effect of link length on the failure mode and deformation capacity is demonstrated (Okazaki et al. 2004).

There are substantial differences between the behavior of short and long links. Although longer links provide more architectural flexibilities, it was experimentally studied that the performance of short links is considerably better than that of long links under severe cyclic loadings in terms of strength and ductility (Roeder and Popov 1977,1978 and Hjelmstad and Popov 1983).

Figure 2.2 shows EBF configurations and corresponding plastic mechanisms. Energy dissipation capacity for EBF system is evaluated by link rotation. In particular, as a link yields in shear or flexure, plastic hinges form allowing link rotation and frame deformation. For that reason, web plate of the link should provide enough stiffness to prevent early web buckling that leads to sudden loss in load-carrying capacity and plastic rotation capacity. Testing shows that a link's inelastic rotation capacity is dependent on the link's length the shorter the length, the larger the rotation capacity (Kasai and Popov 1986a). To develop a large rotation capacity, closely spaced intermediate stiffeners are needed.

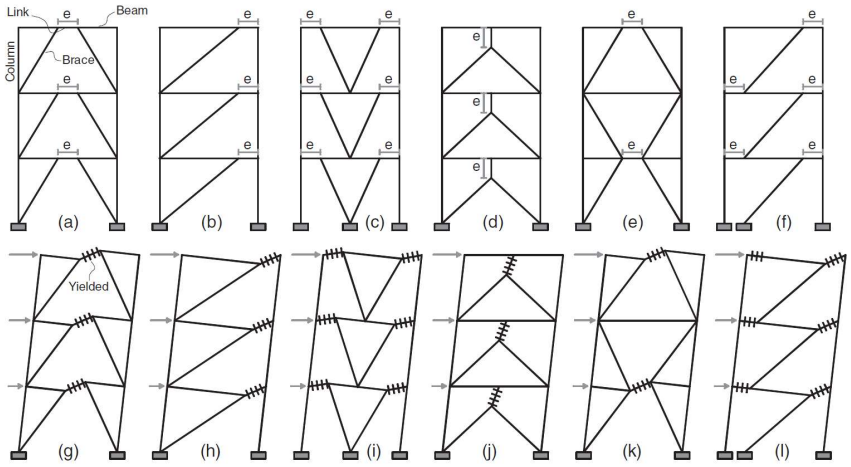

Figure 2.2. EBF configurations and corresponding plastic mechanisms

There are also several challenges associated with links of EBF system. First, shear yielding subjects the surrounding flanges, stiffeners and welds to large forces and inelastic deformation demands. Hence, it is difficult to prevent buckling and fracture in these surrounding elements. Figure 2.3 below shows that EBF links were vulnerable to brittle failure (Bruneau et al. 2012). In order to mitigate buckling, it is required to provide many stiffeners and strict detailing. Furthermore, web plate thickness is only design parameter which does not allow flexibility to separately adjust strength, stiffness, buckling load or ductility of the system.

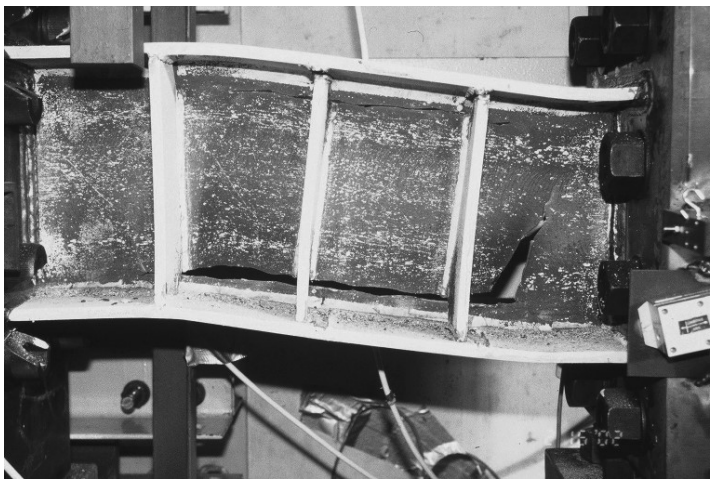

Figure 2.3. Link fracture in web (from Engelhardt, UT Austin)

2.2 Structural Fuses with Engineering Cutouts

2.2.1 Butterfly-Shaped Link

Butterfly-shaped (BF) link is a steel plate with cutouts leaving a tapered shape which is reminiscent of a butterfly-shaped link. This configuration was traditionally introduced for a passive control system that tapered plates bent about minor axis, which was referred as added damping and stiffness (ADAS) flexural beam damper (Bergman and Goel 1987), or with a different shape as triangular-plate added damping and stiffness (TADAS) (Tsai et al. 1993). However, recent research recommended using these dampers in in-plane condition.

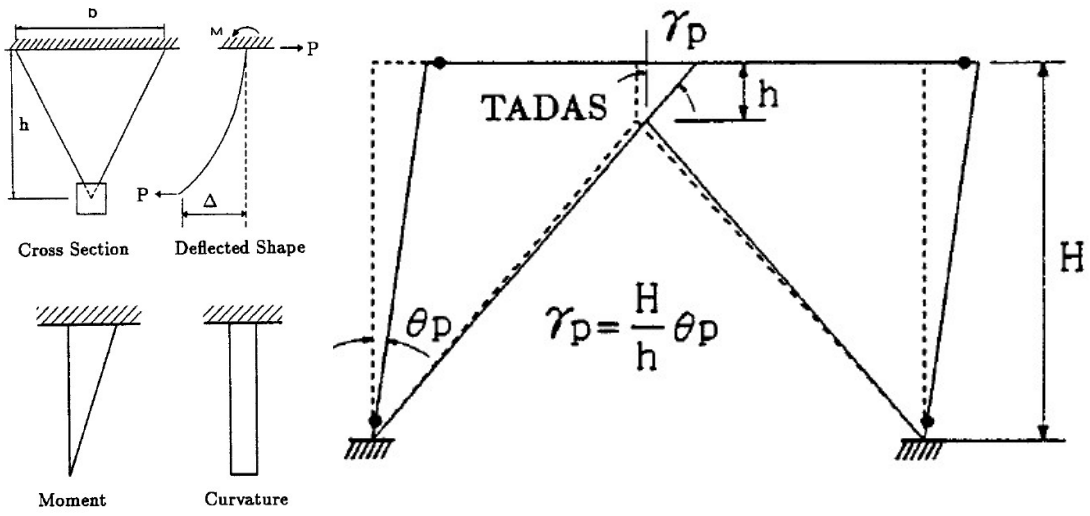

Figure 2.4. TADAS configuration and energy dissipation mechanism (Tsai et al. 1993)

Figure 2.5 illustrates configuration of BF along with moment strength and moment demand. Since the width of a BF link varies linearly between larger ends and middle section, moment strength varies quadratically along the link length as this BF link is subjected to shear load. Moment demand associated with constant shear loading is linear along the length of the BF link. Locations of plastic hinges are where moment capacity intersects with moment demand. Therefore, adjusting geometrical parameters of the link can control the locations of yielding.

Fracture resistance of the link can be improved by locating the plastic hinges away from the corners that are subjected to excessive plastic strain concentration. It is found that ductility of the BF link can be maximized as location of plastic hinge is quarter points which is midway between ends and middle section. Tapered ratio is then *a/b=1/3,* where *a* is the width at middle section and *b* is the width at the end of the link (as shown in Figure 2.5) as suggested by Ma et al. (2010).

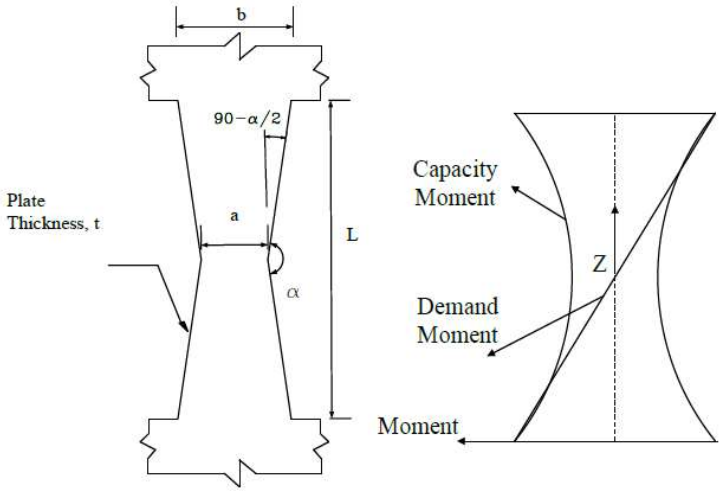

Figure 2.5. BF link configuration with moment demand and capacity (Farzampour and Eatherton, 2019)

The effect of varying geometrical parameters on the behaviors of BF links was investigated by Farzampour and Eatherton (2019). A computational parametric study was conducted to systematically evaluate the effect of geometric parameters on behaviors of this configuration. It was found that behavior of BF link can be controlled by three non-dimensional parameters including taper ratio (*a/b*), slenderness ratio (*L/t*) and width ratio (*b/L*). The effect of geometrical parameters on behavior of BF links was computationally evaluated by prediction equations associated with flexural yielding, shear yielding by Farzampour and Eatherton (2018).

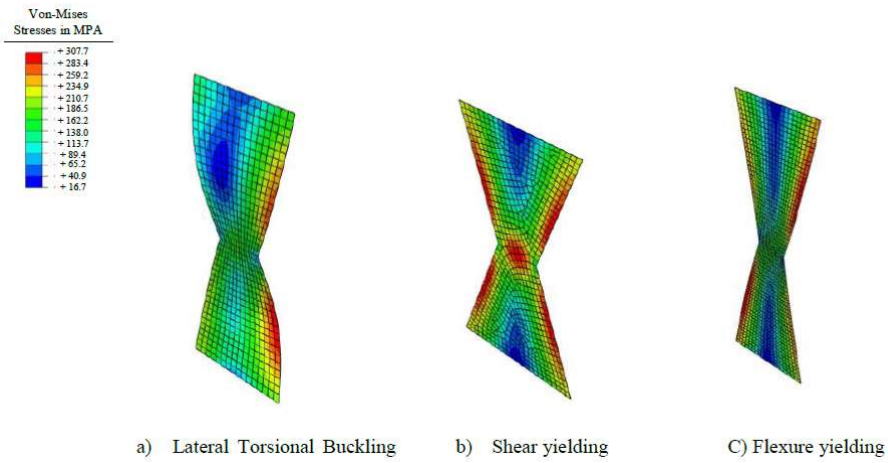

Figure 2.6 Deformed shapes associated with three limit states (Farzampour and Eatherton 2019)

Lateral torsional buckling limit state was also studied by Plaut and Eatherton (2017), Farzampour and Eatherton (2019). Plaut and Eatherton (2017) described the formulation of LTB linear differential equations. This study also provided results using shooting method and assuming uniform torsion for different types of loading including equal and unequal end moments, the consideration of axial load and interaction diagrams, the effect of in-plane shear deformation. Along the same lines, Farzampour and Eatherton (2019) derived LTB differential equation, assuming elastic constitutive material model and negligible warping torsion stresses throughout the butterfly-shaped link. This governing differential equation was then solved using shooting method, followed by the validation by finite element (FE) models.

Farzampour and Eatherton (2018) revealed that while shear yielding is dominant limit state for short BF links, long BF links are more desirable as they are controlled by flexural yielding, thus promoting inelastic deformation, ductility and dissipating more seismic energy. Plate thickness plays an important role in lateral torsional buckling of BF links.

First experimental study on this configuration (referred as honeycomb damper in the literature) was first conducted by Kobori et al. (1992) as illustrated in Figure 2.7. It is reported that BF links associated with taper ratio of *a/b=1/3* are capable of full hysteretic behavior up to 30% shear angle across the link length without fracture and strength degradation (Ma et al. 2011). For these links, plastic hinges form at quarter points and inelasticity spreads along the link length. For some different links that plastic hinges form closer to the ends or reduced section (middle section), shear angle of approximately 0.15–0.2 rad before strength degradation was recorded (Lee et al. 2015, Teruna et al. 2015).

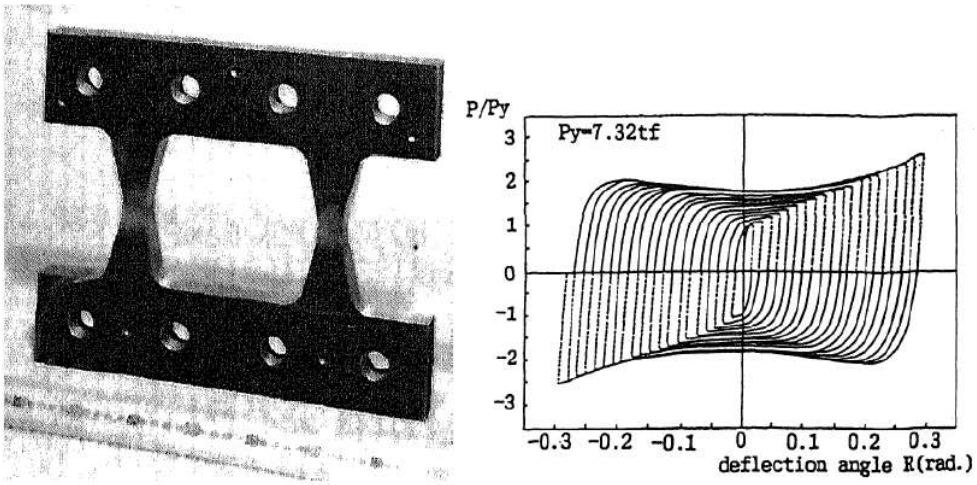

Figure 2.7. Test of honeycomb dampers: (a) Specimen; (b) Hysteretic response (from Kobori et al. 1992)

Butterfly-shaped structural fuses provide several practical applications for different types of structures. Kurokawa et al. (1998) used butterfly-shaped links (referred as "honeycomb-shaped opening" in the literature) between floors of tall building as passive energy dissipation dampers. BF steel plates have also been used in several structures as hysteretic damper (Luth et al. 2008), Kobori et al. 1992). By using the BF links instead of straight links, Luth et al. (2008) mentioned

that the new fuses due to special geometrical properties would show better flexibility. Ma et al. (2010) and Eatherton et al. (2011) used BF seismic fuses to dissipate seismic energy as part of a self-centering seismic force resisting system, as illustrated in Figure 2.8.

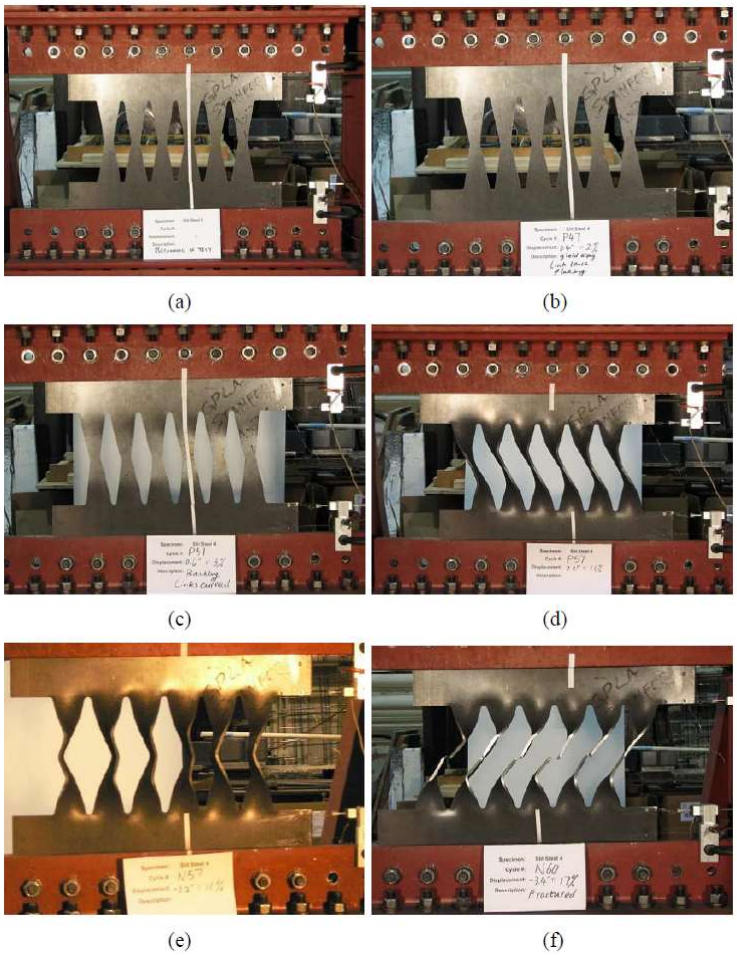

Figure 2.8. Test of BF structural fuse (Ma et al., 2010)

2.2.2 Steel Slit Damper (SSD)

Steel plates with vertical slits evenly spaced which form series of vertical links between the slits are referred to Steel Slit Panels (SSP), as illustrated in Figure 2.9. Under global in-plane shear deformation, those slits act in flexure and behave as beams in double curvature. Plastic

hinges are formed at each end of the link where the curve for moment demand intersect with moment capacity curve.

It was reported that SSP has several advantages: (1) the system is highly ductile; (2) the panels allow for architectural flexibility; (3) the fabrication process is relatively simple; (4) no field welds are required; (5) the panels are easily field bolted to the beams; (6) damaged panels can be easily replaced; (7) the system may be used to retrofit or strengthen existing structures.

A thorough experimental and analytical investigation on steel slit panel was conducted by Hitaka and Matsui (2003). Slit pattern was studied by varying three main parameters including (1) width to thickness ratio (*b/t*), (2) link length to thickness ratio (α), (3) number of rows of links (*m*). In addition, effects of stiffeners on the panels were also examined. Experimental results showed that tested specimens underwent a lateral drift ratio of more than *3%* without cracks and strength degradation. Main cause of strength degradation was found to be out-of-plane displacement.

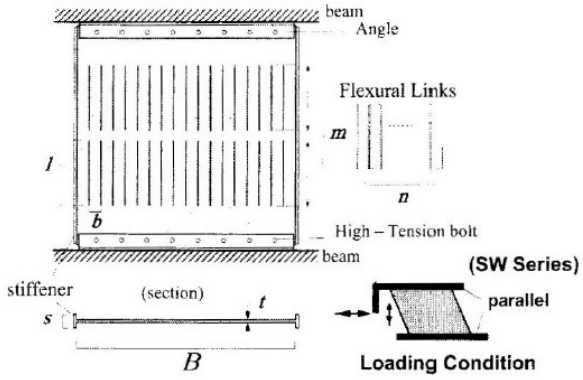

Figure 2.9. Steel Shear Wall with Slits (Hitaka and Matsui 2003)

Hitaka and Matsui (2000) also experimentally investigated the interaction of slit walls with moment frames. Slit walls were mainly used as energy dissipating devices in combination with typical moment resisting frames. There were three buildings designed in Japan using dual systems (i.e the combination of the typical moment frames and slit walls). The steel walls with slits were

reported to take 10% - 25% of the seismic base shear while the remaining base shear was resisted by the moment frames.

Cortes and Liu (2010) experimentally evaluated the seismic resistance of steel slit-panel frame (SSPF) (see Figure 2.10). Compared to the slit wall studied by Hitaka and Matsui (2000), the two main differences are highlighted, (1) entire base shear is resisted by steel slit-panel frames while only 10% - 25% is resisted by steel walls with slits, as mentioned above, and (2) height to width aspect ratio of 2:1 was used for SSPF instead of 1:1 for SSP.

McCloskey (2006) considered different parameters controlling panel behavior. Different limit states including shear buckling and lateral torsional buckling were also examined by McCloskey (2006). It was found that slit width, the plate thickness and the slit geometry do not significantly affect the stress concentrations at the slit ends.

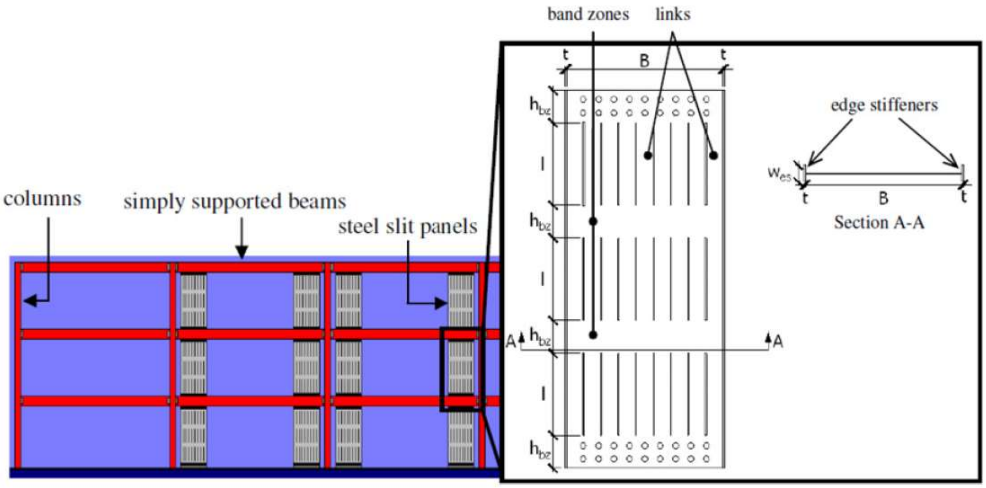

Figure 2.10. Steel Slit Panel Frame (Cortes and Liu, 2010)

2.2.3 Ring-shaped SPSW (RS-SPSW)

Despite of the benefits of conventional SPSW implementation such as (1) a fast and economical construction, (2) thinner wall systems, there are a few issues associated with thin plate

plates such as the pinched hysteretic behavior, implying low level of dissipated energy or there is a need for moment connection as web plates do not provide supplementary stiffness to the system which leads to noticeable expense. New RS-SPSW was proposed to control buckling and promote energy dissipation capacity.

The ring-shaped steel plate shear wall (RS-SPSW) has a unique pattern of cutouts leaving ring shapes which promotes buckling resistance by the mechanics of how a circle deforms into an ellipse (see Figure 2.11). Maurya et al. (2013) proposed main non-dimensional parameters to control buckling including ring slenderness, ring proportioning and global panel slenderness. Additionally, these parameters allow the strength, stiffness, and ductility to be separately controlled to meet specific design objectives. It was reported that the RS-SPSW system has substantially improved stiffness and energy dissipation characteristics as compared to conventional SPSW (Maurya et al., 2013.).

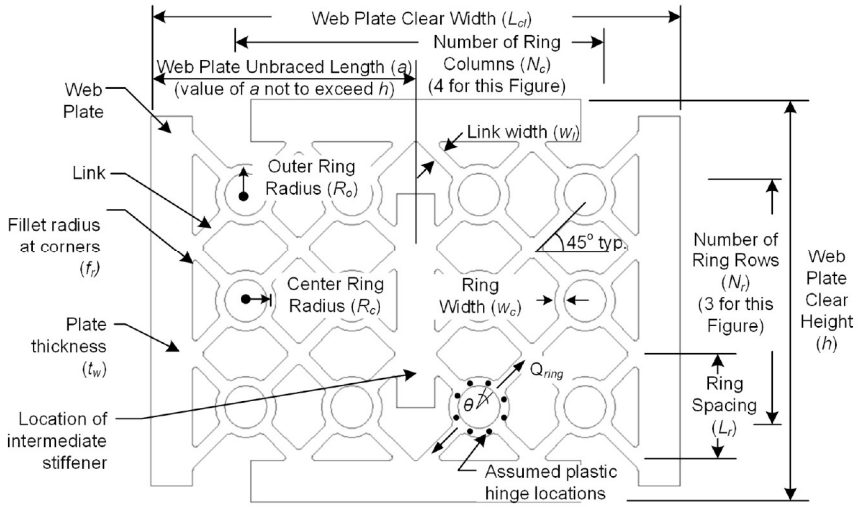

Figure 2.11. RS-SPSW geometric parameters (Phillips and Eatherton, 2016)

A small-scale experimental program was conducted by Egorova et al. (2014) to validate theoretical concepts propose by Maurya (see Figure 2.12). The experimental results confirmed that

RS-SPSW panels were capable of developing plastic hinging of the rings and nearly full hysteretic behavior. Fracture of these specimens were found to be at approximately 8% of story drift.

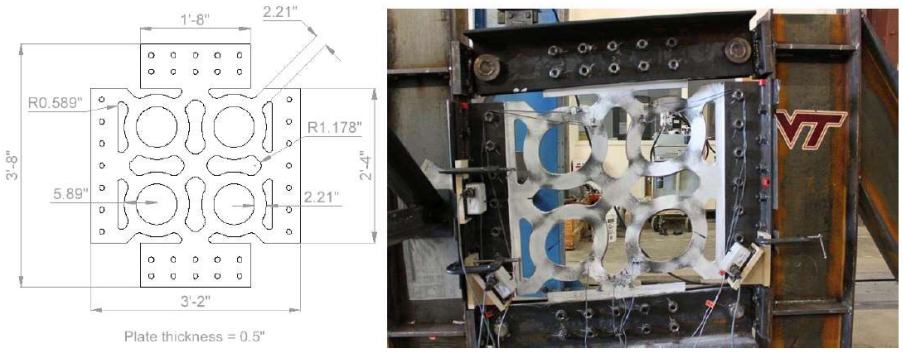

Figure 2.12. Small-scale testing on RS-SPSW panel (from Egorova et al.,2014)

Large-scale testing was performed by Phillips and Eatherton (2018) to further examine the concept of RS-SPSW and investigating boundary elements, HBE and VBE, demands. The experimental results were then used for computational study. Figure 2.13 shows test setup of large-scale testing conducted by Phillips and Eatherton (2018). It was experimentally confirmed that moment connections between HBE and VBE are not long necessary due to the improvements in the behavior of web plate.

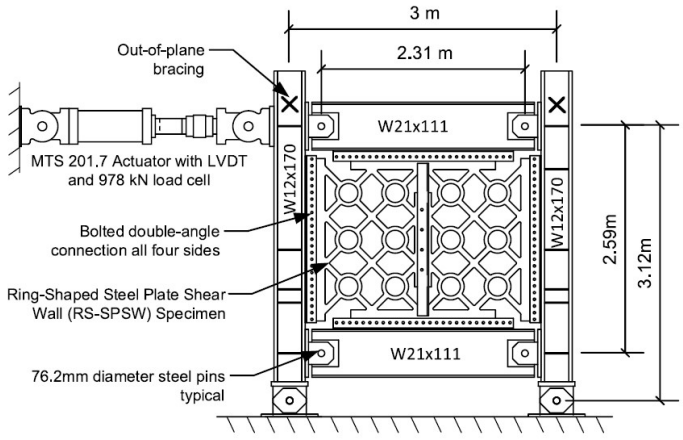

Figure 2.13. Large-Scale Test Setup (Phillips and Eatherton, 2018)

Two distinct modes of buckling including global shear buckling and lateral torsional buckling were identified for the RS-SPSW system (Maurya et al. 2013, Egorova et al. 2014, Phillips and Eatherton 2018), as illustrated in Figure 2.14. It was reported that more severe strength degradation and energy dissipation were observed as specimens experienced lateral torsional buckling. This limit state was found to be related to slenderness of the ring (Egorova et al. 2014). On the other hand, RS-SPSW panels reduced strength and dissipated energy gradually after experiencing global shear buckling. However, it was experimentally confirmed that RS-SPSW demonstrated a better seismic energy dissipation after global shear buckling than the conventional SPSW (Phillips and Eatherton 2018).

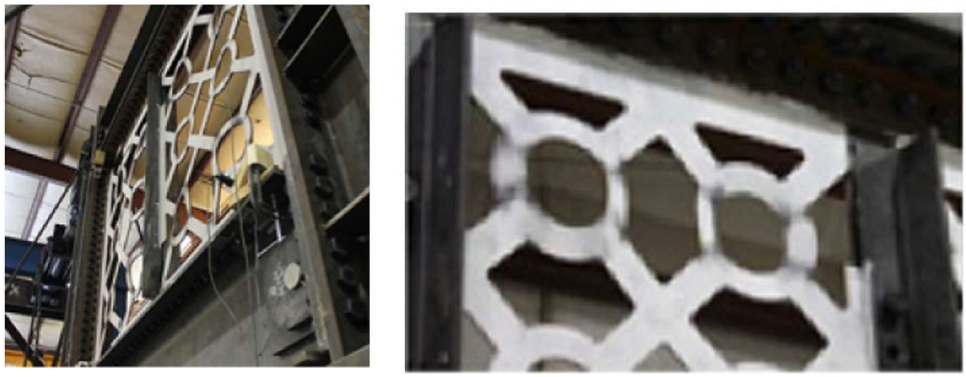

(a) Shear buckling *(b) Lateral torsional buckling*

Figure 2.14 Buckling limit states (Phillips and Eatherton, 2018)

However, stress and strain distributions of the web plate, unexpected deformation modes leading to early fracture the rings, boundary element force distributions, etc were not fully captured by experimental study. Hence, computational study was conducted using finite element analyses to provide further investigation on the behavior of tested RS-SPSW specimens (Phillips and Eatherton 2018). A set of 42 RS-SPSW configurations was computationally examined to study the

effects of main non-dimensional parameteres including panel aspect ratio, plate slenderness and ring slenderness on shear buckling resistance of the panel.

2.2.4 Elliptical Holes

Shin et al. (2017) conducted a study on behavior of wide flange beams with elliptical holes (referred as circular openings in the literature), as illustrated in Figure 2.15. This mechanism associated with one opening is shown in Figure 2.15(a) which is mainly caused by local plastic flexural hinging of the T-section beams above and below the openings. In contrast, for a beam having many openings in the web over the span, a greater reduction in the longitudinal shear capacity may be achieved compared to the transverse shear capacity, and this can lead to the formation of a mechanism showing relative horizontal offsets of the top and bottom portions of the beam. This mechanism is illustrated in Figure 2.15(b), and is associated with local yielding and/or buckling of the ‘‘web posts” that exist between the adjacent openings.

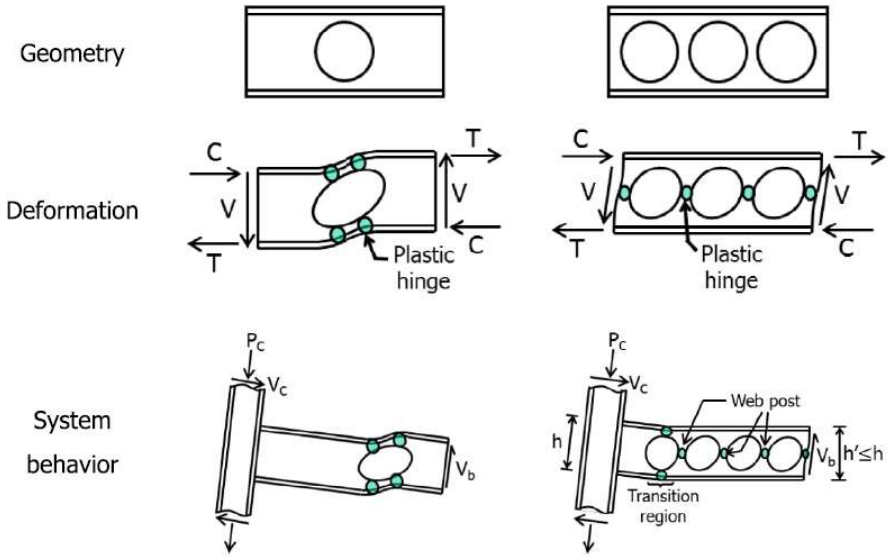

Figure 2.15 (a) One opening; (b) Multiple openings (from Shin et al., 2017)

The web post slenderness ratio, *s/d'*, provides a useful index of the tendency towards flexure-dominated or shear-dominated behavior of the web post. The index *s/d'* is greater than 1.27 analytically demonstrates shear yielding, otherwise, flexural yielding is the controlling limit state as *s/d'* is smaller than 1.27. Two yielding modes are shown in Figure 2.16.

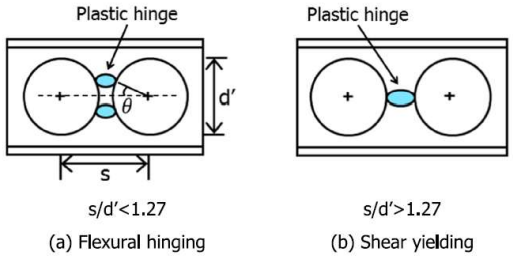

Figure 2.16. Yielding Modes (from Shin et al., 2017)

Along the same line, Vian et al. (2009) conducted an experimental study on perforated steel plate shear walls. This system was designed with two proposed methods to accommodate passage of utilities including (1) web plate with quarter circle cutout into each upper corner of the web plate, as illustrated in Figure 2.17(a), (2) steel panel with series of circular holes, as shown in Figure 2.17 (b). It was found that both systems demonstrated ductile behavior with the capability to resist a drift of 3% or greater. Finite element modeling and analyses, followed by design recommendations for these special perforated SPSWs were then presented by Vian et al. (2009).

Figure 2.17 Perforated SPSW (Vian et al. 2009)

Koppal and Eatherton (2013) conducted a computational study on steel plate shear walls with circular holes around the perimeter of the panel, as shown in Figure 2.18. The effect of sizes, spacing, thickness for perimeter circular hole configuration was investigated by a computational finite element parametric study. Computational results showed that this system exhibits improved performance relative to conventional infill SPSW system.

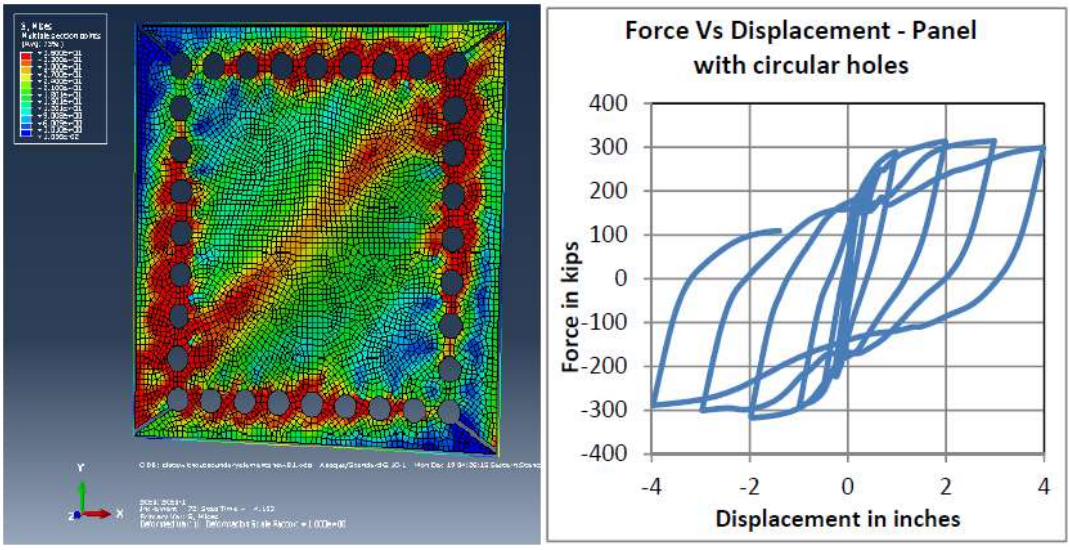

(a) FEM model (b) Hysteresis curve

Figure 2.18 SPSW with circular holes around perimeter (Koppal and Eatherton 2013)

2.2.5 Hourglass-Shaped Damper (HSD)

The hourglass-shaped damper (HSD) is a metallic damper that was proposed based on flexural behavior of the link subjected to shear load. The configuration of the damper was designed so that stresses induced by external load are evenly distributed along the length of the strip. Lee et al. (2014) presented relationship between width and thickness of the link. When all of the cross-sections reach plastic yielding, the strip width has a parabolic profile given constant plate thickness of the link. Figure 2.19 represents configuration of this damper.

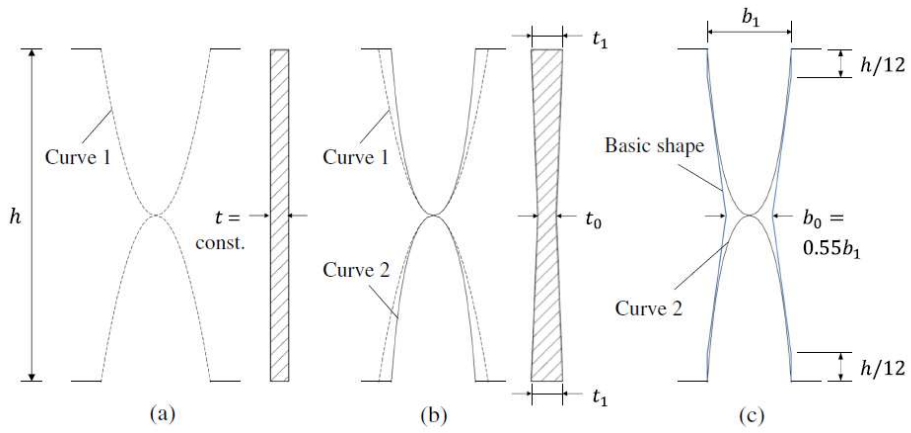

Figure 2.19. Hourglass-shaped Steel Strip (Lee et al., 2014)

It is noted that the middle section should be equal to zero theoretically which is not realistic since hourglass-shaped link could have higher shear stresses at the middle section. Therefore, specified width at middle section is considered with the purpose of resisting shear stresses and avoiding undesirable shear limit state before the formation of plastic hinges.

Lee et al. (2016) experimentally investigated the behavior of hourglass-shaped strip damper subjected to both monotonic and cyclic loadings. It was reported that specimens subjected to cyclic displacement displayed a better deformation and energy dissipation capacities approximately 5 and 6 times, respectively, in comparison to those subjected to monotonically-loaded specimens.

It was experimentally found that damage is not concentrated at the link ends but rather cracks were distributed along the length of strip (Lee et al. 2015). Additionally, crack surface suggested ductile failure, implying that this shape can improve cyclic and fatigue performance. The hourglass-shaped specimens were able to dissipate a decent level of energy after the occurrence of fracture (Lee et al. 2015).

Zhu et al. (2018) proposed new steel shear panel damper optimized by stress contour lines for better energy consumption efficiency. The resulting optimized configuration is similar to an hourglass shape, as shown in Figure 2.20. This study also presented prediction equations for shear strength and elastic stiffness of this shape. Experimental results revealed that this hourglass shaped damper exhibited an increase in hysteretic energy dissipation of approximately 40%-60% relative to conventional rectangular panel damper or straight link.

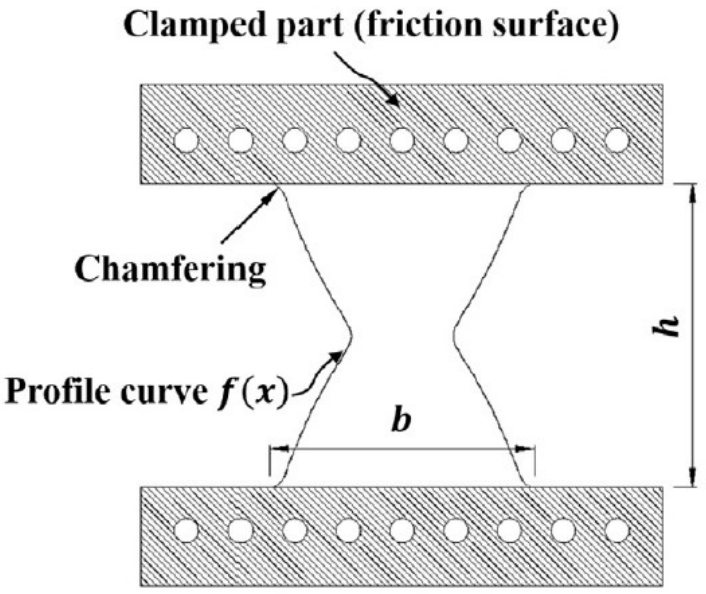

Figure 2.20 Optimized steel shear panel damper (Zhu et al., 2018)

Li and Li (2007) implemented an experiment on "dual function" metallic dampers and one of them is similar to the hourglass shape (referred as double X-shaped damper in the literature), as illustrated in Figure 2.21 (a). It was revealed that this type of damper does not only provide additional stiffness but also demonstrates good energy dissipation capacity (approximately 42%-87% of total input seismic energy).

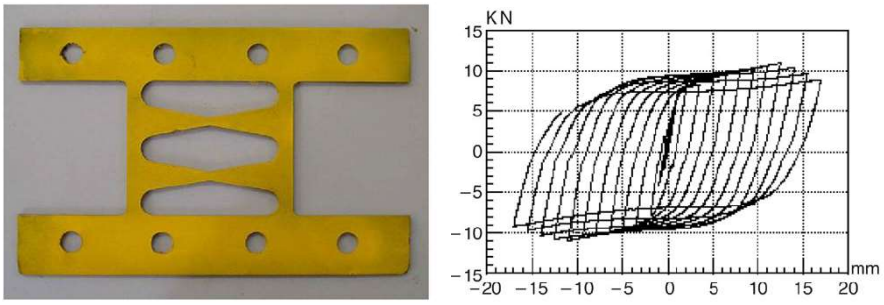

(a) Test specimen (b) Load-deformation curve

Figure 2.21 Double X-shaped damper (Li and Li, 2007)

2.3 Topology Optimization

Shape optimization has also been conducted with the purpose of promoting the hysteretic performance of shear-acting structural fuses. For instance, response surface approximation procedure was implemented for shape optimization of the shear panel dampers (SPD). A minimization problem of maximum cumulative equivalent plastic strain, an index of the deformation ability of SPD is formulated subject to a constraint of total absorbing energy (Liu and Shimoda 2013). Liu and Shimoda (2013) found that the maximum cumulative equivalent plastic strain of the optimal shape is 82.2 % decreased, that can substantially improve the deformation capacity of the shear panel damper. Figure 2.22 compares cumulative equivalent plastic strain distribution of the initial shape and optimized shape

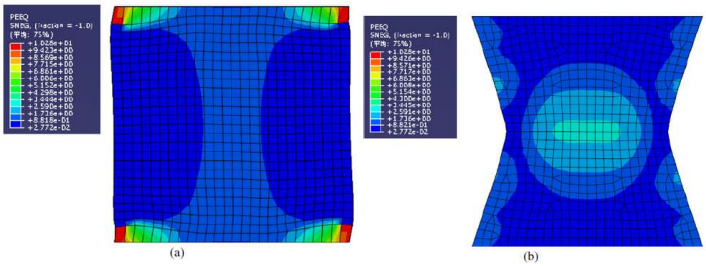

(a) Initial Shape (b) Optimized Shape

Figure 2.22 Cummulative Equivalent Plastic Strain (Liu and Shimoda, 2013).

In addition, modified the bidirectional evolutionary structural optimization (BESO) technique was used to maximize the dissipated total plastic energy of a slit-shaped shear fuse, leading to an optimized topology with improved energy dissipation capacity and even stress distribution (Ghabraie et al. 2010) as illustrated in Figure 2.23. It was reported that energy dissipation capacity was improved by 58%-96%.

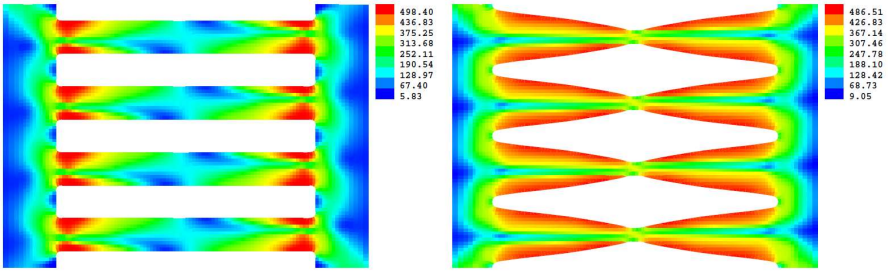

(a) Initial Shape (b) Optimized Shape

Figure 2.23. Stress distribution (Ghabraie et al. 2010)

Along the same lines, Deng et al. (2014) presented a shape optimization method for promoting the low cycle fatigue performance of SDP using simulated annealing (SA) algorithm. However, there was no evident improvement in terms of energy dissipation capacity even though LCF performance was improved (Deng et al. 2014) with SA algorithm.

Avecillas and Eatherton (2019) implemented genetic algorithm (GA) to find optimized topologies to enhance buckling resistance of shear-acting structural fuses. It was found that the new optimized geometries using GA algorithm can resist buckling through inelastic displacement cycles with up to 5 times larger displacements than those that cause buckling in previously studied structural fuse shapes. A new set of topologies is shown in Figure 2.24. Equivalent plastic strains of typical optimized configurations are illustrated in Figure 2.25. One challenge related to the

optimized topologies is large localized equivalent plastic strains which might cause early brittle fracture.

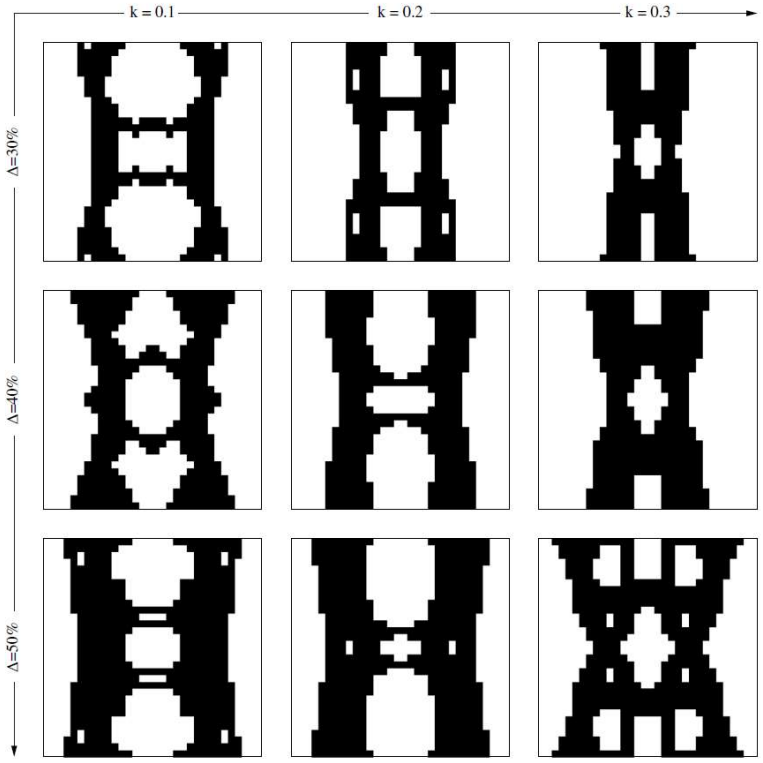

Figure 2.24 Generation of Optimized Topologies (from Avecillas and Eatherton, 2020)

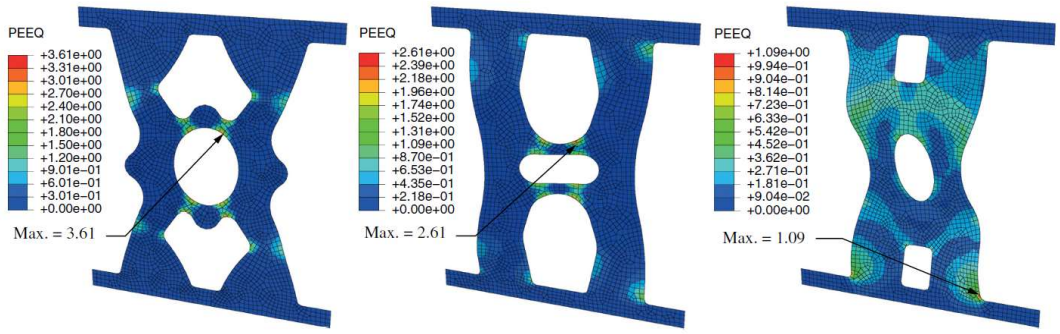

Figure 2.25. Equivalent Plastic Strain Distribution (from Avecillas and Eatherton, 2020)

2.4 Applications of Shear-Acting Structural Fuses in Structural Systems

2.4.1 Possible Implementations of Shear-Acting Structural Fuses

Figure 2.26 illustrates five possible implementations of shear-acting structural fuses. For instance, structural fuses can be replaceable link beams in the EBF system. The structural fuse is design to yield, deform and dissipate hysteretic energy during load reversals, thus limits the forces to the rest of the structures. In addition, structural fuse can be used as ductile mechanism in self-centering steel braced frame (Eatherton et al. 2014). Another application of shear-acting structural fuse is coupling beam between shear walls. Borello and Fahnestock (2011, 2012) conducted studies to investigate the force transfer mechanisms in the coupling beams, the behavior of coupled steel plate shear walls and design methodology. Wide butterfly shaped plates were used between two columns in bridge piers by El-Bahey and Bruneau (2012).

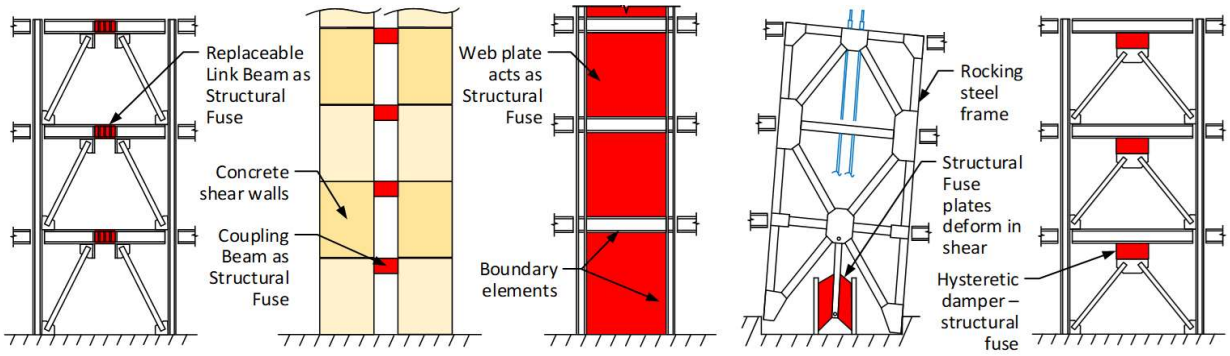

(a) EBF (b) Coupling Beam (c) SPSW (d) Rocking steel frame (e) Damper configuration

Figure 2.26 Implementations of shear-acting structural fuse

2.4.2 Typical Case Studies

Added damping and stiffness (ADAS) devices have been studied by several researchers (Bergman and Goel 1987, Whittaker et al. 1989, 1991). Perry et al. 1993 and Martinez-Romero 1993 reported that the ADAS devices have been used in seismic retrofit of several buildings in the U.S and Mexico, as shown in Figure 2.27.

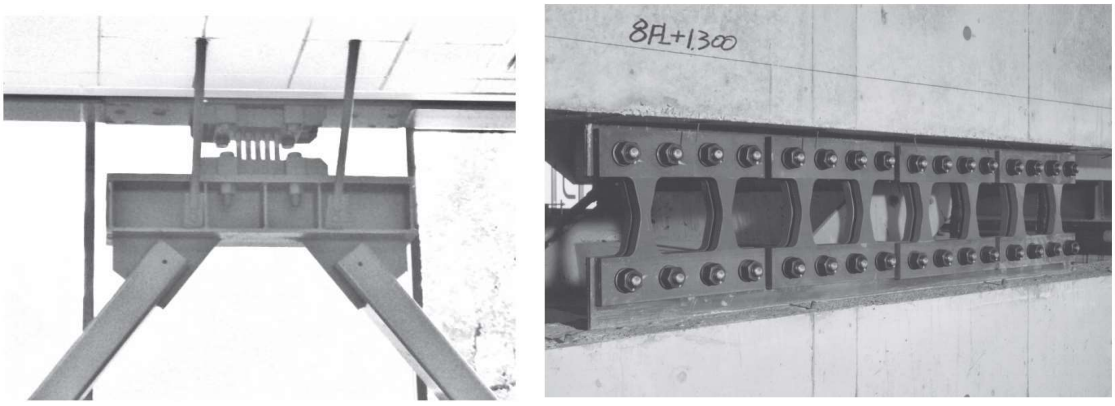

(a) Use of ADAS in San Francisco (b) Use of ADAS in Japan

Figure 2.27 Implementation of ADAS in buildings (from Bruneau et al. 2011)

Similarly, the triangular-plate version of the ADAS or T-ADAS (Tsai et al. 1983) has many applications for retrofit of buildings and steel bridges (Sarraf and Bruneau 1998a, 1998b; Zahrai and Bruneau 1999a, 1999b), as shown in Figure 2.28(a).

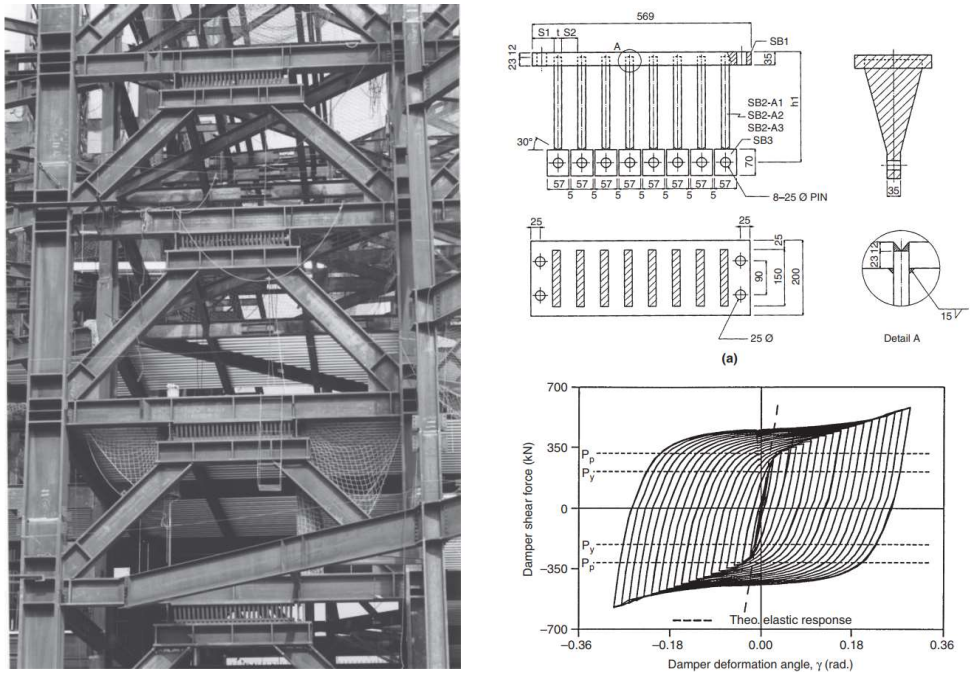

(a) T-ADAS used in a building in Taiwan (b) Hysteretic response

Figure 2.28 Implementation and cyclic testing of T-ADAS (from Bruneau et al. 2011)

Boardman et al. 2000 presented the design and construction of a 12 story office building using triangular plate as dissipating energy device, as shown in Figure 2.29 (Auckland, New Zealand). This study also provided the comparisons with structure with no dissipating devices. It was reported that excess seismic energy is absorbed in the energy dissipating system.

Figure 2.29 Triangular plate energy dissipating device (from Bruneau et al. 2011)

The relationship between demand shear angle and story drift can be calculated using plastic mechanism. Figure 2.30 illustrates the demand shear angle of structural fuse used in frame with braced system. Plastic rotational demand (or demand shear angle) can be calculated as $\gamma_p=(H/h)\theta_p$, where γ_p is the demand shear angle of the structural fuse, θ_p is the story drift, H and h are the height of the story and length of the structural fuse, respectively. For instance, given the value of (H/h) equal 10 and a demand 2% story drift, the corresponding demand shear angle of the structural fuse would be 20% shear angle. Experimental study conducted by Whittaker et al. 1989 was shown that ADAS was capable of maintaining full hysteretic behavior up to 40% shear angle. Similar results have been obtained with the T-ADAS device, as shown in Figure 2.28(b).

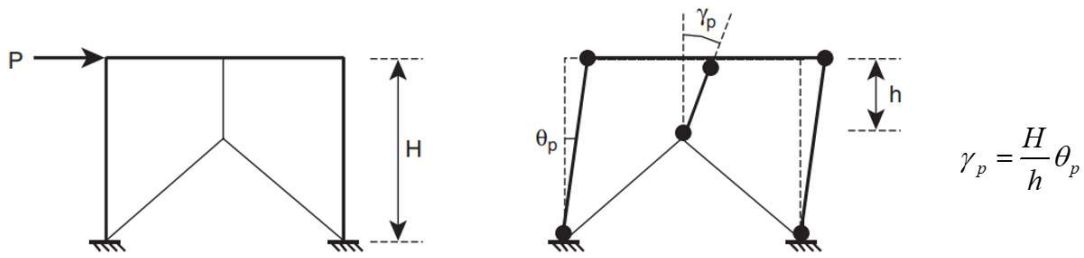

Figure 2.30 Plastic rotational demand of structural fuse used in frame with braced system (from Bruneau et al. 2011)

Luth et al. (2008) presented an analytical and experimental development of innovative "Fused Rotating Wall" system with replaceable structural fuses in the USC School of Cinematic Arts. The concept of using this innovative wall is to separate the overturning moment and shear load paths, thus controls the forces acting on the wall and the resulting deflection. The structural fuses, which are in the form of straight slits and butterfly slits, were welded to the columns and bolted to the embedded plates for ease of replacement, as shown in Figure 2.31. It was reported that the structural fuses were designed to hold the strength to approximately 110% of code minimum. Also, Luth et al. (2008) found that edges of the butterfly-shaped links are more uniformly stressed than those of the straight links, as shown in Figure 3.32.

Figure 2.31 Fused Rotating Walls (Luth et al. 2008)

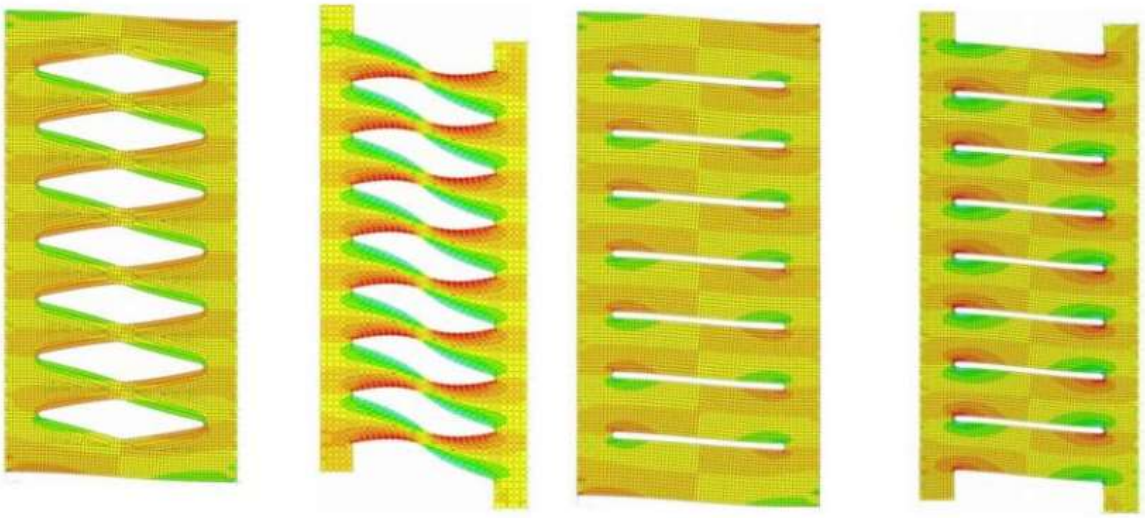

Figure 2.32. SAP studies of Butterfly Shaped Link vs. Straight Link (Luth et al. 2008)

3. COMPUTATIONAL AND EXPERIMENTAL STUDY OF STRUCTURAL FUSES OPTIMIZED TO RESIST BUCKLING

Trai N. Nguyen[1] and Matthew R. Eatherton[2]

[1] Graduate Research Assistant, Department of Civil and Environmental Engineering, Virginia Tech, Blacksburg, USA.
[2] Professor, Department of Civil and Environmental Engineering, Virginia Tech, Blacksburg, USA.

ABSTRACT

The concept of structural fuses, i.e., replaceable hysteretic dampers that limit the forces that can be transferred to the surrounding structure, has been used in research and practice to improve the seismic performance of structural systems. A recent study used topology optimization to develop new structural fuse shapes that discourage buckling and promote stable yielding of shear-acting structural fuses. The objective of the current study is to further validate and develop the optimized shapes to allow the design and application of these optimized structural fuse shapes in practice. First, the pixelated optimized topology was interpreted as a collection of geometric shapes, parameterized to make it accessible for design, and plastic mechanism analysis was used to develop a generalized equation for shear strength. An experimental study was conducted on three specimens that were 711 mm by 762 mm by 25 mm thick, to evaluate strength, stiffness and hysteretic behavior. Finite element models were then validated against the experimental results, and used to conduct a computational parametric study to evaluate the effect of varying key design parameters on strength, stiffness, out-of-plane buckling, effective plastic strain, and energy dissipation. The experimental study showed that one of the optimized geometries possessed a good balance between buckling resistance and fracture resistance reaching approximately 11% shear

angle without either. Design guidance is provided for this topology including a parameterized method for reproducing the shape, design equations, and recommendations for proportioning.

Keywords: Structural Fuse, Seismic Behavior, Topology Optimization, Hysteretic Damper

INTRODUCTION

During an earthquake, seismic energy is transferred to building structures, often resulting in inelastic deformations and associated damage in the structural system which leads to expensive, if not economically impractical repair costs. One approach to designing structures to resist earthquakes is the use of replaceable sacrificial members (i.e structural fuses) that yield and protect the rest of the structure from inelastic deformations. When coupled with a self-centering mechanism or a flexible elastic moment frame, residual drifts can be minimized allowing a targeted structural repair wherein only the structural fuses may need to be replaced.

Structural fuses can be classified into three groups including 1) axial-acting such as buckling restrained braces (e.g Black et al. 2004) in which the core plate yields in both axial tension and compression, 2) shear-acting such as butterfly-shaped shear links (e.g, Ma et al. 2010) where a series of links are subjected to in-plane shear deformations and 3) flexural-acting such as added damping and stiffness (ADAS) devices (e.g, Bergman and Goel 1987) with out-of-plane bending of plates about their minor axis. This research focuses on improving the cyclic behavior of shear-acting structural fuses.

There are several challenges associated with the design and behavior of shear-acting plates in ductile mechanisms as used in conventional seismic force resisting systems. Some are designed with the intent of allowing shear buckling and utilizing post-buckling capacity (e.g conventional

infill steel plate shear wall (SPSW)) and others are designed to prevent shear buckling (e.g shear links of eccentrically braced frame (EBF)). For SPSW, thin web plates buckle at relatively small shear force, resulting in pinched hysteretic behavior, low levels of energy dissipation, and negligible shear resistance during load reversals (e.g Berman and Bruneau 2005, Driver et al.,1998b). In addition, the web plate thickness is the only design variable that does not allow flexibility to adjust strength, stiffness, or ductility of the system separately. For systems that prevent shear buckling and instead promote shear yielding such as shear links of EBF, thick web plates in combination with many stiffeners and strict detailing are required to mitigate the potential for buckling or premature fracture. If flaws exist in the detailing or construction of EBF links, they have been shown to be vulnerable to brittle failure (Bruneau et al. 2014).

Shear-acting structural fuses have been proposed with a strategic removal of material (i.e engineered cutouts) that have improved seismic performance as compared to conventional solid plate shear acting ductile mechanisms. By converting global shear deformations into yielding of local flexural or shear mechanisms, inelastic behavior can be improved as measured by parameters such as ductility, energy dissipation, and stable hysteretic resistance (e.g Phillips and Eatherton 2018). Furthermore, through the addition of design variables associated with the cutout pattern, it is possible to separately tune the strength, stiffness, and buckling resistance.

Previous studies have investigated various configurations of structural fuses with cutouts. Researchers such as Kobori et al. (1992) and Ma et al. (2010) showed that some configurations of butterfly-shaped shear links were capable of full hysteretic behavior up to 30% shear angle across the link length without fracture or loss of strength. This substantial ductility is created because flexural yielding is initiated at quarter points, midway between wider ends and a reduced middle section which moves the yielding away from corners. Other types of non-uniform geometrical

configurations including dumbbell-shaped links, tapered links and hourglass-shaped links have also been shown to have excellent seismic performance with significantly improved ductility (13% to 75%) and energy dissipation capacity (27% to 136%) in comparison to a conventional straight link damper (Lee et al. 2015, Zhu et al. 2018). A different concept for structural fuse shape using ring shapes was computationally and experimentally studied (Egorova et al. 2014, Phillips and Eatherton 2018). It was reported that the ring-shaped specimens exhibited fuller hysteretic behavior than solid plate specimens because of the way a ring shape naturally resists buckling when subjected to shear deformation. Steel slit dampers tested by Cortes and Liu (2011) were shown to be capable of undergoing story drifts of at least 5%. A special detailed perforated panel SPSW with series of circular holes was reported to be a viable alternative to conventional solid SPSW without the need for stiffeners (Vian et al. 2009).

While many shear-acting structural fuse shapes are selected based on theoretical concepts, topology optimization has also been used to create shapes with improved overall seismic performance. For instance, Liu and Shimoda (2013) and Deng et al. (2015) used optimization to find shapes that minimized equivalent plastic strain or increased the low cycle fatigue resistance, resulting in topologies that reduced equivalent plastic strains by approximately 60% to 80% compared to baseline conventional shear panel dampers. Ghabraie et al. (2010) used Bi-directional Evolutionary Structural Optimization (BESO) to maximize dissipated plastic energy, resulting in an optimized topology that was capable of improving energy dissipation capacity by up to 96%. It is noted that the resulting optimized topologies often have a butterfly type shape which demonstrated more evenly distributed inelastic deformations (Ghabraie et al. 2010, Deng et al. 2014) thus improving hysteretic behavior of the metallic dampers. He et al. (2016) optimized the in-plane stiffness which resulted in shapes with interior and boundary perforations.

Much of the previous work on shear-acting structural fuse shapes has focused on increasing ductility, energy dissipation, and stiffness, while neglecting the effects of buckling. Buckling can lead to reduced energy dissipation, loss of shear strength, and fracture at sharp creases. A recent study recognized that resisting shear buckling, while promoting yielding, is a way to improve the behavior of shear-acting structural fuses and used topology optimization to create promising buckling resistant shapes (Avecillas and Eatherton 2020). However, the resulting topologies are pixelated shapes that can be difficult to adapt to different design settings (i.e. building specific needs for strength, deformation capacity, or stiffness). Furthermore, the deformation capacity, ductility, and buckling resistance need to be investigated through experiments before the optimized shape can be used in practice.

The objective of the current study is to create an experimentally validated design approach around selected optimized topologies created by Avecillas and Eatherton (2020). This paper starts with a brief summary of the topology optimization, focusing on the objective function which incentivized buckling resistance by controlling the ratio of elastic eigenbuckling shear load to the shear yield load. To make the optimized structural fuse shape practical for design, the shape is post-processed into a collection of defined curves with all dimensions being a function of five unique design parameters. Then plastic mechanism analysis is used to derive a generalized equation for the shear strength of the parameterized configuration. Three experiments were conducted on specimens that were 711 mm x 762 mm x 25 mm thick to investigate the cyclic load-deformation behavior for these shapes. Finite element models were then validated against the experiments and used to conduct a computational parametric study to evaluate the effect of the design variables on the cyclic behavior of the structural fuse such as strength, stiffness, maximum out-of-plane displacement and maximum equivalent plastic strain. Based on the results of the

experiments, FEM validation and parametric study, design recommendation are provided for practical design.

SUMMARY OF SUPPORTING TOPOLOGY OPTIMIZATION

Since the current research builds on the topology optimization performed by Avecillas and Eatherton (2020), this section provides a brief summary of the optimization with a focus on the objective function and resulting topologies. The goal of the topology optimization was to find the optimal distribution of material within a design space to resist buckling while undergoing yielding. As shown in Fig. 1a., the design space was defined as a square plate with dimension of w=711 mm and constant plate thickness of t=12.7 mm. It is noted that two horizontal boundary elements at the top and bottom of the plate are also included but not considered in the optimization process. This domain has a fixed edge at the bottom and the top edge is only allowed to translate in the x direction as shown in Fig.1a.

Avecillas and Eatherton (2020) introduced the objective function, $f(a)$ given in Eq. (1) and illustrated in Fig. 1b, where a is the vector defining the material distribution. The elastic shear buckling load, V_B, is obtained from a three-dimensional eigen-buckling analysis while the shear yield load, V_Y, is obtained from a planar two-dimensional finite element analysis considering material nonlinearity. The ratio V_Y / V_B was introduced as a measure of the tendency for the structural fuse to yield before buckling. More specifically, the exponential function in Eq. (1) is used to encourage a topology to have a yield-to-buckling ratio, V_Y / V_B, equal a target value, k, which is less than unity (k=0.1 to k=0.3 was used) implying that the structural fuse will experience considerable yielding before buckling occurs. The constant, C_1, was introduced to control the degree to which the first term in Eq. (1) is weighted relative to the second term, and was taken as

50 based on trial studies by Avecillas (2019). The radial term $\sqrt{V_Y^2 + V_B^2}$ in the denominator of Eq. (1) incentivizes new topologies with larger strength without affecting the target value of V_Y / V_B. The term $V_{Y,solid}$ is a normalizing term that represents the shear yield strength of a solid topology as given in Eq. (2), where f_y is the yield stress of the fuse material and Δ is the volume fraction, defined as the ratio of optimized domain volume to total design domain volume. Fig. 1b graphically shows the objective function where the most optimal solutions shown with darker shading have V_Y / V_B close to the specified value, k, and larger values of strength.

$$\underset{a}{\text{minimize}} : f(a) = \exp\left[C_1 \left(\frac{V_Y}{V_B} - k \right)^2 \right] \frac{V_{Y,solid}}{\sqrt{V_Y^2 + V_B^2}} \qquad (1)$$

$$V_{Y,solid} = \frac{f_y}{\sqrt{3}} wt\Delta \qquad (2)$$

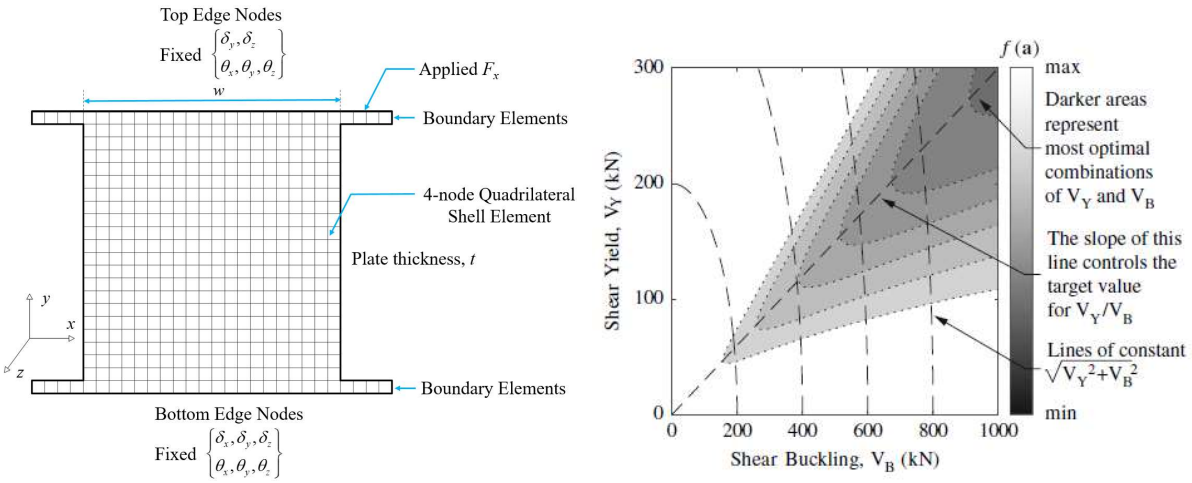

(a) Illustration of domain and FEM

(b) Objective function for k=0.3 (from [Avecillas and Eatherton, 2020])

Fig. 1. Topology Optimization Setup

The set of resulting topologies associated with target values of k=0.1, 0.2, 0.3 and volume fractions of Δ=30%, 40%, 50% are represented in the pixelated shapes in Fig. 2. Additional details on the topology optimization can be found in Avecillas, (2019).

The topology associated with volume ratio of Δ=40% and target value of yield-to-buckling ratio k=0.2 was selected for further study in this paper for the following reasons: (1) the volume ratio of Δ=40% creates a balance between the desire for larger shear strength which comes with larger volume ratio, and minimizing the complexity and number of holes in the topology which also occurs with greater volume ratio, e.g., those with Δ=50%, (2) the shear yield-to-buckling ratio, k=0.2 was selected as a good balance between fracture resistance, which was shown to be improved for larger values of k (Avecillas, 2019), and buckling resistance which by definition occurs with smaller values of k. The topology with volume ratio of, Δ=40%, and yield-to-buckling ratio, k=0.1, was also selected for inclusion in the experimental program to investigate a second topology with increased buckling resistance.

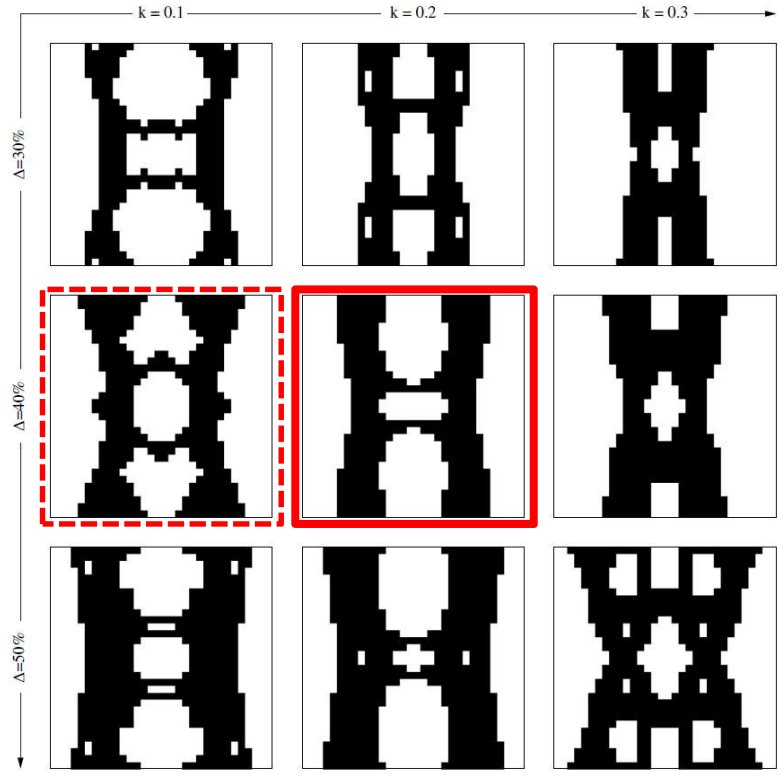

Fig. 2. Buckling-resistant topologies resulting from optimization procedure (from [Avecillas and Eatherton, 2020])

PARAMETERIZATION AND PLASTIC ANALYSIS

It is challenging to implement optimized topologies in practical design situations with specified strength, stiffness or deformation capacity because the geometry is fixed. For a topology to be useful in design, the strength should be predictable and adjustable while the geometry should be adaptable to different configurations and sizes. In this study, the topology associated with k=0.2 and volume fraction of Δ=40% (see Fig. 2) is investigated. A two-part interpretation of this optimized shape is conducted where first smooth curves are fit to the pixilated shape, followed by simplification of the shape using geometrical parameters as shown in Fig. 3. More specifically, this topology consists of two ties (horizontal links) and legs (vertical links) uniquely defined by five design parameters including the tie width, W_T, leg width, W_L, tie radius, R, structural fuse length, L, and plate thickness, t. The relationship between the dependent parts of the geometry and the design parameters is based on the optimized topology and assumed to be linearly related to the design parameters as shown in Fig. 3b. For instance, the original configuration resulting from topology optimization could be completely described by the set of parameters defined as follows: W_T=30.2 mm, W_L=164 mm, R=76.2 mm, L=711 mm and t=12.7 mm, as shown in Fig. 3b. It is worth mentioning, that for the parameterized topology to be geometrically possible, the following limits are required: L/W_T>4.35 and R/W_L>0.5.

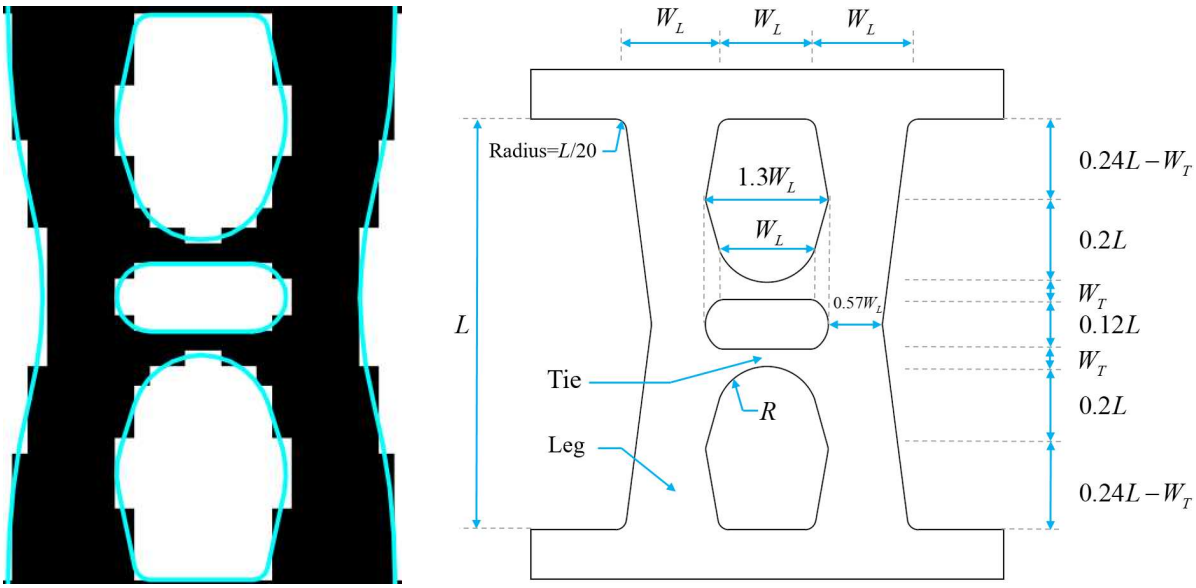

(a) Smooth shape over pixelated shape (b) Parameterized configuration

Fig. 3. Shape parameterization

In order to make this topology adaptable to design situations, an equation for shear strength is derived based on plastic mechanism analysis. The configuration is first idealized by centerline elements as illustrated in Fig. 4a.

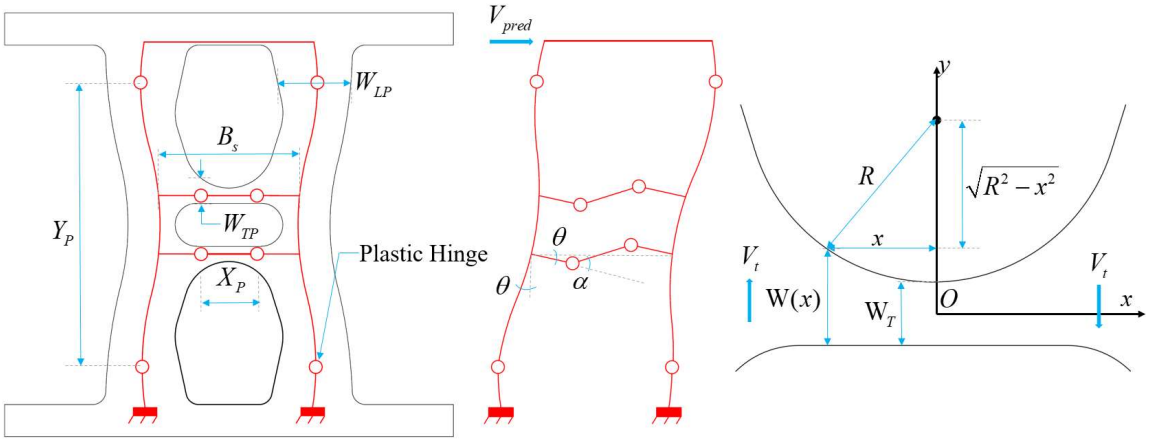

(a) Idealized frame (b) Plastic Mechanism (c) Tie Geometry

Fig. 4. Idealization of optimized topology

The idealized frame shown in Fig. 4a is subjected to shear force, V_{pred}, resulting in a plastic mechanism, as illustrated in Fig. 4b, which includes two plastic hinges in each of the vertical legs and two plastic hinges in each of the horizontal ties. Two key parameters are introduced for plastic analysis: the width of leg at the plastic hinge, W_{LP} and width of the tie at the plastic hinge, W_{TP} as shown in Fig. 4a.

The distance between the plastic hinges in the tie, X_P, can be determined analytically by minimizing the tie shear force associated with plastic hinging. First, the width of the tie, $W(x)$, along its length at any location, x, is given by Eq. (3) with local coordinate system defined in Fig. 4c. Then plastic moment capacity of the tie, M_p, is a function of tie width, $W(x)$, plate thickness, t, and yield stress, f_y, as given by Eq. (4). The moment demand, M_d, is linearly varying as described by Eq. (5) and the shear force at the tie, V_t, is fou by setting moment capacity equal to moment demand as given in Eq. (6). The value of x that minimizes this shear force is found by setting the derivative of the shear strength with respect to x, equal to zero. Two times this value of x gives the distance, X_p, which is given in Eq. (7).

$$\mathrm{W}(x) = W_T + R - \sqrt{R^2 - x^2} \tag{3}$$

$$M_p(x) = f_y \frac{t}{4} \mathrm{W}^2(x) = \frac{tf_y}{4}\left(W_T + R - \sqrt{R^2 - x^2}\right)^2 \tag{4}$$

$$M_d(x) = V_t x \tag{5}$$

$$V_t = \frac{tf_y}{4x}\left(W_T + R - \sqrt{R^2 - x^2}\right)^2 \tag{6}$$

$$X_P = \sqrt{2(W_T + R)\sqrt{(W_T + R)^2 + 8R^2} - 2(W_T + R)^2 - 4R^2} \tag{7}$$

The overall plastic mechanism is shown in Fig. 4b and virtual work is used to determine the shear strength of this optimized configuration. The external work and internal work are given

in Eq. (8) and (9). Equating internal and external work and after substituting Eq. (10), (11), and (12) for plastic moment strength for the leg, M_L, and the tie, M_T, and relationship between the tie angle, α, and the leg angle, θ, the shear strength equation is obtained as given in Eq. (13). Based on assumptions about the location of plastic hinging shown in Fig. 4a, Eq. (13) can be converted to a function of the five design variables by using the following approximations: the location of the leg plastic hinge is approximated as $Y_P \approx L\text{-}0.5W_L$, the length of the tie is approximated as, $B_s \approx 2W_L$ and the width of the leg and tie at the plastic hinges are approximated as, $W_{LP} \approx 0.85W_L$ and $W_{TP} \approx 1.25W_T$, respectively. Distance between plastic hinges at the tie can be calculated using Eq. (7). It is noted, that these approximations are not valid if the design parameters vary too much from the optimized topology. If a more accurate solution is desired, a similar methodology could be used to obtain the location and distance between locations of the leg plastic hinges. Substituting the approximate dimensions results in the shear strength equation given in Eq. (14). Although shakedown analysis can be implemented for more accurate approximation of the shear strength, it is not considered in this study as the resulting predicted equation obtained from shakedown analysis is not expected to make a significant difference compared to Eq. (14).

$$W_{ext} = V_{pred}\left(Y_P\theta\right) \tag{8}$$

$$W_{int} = 4\left(M_L\theta + M_T\theta\right) \tag{9}$$

$$M_L = f_y \frac{tW_{LP}^2}{4} \tag{10}$$

$$M_T = f_y \frac{tW_{TP}^2}{4} \tag{11}$$

$$\alpha \approx \frac{B_S}{X_P}\theta \tag{12}$$

$$V_{pred} = \frac{tf_y}{Y_P}\left(W_{LP}^2 + \frac{B_S W_{TP}^2}{X_P} \right) \tag{13}$$

$$V_{pred} \approx \frac{tf_y}{L - 0.5W_L}\left[\left(0.85W_L\right)^2 + \frac{2W_L}{X_P}\left(1.25W_T\right)^2 \right] \tag{14}$$

EXPERIMENTAL TESTING PROGRAM

Three specimens, two optimized shapes from the topology optimization study and one straight link shape, were tested at the Thomas M. Murray Structural Engineering Laboratory at Virginia Tech. This testing program aims to investigate the behavior of structural fuse shapes resulting from topology optimization and then compare to the baseline straight link specimen.

Test Specimens

Fig. 5 illustrates the geometry of the three specimens and the test matrix is provided in Table 1. The first optimized configuration, referred to as OPT1, is the topology associated with volume ratio of Δ=40% and target value of k =0.2, while the second optimized shape, OPT2, is associated with volume ratio of Δ=40% and target value of k =0.1 (see Fig. 2). It is expected that Specimen OPT2 has greater buckling resistance compared to Specimen OPT1 based on the k value. The conventional straight link structural fuse, named Specimen STL, is expected to develop plastic hinges at the two ends, resulting in early brittle fracture. It is noted that all three specimens have the same link length of L=508 mm and plate thickness of t=25.4 mm. The two optimized configurations were uniformly scaled in both plan dimensions from the original topology size to produce the desired link length. Top and bottom boundaries including bolt holes of the specimens were waterjet-cut with lowest quality while the structural fuse shape at the middle was waterjet-cut with highest quality. The specimens were bolted to the test frame using 28.6 mm diameter, A490 structural bolts.

Table 1. Test Matrix

Specimen Name	Link Length, L (mm)	Plate Thickness, t (mm)	Volume Ratio, Δ	Target Ratio ($k=V_y/V_b$)
OPT1	508	25.4	40%	0.2
OPT2	508	25.4	40%	0.1
STL	508	25.4	N/A	N/A

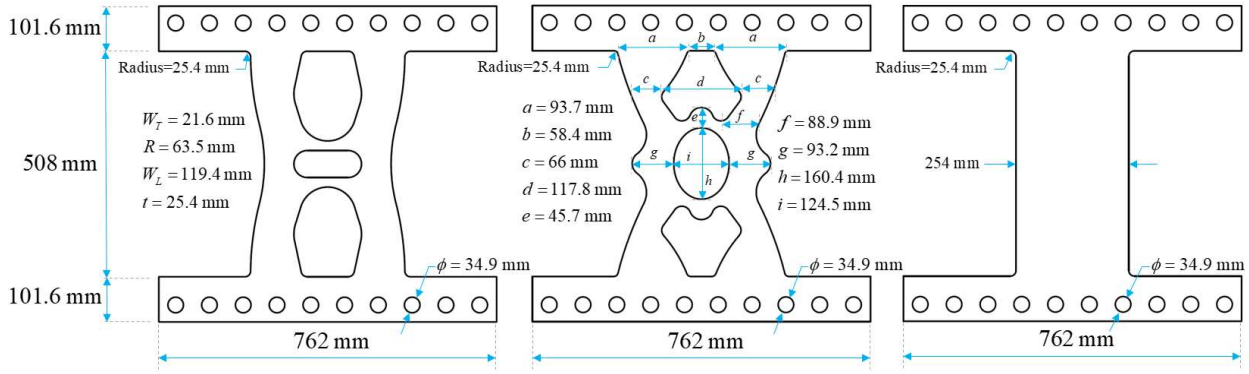

(a) Specimen OPT1, V_Y/V_B=0.2 (b) Specimen OPT2, V_Y/V_B=0.1 (c) Specimen STL

Fig. 5. Drawings of specimen geometries

All three specimens were fabricated from the same heat of steel, from which three tension coupons were tested. Each tension coupon was waterjet cut with geometry in accordance with ASTM standard A370-07a for tension coupons with width of the reduced section equal to 38 mm and gage length of 203 mm. Modulus of elasticity, yield stress, ultimate strength, and fracture elongation were 224,000 MPa, 376 MPa, 533 MPa and 26%, respectively, based on the average of the three coupons.

Test Setup and Details

The test setup, illustrated in Fig. 6, was designed to apply shear displacements to the specimens using an MTS 201.80 hydraulic actuator with capacity of 1468 kN and stroke of ±381 mm. The two struts adjacent to the specimen shown in Fig. 6a were designed with pinned connections to allow horizontal displacements during the test. The top beam of the test frame was restrained against out-of-plane movement by the lateral bracing system shown in Fig. 6b. All bolts used were grade A490. A picture of the overall test setup is shown in Fig. 7a.

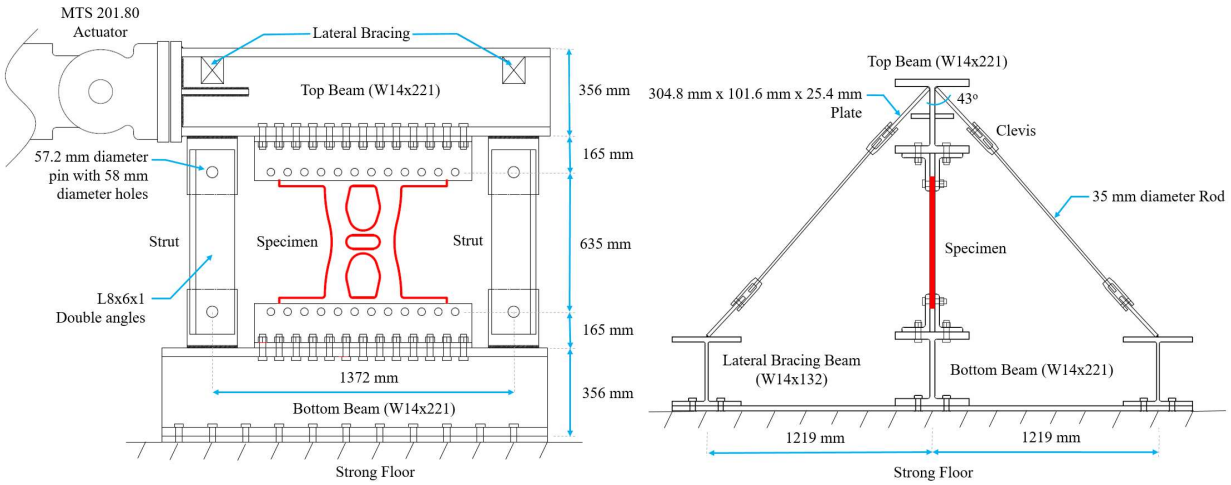

a) Test Frame b) Lateral Bracing

Fig. 6. Test Setup

The FEMA 461 cyclic displacement protocol was adopted with a starting displacement amplitude of 0.762 mm, two cycles at every displacement step, and a 40% increase in displacement from one step to the next. The displacement steps were continued until the specimen experienced near complete loss of lateral strength. The displacement rate at the start of the test was 6.35 mm/min and was doubled at displacements of 2.9 mm, 8 mm, 22 mm, 60.5 mm.

Fig. 7b shows the instrumentation plan which included 1) an internal actuator displacement sensor; 2) actuator load cell; 3) four horizontal string potentiometers, SP1, SP2, SP3, SP4, to measure horizontal displacements at different heights; 4) two diagonal string potentiometers, SP6R and SP7L and two vertical linear potentiometers, LP1R and LP2L, to compute shear distortion angles of the structural fuse; and 5) four strain gages were attached to each angle of the struts as shown in Fig. 7b which was correlated with axial force in the struts. The reported shear angle is the average of the computed shear angles at the left (sensors LP2L and SP6R) and right (sensors LP1R and SP7L) of the specimen using the law of cosines and thus the measured shear angle excludes the effect of specimen rigid body motion. A GOM Correlate Pro Digital Image Correlation (DIC) system was used to obtain strain and displacement fields on the specimen face.

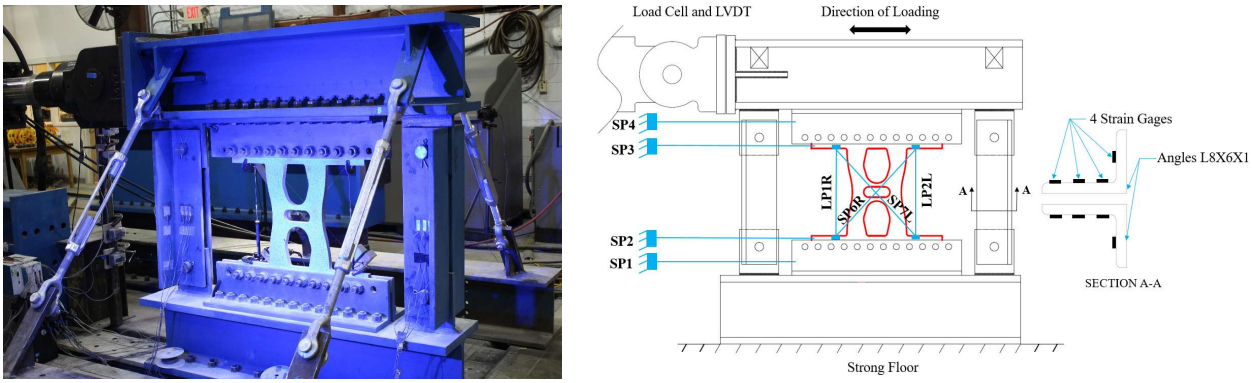

(a) Picture of test setup

(b) Instrumentation plan

Fig. 7. Overall Test Setup

Experimental Behavior

Tests results from the three structural fuse specimens are discussed in this section starting with the single straight link specimen, STL, for context, and then progressing to the optimized shapes, OPT1 and OPT2, respectively. In order to make a relative comparison between specimens, the vertical axes of the hysteretic plots are expressed by normalized shear ratio V/V_{exp} where V is

the recorded shear force and V_{exp} is the yield strength of the specimen obtained from the experiment. More specifically, yield strength, V_{exp}, was calculated as the shear force at the intersection of initial stiffness and line tangent to the hysteresis curve at positive 4% shear angle. The horizontal axis is expressed in terms of shear angle which is conceptually the shear displacement divided by the link length of 508 mm, although the shear angle was measured using diagonal displacement sensors as described in the previous subsection.

Fig. 8 presents the load-deformation curve and summarizes the remarkable events for Specimen STL. This straight link structural fuse was first observed to have yielding at one corner at a shear angle of about 1%. Inelastic deformations continued to spread as evidenced by the whitewash flaking off at all four corners of the specimen, confirming the locations of plastic hinging at the ends of the link. The first fracture occurred at the bottom right corner at the negative peak of the 6.5% shear angle cycle, resulting in a loss of strength and stiffness. The second and third fracture initiated at the bottom left and top right corner, respectively in the next cycle. Eventually, the shear strength of Specimen STL approached zero after the fourth fracture occurred at the bottom left corner (at negative peak of 10.7% shear angle). All four fractures started at the corners and propagated toward the bolts behind the angles as illustrated in Fig. 8. No out-of-plane motion or buckling was observed during the test.

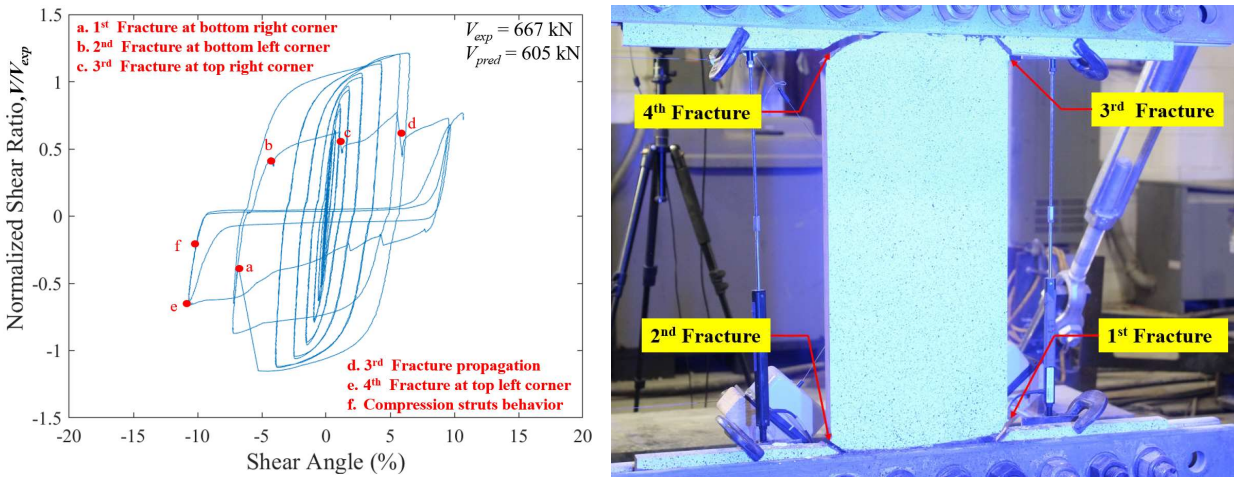

a) Hysteretic curve

b) Picture of Specimen at Point f

Fig. 8. Specimen STL

The hysteretic behavior and summary of behavior for Specimen OPT1 are presented in Fig. 9. First yielding was observed on the ties at 0.8% shear angle although the legs remained relatively elastic up to 2.2% shear angle. The ties were observed to be fully yielded (i.e., all white wash flaked off across the full width) at 3.1% shear angle, followed by full yielding of the legs at 8.5% shear angle. Due to a concentration of inelastic deformations in the ties, fracture started in the tie and led to full tie fracture during the first cycle at 16% shear angle followed by global shear buckling. Fractures initiated in the leg at 22% shear angle, and at 33% shear angle the top right leg fully fractured. It is noted that the fractured parts of the legs were contacting each other during the subsequent cycles leading to some additional strength. Eventually, there was a crack at the bottom left leg and full fracture during the first cycle at 45% shear angle.

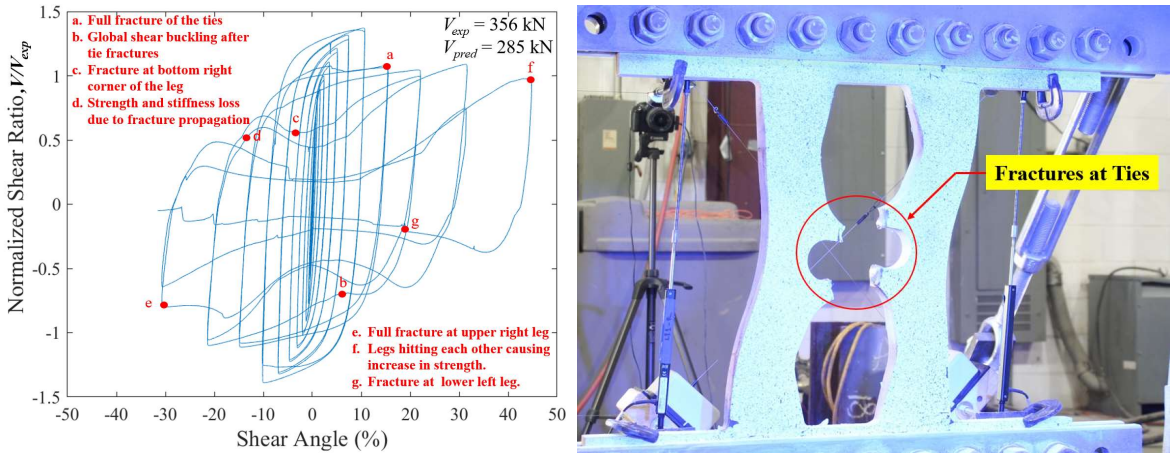

a) Hysteretic curve b) Picture of Specimen at Point a

Fig. 9. Specimen OPT1

Fig. 10 illustrates a summary of behavior for Specimen OPT2. The ties started yielding at 0.8% shear angle, while evidence of yielding in the legs did not occur until 1.6% shear angle. The ties formed visually observable plastic hinges (large plastic rotations) at the locations labeled as tie fractures in Fig. 10b at 3.1% shear angle, followed by full fractures of the ties at the same locations at approximately 12% shear angle. The first, second and third fracture of the legs occurred at the upper left, lower left and upper right plastic hinge, respectively leading to a near complete loss of load carrying strength.

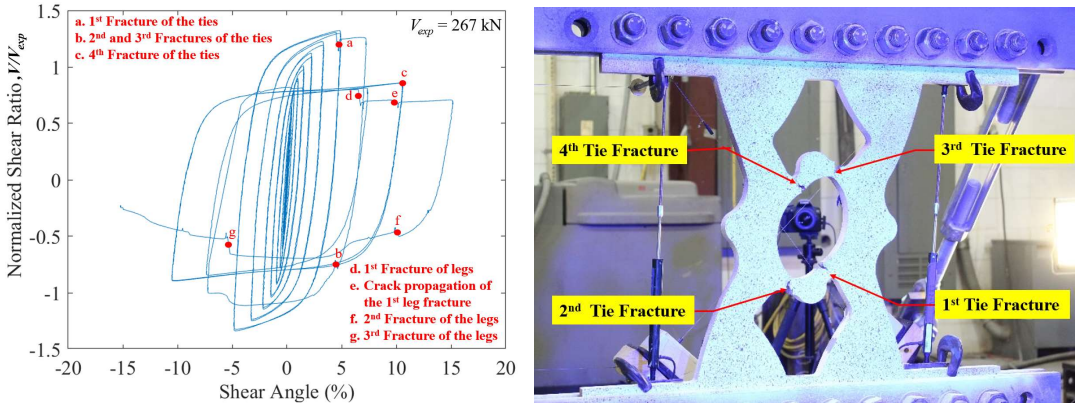

a) Hysteretic curve b) Picture of Specimen at Point c

Fig. 10. Specimen OPT2

Discussion of Experimental Results

A summary of behavior for all three specimens is presented in Table 2. The predicted shear strength for Specimen OPT1 was calculated using Eq. (14), while the predicted shear strength for Specimen STL was calculated based on the plastic section modulus of the rectangular cross-section and assuming a plastic hinge at each end of the straight link. Predicted shear strength was calculated using measured geometry and measured material yield stress. Measured shear yield strength, V_{exp}, was calculated as the shear force at the intersection of the initial stiffness and a line tangent to the hysteretic envelope at positive 4% shear angle. Ultimate shear force is the maximum recorded shear force and overstrength was computed as the ratio of ultimate shear force, V_u and measured shear strength, V_{exp}.

Table 2. Summary of specimen behavior

Specimen	Initial Stiffness (kN/mm)	Predicted Shear Yield Strength V_{pred} (kN)	Measured Shear Yield Strength V_{exp} (kN)	Ultimate Shear Force V_u (kN)	Shear Angle at Peak Force & Final Fracture (%)	Over-strength
STL	191	605	667	810	6.5% & 11%	1.21
OPT1	89	285	356	489	10.7% & 45%	1.38
OPT2	91	N/A	267	354	4.8% & 16%	1.33

As shown in Table 2 Specimen OPT1 and Specimen OPT2 had similar initial stiffness, which is reasonable since the associated topology optimization used the same volume fraction. Specimen STL, on the other hand, did not use the same volume of material or have the same shear strength as the other two specimens, so it is more useful for comparing progression of limit states, deformation capacity, and overstrength.

Specimen OPT1 had approximately 33% larger measured shear yield strength than Specimen OPT2, which is also expected because Specimen OPT 1 had a larger target ratio of shear yield strength to shear buckling strength, V_Y/V_B =0.2, compared to V_Y/V_B =0.1 for Specimen OPT2.

Avecillas and Eatherton (2020) showed that different target values of V_Y/V_B resulted in different values of shear yield strength, V_Y, while the shear buckling strength, V_B, remained similar, suggesting a maximum shear buckling resistance for a given volume fraction. The predicted shear yield strengths were conservatively smaller than the experimentally obtained values by approximately 10% for Specimen STL and 20% for Specimen OPT1. Differences between predicted and measured shear yield strength are likely due to inaccuracies in the location of plastic hinges, spreading of inelasticity so the plastic hinges are not a point, and strain hardening of the material.

The overstrength of a structural fuse is an important parameter because it defines the level of force demands applied to the surrounding structural members. Overstrength is often limited by buckling or fracture of the specimen such as Specimen STL which had the smallest overstrength because fracture occurred before the section at the ends of the link experienced as much material strain hardening as might have occurred in the plastic hinges of the optimized shapes. Values of overstrength for Specimens OPT1 and OPT2 suggest that surrounding structural members should be designed for 40% larger force than the shear yield force (or 70% larger force than the predicted shear force based on Specimen OPT1).

The fundamental objective of the optimized structural fuse shapes is to encourage yielding while resisting buckling, and indeed, Specimen OPT2 did not undergo buckling throughout its entire loading history up to full fracture. Specimen OPT1 did not have observable buckling until after the ties fractured. The results from Specimen OPT1 show that buckling is intimately related to fracture of the ties which cannot be captured with models that do not simulate fracture.

Perhaps the most distinctive aspects of the specimens' behavior was their progression of failure and fracture. Specimen OPT1 exhibited full hysteretic behavior associated with stable

plastic hinging up to the 10.7% shear angle cycles compared to only 6.5% shear angle for Specimen STL, and 4.8% shear angle for Specimen OPT2. The subsequent loss of strength for Specimen STL was due to fracture at the ends of the link, whereas Specimens OPT1 and OPT2 both experienced tie fracture first, while the legs and thus the load path remained intact. Tie fracture led to a reduction in shear strength of approximately 20% and 40%, respectively for Specimens OPT1 and OPT2, but this reduced strength remained stable, with associated substantial energy dissipation, through shear angles of up to 20% and 12%, respectively at which time the legs started to fracture. Conversely, Specimen STL experienced substantial and uncontrolled degradation in strength and energy dissipation capacity after fracture started at the end of the link. Unlike Specimen STL, these results suggest that structural fuse shapes like Specimens OPT1 and OPT2 might have a two-stage behavior with functional shear angle up to 20% and 12%, respectively, while straight link was only useable up to 6.5% shear angle.

In summary, the type of behavior demonstrated by Specimen OPT1 can be advantageous for the following reasons: 1) full hysteretic behavior up to 10% shear angle which may be a reasonable deformation capacity for design at the design earthquake hazard level, 2) after ties fracture at approximately 10% shear angle, the strength drops limiting the amount of overstrength in the structural fuse, 3) the structural fuse shape has a substantial reserve deformation capacity allowing shear angles up to 20% before leg fracture and more than 30% before complete loss of strength. While Specimen OPT2 showed similar characteristics, it demonstrated smaller shear strength and smaller deformation capacity, so it may not be as desirable for use in practical structural fuses.

COMPUTATIONAL STUDY

Specimen OPT1 exhibited promising behavior for a structural fuse, but for practical design situations, it may be necessary to vary the design parameters to produce different stiffness, strength, or fracture resistance. For that reason, a parametric computational study was conducted to evaluate the effects of design variables on structural performance of the OPT1 configuration. First, the finite element (FE) modeling approach is presented and validated against the experiments.

Finite Element Modeling Approach and Validation

The commercial program LS-DYNA was used to create FE models of the specimens. The geometry of each test specimen was modeled and meshed using fully integrated 8-node solid elements with an element size (i.e average length of an 8-node solid element) of 3.8 mm. A nonlinear isotropic hardening and kinematic hardening material model was used for the steel with fracture captured using the model created by Huang and Mahin (2010), referred to as Material 153 in LS DYNA. The plasticity model is a function of five calibrated parameters including yield stress, σ_{yo}, linear isotropic hardening parameter, H_1, nonlinear isotropic hardening parameter, β, linear kinematic hardening parameter, H_2, and nonlinear kinematic hardening parameter, γ. Additionally, three fracture related constants are defined: two calibrated parameters that define the evolution of damage, s and t, and a critical value of damage, D_C, when the material is considered to be fractured. Hardening and fracture parameters were calibrated using trial and error to find the best match for monotonic tension coupon tests and all three structural fuse test specimens, with resulting material parameters: E=224,000 MPa, σ_{yo}=376 MPa, H_1= 414 MPa, β=6, H_2= 3516 MPa, γ=15, s=0.3, t=1.49, D_C=0.5.

In order to capture buckling, geometric nonlinearity was included in the modeling scheme and initial imperfections were applied in the shape of the first eigen-buckling mode shape scaled to a maximum out-of-plane displacement magnitude of $L/1000$, where L is the link length of the structural fuse. Fig. 11 shows an example finite element model with mesh for Specimen OPT1. The nodes along the bottom edge of the model were restrained against all translational motion, while the nodes along the top edge were constrained to a reference node that was subjected to measured histories of motion recorded during the tests. Measured translation along the x-axis (δ_x) was obtained as the difference between horizontal string potentiometers SP2 and SP3. Vertical displacements along the y-axis (δ_y) and rotations about the z-axis (θ_z) were computed based on measurements of the two vertical linear potentiometers, while out-of-plane displacements, δ_z, were obtained from the DIC system. The top and bottom boundaries of the FE model are taken at the bolt lines of the tested specimen. Further details can be found in Nguyen (2022).

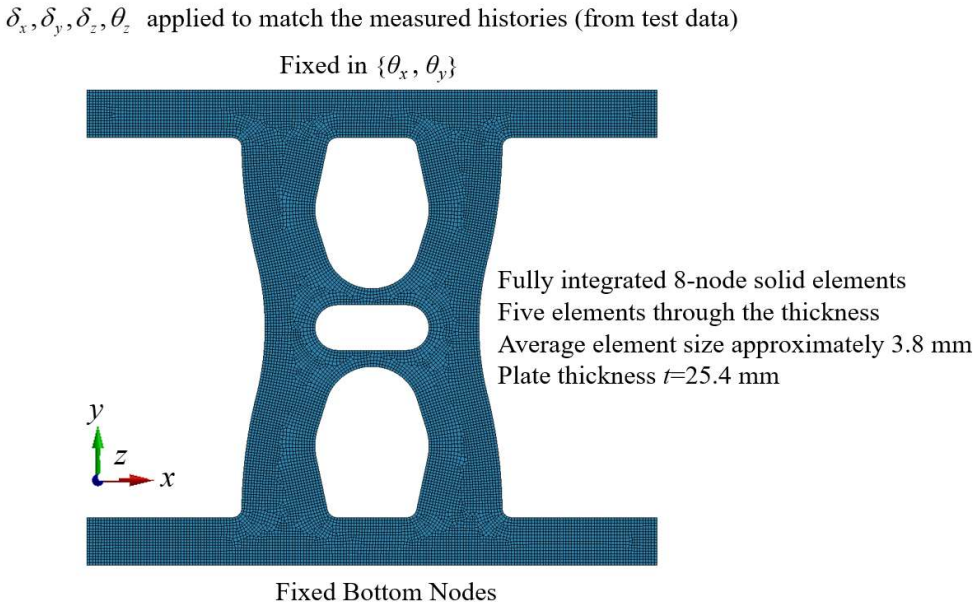

Fig. 11. Example FE model

A comparison of computational model results to experimentally obtained hysteretic behavior is illustrated in Fig. 12. Qualitatively, the overall shape and pinching behavior obtained from computational FE models match the experimental behavior well. While peak forces and stiffness are captured for OPT1 and OPT2, the peak strength obtained from the Specimen STL model overestimated peak forces measured from the experiment, likely due to sources of flexibility in the experiment that were not modeled such as slip of bolted connections at the top and bottom of the specimen.

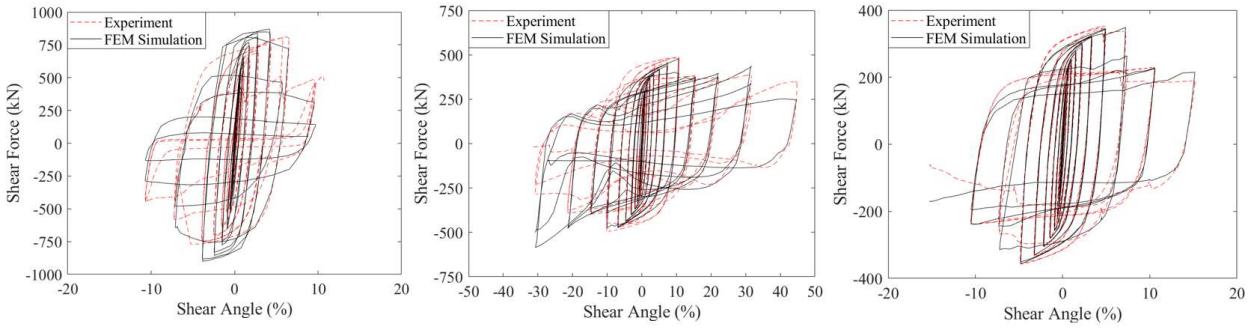

(a) Specimen STL (b) Specimen OPT1 (c) Specimen OPT2

Fig. 12. Hysteresis comparison of experiments to FE models

Although not shown here, the FE models captured the locations where yielding initiated and the evolution of yielding up to full plastic mechanisms as compared to locations observed to yield during the tests as whitewash flaking. Fig. 13 shows the deformed shapes and associated fractures at the end of each of the three tests. The deformed shapes from the models are shown at shear angles of approximately 12%, 40% and 16% for Specimen STL, Specimen OPT1 and Specimen OPT2, respectively. The shear angle amplitude associated with fractures of FE models match well with those from the tests, largely because the fracture parameters were calibrated accordingly. However, it is also observed that fracture locations in the FE models match well with those that occurred during the tests, such as the fracture initiation location and propagation

direction for Specimen STL. For both Specimen OPT1 and OPT2, the FE models captured the progression of behavior starting with fracture of the ties, lateral torsional buckling of the legs in Specimen OPT1, and then final fracture in the legs. The ability of the FE models to capture load-deformation behavior and relevant failure modes implies they are appropriate for use in the parametric study.

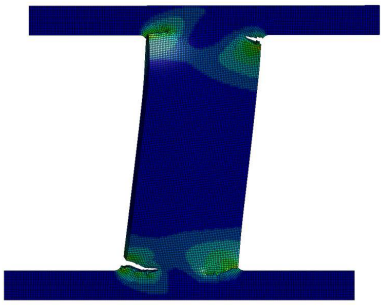

(a) Fractures of STL from FE

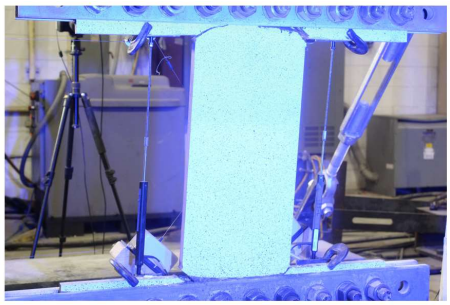

(b) Fractures of STL from testing

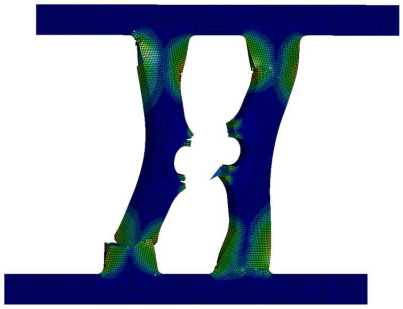

(c) Fractures of OPT1 from FE

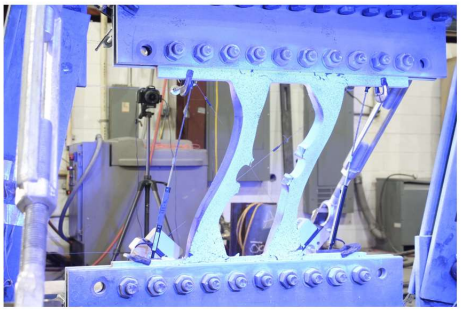

(d) Fractures of OPT1 from testing

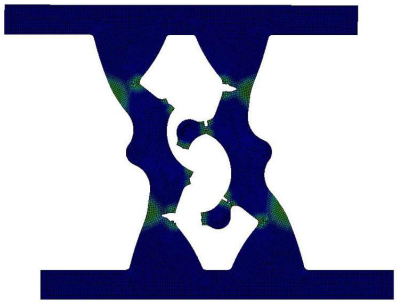

(e) Fractures of OPT2 from FE

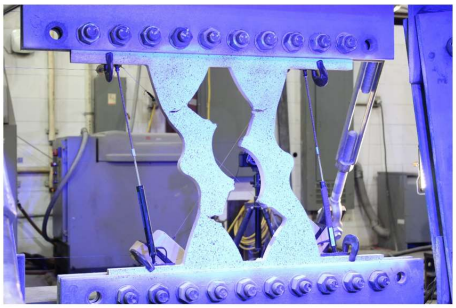

(f) Fractures of OPT2 from testing

Fig. 13. Comparison of fractures and deformed shapes

Parametric Study Description

The experiments showed that Specimen OPT1 exhibited several advantages in behavior compared to the other optimized shape, so the OPT1 shape is selected for further study. The experiments also highlighted the fact that although the topology was optimized to resist buckling, there are other considerations that are important in a structural fuse such as fracture resistance, ductility, and the ability to adjust strength and stiffness to match application specific requirements. Therefore, a parametric computational study was conducted to examine how the five geometric parameters that define the structural fuse shape, affect aspects of the cyclic behavior including stiffness, strength, equivalent viscous damping, buckling and fracture. The goal of the parametric study is to facilitate the design of structural fuse shapes using the OPT1 topology to get a desired strength, stiffness, buckling resistance, and fracture resistance.

The FE modeling approach was identical to that used for validation in the previous section, except that the applied displacement history was modified. While there are many possible configurations for incorporating structural fuses into a building, the context of the eccentrically braced frame (EBF) was selected as a practical setting. In a configuration like EBF, there may need to be struts adjacent to the structural fuse to resist axial forces similar to those used in the experimental program. Therefore, the applied displacement protocol to match this situation consists of a horizontal displacement, δ_x, following the cyclic EBF displacement protocol in AISC 341-16 (AISC, 2016), and a vertical displacement, δ_y, following an arc associated with the constraint enforced by pinned struts.

Each of the five geometric parameters that define the topology, including tie width, W_T, tie radius, R, leg width, W_L, link length, L, and plate thickness, t, were varied individually while holding the other variables constant. The variation in each geometric parameter is described in

Table 4 where the parameters representing the baseline configuration are shown in bold and underlined. The result is five sets of models wherein one parameter is varied in each set with a total of 20 models across the entire study.

Table 4. Range of geometric parameters considered.

Geometric Parameters	Values Used in Parametric Study (mm)
Tie width (W_T)	12.7 ; 19.1 ; **30.2** ; 63.5 ; 101.6
Tie radius (R)	**89** ; 102 ; 127 ; 152 ; 178
Leg width (W_L)	102 ; 127 ; 159 ; **164** ; 178
Link length (L)	508 ; 610 ; **711** ; 914 ; 1219
Plate thickness (t)	6.4 ; **12.7** ; 19.1 ; 25.4

Values in **bold and underlined** represent the baseline configuration

Parametric Study Results on Hysteretic Shape, Strength, and Stiffness

To get an idea of how the geometric parameters affect structural fuse behavior, Fig. 14 presents the hysteretic shear force vs. shear angle response for the baseline configuration along with the response from a model varying each of the five parameters. Comparing Fig. 14b to Fig. 14a shows that increasing the tie width, W_T, from 30.2 mm to 101.6 mm leads to an increase in strength and stiffness, but pinching of the hysteretic shape associated with buckling occurs at approximately 50% smaller shear angle. Because the tie becomes stronger, the plastic mechanism changes, shifting inelasticity away from the ties and into the legs, and as a result the buckling resistance nature of the original optimized topology is compromised, and there is a loss of energy dissipation capacity. On the other hand, tie radius, R, does not have a significant effect on the hysteretic behavior of the topology as seen from the negligible difference between Fig. 14a and Fig. 14c. As observed from Fig. 14d, reducing leg width, W_L, from 164 mm to 102 mm resulted in smaller strength and stiffness, but the topology better resists buckling compared to the baseline configuration because the legs are less prone to lateral torsional buckling. Link length, L, and plate thickness, t, perhaps have the most intuitive effect on load-deformation behavior because they are

directly related to slenderness of the cross-sectional elements. Increasing overall link length, L, from 711 mm to 1219 mm means larger overall slenderness, thus reducing buckling resistance (Fig. 14e), whereas increasing plate thickness, t, from 12.7 mm to 25.4 mm greatly reduces slenderness of the cross-sectional elements and thus has the effect of eliminating pinching due to buckling (Fig. 14f). Also, as expected, smaller link length or larger plate thickness are associated with greater strength and stiffness.

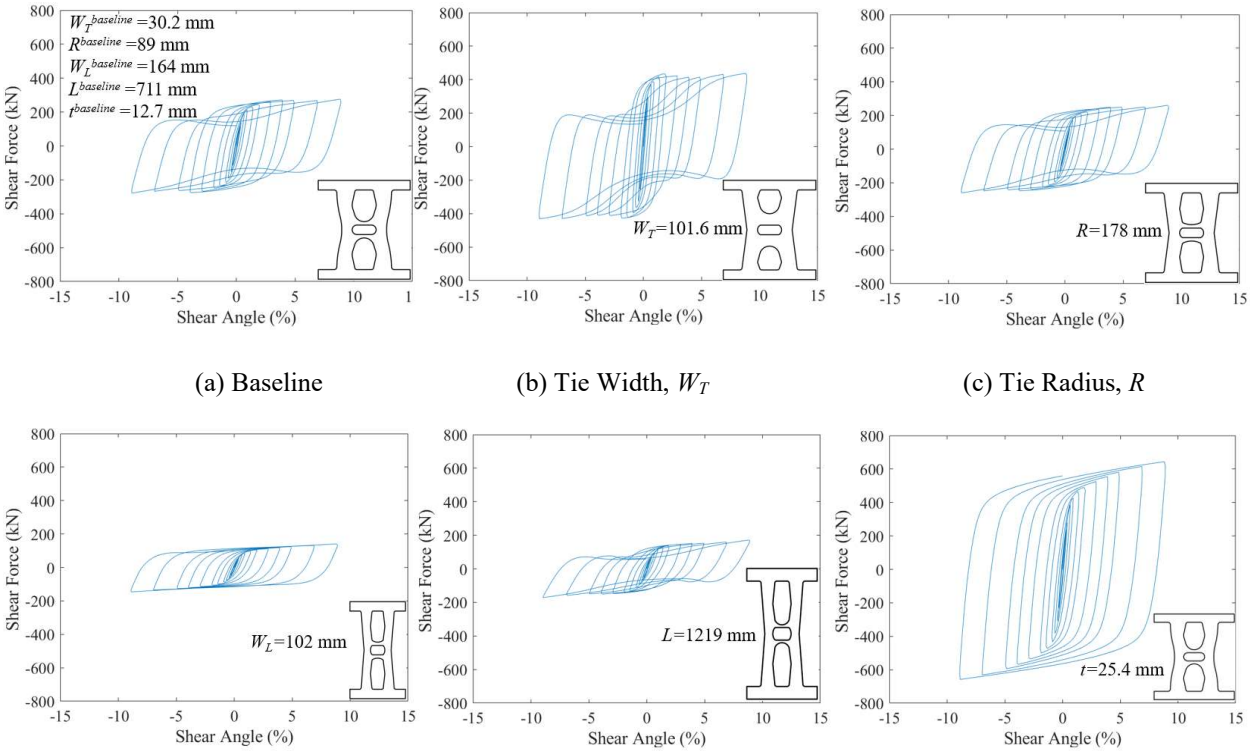

(a) Baseline (b) Tie Width, W_T (c) Tie Radius, R

(d) Leg Width, W_L (e) Length, L (f) Plate thickness, t

Fig. 14. Representative hysteretic curves

To understand the strength and stiffness results from all of the models, Fig. 15 shows the obtained strength and stiffness from each model normalized to the value for the baseline configuration given in a note on the figure. The horizontal axis represents the ratio of the geometric parameter for the model to that of the baseline configuration, and thus a value of unity is associated

with the baseline model. Perhaps one of the most straightforward trends in Fig. 15 is the effect of plate thickness, t, wherein strength and stiffness are proportional to thickness, i.e. doubling thickness will double the strength and stiffness. However, thickness also affects buckling behavior, so it may desirable to use other geometric parameters to individually adjust behavioral aspects. For instance, the stiffness is shown to be more sensitive to link length, L, than strength, as indicated by the steeper slope of the curve in Fig. 15b compared to Fig. 15a. Fig. 15 also shows that both strength and stiffness are more sensitive to leg width, W_L, than tie width, W_T, and not affected significantly by tie radius, R. The legs are therefore more important to the overall strength and stiffness of the structural fuse than the ties, but instead, the ties adjust the degree of coupling between the legs similar in concept to coupled shear walls. Adjusting the leg width and tie width should be done with care, however, because as described in the preceding paragraphs, if the plastic mechanism is changed, the shape may forfeit the buckling resistance for which it was optimized.

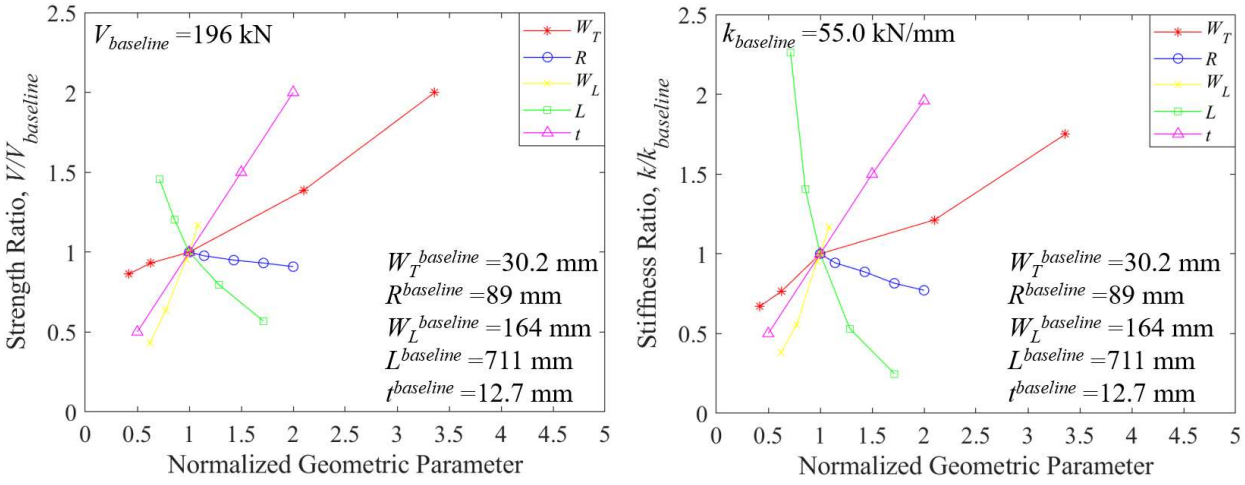

(a) Strength (b) Stiffness

Fig. 15. The effect of geometric parameters on strength and stiffness

In the discussion above, individual geometric parameters were shown to have different effects on stiffness, but in a practical design situation, an equation for stiffness as a function of these geometric variables is necessary. While it may be possible to derive such a formula using Castigliano's Theorem, a regression analysis is employed here to develop an equation with relatively simple form. First, a non-dimensional parameter expected to control the stiffness of the optimized shape, k_{ss}, given by Eq. (15), was determined by examining the relationship between stiffness and each variable shown in Fig. 15b. Then a linear regression analysis was conducted with results from the 20 models as shown in Fig. 16a to determine the constant of proportionality. The resulting equation is given in Eq. (16) to easily obtain stiffness of the structural fuse with geometry in the range of what was included in the parametric study. The stiffness of the baseline configuration, $k_{baseline}$, is given in Fig. 15b, and the geometric parameters, t, W_T, W_L, L, and R are defined in Fig. 3b.

$$k_{SS} = \frac{t(W_T + W_L)^2}{(L+R)^3} \tag{15}$$

$$k = 1011\left(k_{baseline}\right)\left(k_{ss}\right) \tag{16}$$

The observed shear strength from the FE models was compared to the predicted shear strength using Eq. (14) as shown in Fig. 16b. It was found that Eq. (14) accurately predicts the shear strength of the structural fuse shape, with one notable exception at the right side of the plot representing the configuration with largest leg width, W_L, where buckling caused a loss of strength.

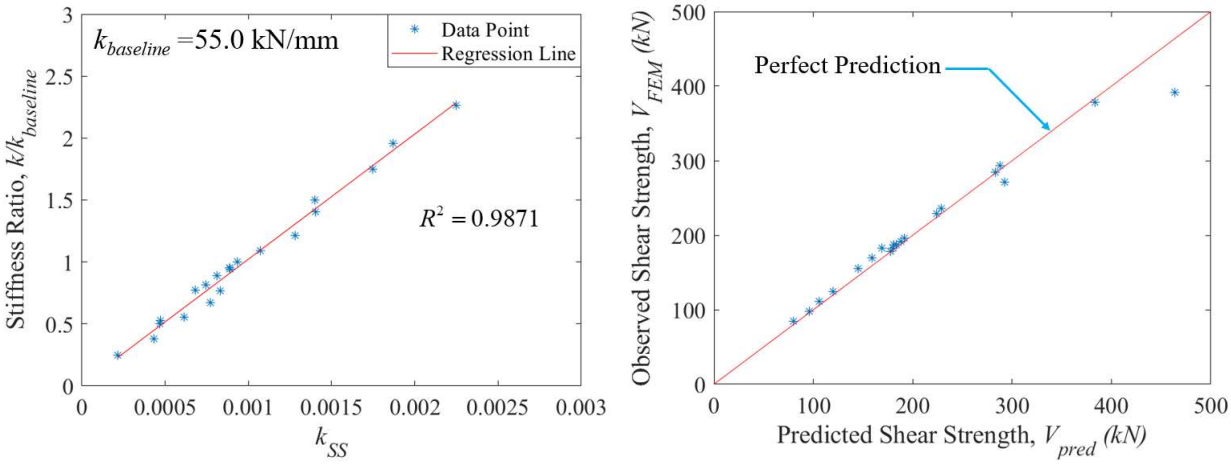

(a) Determining an equation for stiffness (b) Evaluating predicted shear strength from Eq. (14)

Fig. 16. Evaluating strength prediction and regression analysis to determine equation for stiffness

Parametric Study Results on Buckling, Energy, and Fracture

One of the primary purposes of a structural fuse acting as part of a seismic force resisting system is to dissipate seismic energy. Energy is dissipated through hysteretic damping which can be characterized by equivalent viscous damping. If the effective secant stiffness, K_{eff}, is calculated using Eq. (17), where δ^+ and δ^- are the maximum and minimum displacements, and P^+ and P^- are maximum and minimum shear force in the cycle, then equivalent viscous damping, ε_{eq}, can be calculated using Eq. (18) where E_d is the area inside the hysteretic loop for the same cycle.

$$K_{eff} = \frac{|P^+| + |P^-|}{|\delta^+| + |\delta^-|} \tag{17}$$

$$\varepsilon_{eq} = \frac{2}{\pi}\left[\frac{E_d}{K_{eff}(|\delta^+| + |\delta^-|)^2}\right] \tag{18}$$

The effect of four of the geometric parameters on equivalent viscous damping is shown in Fig. 17 for each cycle as a function of shear angle; no plot is included for the tie radius, R, because it was found to have no effect on equivalent viscous damping. The only two models that

demonstrated increasing equivalent viscous damping throughout the entire displacement history were the plates with thickness of 19.1 mm or greater as shown in Fig. 17a. These two models exhibited no pinching of the hysteretic shape associated with buckling. Conversely, the 6.4 mm thick plate has the smallest equivalent viscous damping of any of the models. Fig. 17b shows that even with relatively long link length of L=1219 mm, the structural fuse is still capable of significant equivalent viscous damping. Varying tie width, W_T, in Fig. 17c shows that increasing the tie width above a value of W_T=63.5 mm, leads to less energy dissipation because the plastic mechanism changes, thus leading to earlier buckling. This suggests a limited ability to increase W_T without adverse effects. For leg width, W_L, a similar equivalent viscous damping is observed from models with decreasing width down to W_L =159 mm, after which smaller W_L is associated with increased energy dissipation. This suggests that a design flexibility toward increasing W_L with improved buckling resistance.

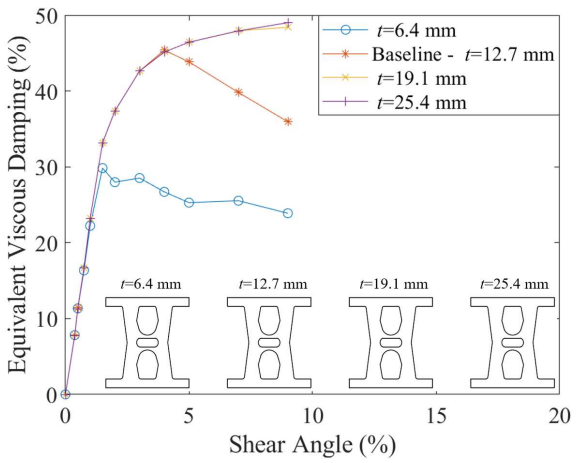

(a) Varying Plate thickness, t

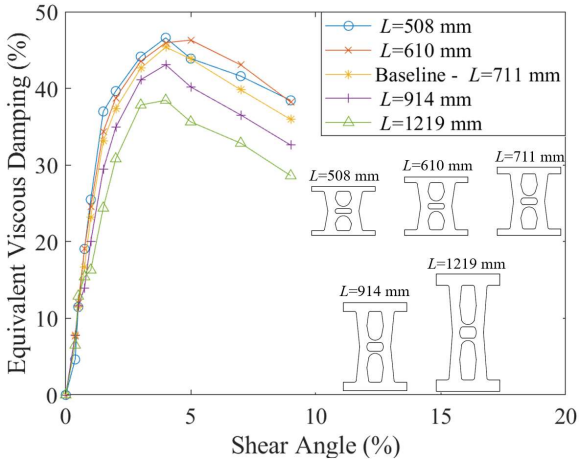

(b) Varying Link length, L

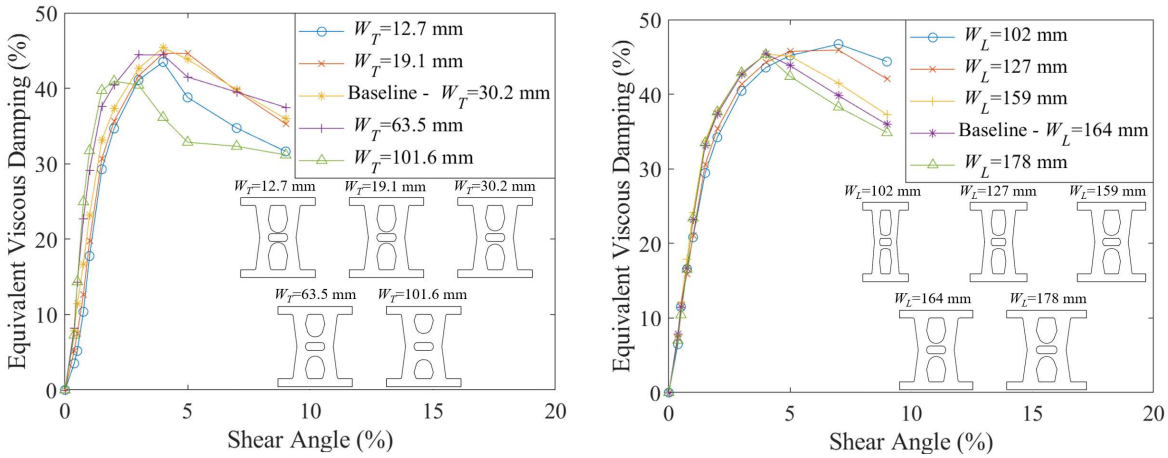

(c) Varying Tie width, W_T (d) Varying Leg width, W_L

Fig. 17. Equivalent Viscous Damping with Variations in Geometric Parameters

Out of plane displacements and effective plastic strain are also analyzed to understand the buckling behavior and fracture potential of these structural fuse shapes. The maximum out-of-plane displacement (δ_z) obtained from FE models at any time during the loading protocol are shown in Fig. 18a where both axes are normalized to the value from the baseline configuration, and the out-of-plane displacement, $\Delta_{z,baseline}$= 58.8 mm for the baseline. The maximum effective plastic strain in the model at any time during the loading history is shown in Fig. 18b, also normalized to the value from the baseline configuration which was $\varepsilon_{baseline}$=2.44 mm/mm.

Increasing the leg width, W_L, leads to the largest increase in out of plane displacements, followed closely by link length, L, as indicated by the slope of the curves in Fig. 18a. Increasing either of these geometric parameters leads to an increased susceptibility to a lateral torsional buckling mode of the legs. Increasing the tie width, W_T, also has the effect of increasing out-of-plane displacements, but not as severely. Changing any of these three geometric parameters, W_L, L, or W_T, did not have a substantial effect on maximum effective plastic strain though as shown in Fig. 18b. Instead, Fig. 18b shows that it is the tie radius, which was shown previously to have

negligible effect on most hysteretic parameters (strength, stiffness, equivalent viscous damping), that is related to effective plastic strain. An increase in the tie radius of 50% or more is shown to decrease the effective plastic strain by 20% which may be advantageous in resisting fracture. Increasing plate thickness was the best way to reduce out of plane buckling displacements as shown in Fig. 18a, but increasing plate thickness also led to increased effective plastic strains (Fig. 18b) as through-thickness strains become larger.

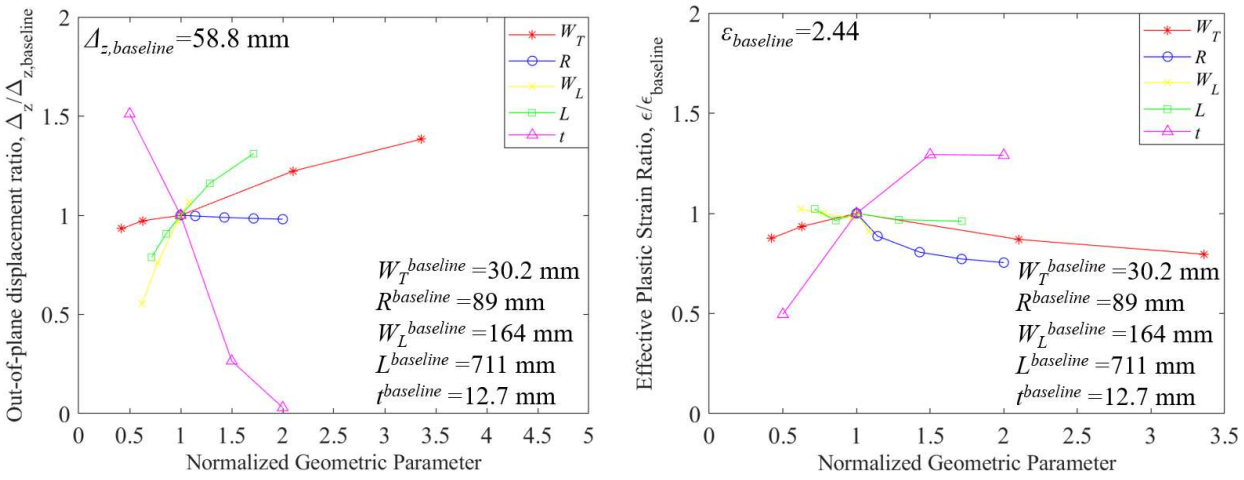

(a) Out-of-Plane Displacement (b) Effective Plastic Strain

Fig. 18. Effect of Design Parameters on Buckling and Fracture

CONCLUSIONS

A combined experimental and computational study was performed to investigate the seismic design and behavior of structural fuse shapes obtained previously from topology optimization to resist buckling while encouraging yielding. Of the two selected topologies, one of the shapes referred to as OPT1 was shown in the experiments to be capable of cyclic deformations up to 10% shear angle with full hysteretic behavior before the ties fractured, after which there was

a stable reserve strength through 20% shear angle before the legs began to fracture, and a shear angle of more than 30% before full loss of strength. This type of behavior offers several advantages as a structural fuse as it is capable of substantial energy dissipation, but then limits overstrength as the ties fracture shifting behavior to flexural hinging of the legs with 80% of the peak strength through large displacements. These characteristics are considerably better than the other optimized shape or the straight link specimen which fractured after 6% shear angle and then suffered uncontrolled degradation in shear strength.

The optimized shape, OPT1, can be uniquely defined using five geometric parameters, allowing the new structural fuse shape to be adapted to different design situations such as specific needs for strength, stiffness and deformation capacity. A parametric computational finite element study was conducted to extend the results of the experiments. To support use in practical design, an equation was derived for shear strength based on plastic mechanism analysis and another equation was obtained for stiffness based on the results of the parametric study. The effect of the five geometric parameters on strength, stiffness, energy dissipation, out of plane buckling, and effective plastic strain were evaluated and ranges of variables for which behavior was not adversely affected were determined.

ACKNOWLEDGEMENTS

This work was supported by the National Science Foundation under Grant No. CMMI-1453960. In-kind funding was provided by AISC and INFRA-METALS. Any opinions, findings, and conclusions or recommendations expressed in this material are those of the authors and do not necessarily reflect the views of the National Science Foundation or other sponsors.

REFERENCES

AISC. 2016. Seismic provision for structural steel buildings. ANSI/AISC 341-1. Chicago, IL: AISC.

ASTM Standard A370-07a. Standard test methods and definitions for mechanical testing of steel products. West Conshohocken, PA: American Standards for Testing and Materials International (ASTM); 2007.

Avecillas, J. (2019) "Topology optimization of steel shear fuses to resist buckling." M.Sc. thesis, Dept. of Civil Engineering, Virginia Polytechnic Institute and State Univ.

Avecillas, J.A., Eatherton, M.R. (2020). Controlling Out-of-Plane Buckling in Shear-Acting Structural Fuses through Topology Optimization. Journal of Structural Engineering. 146. 10.1061/(ASCE)ST.1943-541X.0002692.

Bergman, DM, Goel, SC (1987) Evaluation of cyclic testing of steel plate devices for added damping and stiffness. Report UMCE87-10. Ann Arbor, MI: University of Michigan.

Berman, J.W., and M. Bruneau (2005). "Experimental investigation of light gauge steel plate shear walls." J. Struct. Eng. 131 (2): 259–267.

Black, C. J., N. Makris, and I. D. Aiken. (2004) "Component testing, seismic evaluation and characterization of buckling-restrained braces." J. Struct.Eng. 130 (6): 880–894.

Bruneau, M., Cliffton, C., MacRae, G., Leon, R., and Fussel, A. (2014) Steel Structures Damage from the Christchurch Earthquake of February 22, 2011, NZST, Bulletin of the New Zealand Society of Earthquake Engineering, Vol. 44, No. 4, p. 297-318.

Cortes, G., and J. Liu (2011). "Experimental evaluation of steel slit panel–frames for seismic resistance." J. Constr. Steel Res. 67 (2): 181–191.

Deng, K., Pan, P., Li, W. and Xue, Y. (2015). “Development of a buckling restrained shear panel damper.” Journal of Constructional Steel Research, 106(1), 311-321.

Driver, R. G., Kulak, G. L., Kennedy, D. J., and Elwi, A. E. (1998b). Cyclic test of four-story steel plate shear wall” Journal of Structural Engineering, 124(2), 112-120.

Egorova, N., Eatherton, M. R. and Maurya, A. (2014). “Experimental study of ring-shaped steel plate shear walls.” Journal of Constructional Steel Research, 103, 179-189.

FEMA 461. Interim testing protocol for determining the seismic performance characteristics of structural and nonstructural components. Washington, DC (USA): Federal Emergency Management Agency; 2007.

Ghabraie, K., Chan, R., Huang, X. and Xie, Y. M. (2010). “Shape optimization of metallic yielding devices for passive mitigation of seismic energy.” Engineering Structures, 32(8), 2258-2267.

He, H., Wang, X. and Zhang, X. (2016). Energy-dissipation performance of combined low yield point steel plate damper based on topology optimization and its application in structural control." Advances in Materials Science and Engineering, 2016.

Huang, Y., and Mahin, S. A. (2010). PEER 2010/104 Simulating the inelastic seismic behavior of steel braced frames including the effects of low-cycle fatigue. Berkeley, CA.

Kobori T, Miura Y, Fukuzawa E, Yamanda T, Arita T, Takenaka Y, Miyagwa N, Tanaka N, Fukumoto T (1992). Development and application of hysteresis steel dampers. In: Earthquake Engineering the 10th Conference. Rotterdam: Belkema, 1992.

Lee C., K. Ju Y., Min J., Lho S., and Kim S. (2015), “Non-uniform steel strip dampers subjected to cyclic loadings”, Engineering Structures, 99 (2015), pp. 192–204.

Lemaitre, J., & Chaboche, J. L. (1990). Mechanics of Solid Materials: Cambridge University Press.

Liu, Y., and M. Shimoda. (2013). “Shape optimization of shear panel damper for improving the deformation ability under cyclic loading.” Struct. Multidiscip. Optim. 48 (2): 427–435.

LS-DYNA. 2011-2018 LSTC. http://www.lstc.com/.

Ma, X., Borchers, E., Pena, A., Krawinkler, H. and Deierlein, G. (2010). “Design and behavior of steel shear plates with openings as energy-dissipating fuses.” John A. Blume Earthquake Engineering Center Technical Report, (173).

Phillips, A.R., and M. R. Eatherton (2018). “Large-scale experimental study of ring shaped–steel plate shear walls.” J. Struct. Eng. 144 (8):04018106.

Zhu, B, Wang, T, Zhang, L (2018) Quasi-static test of assembled steel shear panel dampers with optimized shapes. Engineering Structures 172: 346–357.

Vian, D., M. Bruneau, and R. Purba. 2009. “Special perforated steel plate shear walls with reduced beam section anchor beams. II: Analysis and design recommendations.” J. Struct. Eng. 135 (3): 221–228.

4. DEVELOPMENT OF THE TIED BUTTERFLY SHAPE FOR STRUCTURAL FUSES

Trai N. Nguyen[1], Matthew R. Eatherton[2]

[1] Graduate Research Assistant, Department of Civil and Environmental Engineering, Virginia Tech, Blacksburg, USA.
[2] Professor, Department of Civil and Environmental Engineering, Virginia Tech, Blacksburg, USA.

ABSTRACT

Recently, there has been research and interest in structural fuses as a way to concentrate seismic damage in replaceable elements and protect the rest of the structure from inelastic actions. However, there is no consensus on structural fuse shape, particularly for structural fuses consisting of a steel plate subjected to shear deformations, because studies with different objectives arrive at different shapes. For example, studies seeking to optimize the structural fuse shape to maximize fracture resistance often result in something that looks like the butterfly-shaped link, whereas other studies that optimize the form to maximize buckling resistance result in a shape with links that are tied together. In this study, a new structural fuse shape, named the tied butterfly shape, was developed to integrate the advantages of both the buckling-resistant configuration and the butterfly-shaped link. First the concepts for the tied butterfly shape are presented along with plastic mechanism analysis to derive an equation for shear strength. Then, an experimental program is described including three tied butterfly shape structural fuses and one straight link structural fuse for comparison. Finite element models are then validated against the experimental results and a parametric computational study is presented that evaluates the effect of key design variables on the structural behavior of this tied butterfly shape. The experimental study revealed that the tied butterfly shape structural fuse was capable of maintaining stable hysteretic behavior up to a shear angle of 23% before fracture or buckling and that multiple tied butterfly shapes can be connected

together. Based on the plastic mechanism analysis and parametric study, design equations and recommendations for implementation in practice are provided.
Keywords: Structural Fuse, Tied Butterfly Shape, Optimized Topologies, Earthquake Engineering, Seismic Behavior

INTRODUCTION

Conventional structures dissipate seismic energy through the plastic hinging of main structural components including beams and columns which can lead to the excessive damages and high expenses for post-earthquake repair. Structural control systems have been developed with the purposes of minimizing damage induced by earthquake excitation and facilitating repairablity. Structural control systems can be categorized into three groups including (1) passive control systems (2) active control systems and (3) semi-active control systems. Among these three systems, passive control system, also known as passive energy dissipation system which does not require any external power source, has been considered as an effective method to mitigate structural damage induced by earthquake excitation.

Structural fuses are considered as passive control devices that dissipates hysteretic energy through plastic deformation of the metallic plate. Furthermore, structural fuses can be connected and located in a way that is replaceable, thus facilitates faster and more economical repair after significant seismic events while main structural components such as beams and columns remain in the elastic range with little or minor damage. Several researchers have conducted investigations on shear-acting structural fuses which rely on the steel plates subjected to in-plane shear deformations that dissipate seismic energy through global shear yielding or may have cutouts that result in local yielding mechanisms (i.e shear yielding or flexural yielding).

The most basis shear-acting structural fuse is the solid plate, which has no cutouts or engineering design such as link beam in an eccentrically braced frame (EBF) or web plate of a steel plate shear wall (SPSW). Two conventional approaches to the design of these shear-acting solid plate were adopted including (1) allowing shear buckling and relying on the ductile yielding along the tension diagonal (Berman and Bruneau 2003), (2) using stiffeners to prevent out-of-plane instabilities (Popov and Engelhardt 1988). Nevertheless, there are several challenges with these approaches such as (a) early buckling, thus results in pinched hysteretic behavior, (b) little resistance during load reversals, (c) thin plates have large shear strength.

More recently, structural fuses with different cutout patterns have been proposed for improved energy dissipation by converting global shear deformations into local yielding mechanisms (i.e shear yielding or flexural yielding). Egorova et al. 2014, Phillips and Eatherton 2018 reported that structural fuse shape using ring shapes, as shown in Fig. 1a, demonstrated fuller hysteretic behavior than solid plate because of the way a ring shape naturally resists buckling when subjected to shear deformation. An experimental study conducted by Cortes and Liu (2011) showed that the steel slit dampers, as illustrated in Fig. 1b, are capable of undergoing story drifts of at least 5%. Ma et al. 2010 showed that structural fuses with butterfly shaped links have excellent deformation capacity by locating plastic hinging away from the corners of the cutouts. Wide butterfly shaped links were also used between two columns in bridge piers by El-Bahey and Bruneau (2012). Lee et al. (2014) conducted a study on the hourglass shaped link, as shown in Fig. 1d. It was reported that damage is not concentrated at the link ends but rather cracks were distributed along the link length, implying that this shape can improve cyclic and fatigue performance. Additionally, an experimental study conducted by Zhu et al. (2018) showed that the hourglass-shaped link exhibited an increase in hysteretic energy dissipation of approximately 40%-

60% relative to conventional rectangular panel damper or straight link. Perforated SPSW with a series of circular holes, illustrated in Fig. 1e was shown to be a viable alternative to conventional solid SPSW without the need for stiffeners (Vian et al. 2009). A long the same lines, a computational study conducted by Koppal and Eatherton (2013) showed that SPSW with circular hole around the perimeter of the panel exhibits an improved cyclic performance relative to conventional SPSW system. Researchers such as Aschheim and Halterman (2002) and Shin et al. (2017) conducted computational and experimental studies on the different yielding mechanisms of wide flange section beam with elliptical holes (see Fig. 1f). Li and Li (2007) implemented an experiment on "dual function" metallic dampers and one of them is similar to the hourglass shape (referred as double X-shaped damper in the literature), illustrated in Fig. 1g. It was revealed that this shape does not only provide additional stiffness but also demonstrates good energy dissipation capacity (approximately 42%-87% of total input seismic energy).

More recently, topology optimization has been implemented to create new shapes to improve hysteretic performance of shear-acting structural fuses. Liu and Shimoda (2013) minimized cumulative equivalent plastic strain, producing a new shape that reduced the maximum cumulative equivalent plastic strain by approximately 80% that improves the overall deformation capacity of the shear panel damper. Deng et al. (2015) used simulated annealing (SA) algorithm to create a new shape with improved low-cycle fatigue performance. Ghabraie et al. (2010) used Bi-directional Evolutionary Structural Optimization (BESO) to maximize dissipated total plastic energy, resulting in a new shape that has even stress distribution and increased energy dissipation (up to 96%). It is worth mentioning that new optimized shapes obtained from these studies often resemble the butterfly shape. However, none of these studies attempted to control buckling resistance of the shear-acting structural fuse. A recent study conducted by Avecillas and Eatherton

(2020) used genetic algorithm (GA) to resist shear buckling while promoting yielding of the shear panel, creating promising buckling resistant shapes, as shown in Fig. 1g.

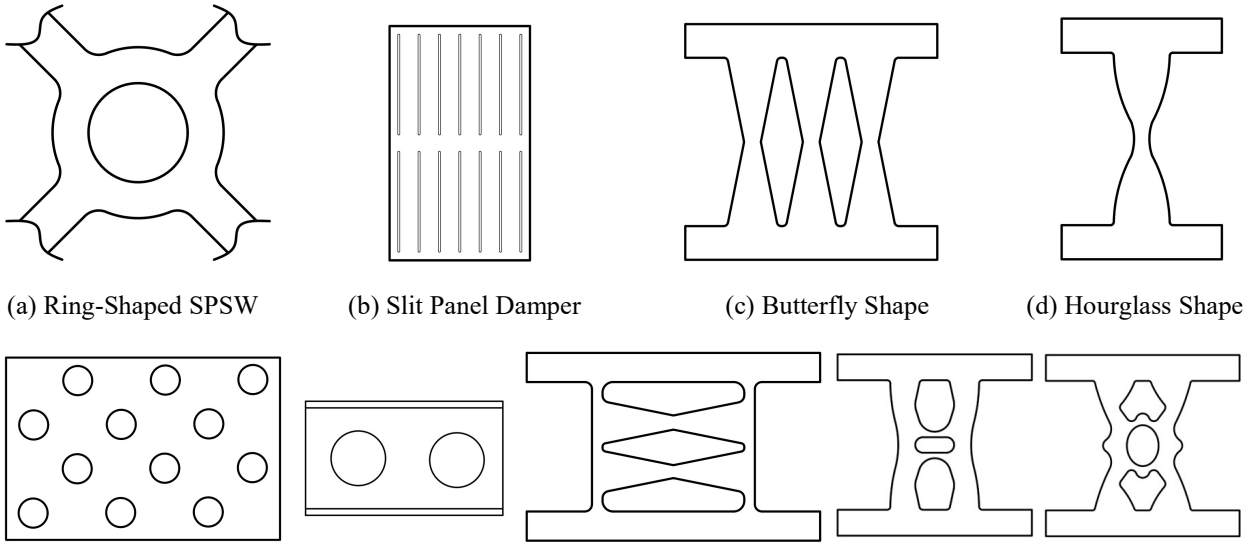

(a) Ring-Shaped SPSW (b) Slit Panel Damper (c) Butterfly Shape (d) Hourglass Shape

(e) Perforated SPSW (f) Elliptical Holes (g) Double X-shaped damper (h) Optimized Shapes

Fig. 1. Different cutout patterns for shear-acting structural fuse

Building on the advantages of butterfly-shaped links and the buckling resistant optimized topology, a new structural fuse shape was developed by integrating geometric characteristics of both into a unique configuration named the tied butterfly shape. The tied butterfly shape is expected to offer a good buckling resistance and low plastic strain concentration, thus maintaining stable hysteretic energy dissipation during load reversals. In this paper, the development of the tied butterfly shape is presented, followed by parameterization of this new shape. A generalized equation for shear strength is then derived using plastic mechanism analysis. Three variations of the tied butterfly shape were tested to evaluate the buckling and fracture resistance and compared a baseline specimen, the straight link. Computational nonlinear finite element models were validated against the experimental results, and a parametric finite element study was conducted to evaluate the effect of geometric parameters on structural performance of the tied butterfly shape.

CONCEPTS FOR THE TIED BUTTERFLY SHAPE

The butterfly-shaped structural fuse consists of a steel plate with cutouts leaving tapered links (i.e butterfly-shaped links), as shown in Fig. 2a. It was reported that butterfly geometries with taper ratio of a/b=1/3, yielding is encouraged to initiate at quarter points, midway between the wider ends and reduced middle section, resulting in full hysteretic behavior up to 30% shear angle across the link length without fracture or strength degradation (Kobori et al., 1992, Ma et al., 2010). Butterfly shaped links that produce flexural hinges at reduced section or link ends were shown to demonstrate full hysteretic behavior up to approximately 15%-20% shear angle (e.g Teruna et al. 2015). Although butterfly-shaped structural fuses have been shown to have substantial ductility and deformation capacity, they have also been shown to be prone to lateral torsional buckling (LTB) (e.g Plaut and Eatherton 2017, Fazampour and Eatherton 2019). LTB was observed and shown to have significant effect on strength, stiffness and energy dissipation of the structural fuses (e.g Eatherton et al. 2014, Ma et al. 2010).

Avecillas and Eatherton (2020) conducted a topology optimization with the objective to produce a new set of structural fuse topologies that resist out-out-plane instabilities and promote yielding when subjected to lateral loading. Fig. 2b illustrates one of the resulting topologies associated with a ratio of shear yield strength to elastic shear buckling load, V_y/V_b=0.2 and volume fraction of Δ=40%. This optimized topology was showed that they were capable to resist buckling up to about 9% shear angle, demonstrating full and stable energy dissipation (Avecillas and Eatherton 2020). Nguyen and Eatherton (2022) conducted a full-scale testing of this optimized topology to experimentally validate the bucking resistance capacity. The experimental results showed that this shape was capable of cyclic deformations up to 10% shear angle with full hysteretic behavior before the ties fractured, after which there was a stable reserve strength through

20% shear angle before the legs began to fracture, and a shear angle of more than 30% before full loss of strength, thus offers several advantages as a structural fuse as it is capable of substantial energy dissipation. This study confirmed two previous findings by Avecillas and Eatherton (2020) (1) this topology exhibits excellent buckling resistance capacity, thus stable energy dissipation, (2) large localized equivalent plastic strain, leading to potential for fracture, is one of the challenges associated with this configuration.

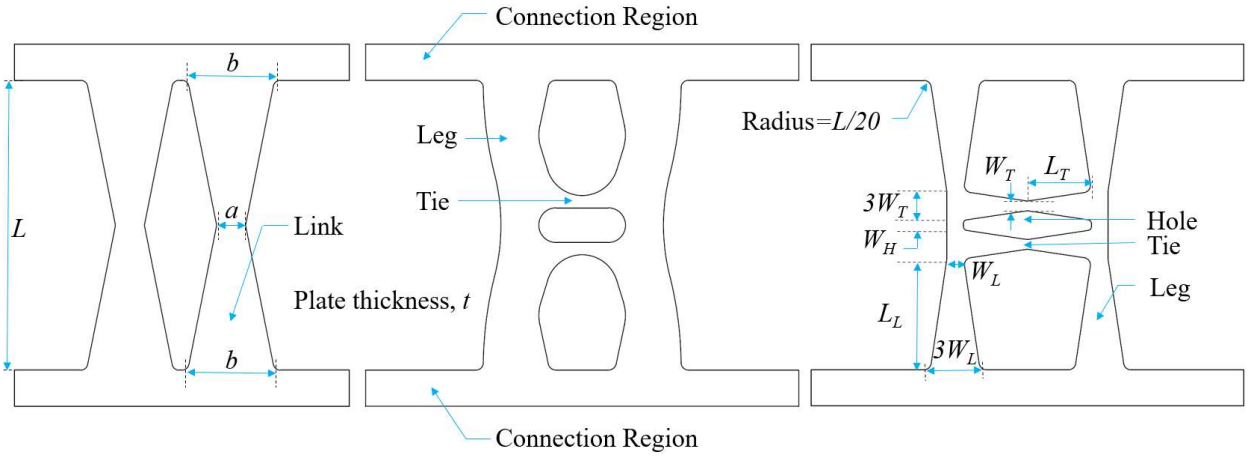

(a) Butterfly-Shaped Links (b) Optimized Shape (c) Tied Butterfly Shape

Fig. 2. Configurations of structural fuses

The new configuration, named the tied butterfly shape (TBF) was developed to integrate advantages of both the optimized topology (i.e good buckling resistance) and butterfly geometry (i.e good fracture resistance). The buckling-resistant optimized shape in Fig. 2b with two curving legs and two rounded ties is reimagined in Fig. 2c as two butterfly shaped legs with two butterfly shaped ties. A taper ratio of a/b=1/3 is selected for both legs and ties based on past research described above which shows inelastic strains forming away from corners and thus promoting fracture resistance. The new shape, tied butterfly shape, is therefore expected to limit out-of-plane displacement like the optimized shape while mitigating fracture potential like the butterfly shape, thus allowing larger total seismic energy dissipation.

The tied butterfly shape is a function of six unique geometric design parameters including tie width, W_T, tie length, L_T, leg width, W_L, leg length, L_L, overall length, L and plate thickness, t, as illustrated in Fig. 1c. A seventh variable, hole width W_H, is a dependent variable that is defined by variables L, L_L, and W_T. The radius at the intersection of all straight lines is given as a function of the length, $L/20$.

PLASTIC ANALYSIS

For the purposes of plastic analysis, the tied butterfly shape is idealized by centerline elements and locations of plastic hinges at the ties and legs are illustrated in Fig. 3a. The plastic hinges were assumed to form at quarter points since the taper ratio of a/b=1/3 was used (Ma et al., 2010). Elastic perfectly plastic moment curvature behavior was assumed and the legs and ties are assumed to have sufficient rotational ductility that the full plastic mechanism can form without fracture or buckling. This assumption will be verified in the experiments.

Fig. 3b illustrates plastic mechanism and tie configuration when subjected to shear force, V. The plastic moment capacity of the leg, M_{LP}, and tie, M_{TP}, at the plastic hinges are given in Eq. (1) where the width at the quarter point is twice the width at the narrow end, W_L, and W_T, respectively, and f_y is the material yield stress. The internal work, W_{int}, given in Eq. (2), is then obtained from tie angle, α, and leg angle, θ shown in Fig. 2b and external work, W_{ext}, given in Eq. (3), is a function of vertical distance between leg plastic hinges, Y_P, leg angle, θ and external shear force, V. By equating internal work, W_{int}, and external work, W_{ext}, Eq. (5) is produced by substituting the tie angle, tie angle, α, given in Eq. (4), and the distance between leg plastic hinges, $Y_P=L-L_L$, as shown in Fig. 2a. The resulting Eq. (5) gives the predicted shear strength of the tied butterfly shape as a function of the six unique geometric design variables and the yield stress of the material. Although shakedown analysis can be implemented for more accurate approximation

of the shear strength, it is not considered in this study as the resulting predicted equation obtained from shakedown analysis is not expected to make a significant difference compared to Eq. (5).

$$M_{TP} = \frac{tf_y}{4}\left(2W_T\right)^2 \tag{1}$$

$$W_{\text{int}} = 4(M_{LP}\theta + M_{TP}\alpha) \tag{2}$$

$$W_{ext} = V(Y_P\theta) \tag{3}$$

$$\alpha = \left(\frac{2L_T + W_L}{L_T}\right)\theta \tag{4}$$

$$V = \frac{4f_y t}{L - L_L}\left[W_L^2 + W_T^2\left(2 + \frac{W_L}{L_T}\right)\right] \tag{5}$$

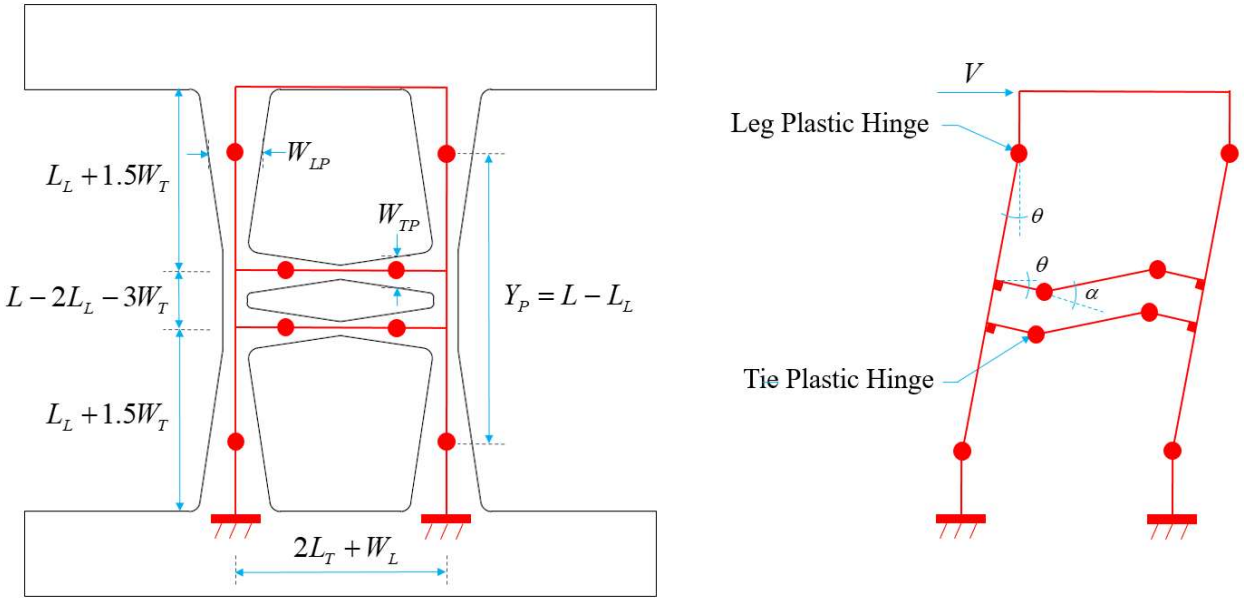

(a) Idealized Frame (b) Plastic Mechanism

Fig. 3. Plastic Analysis of tied butterfly shape

EXPERIMENTAL TESTING PROGRAM

Four specimens, three tied butterfly shapes and one straight link, were tested at the Thomas M. Murray Structures Laboratory at Virginia Tech. The purpose of this testing program was to investigate the cyclic behavior of tied butterfly shapes and then compare to the conventional straight link.

Test Specimens

Fig. 4 illustrates the geometry of the four specimens. The straight link Specimen STL acts as a baseline specimen for context as this represents a shape with no cutouts or engineering design. All specimens have the same link length of L=508 mm and plate thickness of t=25.4 mm. It is worth mentioning that Specimen TBF3, is proposed to test the effectiveness of connecting multiple tie butterfly shapes in series.

Specimens were cut using waterjet which was found to be cost-effective way to create smooth cuts as well as avoiding heat related affects along the cut edge. Top and bottom boundaries including bolt holes of the specimens were waterjet-cut with lowest quality while the main structural fuse part at the middle was waterjet-cut with highest quality. Specimen TBF3 had a defect at one of the ties due to fabrication, likely at the start of a cut that gouged deeper than intended, which was subsequently ground smooth to approximately 10 mm radius (see Nguyen, 2022 for details).

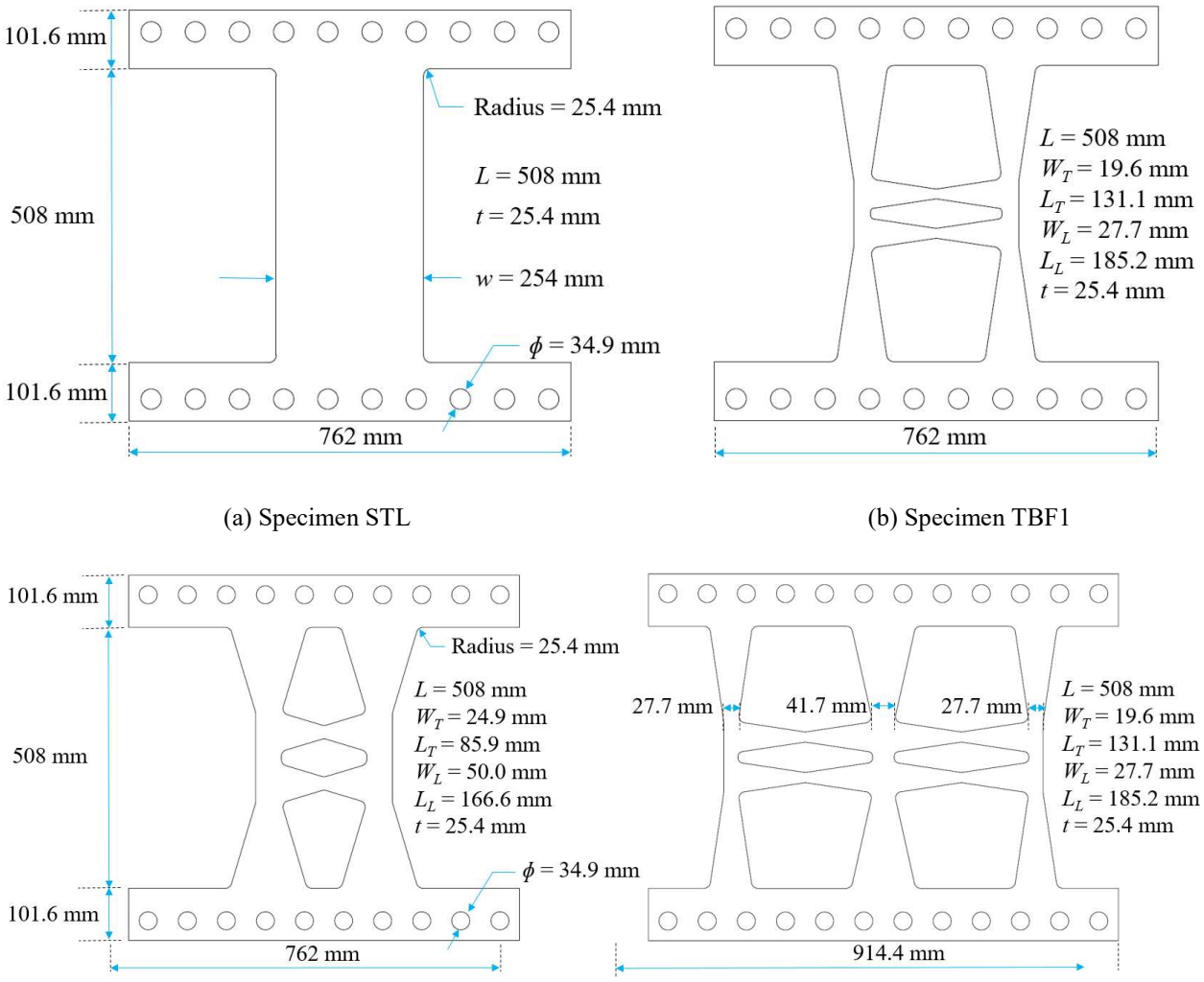

(a) Specimen STL

(b) Specimen TBF1

(c) Specimen TBF2

(d) Specimen TBF3

Fig. 4. Drawings of specimen geometries

All three specimens were fabricated from the same heat of steel, from which three tension coupons were also tested. Each tension coupon was waterjet cut with geometry in accordance with ASTM standard A370-07a for tension coupons with a plate thickness of 25.4 mm, width of the reduced section equal to 38.1 mm and gage length of 203.2 mm. Modulus of elasticity, yield stress, ultimate strength, and fracture elongation were 224,000 MPa, 376 MPa, 533 MPa and 26%, respectively, based on the average of the three coupons.

Test Setup and Details

The test setup illustrated in Fig. 5 was designed to apply shear displacements to the specimens using an MTS 201.08 hydraulic actuator with capacity of 1468 kN and stroke of ±381 mm. The specimen is bolted to the double angles, which are connected to the top beam and bottom beam, as illustrated in Fig. 5a. The pinned struts were designed to allow cyclic in-plane shear displacement. In addition, the test frame was restrained against out-of-plane motion at the top beam by a threaded rod system. All bolts used are grade A490 are fully pretensioned to prevent slip during the test.

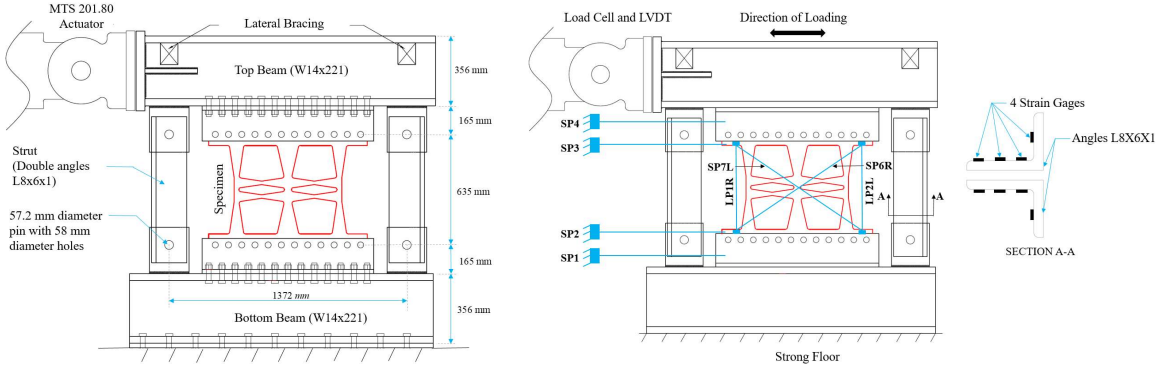

(a) Test Frame (b) Instrumentation Plan

Fig. 5. Test Setup

The FEMA 461 cyclic displacement protocol was adopted with a starting displacement of 0.762 mm, two cycles per displacement step, and a 40% increase in amplitude between displacement steps, until the specimen experienced near complete loss of lateral strength. The displacement rate started as 6.35 mm/min and was doubled at each of the following displacement steps: 2.9 mm, 8 mm, 22 mm, and 60.5 mm, with a final rate of 101.6 mm/min.

Fig. 5b shows the instrumentation plan which included 1) an internal actuator displacement sensor; 2) actuator load cell; 3) four horizontal string potentiometers, SP1, SP2, SP3, SP4, to measure horizontal displacements at different heights; 4) two diagonal string potentiometers, SP6R

and SP7L and two vertical linear potentiometers, LP1R and LP2L, to compute shear angles of the structural fuse; and 5) four strain gages were attached to each angle of the struts as shown in Fig. 5b which was correlated with axial force in the struts. The reported shear angle is the average of the computed shear angles at the left (sensors LP2L and SP6R) and right (sensors LP1R and SP7L) of the specimen using the law of cosines and thus the measured shear angle excludes the effect of specimen rigid body motion. Before the testing program, a calibration test was conducted where a vertical jack and reference load cell were inserted in place of the specimen and a conversion factor between average strut strain and force was obtained for each of the struts. A GOM Correlate Pro Digital Image Correlation (DIC) system was used to obtain strain and displacement fields on the specimen face.

Experimental Behavior

This section presents experimental results of four test specimens starting with the straight link Specimen STL for context, and then progressing to the tied butterfly shape Specimens, TBF1, TBF2 and TBF3, respectively. For the purposes of relative comparison between specimens, the *y*-axis of the plots is expressed by normalized shear ratio V/V_{exp} where V is the shear force obtained from the test and V_{exp} is the shear yield force of the specimen, calculated as the shear force at the intersection of the initial stiffness and a line tangent to the hysteresis curve at positive 4% shear angle. The *x*-axis is expressed in terms of shear angle obtained from two sets of sensors as discussed in the above section. For each specimen, the normalized shear force vs. shear angle is presented along with a picture identifying locations of fractures. The progression of limit states and failure modes of the four specimens are presented including a description of fractures and buckling.

Fig. 6 presents the hysteretic curve and summarizes the behavior for Specimen STL. This specimen was first observed to have yielding at one of the corners at a shear angle of approximately 1%. Inelastic deformations continued to spread out as evidenced by the whitewash flaking off at all four corners of the specimen, confirming the locations of plastic hinging. Then, the first fracture at the bottom right corner occurred during the 6.5% shear angle cycle, resulting in a loss of strength and stiffness. Due to a concentration of inelastic strain at the corner intersections of the link and boundary elements, the second and third fracture initiated at the bottom left and top right corner, respectively in the next cycle. Eventually, Specimen STL exhibited near zero shear strength after the fourth fracture occurred at the bottom left corner (at negative peak of 11% shear angle). All four fractures started at the corners and propagated toward the bolts behind the angles as illustrated in Fig. 6b. No out-of-plane motion or buckling was observed during the test.

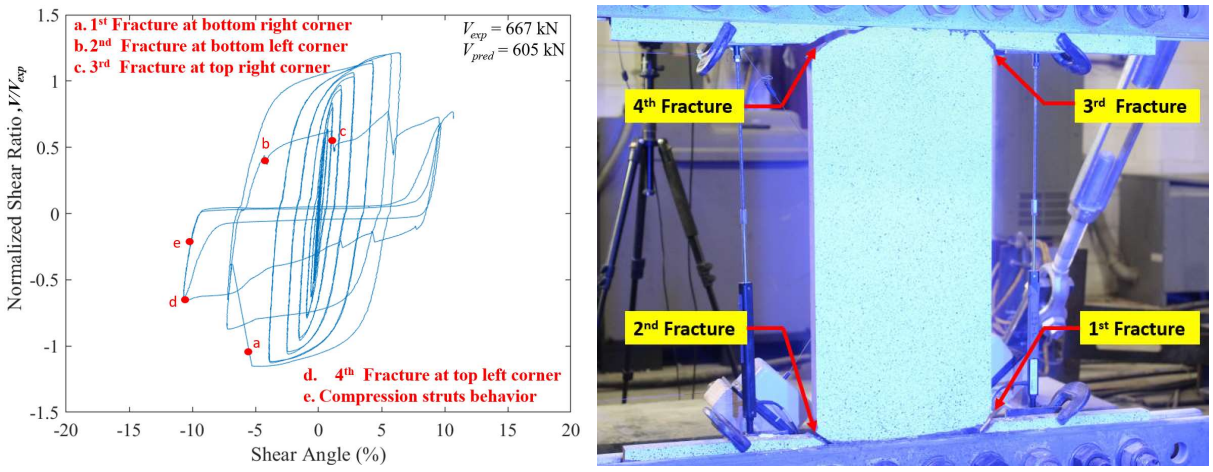

(a) Hysteretic curve (b) Picture of specimen at Point d

Fig. 6. Specimen STL

Fig. 7 illustrates the hysteretic curve and summary of events for Specimen TBF1. The first signs of yielding at the ties were observed at a shear angle of approximately 1%, followed by yielding of the legs at approximately 1.6% as evidenced by the whitewash flaking off. Due to the

concentration of inelastic strain, a fracture formed in the bottom tie, followed by crack propagation through this tie, resulting in the full fracture of the tie during the 23% shear angle cycle. In the second cycle of this shear angle, global shear buckling was observed as both legs started twisting. This twisting led to full fracture of the left and right legs at approximately 33% shear angle cycle, as shown in Fig. 7b.

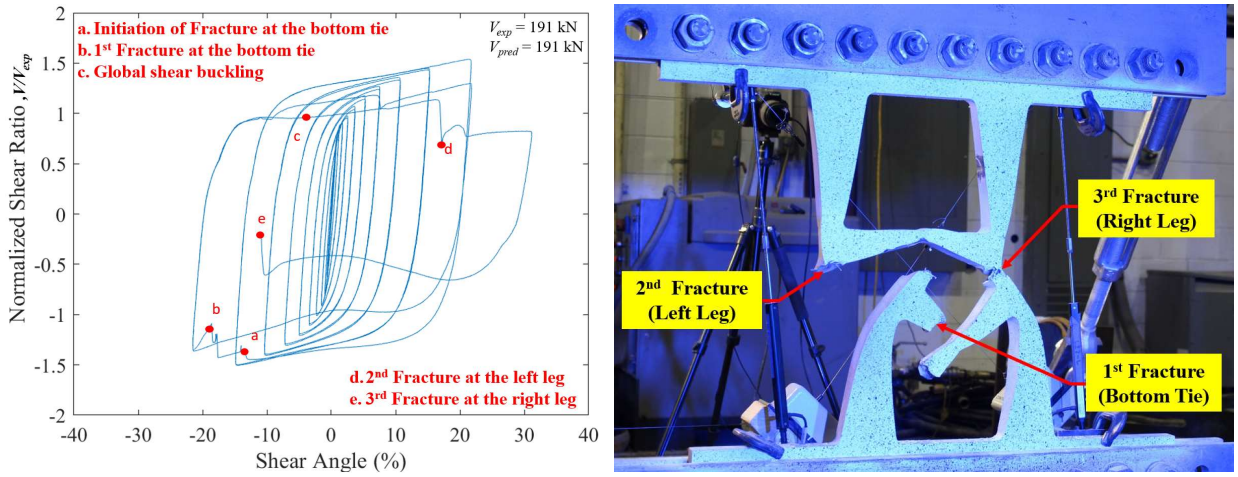

(a) Hysteretic curve

(b) Picture of specimen at Point e

Fig. 7. Specimen TBF1

Hysteretic loop and summary of behavior for Specimen TBF2 are shown in Fig. 8. Specimen TBF2 initiated yielding at the tie at the shear angle of approximately 1% which was similar to Specimen TBF1. The two legs then started to yield and continued to spread out inelasticity along the length in the next cycle as observed from the whitewash flaking off. The specimen was not observed to experience out-of-plane displacement until the first cycle of 17% shear angle. Out-of-plane displacement became severe at the end of this cycle, leading to loss of strength in the next two cycles. This was followed by the snap-through type instabilities. Due to concentration of inelastic strain, full fractures at the ties occurred during the 23% shear angle cycle, as illustrated in Fig. 8b. The tie failures in combination with the twisting of the overall specimen

due to global shear buckling resulted in full fracture at the reduced section of the lower left leg during the 23% shear angle cycles.

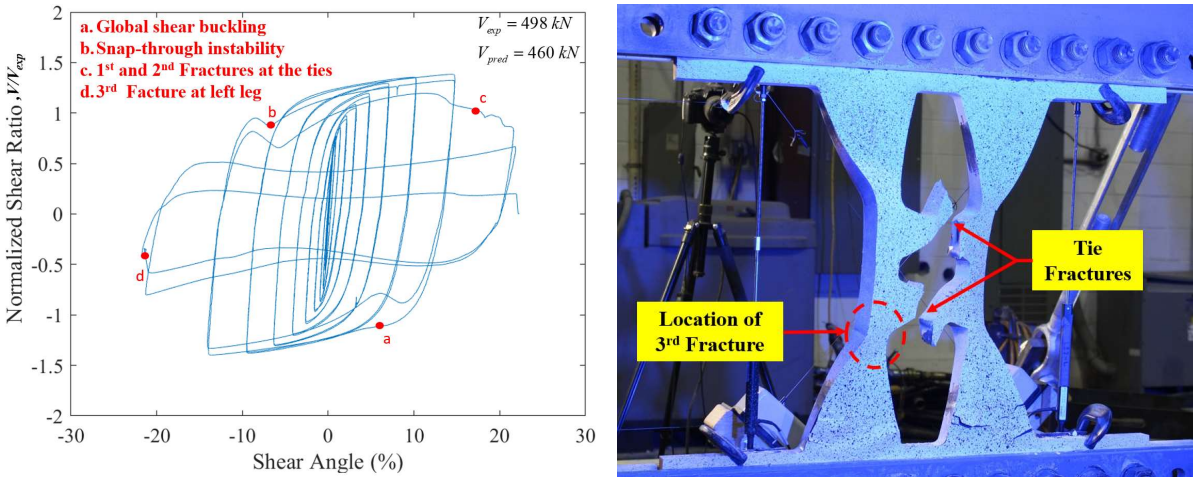

(a) Hysteretic curve (b) Picture of specimen at Point c

Fig. 8. Specimen TBF2

Fig. 9 illustrates hysteretic curve and remarkable events of Specimen TBF3. The flaking of whitewash at the ties and legs was visually observed at approximately 1.6% shear angle cycles, indicating first signs of yielding. The specimen maintained a stable and full hysteretic behavior up to the second positive peak of 17% shear angle cycles. Fracture of the tie at the location of the defect was found at second positive peak of 17% shear angle cycles. Specimen TBF3 was capable of surviving within approximately two cycles until the occurrence of fracture at the other tie. This was followed by the full fracture of the middle section of the interior leg, left leg and right leg, respectively during the 23% shear angle cycles, as shown in Fig. 9b.

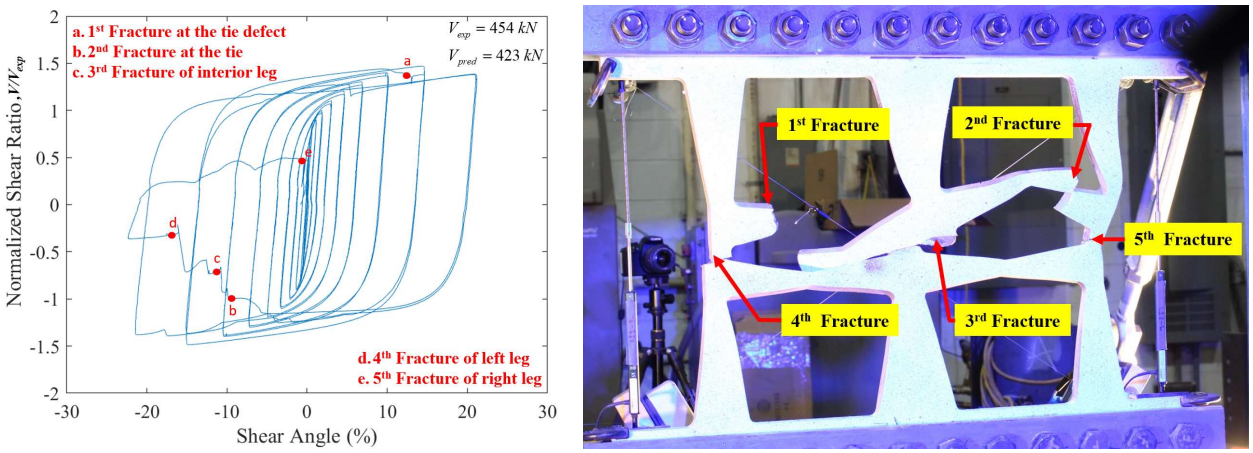

(a) Hysteretic curve (b) Picture of specimen at Point e

Fig. 9. Specimen TBF3

Discussion of Experimental Results

Table 1 lists the summary of specimen behavior. Predicted shear strength, V_{pred} was computed from generalized equation (7) while measured shear strength, V_{exp} was obtained from load-deformation curve. In addition, overstrength was computed as the ratio of ultimate shear force, V_u and measured shear strength, V_{exp}.

Table 1. Summary of specimen behavior

Specimen	Initial Stiffness (kN/mm)	Predicted Shear Strength V_{pred} (kN)	Measured Shear Strength V_{exp} (kN)	Ultimate Shear Force, V_u (kN)	Shear Angle at Peak Force (%)	Over-strength
STL	191	605	667	810	7	1.21
TBF1	42	191	191	291	22	1.52
TBF2	85	460	498	634	15	1.27
TBF3	98	423	454	608	15	1.34

For Specimen TBF1, the legs and ties initiated yielding at about the same time. Locations of plastic hinges at the ties and legs were observed to be at quarter points, midway between the reduced section and wider end and inelasticity was evenly distributed along the length of the ties and legs. In addition, the recorded shear strength matched well with the predicted strength. This specimen maintained full hysteretic behavior through the 22% shear angle cycles, indicating stable

energy absorption capacity. There was a gradual degradation in strength and stiffness after the full fracture of the bottom tie. This specimen then experienced global shear buckling, leading to the twisting of the legs and pinched hysteretic loop. However, it continued to demonstrate good amount of dissipated seismic energy until full fractures of the left and right legs, respectively.

Similar to Specimen TBF1, Specimen TBF2 also started yielding at the ties and legs, respectively. However, while plastic hinges formed at quarter points for the ties, they were found at the reduced sections for the legs, as visible by the areas of whitewash flaking off. The measured shear strength obtained from the experiment matched relatively well with the predicted strength with the error of approximately 8%, implying that plastic mechanism was not as accurate as proposed. More specifically, plastic hinging did not occur at the quarter points for the legs but was observed adjacent to the hole, likely due to shear yielding. Nevertheless, Specimen TBF2 was capable of maintaining full hysteretic behavior up to approximately 15% shear angle before a gradual degradation in strength and stiffness due to out-of-plane motion and snap-through buckling, likely due to the twisting of the top beam. However, good amount of hysteretic energy was still dissipated during load reversals until the full fractures of the ties (at approximately 23% shear angle cycle). This led to significant loss of strength and stiffness, followed by fracture of the left leg. The specimen then showed no signs of carrying additional load.

Similar to Specimen TBF1 and Specimen TBF2, Specimen TBF3 initiated yielding the ties and legs, approximately at the same time. The areas of whitewash flaking at the middle leg and four ties were found to be more than those of the exterior legs implied that inelasticity was concentrated in interior region. Plastic hinges were also found at the quarter points and yielding was spread along the length of the ties and legs, implying that flexural yielding was the controlling limit state. Full hysteretic behavior was maintained until the first fracture of the tie due to the

encouraging of inelastic deformation at the defect. However, this specimen showed no signs of out-of-plane displacement or significant loss in strength and stiffness after this tie failure. Dissipated hysteretic energy was still stable until the second fracture of the other tie. This resulted in a significant loss of strength and stiffness. Consequently, the specimen showed no sign of carrying additional load after the fractures of the interior, left and right legs, likely due to shear yielding.

Table 2 revealed that even though Specimen STL has highest initial stiffness and strength among four specimens, early yielding resulted in plastic concentration at four corners, thus leading to brittle fractures at these locations. This was also proved by the smallest over-strength factor among the four specimens. This specimen showed no signed of carrying additional load after the occurrence of fractures, resulted in pinched hysteretic loop indicating low level of dissipated energy.

COMPUTATIONAL STUDY

The previous section provided the experimental results of only three tied butterfly shape specimens which are not sufficient for practical design. Therefore, this section presents a computational study to explore the design space and provide design recommendations. More specifically, FE modeling is first validated against experiments, then parametric study is conducted to evaluating the effect of design variables on cyclic behavior of the tied butterfly shape. Based on the experimental results, FE validation and computational parametric study, design recommendations are provided.

Finite Element (FE) Modeling Approach and Validation

The commercial program LS-DYNA was used to create FE models of the specimens. The geometry of each test specimen was modeled and meshed using fully integrated 8-node solid elements with an average element size (i.e average length of an 8-node solid element) of 3.8 mm. A nonlinear isotropic hardening and kinematic hardening material model was used for the steel with fracture captured using the model created by Huang and Mahin (2010), referred to as Material 153 in LS DYNA. The plasticity model is a function of five calibrated parameters including yield stress, σ_{yo}, linear isotropic hardening parameter, H_1, nonlinear isotropic hardening parameter, β, linear kinematic hardening parameter, H_2, and nonlinear kinematic hardening parameter, γ. Additionally, three fracture related constants are defined: two calibrated parameters that define the evolution of damage, s and t, and a critical value of damage, D_C, when the material is considered to be fractured. Hardening and fracture parameters were calibrated using trial and error to find the best match for monotonic tension coupon tests and all three structural fuse test specimens, with resulting material parameters: E=224,000 MPa, σ_{yo}=376 MPa, H_1= 414 MPa, β=6, H_2= 3516 MPa, γ=15, s=0.3, t=1.49, D_C=0.5.

In order to capture buckling, geometric nonlinearity was included in the modeling scheme and initial imperfections were applied in the shape of the first eigen-buckling mode shape scaled to a maximum out-of-plane displacement magnitude of $L/1000$, where L is the link length of the structural fuse. Fig. 10a. shows an example finite element model with mesh for Specimen TBF1. The nodes along the bottom edge of the model were restrained against all translational and rotational motion, while the nodes along the top edge were constrained to a reference node that was subjected to measured histories of motion recorded during the tests. Measured translation along the x-axis (δ_x) was obtained as the difference between horizontal string potentiometers SP2

and SP3. Vertical displacements along the *y*-axis (δ_y) and rotations about the *z*-axis (θ_z) were computed based on measurements of the two vertical linear potentiometers, while out-of-plane displacements were obtained from the DIC system. The top and bottom boundaries of the FE model are taken at the bolt lines of the tested specimen.

Fig. 10. illustrates load-deformation curves of experiments and computational models. Qualitatively, the overall shape and pinching behavior obtained from computational FE models match the experimental behavior well. Even though the FE model of Specimen TBF1 was not capable of capturing the fractures observed in the experiment during the last few cycles, the main behavior of Specimen TBF1 was captured such as the formation of plastic hinging, plastic mechanism, deformed shape, etc. The FE model of Specimen TBF2 is shown to capture more complete experimental behavior including plastic mechanism, out-of-plane displacement, strength and stiffness degradation due to fracture and buckling, locations of fractures, etc.

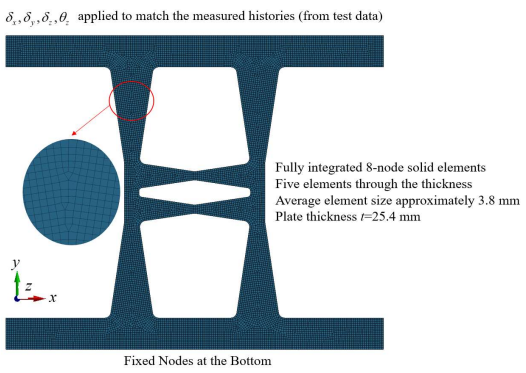

(a) Example FE Setup

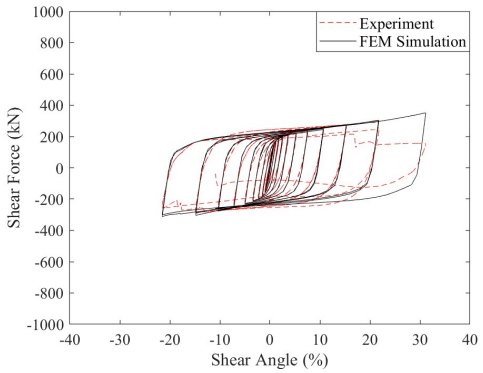

(b) Specimen TBF1

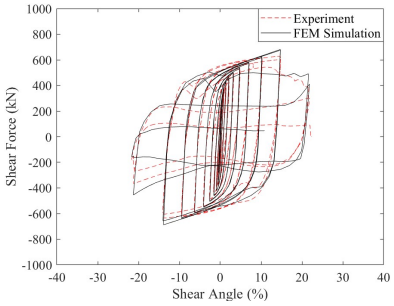

(c) Specimen TBF2

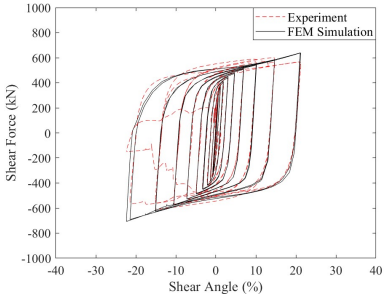

(d) Specimen TBF3

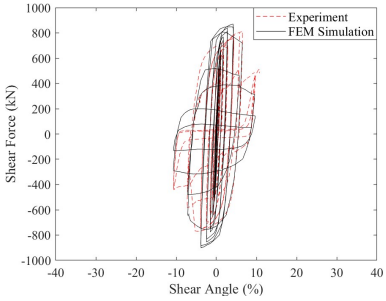

(e) Specimen STL

Fig. 10. Hysteresis comparison of experiments to FE models

It can be seen from Fig. 10d that the FE model of Specimen TBF3 well predicted the cyclic behavior of this specimen up until fractures occurred in the experiment. The inability of the FE model to capture these fractures may be due to the defect on the tie which encouraged strain concentration in the experiment and may have led to early fracture. Regardless, the initial stiffness, yield strength, locations of plastic hinging, spread of inelasticity, and peak force were captured well by the FE model.

For Specimen STL, peak forces obtained from the FE model overestimated those measured from the experiment, likely due to several flexibilities in experimental sources that were not modeled such as pinhole tolerance, flexibility of bolted specimen to top and bottom angles, initial imperfection, etc. However, this also does not affect the ability to capture web plate behavior of

specimen STL. Plastic concentration and fractures at four corner of the link were well captured in the FE model. This implies that plastic mechanism is accurately predicted.

Fig. 11 presents locations of fractures and deformed shapes for four specimens approximately at the end of each test. For FE models that were not capable of actual fractures such as TBF1 and TBF3, captured photos of the specimens were taken prior to the occurrence of fractures. Overall, four computational FE models captured the plastic mechanism accurately as the plastic hinging observed from FE models match well with plastic hinges formed during the tests. It is noted that fractures captured from FE models match well with those occurred during the tests. In addition, the cycles and displacements associated with fractures of FE models match well with those in the tests. For instance, regarding Specimen STL, the FE model revealed that first fracture was observed at the bottom right corner of the specimen at approximately the first negative peak of 6% shear angle which matched well with the experiments.

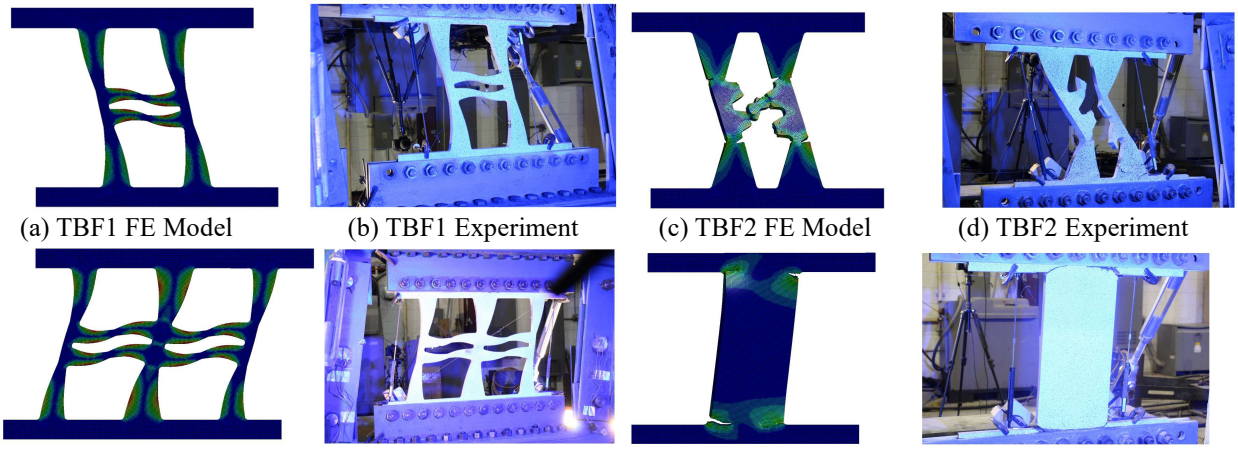

(a) TBF1 FE Model (b) TBF1 Experiment (c) TBF2 FE Model (d) TBF2 Experiment

(e) TBF3 FE Model (f) TBF3 Experiment (g) STL FE Model (h) STL Experiment

Fig. 11. Comparison of fractures and deformed shapes

Parametric Study Description

The FE modeling approach was identical to that used for validation in the previous section, except that the applied displacement history was modified. While there are many possible

configurations for incorporating structural fuses into a building, the context of the eccentrically braced frame (EBF) was selected as a practical setting. In a configuration like EBF, there may need to be struts adjacent to the structural fuse to resist axial forces similar to those used in the experimental program. Therefore, the applied displacement protocol to match this situation consists of a horizontal displacement, δ_x, following the cyclic EBF displacement protocol in AISC 341-16 (AISC, 2016), and a vertical displacement, δ_y, following an arc associated with the constraint enforced by pinned struts. It is noted that the strut is assumed to be rigid and its elongation and shortening are neglected.

This parametric study consists of a two-part study to evaluate how five nondimensional geometric parameters affect the structural behavior of the tied butterfly shape. First, the main study includes the investigation of three nondimensional parameters associated with the geometry of the ties and legs and their relationship. It is noted that overall slenderness, L/t, is kept unchanged for this study. Second, a sub-study is conducted to evaluate two non-dimensional parameters associated with the relative geometry of the middle hole to the tie width, W_H/W_T and overall slenderness L/t associated with different plate thicknesses.

For the main study, overall slenderness remains constant, L/t=40, with overall link length L=508 mm and thickness t=12.7 mm, and the width of the hole is equal to the width of the tie, W_H/W_T=1. The geometry of the ties and legs are expected to have significant effect on the structural behavior of the tied butterfly shape, so three nondimensional parameters that might be useful in controlling behavior are tie slenderness, W_T/L_T, leg slenderness, W_L/L_L and the relationship between the width of the tie and leg, $(W_L/W_T)^2$ (because the ratio of the strength of the leg to strength of the tie is a function of $(W_L/W_T)^2$). The entire geometry of the tied butterfly shape can be defined based on three nondimensional parameters, and three constraints given on L, t and W_H.

Table 2 summarizes the values of the three nondimensional parameters for this study where each parameter takes four values and the parametric combination of all possible parameters results in 64 total models.

Table 2. Ranges of nondimensional parameters for main study

Leg Slenderness (W_L/L_L)	**Relationship between Leg and Tie** $(W_L/W_T)^2$	**Tie Slenderness** (W_T/L_T)
0.15	1.5	0.15
0.2	2	0.2
0.25	3	0.25
0.3	4	0.3

Table 3 lists values of nondimensional parameters for the sub-study. Another 8 computational models are included for the sub-study to evaluate the effect of the hole geometry and overall slenderness on structural behavior of this shape. Details about all values of individual geometrical parameters and graphical configurations can be found in Nguyen (2022).

Table 3. Ranges of nondimensional parameters for sub-study

Relationship between Hole and Tie (W_H/W_T)	**Overall Slenderness** (L/t)
0.25	120
0.5	60
1	40
2	30

5.3 Parametric Study Results - Hysteretic Behavior

This section discusses the hysteretic behavior of all FE models. Fig. 12 provides the comparison of 2 representative groups hysteretic curves associated with varying two out of the three nondimensional parameters, W_L/L_L and W_T/L_T.

Fig. 12a shows the representative hysteretic curves of the TBF shapes that corresponds to the varying leg slenderness, W_L/L_L. Given the same tie slenderness, W_T/L_T, and leg width to tie width ratio, $(W_L/W_T)^2$, the leg slenderness plays an important role in controlling the amount of

dissipated hysteretic energy as the increasing leg slenderness, W_L/L_L, results in improved hysteretic response. More specifically, as the leg gets stockier (i.e larger values of W_L/L_L), strength and stiffness of the TBF shape increase remarkably. Conversely, tie slenderness, W_T/L_T, has slight effect on the strength and stiffness of the TBF shapes. However, as the ties and legs get stockier (i.e large values of W_L/L_L and W_T/L_T), the TBF shape is prone to buckling and fracture, resulting the strength and stiffness degradation (more details are discussed in later section), as shown in Fig. 12b. This suggests that slender ties and legs are desirable for practical design.

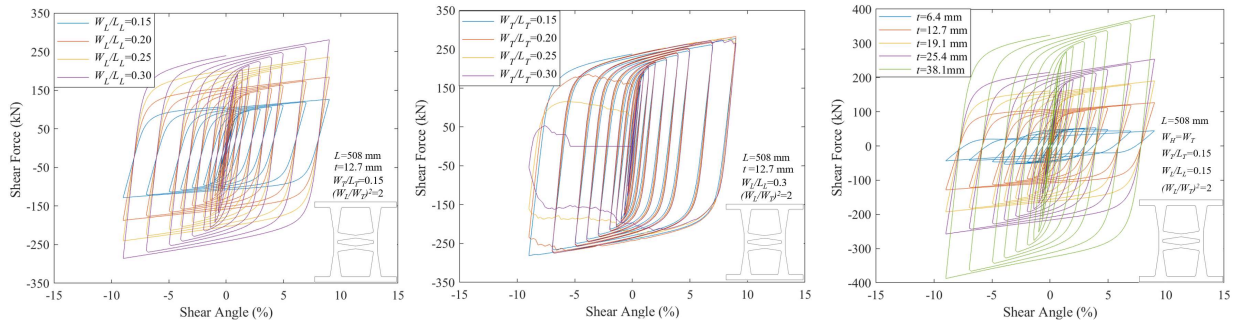

(a) Varying leg slenderness, W_L/L_L (b) Varying tie slenderness, W_T/L_T (c) Varying plate thickness, t

Fig. 12. Representative hysteretic curves

The effect of plate thickness (or overall slenderness, L/t) and width of the hole, W_H, on the hysteretic behavior of the TBF shape is illustrated in Fig. 12c. The representative model selected for this FE study is the TBF with tie slenderness and leg slenderness of 0.15, leg width to tie width ratio, $(W_L/W_T)^2$=2, and overall length of L=508 mm. The only plate thickness that results in the pinched hysteretic response, is t=6.4 mm, implying that small plate thickness means larger overall slenderness, L/t, thus leads to reduced hysteretic energy dissipation.

It is worth mentioning that the remaining nondimensional parameter, $(W_L/W_T)^2$, does not show a significant importance in the hysteretic response, given the same tie slenderness, W_T/L_T, and leg slenderness, W_L/L_L. Similarly, the width of the hole at the middle of the TBF shape, W_H,

does not show a significant effect on the hysteretic behavior of the TBF shape (see Nguyen 2022 for details).

5.4 Parametric Study Results - Strength and Stiffness

Fig. 13a reveals that the strength equation derived in previous section is relatively good in predicting the shear strength of the TBF shape as the error is approximately ±5%. As the ties or legs get stockier (i.e larger values of W_T/L_T), this equation is less accurate as the assumed plastic mechanism is no longer valid. The outlier in strength, as shown in Fig. 13(a), is associated with stocky leg and stocky tie (i.e slenderness of 0.3). This suggests that the reasonable slenderness for ties and legs should be less or equal 0.25 for a good strength prediction of the derived design equation (i.e Eq. (5)).

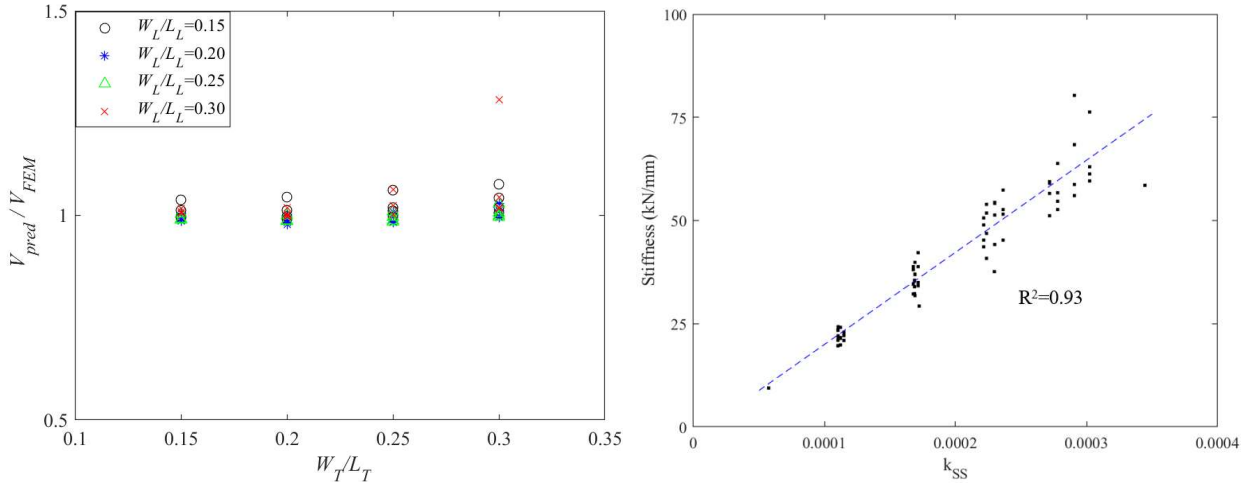

(a) Accuracy of prediction equation (b) Effect of k_{ss} on stiffness of TBF shape

Fig. 13. Strength and Stiffness

This section also introduces a nondimensional parameter expected to control the stiffness of the TBF shape, k_{SS}, as shown in Eq. (6). Fig. 13b illustrates the effect of this nondimensional parameter on the stiffness of the TBF shape. Stiffness of the TBF shape, k, can be predicted using regression which are provided in Eq. (7).

$$k_{SS} = \frac{(W_T^2 + W_L^2)t}{(2L_L + 7W_T)^3} \qquad (6)$$

$$k \approx 223{,}000\, k_{SS} \qquad (7)$$

5.5 Parametric Study Results - Buckling

For the purposes of this study, buckling is quantified by the maximum out-of-plane displacement (Δ_z) obtained from FE models. The effect of geometric parameters on buckling of TBF shape is illustrated in Fig. 14. The *x*-axis is expressed in terms of tie slenderness, W_T/L_T while the *y*-axis represents the maximum out-of-plane displacement, Δ_z, of the TBF shape.

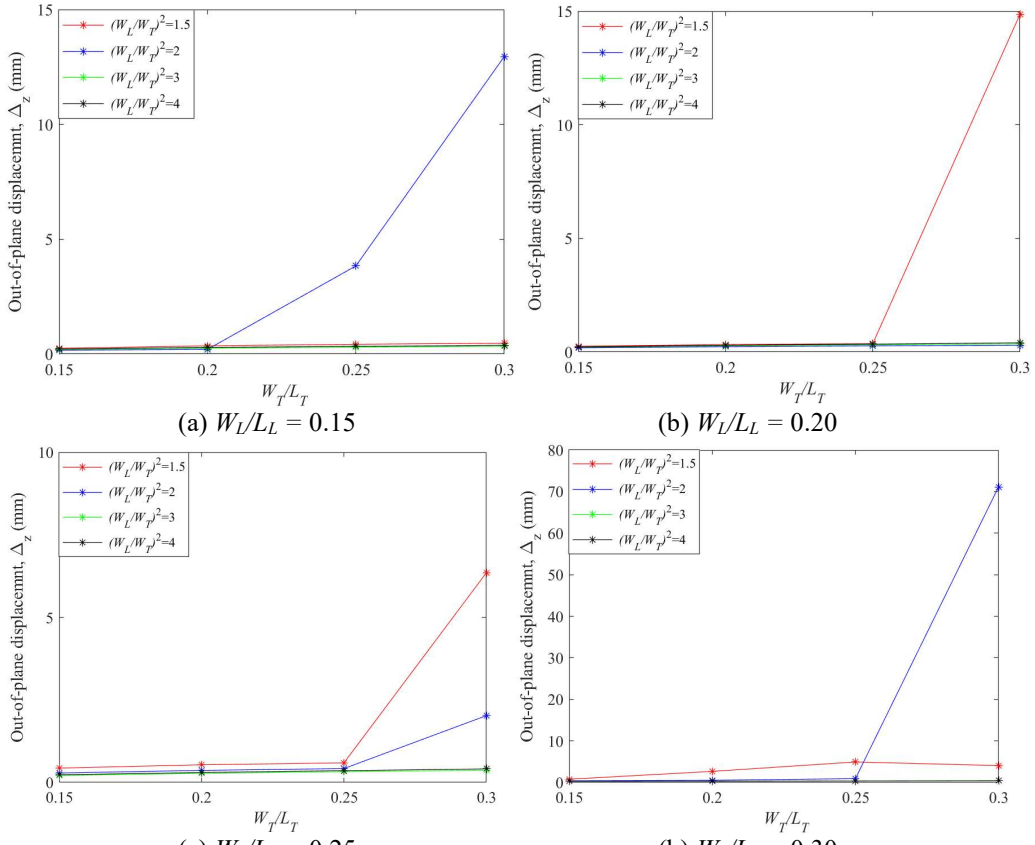

(a) W_L/L_L = 0.15 (b) W_L/L_L = 0.20

(c) W_L/L_L = 0.25 (b) W_L/L_L = 0.30

Fig. 14. The effect of design variables on buckling

As shown in Fig. 14, as the legs and ties get stockier (i.e large W_T/L_T and W_L/L_L), thus the TBF structural fuse is less resistant to buckling.

5.6 Parametric Study Results - Equivalent Plastic Strain

Fig. 15 exhibits that effect of design parameters on worst equivalent plastic strain of the TBF shape obtained from FE models. Similar to the previous part, TBF shape with stocky ties and legs is shown to have large equivalent plastic strains. More specifically, as the ties and legs get stockier, plastic strain concentration occurs at the reduced sections of the ties and legs (i.e shear dominated behavior), potentially leading to early fracture. The other locations that concentrate plastic deformation are the two legs adjacent to the middle hole. As observed from Fig. 15, the relationship between the leg and the tie, $(W_L/W_T)^2$=2, resulted in small equivalent plastic strain.

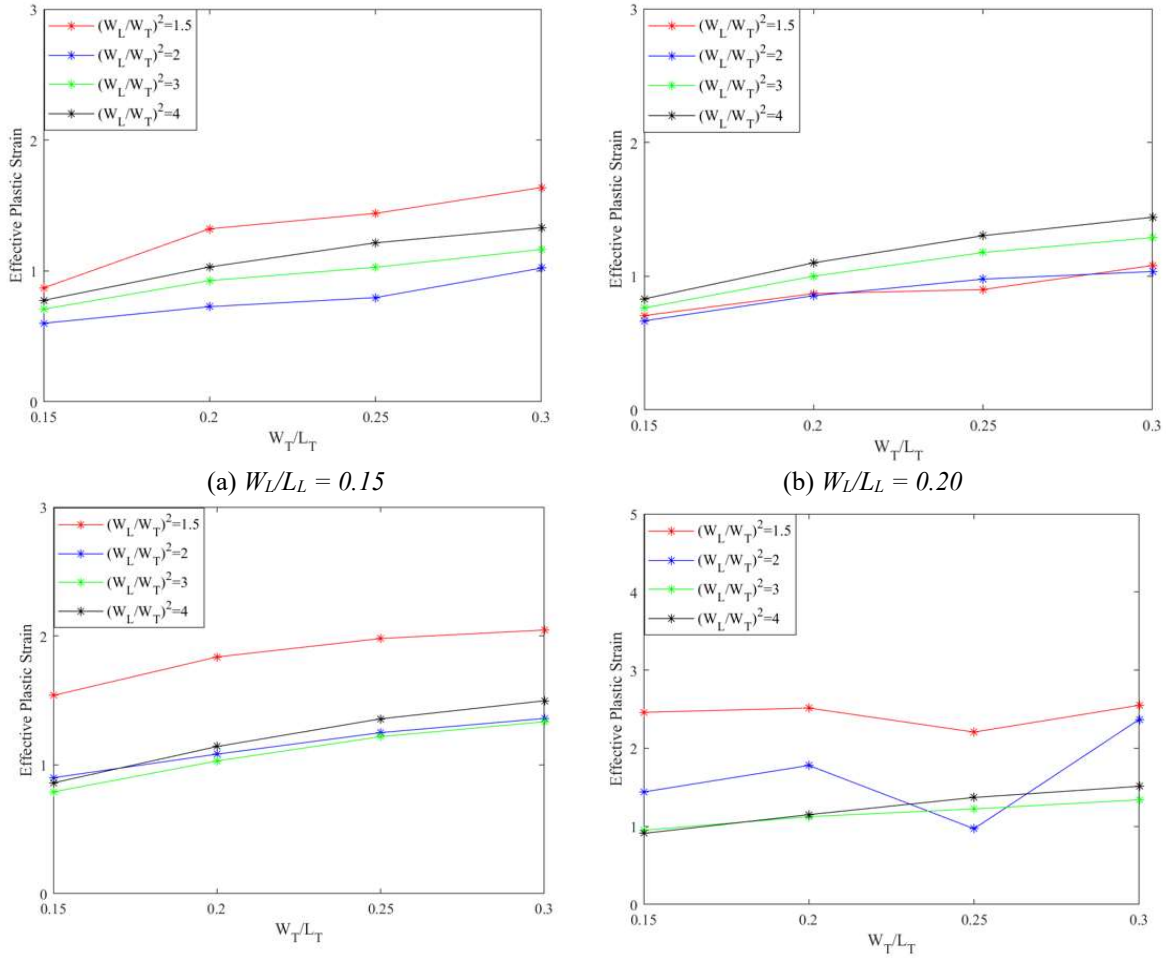

(a) $W_L/L_L = 0.15$ (b) $W_L/L_L = 0.20$

(c) $W_L/L_L = 0.25$ (d) $W_L/L_L = 0.30$

Fig. 15. The effect of design variables on equivalent plastic strain

In summary, the above findings suggests that a good TBF configuration should have (1) slender ties and legs (i.e less than 0.2), (2) ratio of leg width to tie width, $(W_L/W_T)^2$=2, (3) large W_L at the area adjacent to the middle to resist large shear force and avoid plastic concentration.

CONCLUSIONS

The main findings of these study can be summarized as follows:

(a) Three specimens associated with the tied butterfly shape, Specimen TBF1, Specimen TBF2 and Specimen TBF3, have shown to maintain full hysteretic behavior up to shear angle of approximately 23.3%, 11.9%, and 16.7%, respectively.

(b) Generalized equation well predicted shear strength of Specimen TBF1 with error of 0.5% while it showed less accuracy for specimen TBF2 with the error of 7.6%. This can be explained that plastic mechanism of specimen TBF2 is not similar to the proposed mechanism used for the derivation.

(c) The good cyclic behavior of specimen TBF3 indicates that adding multiple shapes is promising way to create a new shape to adapt different design settings in practice as this shape was shown to maintain stable hysteretic behavior up to 16.7% shear angle.

(d) The parametric study suggested that a desirable TBF shape for buckling and fracture resistance has slender ties and legs (i.e less than 0.2) and ratio of leg width and tie width, $(W_L/W_T)^2$ of 2. This was also confirmed by the experimental results of Specimen TBF1. In addition, if strength and stiffness are desired for practical design, TBF shape with stocky ties and legs, for instance, TBF2, is recommended. However, these shapes might experience early buckling or fracture, as confirmed by the experimental results of specimen TBF2.

(e) Nondimensional, k_{SS}, was introduced as a simple approach to predict the stiffness of the TBF shape.

ACKNOWLEDGEMENTS

This work was supported by the National Science Foundation under Grant No. CMMI-1453960. In-kind funding was provided by AISC and INFRA-METALS. Any opinions, findings, and conclusions or recommendations expressed in this material are those of the authors and do not necessarily reflect the views of the National Science Foundation or other sponsors.

RERFERENCES

AISC. 2016. Seismic provision for structural steel buildings. ANSI/AISC 341-1. Chicago, IL: AISC.

ASTM Standard A370-07a. Standard test methods and definitions for mechanical testing of steel products. West Conshohocken, PA: American Standards for Testing and Materials International (ASTM); 2007.

Aschheim M.and Halterman A. (2002), "Reduced Web Section Beams: Phase One Experimental Findings And Design Implications". The Earthquake Engineering Online Archive, NISEE e-Library.

Avecillas, J.A., Eatherton, M.R. (2020). Controlling Out-of-Plane Buckling in Shear-Acting Structural Fuses through Topology Optimization. Journal of Structural Engineering. 146. 10.1061/(ASCE)ST.1943-541X.0002692.

Berman, J., and M. Bruneau. 2003. "Plastic analysis and design of steel plate shear walls." J. Struct. Eng. 129 (11): 1448–1456.

Cortes, G., and J. Liu (2011). "Experimental evaluation of steel slit panel–frames for seismic resistance." J. Constr. Steel Res. 67 (2): 181–191.

Deng, K., Pan, P., Li, W. and Xue, Y. (2015). "Development of a buckling restrained shear panel damper." Journal of Constructional Steel Research, 106(1), 311-321.

Eatherton, M. R., X. Ma, H. Krawinkler, D. Mar, S. Billington, J. F. Hajjar, and G. G. Deierlein (2014). "Design concepts for controlled rocking of self-centering steel-braced frames." J. Struct. Eng. 140 (11): 04014082.

Egorova, N., Eatherton, M. R. and Maurya, A. (2014). "Experimental study of ring-shaped steel plate shear walls." Journal of Constructional Steel Research, 103, 179-189.

El-Bahey S, Bruneau M. Bridge piers with structural fuses and Bi-steel columns. I: Experimental Testing. J Bridge Eng 2012;17(1).

El-Bahey S, Bruneau M. Bridge piers with structural fuses and Bi-steel columns. II: Analytical Investigation. J Bridge Eng 2012;17(1).

Farzampour A. and Eatherton M. (2019), "Yielding and lateral torsional buckling limit states for butterfly-shaped shear links ", Engineering Structures, vol. 180, pp. 442-451.

Ghabraie, K., Chan, R., Huang, X. and Xie, Y. M. (2010). "Shape optimization of metallic yielding devices for passive mitigation of seismic energy." Engineering Structures, 32(8), 2258-2267.

Kobori T, Miura Y, Fukuzawa E, Yamanda T, Arita T, Takenaka Y, Miyagwa N, Tanaka N, Fukumoto T (1992). Development and application of hysteresis steel dampers. In: Earthquake Engineering the 10th Conference. Rotterdam: Belkema, 1992.

Koppal and Eatherton (2013), "Perforated Steel Plate Shear Walls for Tunable Seismic Resistance", Structure Congress.

Lee C., Woo S., K. Ju Y., Lee D., Oh J., Kim S. (2014), "Modified Fatigue Model for Hourglass-Shaped Steel Strip Damper Subjected to Cyclic Loadings", Journal of Structural Engineering, 141 (8).

Li, H. N. and Li, G. (2007). "Experimental study of structure with "dual function" metallic dampers." Engineering Structures, 29, pp.1917–1928.

Liu, Y., and M. Shimoda. (2013). "Shape optimization of shear panel damper for improving the deformation ability under cyclic loading." Struct. Multidiscip. Optim. 48 (2): 427–435.

Ma, X., Borchers, E., Pena, A., Krawinkler, H. and Deierlein, G. (2010). "Design and behavior of steel shear plates with openings as energy-dissipating fuses." John A. Blume Earthquake Engineering Center Technical Report, (173).

Phillips, A.R., and M. R. Eatherton (2018). “Large-scale experimental study of ring shaped–steel plate shear walls.” J. Struct. Eng. 144 (8):04018106.

Plaut, R. and Eatherton, M. (2017) "Lateral-Torsional Buckling of Butterfly-Shaped Beams with Rectangular Cross Section" Engineering Structures, v.136 , 2017 , p.210

Popov, E. P., and M. D. Engelhardt. 1988. “Seismic eccentrically braced frames.” J. Constr. Steel Res. 10 (Jan): 321–354.

Teruna D, Majid TA, Budiono B. Experimental study of hysteretic steel damper for energy dissipation capacity. Adv Civ Eng 2015. Hindawi Publishing Corporation.

Vian, D., M. Bruneau, and R. Purba. 2009. “Special perforated steel plate shear walls with reduced beam section anchor beams. II: Analysis and design recommendations.” J. Struct. Eng. 135 (3): 221–228

Zhu, B, Wang, T, Zhang, L (2018) Quasi-static test of assembled steel shear panel dampers with optimized shapes. Engineering Structures 172: 346–357.

5. EXPERIMENTAL STUDY ON THE LIMIT STATES OF BUTTERFLY SHAPED STRUCTURAL FUSES

Trai N. Nguyen[1], Matthew R. Eatherton[2]

[1] Graduate Research Assistant, Department of Civil and Environmental Engineering, Virginia Tech, Blacksburg, USA.
[2] Professor, Department of Civil and Environmental Engineering, Virginia Tech, Blacksburg, USA.

ABSTRACT

Structural fuses are replaceable elements of a structure that are designed to yield and protect the surrounding members from damages, and then be replaceable after a major seismic event. One type of structural fuse consists of a steel plate with cutouts leaving butterfly-shaped links (i.e butterfly-shaped structural fuse) which has been shown to produce advantageous behavior such as (1) promoting yielding along the link length, thus maximizing the amount of dissipated seismic energy, (2) maintaining full and stable hysteretic behavior up to large lateral drift. Prior research has identified the three main limit states for butterfly-shaped links to be flexural yielding, shear yielding, and lateral torsional buckling although most studies focus on flexural yielding because it is a desirable limit state that promotes the largest ductility. However, it is important to understand the limit states of shear yielding and lateral torsional buckling for proper structural fuse design.

This study systematically examines the three limit states of butterfly-shaped structural fuses through analytical and experimental programs. First, each limit state is described and generalized predicted equations are presented. An experimental program is then conducted including eight full-scale specimens to investigate the behavior of butterfly-shaped structural fuses undergoing these limit states.

Keywords: Structural Fuse, Steel Plate, Butterfly-Shaped Link, Energy Dissipation, Earthquake Engineering

INTRODUCTION

Structural fuses have been used as the ductile mechanism in some earthquake resistant structures because they can reduce earthquake-related repair costs and related business downtime. This improved performance is accomplished by concentrating inelastic deformations in the structural fuses, protecting surrounding structural elements from damage and allowing targeted fuse replacement after a major seismic event. There are many possible ways that structural fuses can be implemented in a building, with a few examples including use as the link beams in an eccentrically braced frame (Popov and Engelhardt 1988), coupling beams in a coupled shear wall (Borello and Fahnestock 2013), hysteretic dampers in self-centering rocking frame structures (Eatherton et al. 2014). Structural fuses are sometimes coupled with a self-centering mechanism or a flexible elastic moment frame to minimize residual drifts and further minimize structural repair costs.

Several forms of structural fuses have been developed and shown to possess sufficient ductility and energy dissipation capacity (e.g Vian et al. 2009, Egorova et al. 2014, Nguyen and Eatherton 2022, Aschheim and Halterman, 2002). One type of structural fuse, called butterfly-shaped, consists of a steel plate with diamond-shaped cutouts leaving tapered links that are wide at the ends and narrow at the middle. As the butterfly-shaped link is subjected to shear force, a reversed moment develops that varies linearly along the link length, while the plastic moment strength varies quadratically. The relationship between the plastic moment capacity and moment demand provides two advantages including (1) the location of flexural plastic hinging can be controlled by adjusting the slope of the sides of the link and furthermore can be located away from

the sharp corners to promote fracture resistance; (2) if the butterfly link is proportioned properly, the shape of moment demand and moment strength are such that yielding is encouraged to spread along the link length, leading to substantial energy dissipation.

Butterfly-shaped structural fuses have been applied in engineering practice. They have been used as energy dissipation dampers (referred to as Honeycomb Dampers in the literature) between floors of buildings (e.g Kobori et al. 1992 and Kurokawa et al. 1998) by engineers at the Kobori Research Complex in the design of 28 new buildings and the retrofit of 6 buildings (e.g Lynch 1998). More recently, Luth et al. (2008) used butterfly-shaped structural fuses in the seismic design of the USC School of Cinema.

In the past three decades, butterfly-shaped structural fuses have been studied with experimental and computational programs. Experimental investigations have included the study on the structural behavior of butterfly-shaped links (e.g Kobori et al. 1992, Teruna et al. 2015). Prediction equations for shear strength of the link when undergoing flexural yielding was derived by Ma et al. (2010) and then validated against experiments. The same study found that if the taper ratio, the ratio of the reduced width at the middle section to the wider width at link ends, equals one third, that yielding initiates at quarter points away from corners increasing fracture resistance. In fact, tests on associated geometries revealed that butterfly-shaped links are capable of maintaining full hysteretic behavior up to 30% shear angle across the link length. Butterfly-shaped links with other values for the taper ratio that produce flexural hinges closer to the reduced section or ends of the links have shown to maintain full hysteretic behavior up to approximately 15%-20% shear angle (e.g Teruna et al. 2015). Separately, researchers have used topology optimization to find structural fuse shapes that minimize equivalent plastic strain (e.g Liu and Shimoda 2013) or maximize total plastic energy dissipation (e.g Ghabraie et al. 2010), and end up with shapes

strongly resembling butterfly-shaped links. This further reinforces the advantages of the butterfly-shaped structural fuse.

Even though there has been some study of the limit states of butterfly-shaped structural fuses, there are still research gaps that are the focus of this work. Some researchers have examined limit states such as yielding and lateral torsional buckling (LTB) of the butterfly-shaped link (e.g Ma et al., 2010, Farzampour and Eatherton 2019, Plaut and Eatherton 2017). For some applications, the LTB limit state can be considered advantageous as strength degradation due to buckling means less resistance against restoring force for applications in a self-centering system (e.g., Eatherton et al. 2014). The predicted shear strength of links associated with LTB limit state was derived by solving the governing differential equation (e.g Plaut and Eatherton 2017, Farzampour and Eatherton 2019). However, this equation was derived based on the assumption of elastic material model and has not been validated by experiments. Similarly, predicted shear strength of butterfly-shaped links associated with shear yielding has also been derived (e.g Ma et al., 2010 and Farzampour and Eatherton, 2019), but this equation for shear yielding has yet to be validated by experiments, nor the transition between shear and flexural yielding limit states. Furthermore, some of the past testing programs were conducted on relatively small specimens which may not be representative of full-scale structural fuse behavior in real structures.

This paper describes an experimental study on full-scale butterfly-shaped structural fuses specimens to investigate the relevant limit states including (1) flexural yielding, (2) shear yielding, including understanding the transition between limit states of shear yielding and flexural yielding, and (3) lateral torsional buckling. First, a description of the limit states is presented along with governing equations. Then, an experimental program is conducted to evaluate cyclic behavior of

full-scale butterfly-shaped structural fuses associated with each of the limit states. Based on the results of experiments, design recommendations are provided for practical design.

GENERALIZED DESIGN EQUATIONS

This section describes concepts related to butterfly-shaped links and equations for the three limit states of flexural yielding, shear yielding and lateral torsional buckling. Fig. 1(a) illustrates an isolated butterfly-shaped link with middle width, a, end width, b, overall link length, L and plate thickness, t. The link is subjected to constant shear and reversed end moments as shown in Figure 1(b). As illustrated in Fig. 1(c), shear demand, V, is constant while the shear strength linearly varies over the link length. Shear yielding occurs if the shear strength is reduced enough such that the shear strength of the link at the middle section is equal to the shear demand, $V_s = V$. Similarly, the link undergoes flexural yielding wherever moment demand, M_d equals moment strength, M_s in Fig. 1(d).

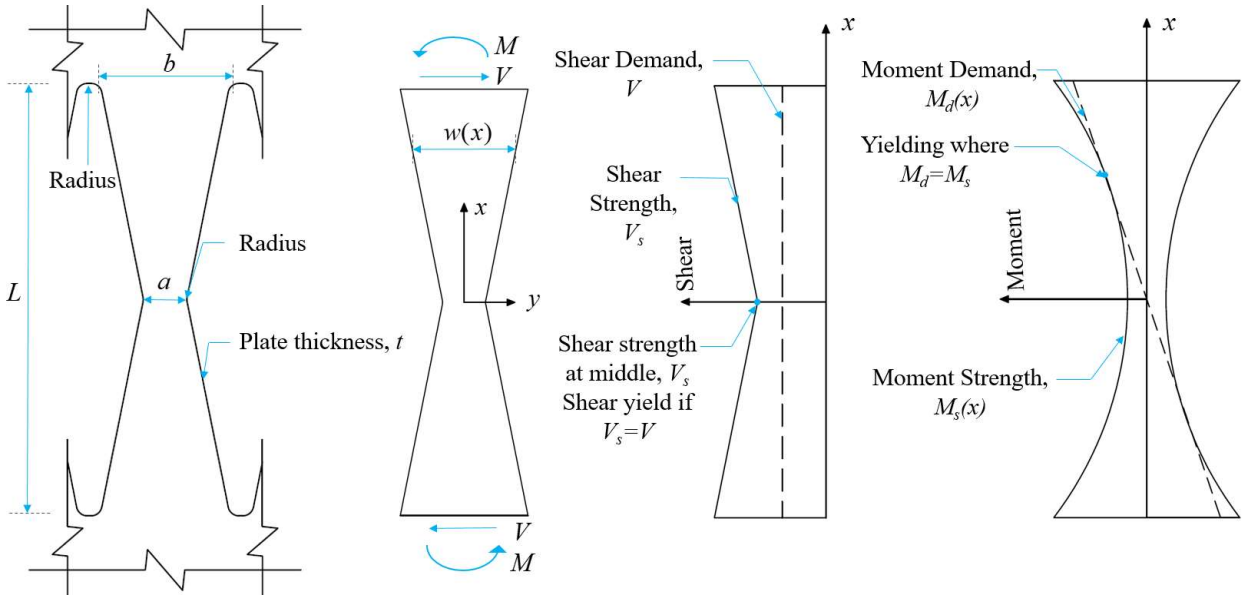

(a) Isolated butterfly-shaped link (b) Loading (c) Shear (d) Moment

Fig. 1. Idealized loading and behavior of butterfly-shaped links

Equations are derived for the flexural and shear strength of the section based on the following assumptions which are used throughout this section:

(1) Stresses associated with moment and shear are considered independent with respect to yielding, i.e., interaction of shear and normal stresses are neglected.

(2) Plane stress condition was assumed as the plate thickness is relatively small relative to the plan dimensions.

(3) The butterfly-shaped link is subjected to idealized loading conditions including shear and equal but opposite moments at each end. The links are assumed not to be subjected to any external axial force.

(4) The effect of radii at the intersections are ignored.

(5) Fracture is not considered in this section, but instead will be investigated in the subsequent sections associated with the experimental program.

Plastic moment strength is given by Eq. (1) as a function of link width, $w(x)$ as given in Eq. (2), and steel yield stress, f_y. Dimensions, a, b, L, and t are identified in Fig. 1(a) and the definition of the location x is shown in Fig. 1(b). Moment demand can be idealized with Eq. (3) and the shear force associated with the formation of plastic hinges can be obtained by equating moment demand and moment strength, as expressed in Eq. (4). Then, setting the derivative of Eq. (4) equal to zero reveals the plastic hinge location, x_p that produces the minimum shear strength as given in Eq. (5). The shear force associated with flexural hinges, V_M can be obtained by substituting Eq. (5) into Eq. (4), as given in Eq. (6). However, it is noted that plastic hinge forming outside of the link length does not have physical significance, thus the constraint $x_p \leq$ L/2, or $a/b \leq 0.5$, is imposed. This implies that if $a/b > 0.5$, plastic hinges form at the ends of the link similar to the

behavior of a straight link. Eq. (7) describes the shear strength of butterfly-shaped link associated with plastic hinging at ends.

$$M_s(x) = tf_y \frac{\left[w(x)\right]^2}{4} \tag{1}$$

$$w(x) = a + 2\left(\frac{b-a}{L}\right)x \tag{2}$$

$$M_d(x) = Vx \tag{3}$$

$$V = tf_y \frac{\left[a + 2\left(\frac{b-a}{L}\right)x\right]^2}{4x} \tag{4}$$

$$x_p = \frac{aL}{2(b-a)} \tag{5}$$

$$V_M = 2f_y t \frac{a(b-a)}{L} \quad \text{for } a/b \leq 0.5 \tag{6}$$

$$V_M = f_y t \frac{b^2}{2L} \quad \text{for } a/b > 0.5 \tag{7}$$

The shear strength, V_V associated with plastic shear yielding of the cross-section at the middle of the link is expressed in Eq. (8). Flexural yielding will be the controlling limit state if shear strength due to flexure, V_M, as given in Eq. (6) is less than shear strength due to shear, V_V, as given in Eq. (8). The resulting criterion for when flexural yielding will control is expressed by Eq. (9).

$$V_V = \frac{f_y}{\sqrt{3}} at \tag{8}$$

$$\frac{b-a}{L} < 0.28 \quad \text{then flexural yielding controls} \tag{9}$$

Ma et al. (2010) reported that the taper ratio, a/b=1/3, results in plastic hinges at the quarter points. This is confirmed by substituting $b=3a$ into Eq. (5), resulting in x_p=L/4, indicating plastic hinges midway between the wider ends and reduced section.

In addition, Ma et al. (2010) introduced the band zones which are the regions to be clamped by fixture devices such as back to back double angles. The band zones were reported to have no effect on the strength of the link governed by flexural yielding but do have an effect on the stiffness of the link. Thus, a prediction equation for stiffness of a butterfly shaped link was also derived, as shown in Eq. (10), where c is the distance between the link ends and the edges of fixtures and E is the modulus of elasticity.

$$k = \frac{1}{1+2.8c/L} 0.47Et\left(\frac{b}{L}\right)^3 \tag{10}$$

Shear strength associated with elastic lateral torsional buckling limit state was derived by solving the governing differential equation (Farzampour and Eatherton, 2019), and an approximate solution is given in Eq. (11), where ν is the Possion's ratio and A_{end} is the cross section area of link end. Table 1 summarizes the limit states of the butterfly shaped link.

$$V_{LTB} = \frac{2EA_{end}}{\left(L/t\right)^2\sqrt{1+\nu}}[0.096(\frac{a}{b})^3 - 0.281(\frac{a}{b})^2 + 0.547(\frac{a}{b}) + 0.533] \tag{11}$$

Table 1. Summary of Limit States of the Butterfly-Shaped Link

Limit State	1a. Flexural Yielding at Ends	1b. Flexural Yielding Along the Link	2. Shear Yielding at Mid-Height
Criteria	$\frac{a}{b} > 0.5$	$\begin{cases} \frac{a}{b} < 0.5 \\ \frac{b-a}{L} < 0.28 \end{cases}$	$\begin{cases} \frac{a}{b} < 0.5 \\ \frac{b-a}{L} > 0.28 \end{cases}$
Predicted Shear Strength	$V_M = f_y t \frac{b^2}{2L}$	$V_M = 2 f_y t \frac{a(b-a)}{L}$	$V_V = \frac{f_y}{\sqrt{3}} at$
Graphical Presentation	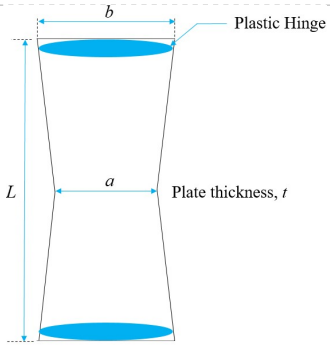	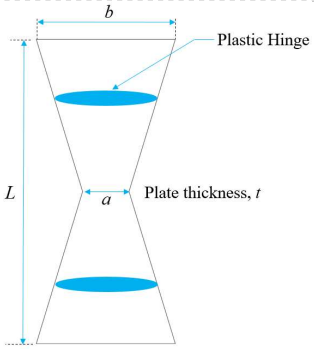	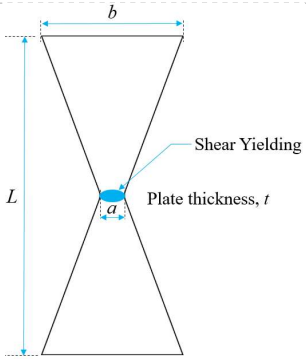
3. Elastic Lateral Torsional Buckling Limit State: $V_{LTB} = \frac{2EA_{end}}{\left(L/t\right)^2 \sqrt{1+\nu}} [0.096(\frac{a}{b})^3 - 0.281(\frac{a}{b})^2 + 0.547(\frac{a}{b}) + 0.533]$			

EXPERIMENTAL TESTING PROGRAM

Eight butterfly shaped structural fuse specimens were tested at the Thomas M. Murray Structures Laboratory at Virginia Tech with the goal of investigating the cyclic behavior of these structural fuses while undergoing different limit states.

Test Specimens

Fig. 2 illustrates the geometry of the eight specimens and the test matrix is provided in Table 2. Specimen BF1 is expected to undergo flexural yielding (i.e *(b-a)/L*=0.2 which is less than

0.28) while the Specimen BF2 is designed to experience shear yielding (i.e (*(b-a)/L*=0.55 which is greater than 0.28). Specimen BF3 is designed to be in the transition between limit states of flexural yielding and shear yielding with the ratio of (*(b-a)/L*=0.28. These three specimens have the same taper ratio, *a/b*=1/3, defined to encourage yielding at the quarter points away from the corners and thus maximize deformation capacity, while varying the shear ratio, *(b-a)/L*, to change from flexural to shear yielding. Two specimens, Specimen BF4 and Specimen BF5, are designed to form plastic hinges near the reduced section and link ends, respectively, by varying the taper ratio, *a/b*, to be less than and greater than one third, while holding the shear ratio of *(b-a)/L* below 0.28 to encourage flexural yielding instead of shear yielding. It is noted that all five of these specimens exploring flexural hinging and shear yielding, Specimens BF1 to BF5, have the same plate thickness of 25.4 mm. Four specimens, Specimen BF1, Specimen BF6, Specimen BF7 and Specimen BF8 are designed to explore the LTB limit state by holding the taper ratio and shear ratio constant while varying the plate thickness. All test specimens have three butterfly-shaped links to capture potential interaction between links and are large enough to represent the size and capacity that might be expected for full-scale structural fuses in engineering practice.

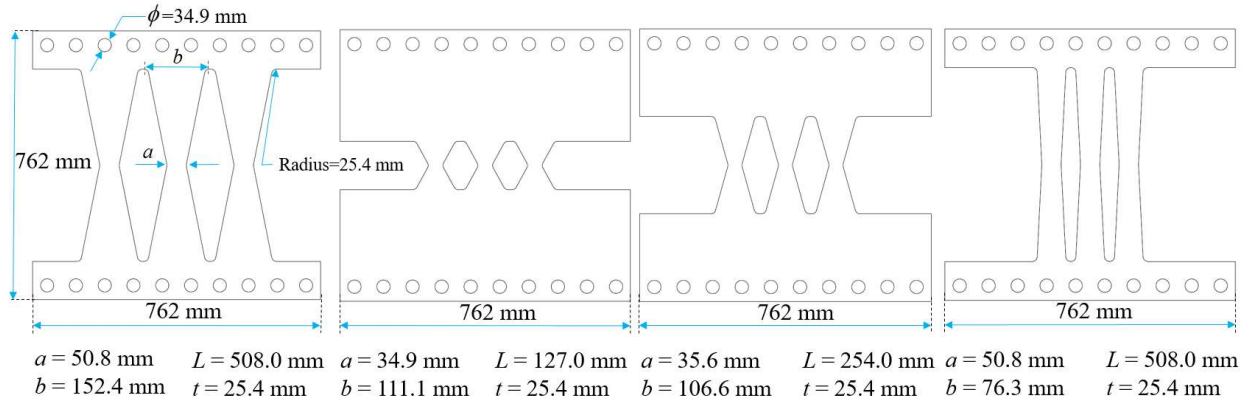

(a) Specimen BF1 (b) Specimen BF2 (c) Specimen BF3 (d) Specimen BF4

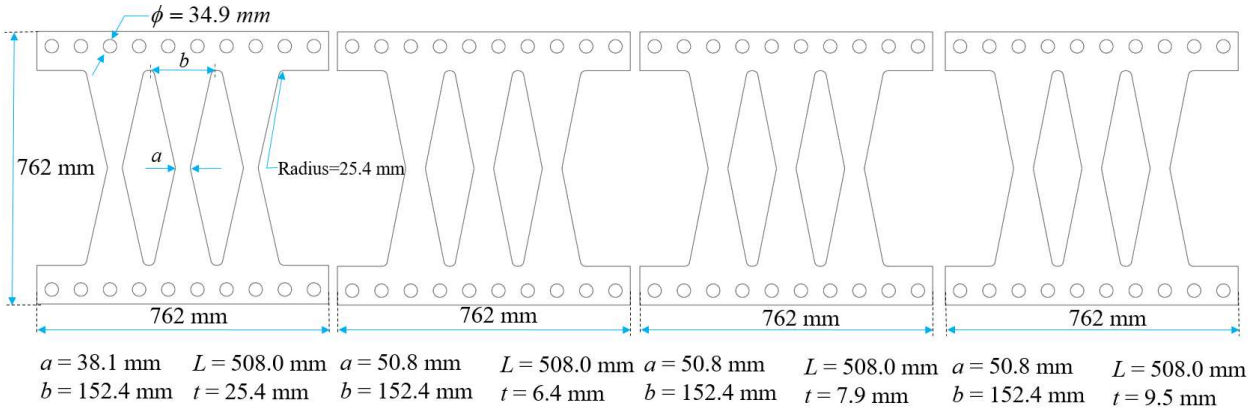

(e) Specimen BF5 (f) Specimen BF6 (g) Specimen BF7 (h) Specimen BF8

Fig. 2. Drawings of specimen geometries

Table 2. Test Matrix

Specimen	Plate Thickness, *t* (mm)	Middle Width *a* (mm)	End Width, *b* (mm)	Link Length, *L* (mm)	Non-Dimensional Parameters		Expected behavior
					a/b	*(b-a)/L*	
BF1	25.4	50.8	152.4	508	0.33	0.2	Flexural yielding at quarter points
BF2	25.4	34.9	111.1	127	0.33	0.55	Shear yielding at reduced section
BF3	25.4	35.6	106.6	254	0.33	0.28	Flexural yielding + shear yielding
BF4	25.4	50.8	76.3	508	0.667	0.05	Flexural yielding near link ends
BF5	25.4	38.1	152.4	508	0.25	0.225	Flexural yielding near reduced section
BF6	6.4	50.8	152.4	508	0.33	0.2	Elastic lateral torsional buckling
BF7	7.9	50.8	152.4	508	0.33	0.2	Inelastic lateral torsional buckling
BF8	9.5	50.8	152.4	508	0.33	0.2	Inelastic lateral torsional buckling

Three tension coupons for each of the four different plate thicknesses, *t*=6.45 mm, *t*=7.9 mm, *t*=9.5 mm and *t*=25.4 mm, were tested in accordance with ASTM standard A370-07a. All

plates of a given thickness were obtained from the same heat. Each tension coupon was waterjet cut with the width of the reduced section equal to 38.1 mm and gage length of 203.2 mm. Table 3 gives average results for the three tension coupons.

Table 3. Material Properties

Plate thickness (mm)	Yield Stress (MPa)	Ultimate Stress (MPa)	Fracture Elongation (%)
6.35	483	527	16.2
7.94	376	499	25.3
9.53	390	505	25.4
25.4	376	533	26.1

Test Setup and Details

The test setup illustrated in Fig. 3 was designed to apply shear displacements to the specimens using an MTS 201.8 hydraulic actuator with capacity of 1468 kN and stroke of ±381 mm. The two pin-pin struts of the test frame were designed to allow horizontal displacements during the test. In addition, the test frame, as shown in Fig. 3(a), was restrained against out-of-plane movement at the top beam by lateral bracing system as shown in Fig. 3(b). All bolts used were grade A490. A picture of the overall test setup is shown in Fig. 4(a).

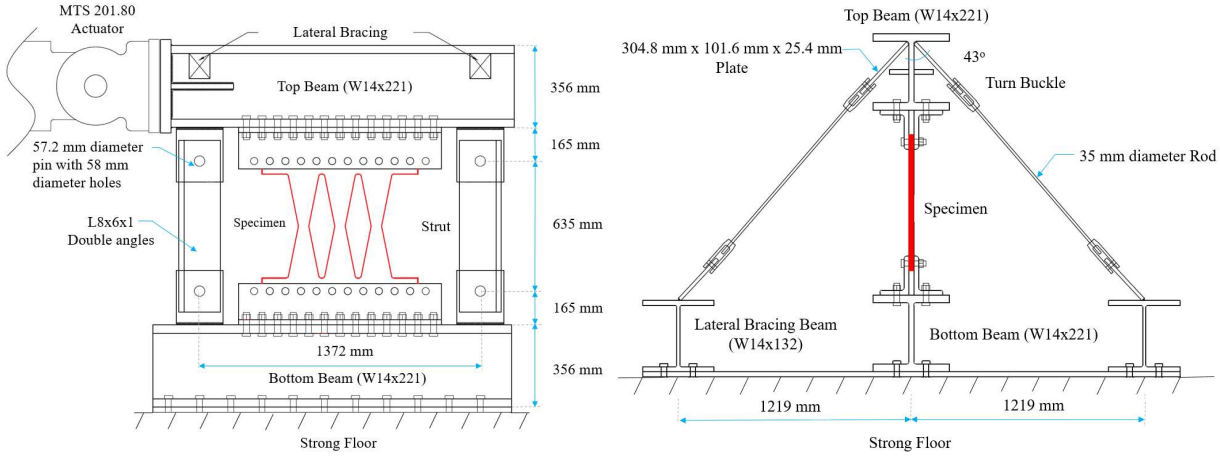

a) Test Frame b) Lateral Bracing

Fig. 3. Test Setup

The FEMA 461 cyclic displacement protocol was adopted starting with the smallest shear angle of γ_0=0.15%. Each shear angle step has two cycles and the amplitude of the next step, γ_{i+1}, is 140% the amplitude of the previous step, γ_i, (i.e., $\gamma_{i+1} = 1.4\gamma_i$). The shear angle steps were continued until the specimen experienced near complete loss of lateral strength.

Fig. 4(b) shows the instrumentation plan which includes 1) an internal actuator displacement sensor 2) actuator load cell 3) four horizontal string potentiometers, SP1, SP2, SP3, SP4, to measure horizontal displacements at different heights; 4) two diagonal string potentiometers, SP6R and SP7L and two vertical linear potentiometers, LP1R and LP2L, to compute shear distortion angles of the structural fuse; and 5) four strain gages were attached to each angle of the struts as shown in Fig. 4(b) to obtain axial strain. The reported shear angle is the average of the computed shear angles at the left (sensors LP2L and SP6R) and right (sensors LP1R and SP7L) of the specimen using the law of cosines and thus the measured shear angle excludes the effect of specimen rigid body motion. Before the testing program, a calibration test was conducted where a vertical jack and reference load cell were inserted in place of the specimen and a conversion factor between average strain in the strut strain gages and force was obtained for each of the struts. A GOM Correlate Pro Digital Image Correlation (DIC) system was used to obtain strain and displacement fields on the specimen face.

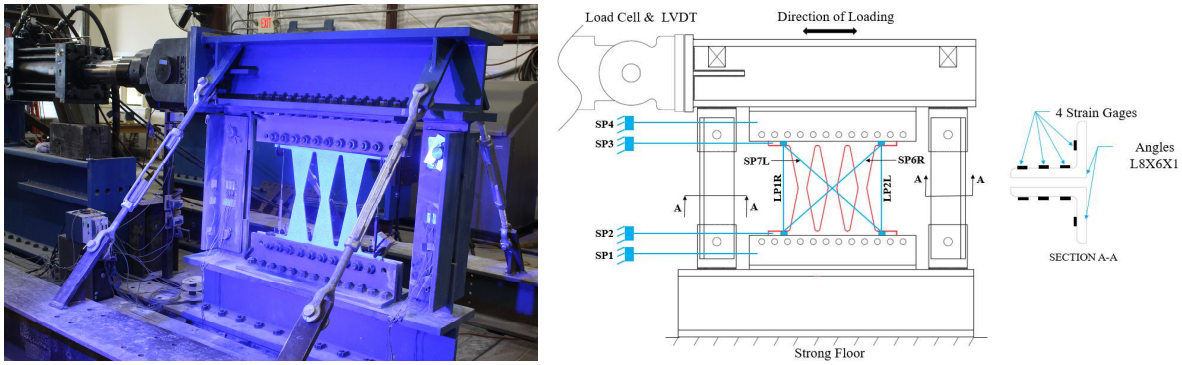

(a) Picture of Test setup (b) Instrumentation Plan

Fig. 4. Overall Test Setup

Specimen Behavior

The results of the eight structural fuse shear tests are discussed in this section starting with specimens undergoing shear yielding or flexural yielding including Specimen BF1, Specimen BF2, Specimen BF3, Specimen BF4, Specimen BF5 and then progressing to the specimens undergoing lateral torsional buckling, Specimen BF6, Specimen BF7 and Specimen BF8, respectively. In order to make a relative comparison between specimens, the vertical axes of the hysteretic plots are expressed by normalized shear ratio V/V_{exp} where V is the recorded shear force and V_{exp} is the yield strength of the specimen obtained from the experiment. More specifically, measured shear strength, V_{exp} was obtained from the experimental results as the shear force at the intersection of initial stiffness and line tangent to the hysteresis curve at positive 4% shear angle. The horizontal axes are expressed in term of shear angle, which, as discussed in the previous section was taken as the average between two pairs of sensors. For each specimen, the normalized shear force vs. shear angle is presented along with a picture identifying locations of fractures and buckling. The progression of limit states and failure modes of eight specimens are presented including description of fractures and buckling.

Fig. 5(a) illustrates the hysteretic curve and summarizes events of the Specimen BF1. First signs of yielding were observed during the 0.8% shear angle cycles as the whitewash started flaking off at the quarter points of the links, implying the locations of plastic hinging. BF1 maintained full hysteretic behavior through the 15% shear angle cycles, then buckling of the web plate began to cause pinching in the hysteretic behavior in the next cycle (at approximately 22% shear angle). This was followed by the first fracture occurred at the reduced section of the left link at approximately 32% shear angle cycles due to significant inelastic deformations, as shown in Fig. 5(e). At the conclusion of the test, it did not show signs of carrying additional loads after the second and third fractures at the right and middle links in the next cycle, respectively.

The hysteretic behavior and summary of behavior for Specimen BF2 are presented in Fig. 5(b). BF2 displayed a visually observable yielding during the 0.4% shear angle cycles as evidenced by the whitewash flaking off, confirming the locations of yielding at the reduced sections of the link. BF2 had full hysteretic behavior up to approximately 6% shear angle cycles. It is worth mentioning that outside links were observed to have diagonal yielding patterns, likely due to the significant axial forces acting on these links. This implies that outside links had more yielding in comparison to the middle link. Consequently, these outside links fractured at approximately 11% shear angle cycle, resulting in significant strength and stiffness degradation. Eventually, the middle link fractured at about 15% shear angle cycle, as illustrated in Fig. 5(f). No out-of-plane motion or buckling was observed during the test.

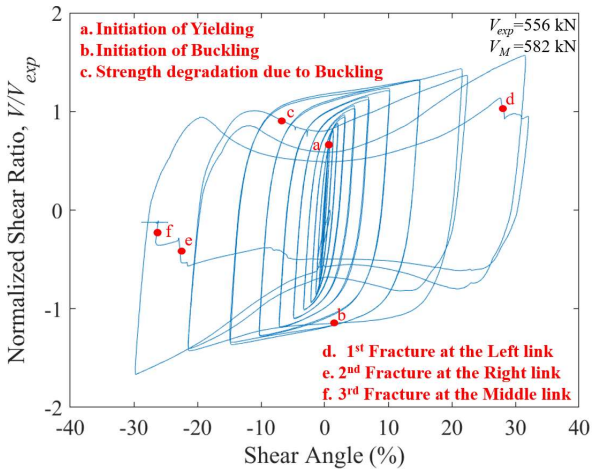

(a) BF1 Flexural Yielding @ 1/4 Points

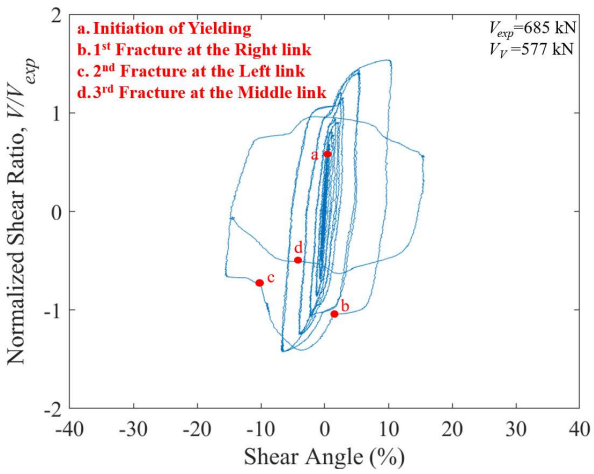

(b) BF2 Shear Yielding

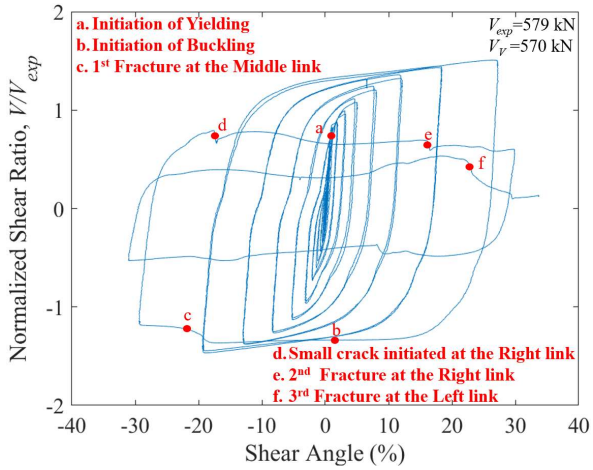

(c) BF3 Flexure / Shear Transition

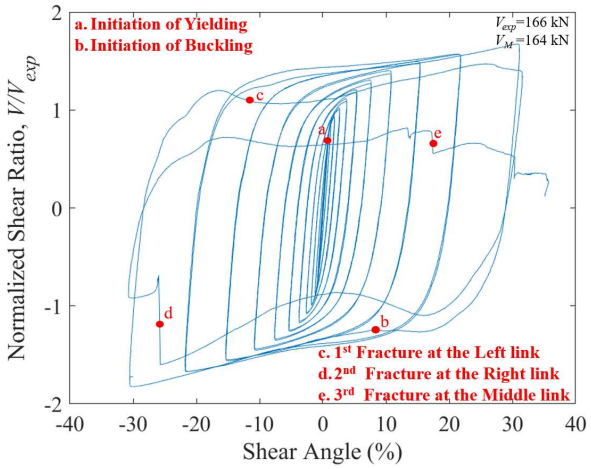

(d) BF4 Flexural Yielding Near Ends

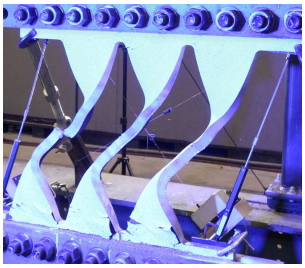

(e) BF1 at point d

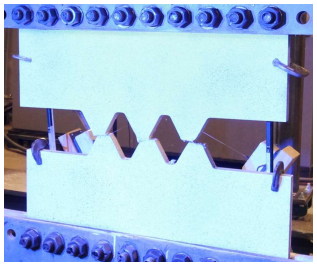

(f) BF2 at point d

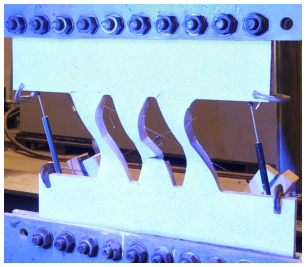

(g) BF3 at point c

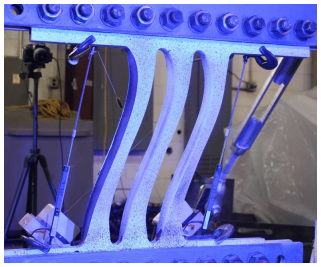

(h) BF4 at point b

Fig. 5. Hysteretic Behavior and Pictures at Key Stages for BF1 through BF4

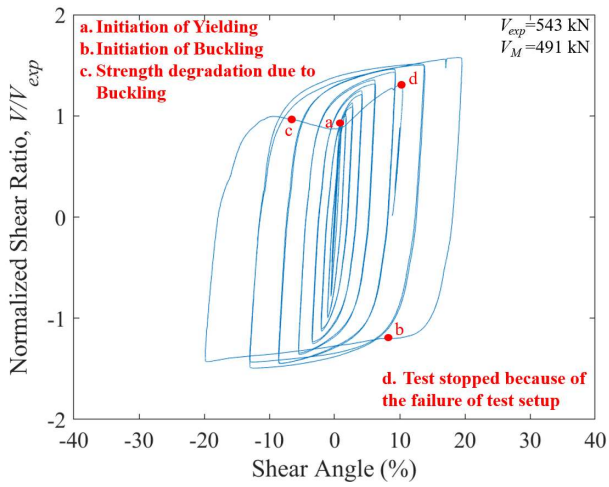

(a) BF5 Flexural Yielding Near Reduced Sections

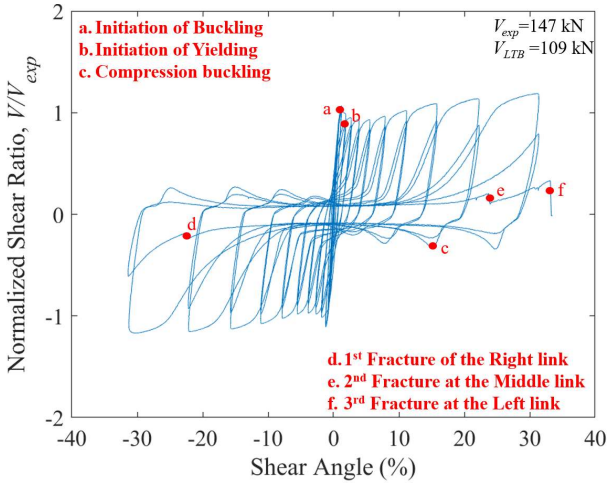

(b) BF6 Elastic LTB, t=6.4 mm

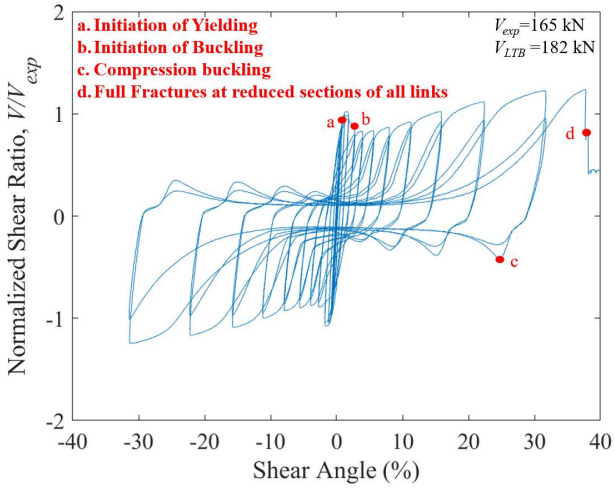

(c) BF7 Inelastic LTB, t=7.9 mm

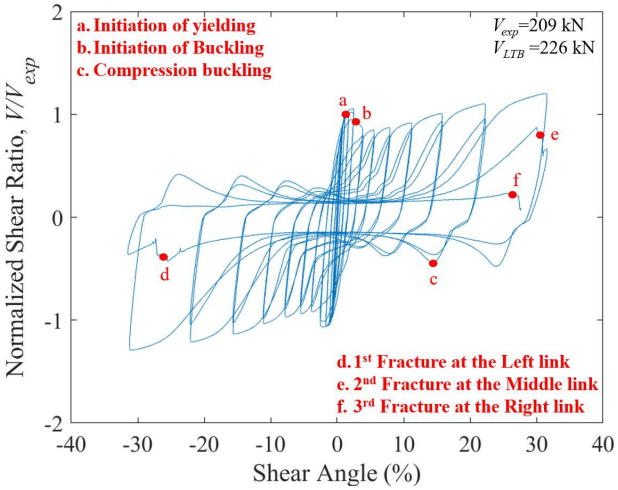

(d) BF8 Inelastic LTB, t=9.5 mm

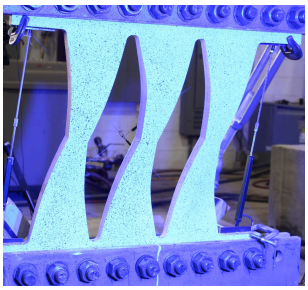

(e) BF5 @ point d

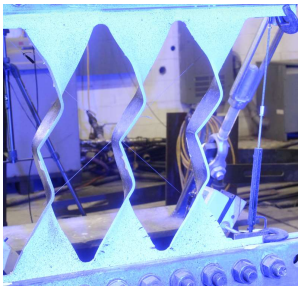

(f) BF6 @ point c

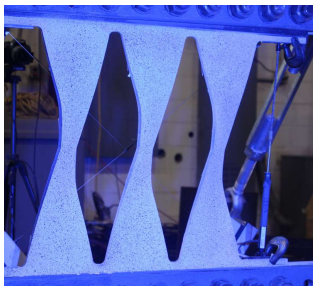

(g) BF7 @ point b

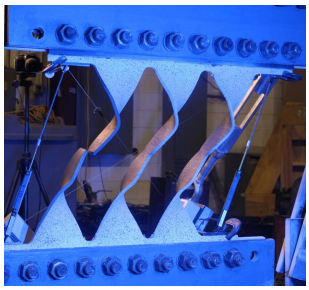

(h) BF8 @ point d

Fig. 6. Hysteretic Behavior and Pictures at Key Stages for BF5 through BF8

Hysteretic curve and summary of behavior for Specimen BF3 are shown in Fig. 5(c). BF3 was observed to initiate yielding at approximately 1.1% shear angle as evidenced by the whitewash flaking off, indicating the locations of yielding at the edges and reduced sections of the links. BF3 maintained full hysteretic behavior up to approximately 20% shear angle cycle, prior to a slight pinching in hysteretic behavior due to buckling in the next cycle (at approximately 27% shear angle). This was followed by the full fracture at bottom quarter point of the middle link as shown in Fig. 5(g), leading to a significant strength and stiffness degradation. Due to flexural hinging and buckling, crack initiated at the quarter point at the right link and then propagated, followed by the full fracture at approximately 30% shear angle cycle, resulting in the significant loss of strength and stiffness. The specimen eventually failed after the full fracture of the left link in the next cycle.

Fig. 5(d) summarizes the behavior for the BF4. This specimen started yielding at approximately 0.7% shear angle. Inelastic deformations continued to spread out as evidenced by the whitewash flaking off, confirming the locations of plastic hinging at the ends of the link. BF4 demonstrated a full hysteretic behavior up to the 20% shear angle cycle, prior to the out-of-plane motion at the 30% shear angle cycle, resulting in the pinched hysteretic response. Due to concentration of inelasticity, first fracture occurred at the end of the left link (at approximately 30% shear angle cycle). Eventually, the shear strength of BF4 approached zero after the second and third fractures occurred at the right and middle links, respectively, in the next cycle.

Fig. 6(a) shows the hysteretic curve and summary of events for Specimen BF5. First signs of yielding were observed at approximately 0.7% shear angle cycles. Yielding appeared to be at quarter points and distributed over the link length as evidenced by areas of whitewash flaking off. BF5 had a full hysteretic behavior up to approximately 13% shear angle cycles before the three links began to buckle, as shown in Fig. 6(e), at approximately 20% shear angle. This resulted in a

remarkable pinching in the hystertic response. Due to the twisting of the top loading beam, the weld at the pin on lower left strut fractured.

The hysteretic curve and a summary of events for Specimen BF6 are presented in Fig. 6(b). BF6 exhibited a visually observable out-of-plane motion at approximately 1% shear angle cycles. The areas of whitewash flaking off implies the initiation of yielding of the links (at approximately 1.5% shear angle cycles), confirming the locations of plastic hinging at the quarter points of the links. It is worth mentioning that these areas had cresent shapes and flaked off on twisted portion of the links, implying that yielding was most likely due to lateral torsional buckling rather than flexural yielding. Due to both buckling and yielding, BF6 demonstrated a significant pinching in the hystertic behavior, indicating the low level of energy dissipatio. The specimen experienced a mechanism during load reversals where inelasticities concentrated at the reduced section of the links likely due to compression buckling, leading to the abrupt bumps in the hysteretic curve, as shown in Fig. 6(f). Due to inelasticity concentration, three links fractured at the reduced sections of the links at approximately 32% shear angle cycles.

Fig. 6(c) and 6(d) summarize the behavior of Specimen BF7 and Specimen BF8. In general, the overall behavior of these two specimens was similar to the Specimen BF6. Nevertheless, they initiated yielding before undergoing out-of-plane motion. More specifically, BF7 and BF8 were observed to initiate yielding at the shear angle of approximately 1.5%, as evidenced by the whitewash flaking off, followed by buckling. It was not until the 2.2% shear angle cycles that out-of-plane displacements were observable for BF7 while BF8 did not experience buckling until the shear angle of approximately 3%. Subsequently, BF7 and BF8 had the same failure mode as BF6 since they underwent the same mechanism during load reversals, as mentioned in previous section. This mechanism, as illustrated in Fig. 7, was also previously described by Ma et al. 2010.

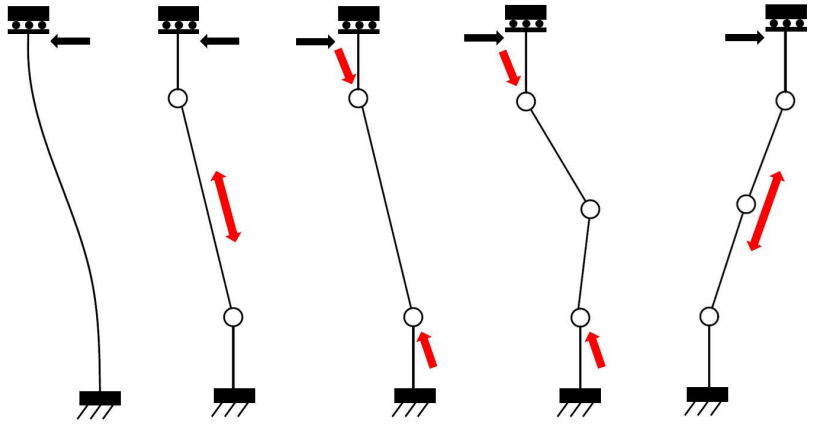

Fig. 7 Mechanism associated with the failure of lateral torionsal buckling

Comparison of Specimen Behavior

Table 4 presents a summary of specimen behavior where design shear strength is computed as the minimum of flexural yielding (Eq. (6) or Eq. (7) as applicable), shear yielding (Eq. (8)), and elastic LTB (Eq. (11)). Yielding mechanism, types of limit state, the evaluations of the prediction equations, buckling and fracture resistance are discussed in this section. In addition, predicted stiffness is also calculated using Eq. (10) derived by Ma et al. (2010), for comparison.

Table 4. Summary of specimen behavior

Specimen	Measured Shear Strength, V_{exp} (kN)	Predicted Shear Strength (kN)			Measured Stiffness (kN/mm)	Predicted Stiffness (kN/mm)	Shear Angle at Buckling (%)	Shear Angle at 1st Fracture (%)	Predicted / Measured Shear Strength
		V_M	V_V	V_{LTB}					
BF1	556	**582**	840	7002	122	190	22	32	1.05
BF2	685	1100	**577**	77024	1202	782	N/A	11	0.84
BF3	579	**570**	**570**	10606	224	222	27	27	0.98
BF4	166	**164**	840	4079	35	24	30	30	0.99
BF5	543	**491**	630	6656	126	190	20	N/A	0.9
BF6	147	187	270	**109**	38	42	1	33	0.74
BF7	165	**182**	263	214	43	53	2.2	36	1.1
BF8	209	**226**	326	369	50	64	3	32	1.08

Values in **bold and underline** represent the design shear strength

Fig. 8 illustrates the example whitewash associated with different limit states including flexural yielding, shear yielding, transition between the limit states of flexural yielding and shear yielding, lateral torsional buckling. For BF1 designed to undergo flexural yielding, yielding

initiates at quarter points and then inelasticity continued to spread out and distribute over the link length, as illustrated in Fig. 8(a). Conversely, inelasticity concentrates at the reduced section at mid-height of the link for specimen undergoing shear yielding for BF2, as shown in Fig. 8(b). For BF3, whitewash flaked off at both the quarter points and reduced sections for the transition between the limit states of flexural yielding and shear yielding, as presented in Fig. 8(c).

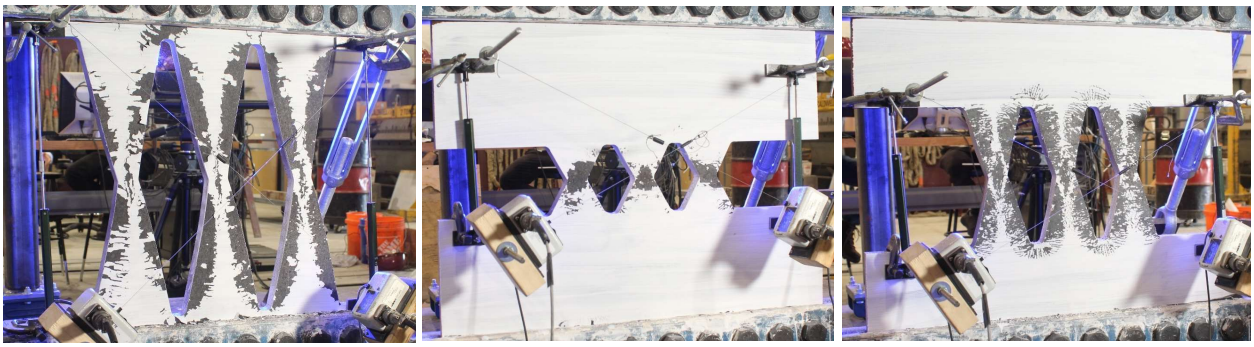

(a) BF1 Flexural Yielding (b) BF2 Shear Yielding (c) BF3 Flexure/Shear Transition

Fig. 8. Example whitewash of different limit states

In addition, Fig. 9 shows the effective strain fields obtained from DIC at approximately 20% shear angle, except 10% shear angle for BF2. The effective strain, ε_{eff}, given in Eq. 12, is an instantaneous (i.e., noncumulative) strain measure that is analogous to the von Mises stress which is useful for evaluating the level of inelasticity. The maximum effective strain of the test specimens is shown to be approximately 30-40 times the strain of yielding of steel material (i.e strain at yield is approximately 0.002). These DIC results further confirm the locations of yielding and yielding pattern associated with each limit state apart from those verified from the whitewash flaking. Second, Fig. 9a, 9b and 9c validate the criteria to determine controlling limit state, listed in Table 1. More specifically, as the taper ratio, *a/b,* are kept constant and less than 0.5 (*a/b*=0.33), varying the shear ratio of *(b-a)/L* leads to different controlling limit state (i.e flexural yielding, shear yielding or transition between shear yielding and flexural yielding).

Locations of plastic hinging for specimens undergoing flexural yielding including BF1, BF4 and BF5, are presented in Fig. 9(d), 9(e) and 9(f). This verifies that taper ratio, *a/b*, plays an important role in the locations of plastic hinging. As this ratio, *a/b*, is greater than 0.5, plastic hinges are encouraged to form at link ends while this ratio being less than 0.5 results in plastic hinges occurred away from the link ends. It is noted that BF5 was designed to have plastic hinging close to the reduced sections. However, the experimental result revealed that plastic hinging actually formed closer to the quarter points, as shown in Fig. 9(f).

$$\varepsilon_{eff} = \sqrt{\frac{2}{3}\varepsilon_{ij}\varepsilon_{ij}} \tag{12}$$

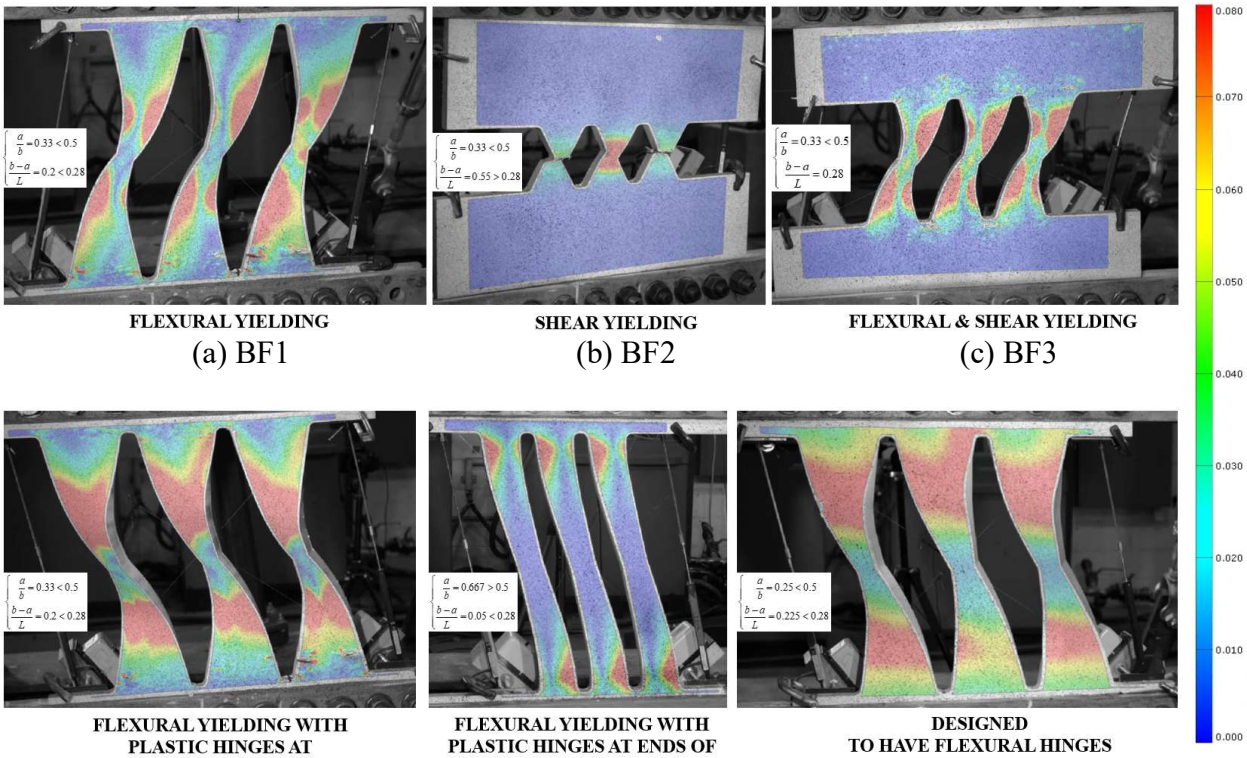

Fig. 9. Yielding Pattern and Limit State of Test Specimens

Fig. 10 represents the DIC images to compare the out-of-plane displacement of the four specimens, BF1, BF6, BF7, BF8. DIC results were taken at approximately 8% shear angle. It is noted that these four specimens have the same configuration but different thicknesses. It can be seen that the displacement fields of three specimens, BF6, BF7, BF8 are similar, as illustrated in Fig. 10(a), 10(b), 10(c) indicating fairly similar out-of-plane motions. Conversely, Specimen BF1 demonstrated a better bucking resistance, as shown in Fig. 10d, due to greater plate thickness, comfirming that plate thickness, t is an important parameter in controlling buckling resistance of the structural fuse, as expected.

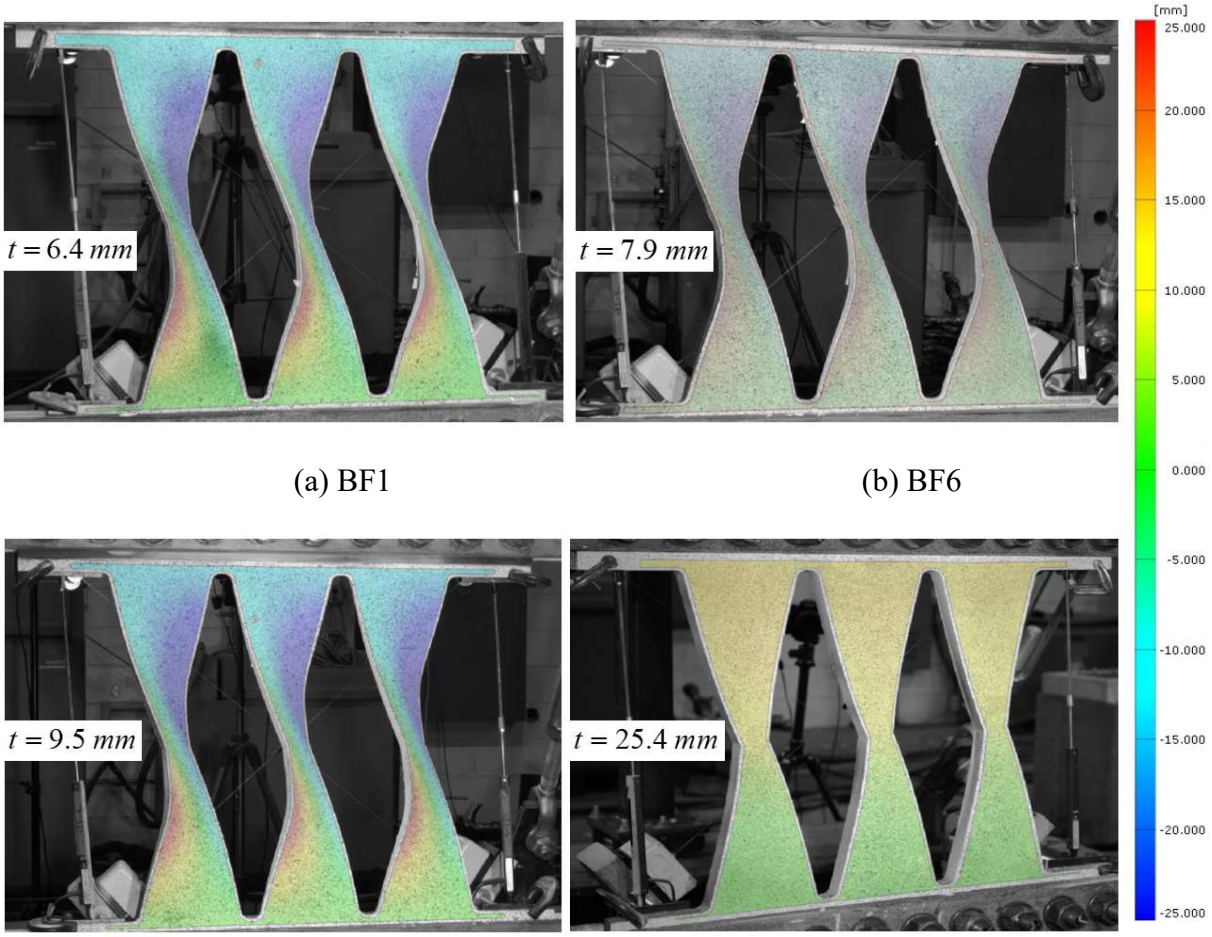

(a) BF1 (b) BF6

(c) BF7 (d) BF8

Fig. 10. Out-of-plane displacement

Regarding the accuracy of the predicted equation, the predicted shear strength of test specimens is compared to the measured shear strength, as presented in Table 4. The accuracy of the predicted equation is expressed in terms of the predicted strength divided by the measured strength. This ratio being greater than unity implies that the predicted shear strength is greater than measured shear strength, or overestimation while this ratio being less than unity corresponds to the underestimation of the predicted equations. Table 4 shows that, in general, the derived equations (i.e Eq. (6) and Eq. (7)) are relatively good in predicting shear strength of the test specimens as these ratios are relatively close to unity. Predicted equation of Specimen BF2 (Eq. (8)) had the least accuracy among specimens designed to undergo either flexural or shear yielding. This is likely due to the axial forces acting on the links. Another reason could be the rotation of the upper part of the specimen as the BF2 links are relatively short compared to the overall length of the specimen. This suggests that ratio of the link length, L, to the overall length of the specimen plays an important role in the behavior of the specimen. Similarly, predicted equation of Specimen BF6 has the least accuracy among specimens designed to under lateral torsional buckling, Specimen BF6, Specimen BF7 and Specimen BF8. This suggests that more work is necessary to evaluate the accuracy of the elastic LTB equation.

For buckling resistance, BF1, BF2, BF3, BF4 and BF5 demonstrated a good buckling resistance as the peak shear angle associated with buckling ranges from 20% to 30%. It is noted that BF2 did not display visually observable buckling during the test. For specimens designed to experience lateral torsional buckling, BF6, BF7 and BF8, the initiation of out-of-plane deformations began early in the range of approximately 1%-2% of shear angle, as expected. It is worth mentioning that BF1 and BF8 are similar shapes but different in plate thickness (i.e 25.4

mm for BF1 vs. 9.5 mm for BF8) which resulted in a significant improved buckling resistance for BF1 in comparison to BF8, as presented in Table 4.

Even though lateral torsional buckling test specimens, BF6, BF7, BF8, had pinched hysteretic responses due to early initiation of buckling, they displayed a remarkable fracture resistance as the peak shear angle associated with first fracture ranges from 30%-36% shear angle, as listed in Table 4. BF2 designed to have shear yielding exhibited a low level of fracture resistance since the peak shear angle associated with first fracture is approximately 11%. Conversely, test specimens undergoing flexural yielding including BF1, BF3, BF4, BF5 showed a relatively good fracture resistance as the average peak shear angle associated with first fracture is approximately 30% due to the distribution of yielding over the link length which promotes ductility.

CONCLUSION

The main findings of these study can be summarized as follows:

(a) Yielding mechanism, locations of plastic hinging associated with each limit state (i.e shear yielding, flexural yielding, transition between the limit state of shear yielding and flexural yielding, and lateral torsional buckling) was experimentally validated. The generalized design equations derived in previous section can be used for practical design of the butterfly-shaped structural fuse

(b) If energy dissipation, buckling resistance and fracture resistance are desirable in practical design, structural fuses undergoing flexural yielding consisting of Specimen BF1, Specimen BF3, Specimen BF4 and Specimen BF5 are recommended. If strength and stiffness are desired for design, specimen with shear yielding, such as Specimen BF2, is recommended. Lateral torsional buckling specimens such as Specimen BF6, Specimen BF7, Specimen BF8 can be

advantageous for some applications in self-centering systems as they displayed a remarkable fracture resistance despite of early buckling.

ACKNOWLEDGEMENTS

This work was supported by the National Science Foundation under Grant No. CMMI-1453960. In-kind funding was provided by AISC and INFRA-METALS. Any opinions, findings, and conclusions or recommendations expressed in this material are those of the authors and do not necessarily reflect the views of the National Science Foundation or other sponsors.

REFERENCES

AISC. 2016. Seismic provision for structural steel buildings. ANSI/AISC 341-1. Chicago, IL: AISC.

ASTM Standard A370-07a. Standard test methods and definitions for mechanical testing of steel products. West Conshohocken, PA: American Standards for Testing and Materials International (ASTM); 2007.

Aschheim M.and Halterman A. (2002), "Reduced Web Section Beams: Phase One Experimental Findings And Design Implications". The Earthquake Engineering Online Archive, NISEE e-Library.

Borello, Daniel J., and Larry A. Fahnestock. "Seismic design and analysis of steel plate shear walls with coupling." *Journal of Structural Engineering* 139.8 (2013): 1263-1273.

Eatherton, M. R., X. Ma, H. Krawinkler, D. Mar, S. Billington, J. F. Hajjar, and G. G. Deierlein (2014). "Design concepts for controlled rocking of self-centering steel-braced frames." J. Struct. Eng. 140 (11): 04014082.

Egorova, N., Eatherton, M. R. and Maurya, A. (2014). "Experimental study of ring-shaped steel plate shear walls." Journal of Constructional Steel Research, 103, 179-189.

Farzampour A. and Eatherton M. (2019), "Yielding and lateral torsional buckling limit states for butterfly-shaped shear links ", Engineering Structures, vol. 180, pp. 442-451.

FEMA 461. Interim testing protocol for determining the seismic performance characteristics of structural and nonstructural components. Washington, DC (USA): Federal Emergency Management Agency; 2007.

Ghabraie, K., Chan, R., Huang, X. and Xie, Y. M. (2010). "Shape optimization of metallic yielding devices for passive mitigation of seismic energy." Engineering Structures, 32(8), 2258-2267.

Kobori T, Miura Y, Fukuzawa E, Yamanda T, Arita T, Takenaka Y, Miyagwa N, Tanaka N, Fukumoto T (1992). Development and application of hysteresis steel dampers. In: Earthquake Engineering the 10th Conference. Rotterdam: Belkema, 1992.

Kurokawa Y, Sakamoto M, Yamada T, Kurino H, Kunisue A. Seismic design of a tall building with energy dissipation damper for the attenuation of torsional vibration. Struct Des Tall Buil 1998;7:21–32.

Lemaitre, J., & Chaboche, J. L. (1990). Mechanics of Solid Materials: Cambridge University Press.

Liu, Y., and M. Shimoda. (2013). "Shape optimization of shear panel damper for improving the deformation ability under cyclic loading." Struct. Multidiscip. Optim. 48 (2): 427–435.

LS-DYNA. 2011-2018 LSTC.

Luth GP, Sargunuraj S, Krawinkler H, McDonald B. USC school of cinema an example of reparable performance based design. SEAOC Convention Proceedings. 2008.

Lynch JP. Active structural control research at Kajima Corporation. Stanford, CA:National Science Foundation's Summer Institute in Japan Program, Stanford Univ.;1998.

Ma, X., Borchers, E., Pena, A., Krawinkler, H. and Deierlein, G. (2010). "Design and behavior of steel shear plates with openings as energy-dissipating fuses." John A. Blume Earthquake Engineering Center Technical Report, (173).

Nguyen, T.N. (2022). "Computational and Experimental Investigation of Seismic Structural Fuse Shapes for Resilient Structural Systems." PhD Dissertation. Dept. of Civil Engineering, Virginia Polytechnic Institute and State Univ.

Plaut, R. and Eatherton, M. (2017) "Lateral-Torsional Buckling of Butterfly-Shaped Beams with Rectangular Cross Section" Engineering Structures, v.136, 2017, p.210

Popov, E. P., and M. D. Engelhardt. 1988. “Seismic eccentrically braced frames.” J. Constr. Steel Res. 10 (Jan): 321–354.

Teruna D, Majid TA, Budiono B. Experimental study of hysteretic steel damper for energy dissipation capacity. Adv Civ Eng 2015. Hindawi Publishing Corporation.

Vian, D., M. Bruneau, and R. Purba. 2009. “Special perforated steel plate shear walls with reduced beam section anchor beams. II: Analysis and design recommendations.” J. Struct. Eng. 135 (3): 221–228

6. SEISMIC STRUCTURAL FUSES WITH HOURGLASS-SHAPED LINKS AND ELLIPTICAL HOLES

Trai N. Nguyen[1], Matthew R. Eatherton[2]

[1] Graduate Research Assistant, Department of Civil and Environmental Engineering, Virginia Tech, Blacksburg, USA.
[2] Professor, Department of Civil and Environmental Engineering, Virginia Tech, Blacksburg, USA.

ABSTRACT

Shear-acting structural fuses with hourglass-shaped links or elliptical holes are two new types of seismic fuses which have recently been examined. However, studies on the seismic behavior of these configuration are limited since the focus was on the flexural yielding limit state of the links, prediction equations for shear strength were lacking, and there was no information about whether shear yielding would control over a plastic hinging mechanism.

This paper presents a combined analytical and experimental study on hourglass-shaped structural fuse links and structural fuses with elliptical holes. The two main limit states of these shear-acting seismic fuses including flexural yielding and shear yielding are examined and associated design equations are derived. An experimental program is then conducted including six structural fuses, three with hourglass-shaped links, and three with elliptical holes. The results of the experiments are used to evaluate the derived design equations and recommendations are made for use in practical design.

The experimental results confirmed that the hourglass shaped link encourages the distribution of yielding over the entire link length, thus improves the ductility. For instance, the hourglass shaped link undergoing flexural yielding limit state was able to resist fracture up to 30% shear angle. Similarly, specimen with elliptical-shaped holes undergoing flexural yielding also

demonstrated relatively good energy dissipation as it was capable of maintaining full hysteretic behavior up to approximately 20% shear angle.

Keywords: Structural Fuse, Hourglass-Shaped, Elliptical-Shaped Hole, Seismic Behavior, Earthquake Engineering

INTRODUCTION

Traditional seismic design of structures achieves required lateral drifts and seismic energy dissipation through inelasticity in structural components that can lead to extensive structural damage after a major seismic event. An alternative design approach is using metallic dampers as passive energy-dissipating devices that concentrate inelastic deformations and limits the forces that can be transferred, and thus protects the main structural components from damage. In some structural configurations, these passive metallic dampers can be made of steel plates cut into different shapes and configurations to localize yielding, thus promoting ductility. The use of metallic dampers offers several advantages including (1) replaceablity, (2) the strategic cut-outs add more design variables to tune the strength, stiffness, etc.

Steel shear dampers were proposed by Kelly et al. (1972), which has been used widely since then due to benefits such as using a simple configuration and excellent seismic performance. The key component of this damper is a steel shear panel to dissipate seismic energy. Fig. 1 illustrates three possible ways that a shear-acting structural fuse can be implemented in lateral force resisting systems including use as a replaceable link in the linked column frame system as illustrated in Fig. 1(a) (Lopes et al. 2012), damper configuration, as illustrated in Fig. 1(b) (Teruna et al. 2015), or eccentrically braced frame , as shown in Fig. 1(c) (Popov and Engelhardt 1988).

Several studies have been conducted to investigate structural fuses with several cutout patterns such as the slit panel with straight strips of steel called links (e.g., Cortes and Liu 2011, Hitaka and Matsui, 2003), a ring-shaped structural fuse (e.g., Egorova et al. 2014), steel plate shear wall with circular holes (e.g, Vian et al. 2009), and structural fuses with butterfly-shaped links (e.g Ma et al. 2010, Plaut and Eatherton 2017, Farzampour and Eatherton 2019).

Two configurations of structural fuses that have been examined recently are the structural fuses with elliptical holes and hourglass-shaped links. The hourglass-shaped link as illustrated in Fig. 1(d) was designed to spread inelasticity over the entire link length (e.g Lee et al. 2015) while the structural fuse with elliptical holes as shown in Fig. 1(e) has no sharp corners, and thus is expected to exhibit good fracture resistance. Lee et al. (2015) tested several hourglass-shaped dampers and revealed that the tested specimens demonstrated improved energy dissipation compared to straight link dampers by approximately 230%. Also, the fracture surfaces suggested that these dampers experienced ductile failure, implying that this hourglass shape is a promising configuration for improving cyclic and fatigue performance of the damper (Lee et al. 2014). Along the same lines, Lee et al. (2015) conducted cyclic tests to examine the low cycle fatigue characteristics of the hourglass-shaped damper. It was reported that cracks were distributed along the link length, indicating that maximum seismic energy was absorbed by the damper. In addition, several hourglass-shaped link dampers were monotonically and cyclically tested under various conditions including loading rate, material strength, and number of links (Lee et al. 2015). Zhu et al. (2018) proposed new steel shear panel damper optimized by stress contour lines for better energy consumption efficiency and the resulting optimized configuration is similar to an hourglass shape. Experimental results revealed that this shape exhibited an increase in hysteretic energy dissipation of approximately 40%-60% relative to conventional rectangular panel damper.

Aschheim and Halterman (2002) studied a beam with elliptical holes in the web, to shift the yielding from the connection to that of the beam and thus improve ductility. In subsequent research, different yielding mechanisms of this reduced beam section including flexural yielding and shear yielding have been computationally studied by Shin et al. 2017. Koppal and Eatherton (2013) designed a perforated steel plate shear wall (SPSW) with the thicker plate for less demand

on boundary elements and delaying buckling compared to conventional solid steel plate shear wall. Similarly, a special detailed perforated panel SPSW with series of circular holes was reported to be a viable alternative to conventional solid SPSW without the need for stiffeners (Vian et al. 2009).

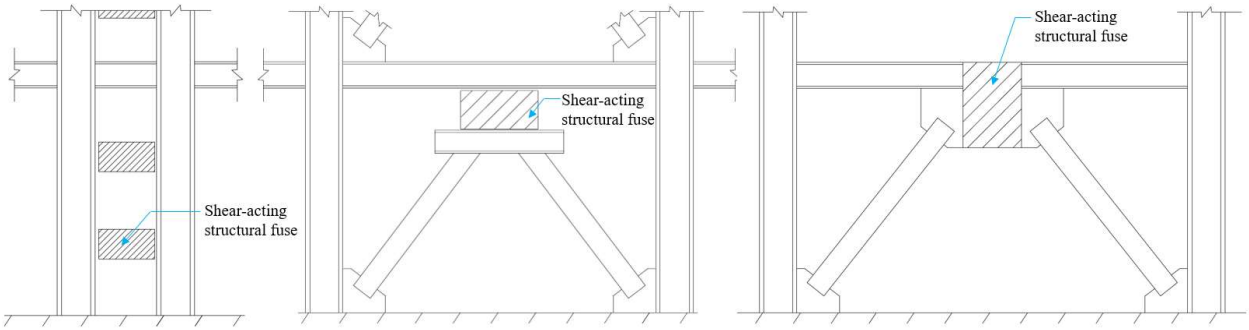

(a) Linked column (b) Damper configuration (c) Eccentrically braced frame

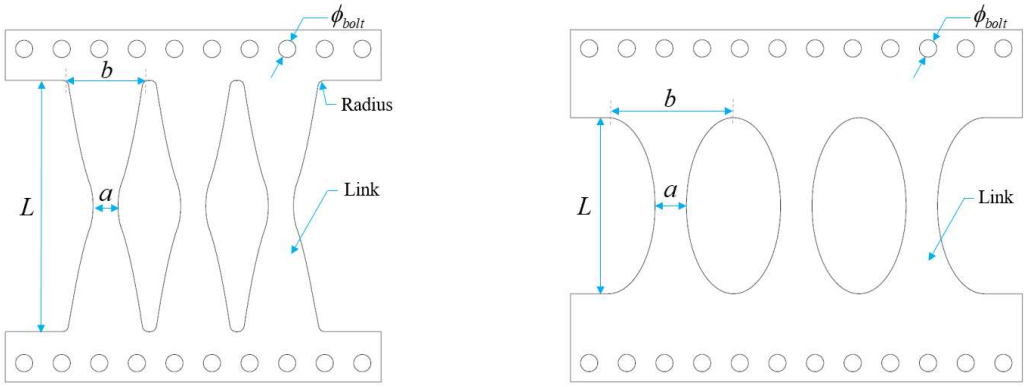

(d) Hourglass-shaped Structural Fuse (e) Structural Fuse with Elliptical Holes

Fig. 1. Possible implementation of shear-acting structural fuses

In this study, two key limit states including shear yielding, flexural yielding. This includes of the analytical derivation of generalized design equations for these two shapes associated with each limit state. Six experiments were conducted on specimens to investigate the cyclic load-deformation behavior for these shapes. Based on the results of the experiments, design recommendation are provided for practical design.

CONCEPTS AND GENERALIZED DESIGN EQUATIONS

In this section, two main limit states are discussed including flexural yielding, shear yielding for the structural fuses with hourglass shaped links and elliptical holes.

Assumptions used in this section include the following:

(1) Stresses associated with moment and shear are considered independently with respect to yielding, i.e., interaction of shear and normal stresses are neglected.

(2) Plane stress condition was assumed as the plate thickness is relatively small relative to the plan dimensions.

(3) The link is subjected to idealized loading conditions including shear, equal but opposite moments at each end, and no axial force.

(4) The effect of radii at the intersections are ignored.

(5) Fracture is not considered in this section, but instead will be investigated in the subsequent sections associated with the experimental program.

Hourglass-Shaped Link

The hourglass-shaped structural fuse as illustrated in Fig. 2 is designed to have uniform yielding along the link length. More specifically, the width of hourglass-shaped is derived based on the idea of having plastic moment demand equal plastic moment strength at every location along the link length, x. As the hourglass-shaped link is subjected to shear force, V, moment demand, M_d, linearly varies along the link length as given in Eq. (1). Moment strength of the link, M_s, varies quadratically along the link length, x, and is given in Eq. (2). Equating moment strength to moment demand gives the width of the hourglass-shaped link, $w(x)$, in terms of location x as shown in Eq. (3).

$$M_d(x) = V\,|x| \tag{1}$$

$$M_s(x) = f_y \frac{t\left[w(x)\right]^2}{4} \tag{2}$$

$$w(x) = \sqrt{\frac{4V\,|x|}{tf_y}} \tag{3}$$

where:
V = Applied shear force
M_d = Moment demand of the hourglass shaped link
M_s = Moment strength of the hourglass shaped link
$w(x)$ = Width of the link at location x
f_y = Yield stress
t = Plate thickness

The local coordinate system is illustrated in Fig. 2(a). At the link ends where x=L/2 (see Fig. 2(a)), width b, is expressed in Eq. (4). Expressing Eq. (3) in terms of end width, b, and link length, L along the link length is given in Eq. (5). The theoretical shape of the hourglass-shaped link based on Eq. (5) is shown in Fig. 2(a).

$$b = \sqrt{\frac{2VL}{tf_y}} \tag{4}$$

$$w(x) = b\sqrt{\frac{2|x|}{L}} \tag{5}$$

It is noted that at the middle section where x=0, the width is zero which is not reasonable due to an inability to transfer shear force (see Fig. 2(a)). Therefore, a practical geometry of the hourglass-shaped link should have specified middle width, a, to resist shear as shown in Fig. 2(b). The edges at the middle section are created using three-point arcs such that (1) width at middle section equals to a, (2) edges along the link length are smooth and continuous to avoid brittle

fracture. Shear force associated with flexural yielding is obtained by equating moment strength, M_s, and moment demand, M_d, as given in Equation (6)

$$V = tf_y \frac{\left[w(x)\right]^2}{4|x|} \tag{6}$$

Substituting Eq. (5) into Eq. (6) gives the shear load associated with flexural limit state, given in Eq. (7). In addition, the shear load associated with shear yielding is expressed in Eq. (8).

$$V_M = tf_y \frac{b^2}{2L} \tag{7}$$

$$V_V = tf_y \frac{a}{\sqrt{3}} \tag{8}$$

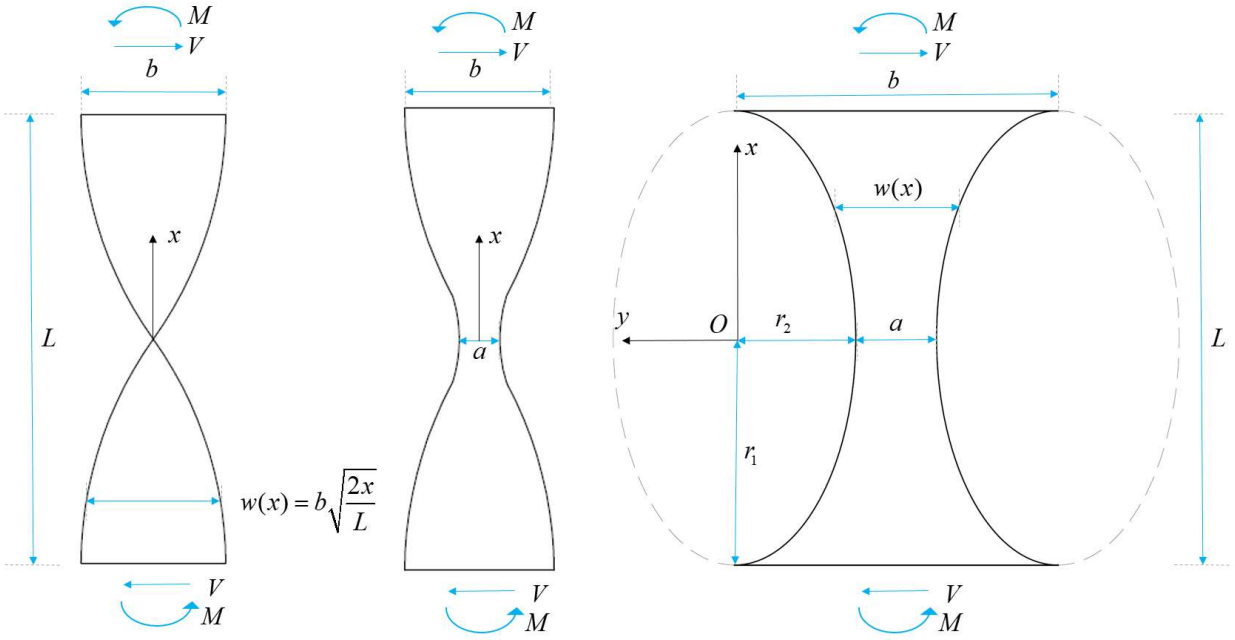

(a) Theoretical hourglass-shaped link (b) Practical hourglass-shaped link (c) Elliptical holes

Fig. 2. Hourglass-Shaped Link and Elliptical holes

The hourglass-shaped link is controlled by flexural yielding when flexural strength is less than shear strength or Eq. (8) being greater than Eq. (7) results in Eq. (9) presenting an inequality

for flexural limit state in terms of two non-dimensional parameters taper ratio, *a/b*, and width ratio, *b/L*. Table 1 summarizes three discussed limit states and corresponding criteria.

$$\frac{a}{b} > 0.866\frac{b}{L} \qquad \text{then flexural yielding controls} \qquad (9)$$

2.2 Structural Fuse with Elliptical Holes

Fig. 2(c) illustrates a structural fuse with elliptical holes. The equation for an ellipse is presented in Eq. (10) with local coordinate system shown in Fig. 2(c). The width of the link at any location along the length, *w(x)*, is obtained and given in Eq. (11), where r_1, r_2 are radii of the ellipse in the *x* and *y* direction (see Fig. 2(c)), respectively and *a* is the width at the middle section of the link. Similar to the previous section, shear force, *V* is obtained by equating plastic moment demand, M_d, given in Eq. (12) and plastic moment strength, M_s, expressed in Eq. (13) of the link, as given in Eq. (14). This equation is a function of the link width along its length, indicating that the location of flexural yielding and related link shear strength is dependent on the radii of the ellipse and width of middle section, *a*.

$$\frac{x^2}{r_1^2} + \frac{y^2}{r_2^2} = 1 \qquad (10)$$

$$w(x) = 2r_2 + a - 2r_2\sqrt{1 - \frac{x^2}{r_1^2}} \qquad (11)$$

$$M_d(x) = Vx \qquad (12)$$

$$M_s(x) = f_y \frac{t\left[w(x)\right]^2}{4} \qquad (13)$$

$$V = tf_y \frac{\left[w(x)\right]^2}{4x} \qquad (14)$$

Taking the derivative of this shear strength, Eq. (14), with respect to location x results in the location of plastic hinges that causes the minimum shear strength. This expression for x_p can be simplified in terms of the width of the link at ends ($x=L/2$), $b=a+2r_2$, as given in Eq. (15).

$$x_p = \frac{r_1}{2\sqrt{2}r_2}\sqrt{b\sqrt{b^2+32{r_2}^2}-(b^2+8r_2^2)} \tag{15}$$

Substituting Eq. (15) for the location of plastic hinges, x_p, into Eq. (11) for link width, $w(x)$, gives the width of the link at plastic hinge as presented in Eq. (16). This equation can be simplified and expressed in Eq. (17).

$$w(x_p) = b - 2r_2\sqrt{1-\frac{{x_p}^2}{{r_1}^2}} \tag{16}$$

$$w(x_p) = b - \frac{\sqrt{2}}{2}\sqrt{b^2+16{r_2}^2-b\sqrt{b^2+32{r_2}^2}} \tag{17}$$

The shear strength of the link associated with flexural hinging can then be calculated by Eq. (18). Strength associated with shear yielding is expressed in Eq. (19), and the plastic hinging is expected to form at middle section (x=0).

$$V_M = \frac{tf_y}{4}\frac{\left[w\left(x_p\right)\right]^2}{x_p} \tag{18}$$

$$V_V = at\frac{f_y}{\sqrt{3}} \tag{19}$$

This link will be flexural dominated if the shear strength associated with flexural hinging in Eq. (18) is greater than the strength associated with shear yielding in Eq. (19). This can be expressed in Equation (20).

$$\frac{w^2(x_p)}{x_p} < \frac{4a}{\sqrt{3}} \tag{20}$$

The link width at ends ($x=L/2$), b, can be expressed in terms of ratio of the middle width and radius in the y direction, $k=a/r_2$, and is given in Eq. (21). Then the criterion for flexural limit state (Eq. (20)) can be further simplified as expressed in Eq. (22), (23). This equation implies that behavior of the link is controlled by all non-dimensional parameters including (1) ratio of two radii of the ellipse, r_1/r_2 and (2) ratio of the middle width and radius in the y direction, $k=a/r_2$. Expressed in other words, the ellipse geometry and width of middle section control structural behavior of the link. Table 1 provides summary of limit states for structural fuse with elliptical holes.

$$b=\left(2+k\right)r_2 \tag{21}$$

$$\frac{w^2(x_p)}{x_p}=\frac{\sqrt{2}r_2^2}{r_1}\frac{\left[\sqrt{2}\left(2+k\right)-\sqrt{\left(2+k\right)^2+16-\left(2+k\right)\sqrt{\left(2+k\right)^2+32}}\right]^2}{\sqrt{\left(2+k\right)\sqrt{\left(2+k\right)^2+32}-\left[\left(2+k\right)^2+8\right]}}<\frac{4kr_2}{\sqrt{3}} \tag{22}$$

$$\frac{r_1}{r_2}>Z_e=\frac{\sqrt{6}}{4}\frac{\left[\sqrt{2}\left(2+k\right)-\sqrt{\left(2+k\right)^2+16-\left(2+k\right)\sqrt{\left(2+k\right)^2+32}}\right]^2}{k\sqrt{\left(2+k\right)\sqrt{\left(2+k\right)^2+32}-\left[\left(2+k\right)^2+8\right]}} \tag{23}$$

Table 1. Summary of limit states for structural fuse with hourglass-shaped link and elliptical holes

	Flexural Yielding	Shear Yielding
Structural Fuse with Hourglass Shaped Link		
Criteria	$\frac{a}{b} > \frac{\sqrt{3}}{2}\frac{b}{L}$	$\frac{a}{b} < \frac{\sqrt{3}}{2}\frac{b}{L}$
Shear Strength	$V_M = tf_y\frac{b^2}{2L}$	$V_V = tf_y\frac{a}{\sqrt{3}}$
Graphical presentation	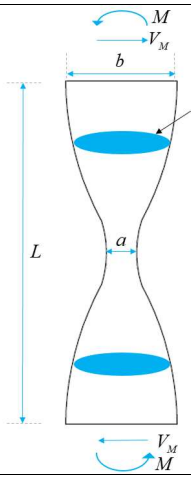	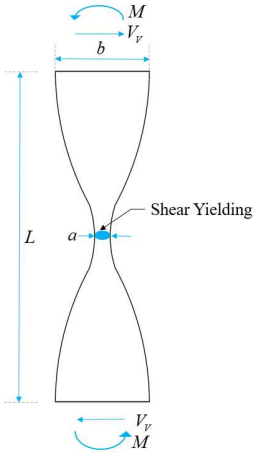
Structural Fuse with Elliptical Holes		
Criteria	$\frac{r_1}{r_2} > Z_e$	$\frac{r_1}{r_2} < Z_e$
Shear Strength	$V_M = f_y\frac{t\left[w\left(x_p\right)\right]^2}{4x_p}$	$V_V = \frac{f_y}{\sqrt{3}}at$
Graphical presentation	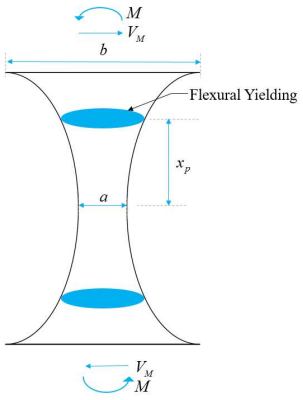	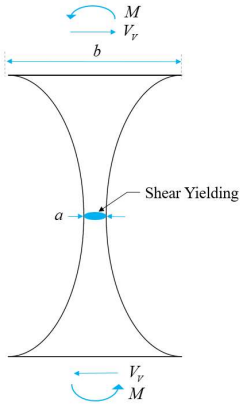

EXPERIMENTAL TESTING PROGRAM

Six specimens were tested at the Thomas M. Murray Structures Laboratory at Virginia Tech. The purpose of this testing program was to investigate the structural behavior of structural fuses with hourglass-shaped links and elliptical holes associated with two limit states (1) flexural yielding, (2) shear yielding.

3.1 Test Specimens

Fig. 3 illustrates geometry of the six specimens and the test matrix is provided in Table 2 and 3. The first three specimens are the hourglass-shaped links, named Specimen HG1, Specimen HG2 and Specimen HG3, were designed to undergo flexural yielding, shear yielding and transition between limit states of flexural yielding and shear yielding, respectively. All of these three specimens have the same link length, L, and end width, b. The only dimension that varies is the reduced width at the middle section, a. Along the same lines, three specimens associated the structural fuses with elliptical holes are Specimen EL1, Specimen EL2 and Specimen EL3 were also tested to evaluate their cyclic behavior associated with flexural yielding, shear yielding and transition between limit states of shear yielding and flexural yielding, respectively. For these three specimens, the geometry of the ellipse, r_1 and r_2, and width at middle of the link, a, are varied for different desired limit states. All six test specimens have the same plate thickness of 25.4 mm and three links.

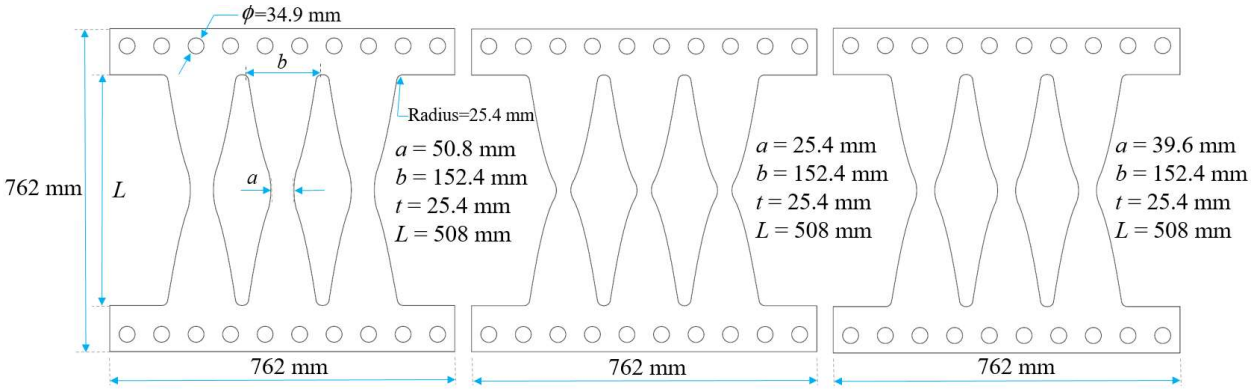

(a) Specimen HG1 (b) Specimen HG2 (c) Specimen HG3

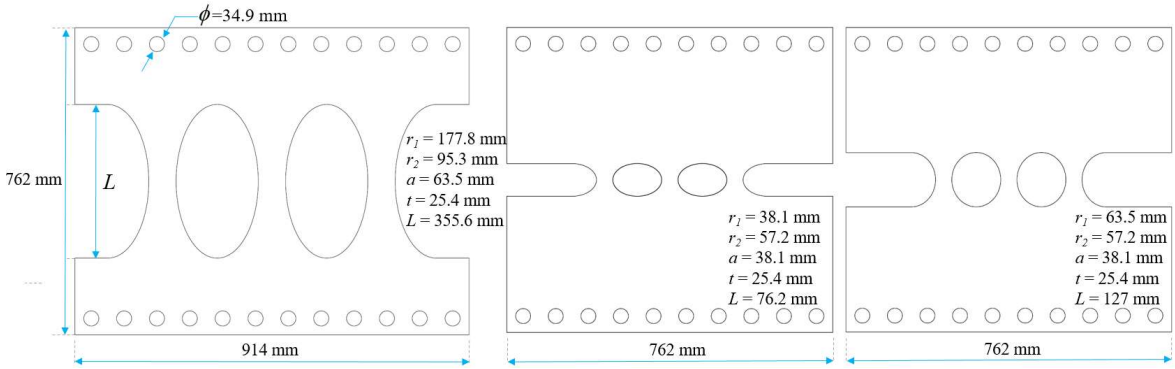

(d) Specimen EL1 (e) Specimen EL2 (f) Specimen EL3

Fig. 3. Geometry of test specimens

Table 2. Test matrix for Structural Fuses with Hourglass-Shaped Links

Specimen	**End Width *a (mm)***	**Reduced Width *b (mm)***	**Link Length *L (mm)***	**Non-Dimensional Ratio**		**Expected behavior**
				a/b	$\frac{\sqrt{3}}{2}(b/L)$	
HG1	50.8	152.4	508	0.33	0.26	Distributed flexural yielding
HG2	25.4	152.4	508	0.167	0.26	Shear yielding at middle
HG3	39.6	152.4	508	0.26	0.26	Flexural and shear yielding

Table 3. Test matrix for Structural Fuses with Elliptical Holes

Specimen	Geometry of Ellipse		Reduced Width	Link Length	Non-Dimensional Ratios		Expected behavior
	r_1 (mm)	r_2 (mm)	a (mm)	L (mm)	r_1/r_2	Z_e	
EL1	177.8	95.25	63.5	355.6	1.88	1.12	Flexural yielding at quarter points
EL2	38.1	57.15	38.1	76.2	0.67	1.12	Shear yielding at middle
EL3	63.5	57.15	38.1	127	1.12	1.12	Flexural and shear yielding

All three specimens were fabricated from the same heat of steel, from which three tension coupons were also tested. Each tension coupon was waterjet cut with geometry in accordance with ASTM standard A370-07a for tension coupons with a plate thickness of 25.4 mm, width of the reduced section equal to 38.1 mm and gage length of 203.2 mm. Modulus of elasticity, yield stress, ultimate strength, and fracture elongation were 224,000 MPa, 376 MPa, 533 MPa and 26%, respectively, based on the average of the three coupons.

Test Setup and Details

The test setup illustrated in Fig. 4 was designed to apply shear displacements to the specimens using an MTS 201.08 hydraulic actuator with capacity of 1468 kN and stroke of ±381 mm. The test setup can be divided into three parts including reaction block, test frame and lateral bracing. The two pin-pin struts of the test frame were designed to allow horizontal displacements during the test. In addition, the test frame was restrained against out-of-plane movement at the top beam by lateral bracing system as shown in Fig. 4(b). All bolts used were grade A490. A picture of the overall test setup is shown in Fig. 5(b).

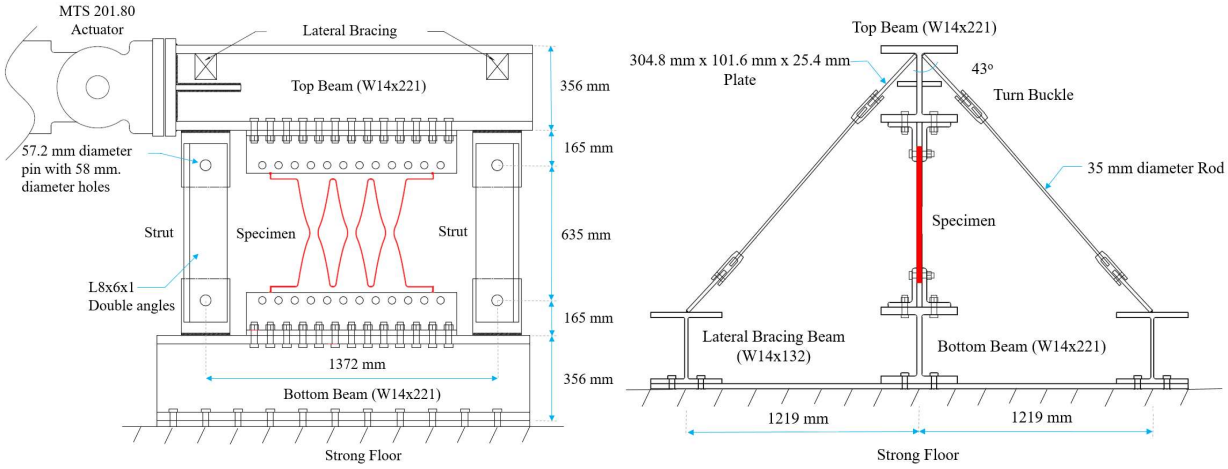

a) Test Frame b) Lateral Bracing

Fig. 4. Test Setup

The FEMA 461 cyclic displacement protocol was adopted starting with the smallest shear angle of γ_0=0.15%. Each shear angle step has two cycles and the amplitude of the next step, γ_{i+1}, is 140% the amplitude of the previous step, γ_i, (i.e., $\gamma_{i+1}= 1.4\gamma_i$). The shear angle steps were continued until the specimen experienced near complete loss of lateral strength.

Fig. 5 shows the instrumentation plan which includes 1) an internal actuator displacement sensor with stroke of ±381 mm; 2) load cell with the capacity of 1468 kN; 3) four horizontal string potentiometers, SP1, SP2, SP3, SP4, to measure horizontal displacements at different heights; 4) two diagonal string potentiometers, SP6R and SP7L and two vertical linear potentiometers, LP1R and LP2L, to compute shear distortion angles of the structural fuse; and 5) four strain gages were attached to each angle of the struts as shown in Fig. 5(a) to obtain axial strain. The reported shear angle is the average of the computed shear angles at the left (using LP2L and SP6R) and right (using LP1R and SP7L) of the specimen using the law of cosines. Before the testing program, a calibration test was conducted where a vertical jack and reference load cell were inserted in place of the specimen and a conversion factor between average strut strain and force was obtained for

each of the struts. All displacements, strain, force measurements were collected using a National Instrumentation (NI) data acquisition system. Furthermore, a GOM Correlate Pro Digital Image Correlation (DIC) system was used to obtain strain and displacement fields by tracking the motion of a speckle pattern painted on the specimen surface.

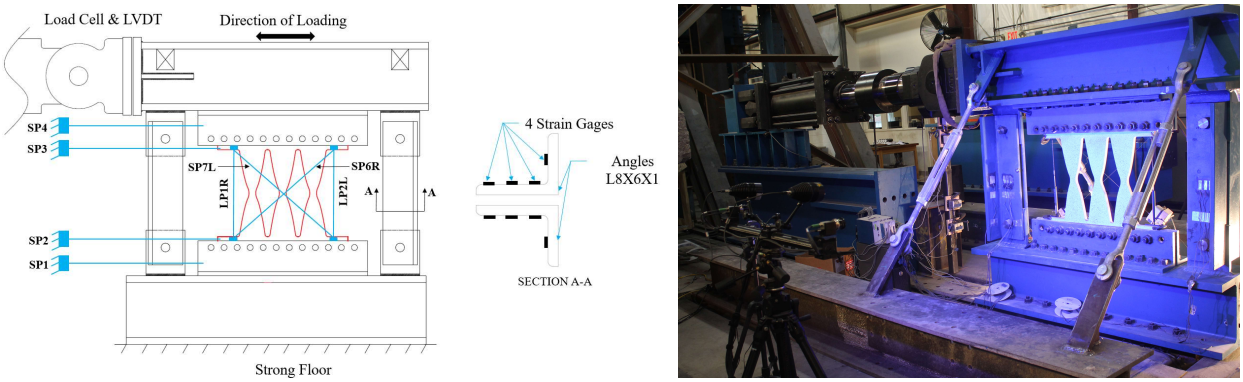

(a) Instrumentation plan (b) Picture of Test setup

Fig. 5. Overall Test Setup

Specimen Behavior

This section presents the experimental results of six tested specimens consisting three variations of hourglass-shaped links and three specimens with elliptical holes. For the purposes of relative comparison between specimens, vertical axis of the hysteretic behavior is expressed by normalized shear ratio V/V_{exp} where V is the shear force obtained from the test and V_{exp} is the shear strength of the tested specimen obtained from the experiment. The horizontal axis is expressed in term of shear angle which was taken as the average between two pairs of sensors as discussed in previous section. For each specimen, the normalized shear force vs. shear angle is presented along with a picture identifying locations of fractures. The progression of limit states and failure modes are presented including description of fractures and buckling.

Fig. 6(a) represents hysteretic response and summary of behavior for specimen HG1. This specimen was first observed to initiate yielding at approximately 0.8% shear angle. Inelasticity continued to spread out as visually observed by the whitewash flaking off along the edges and reduced sections of the links. This confirms that the hourglass configuration encourages yielding to evenly distribute along the link length, as mentioned in previous section. The specimen underwent out-of-plane motion at approximately 14% shear angle, resulting in a slight pinching in the hysteretic curve. The first fracture occurred at the right link, as shown in Fig. 6(b), at approximately 30% shear angle, indicating the excellent fracture resistance of the hourglass-shaped link. This resulted in a significant loss of strength and stiffness. The remaining two links then experienced substantial buckling, leading to the second and third fractures (at approximately 40% shear angle) at the right and middle links. It is noted that these two fractures occurred at the reduced sections of the links due to excessive inelastic deformations. This failure mechanism is similar to that of the butterfly-shaped link undergoing lateral torsional buckling as described in Nguyen and Eatherton (2022). This indicates that structural fuse undergoing large shear deformations are likely to fail under the pinned-column mechanism (Ma et al. 2010, Nguyen and Eatherton, 2022).

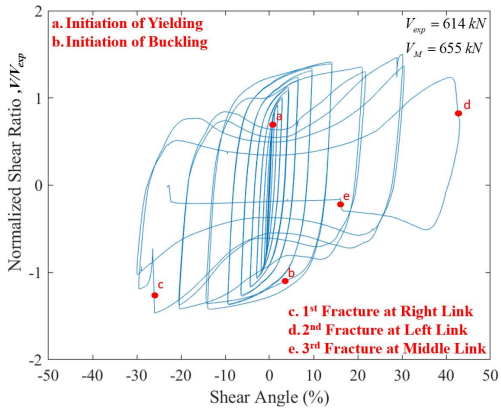

(a) Hysteretic Curve HG1

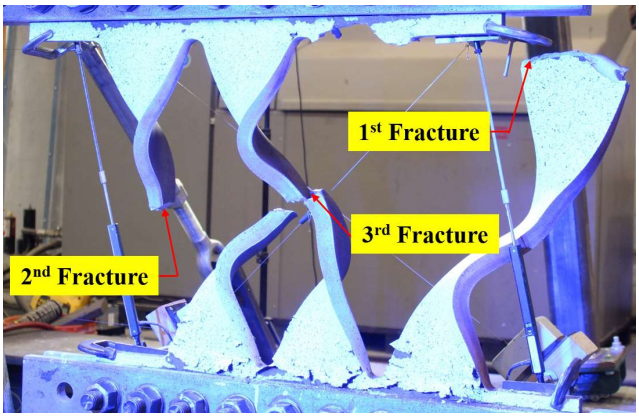

(b) Picture of HG1 at point e

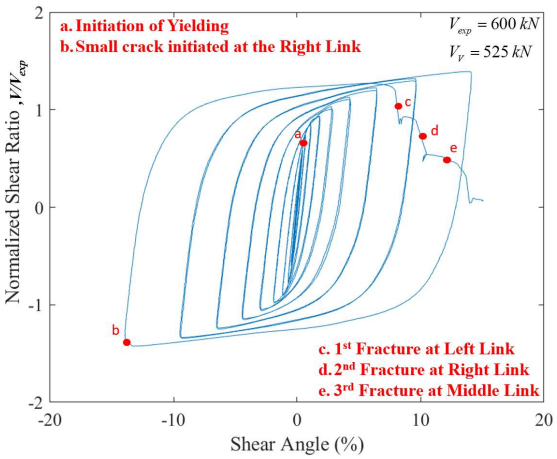

(c) Hysteretic Curve HG2

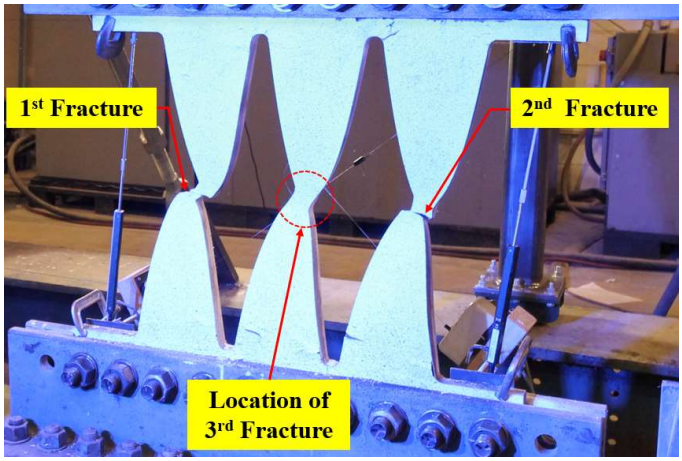

(d) Picture of HG2 at point d

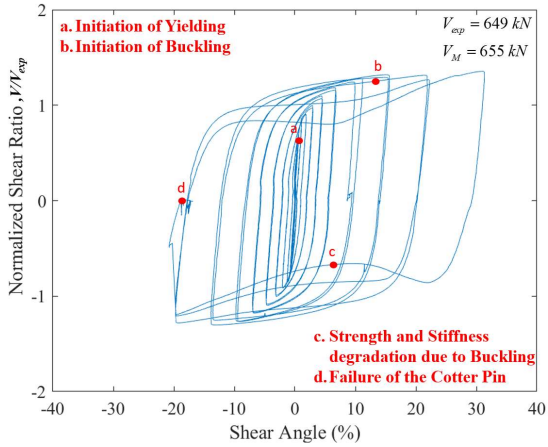

(e) Hysteretic Curve HG3

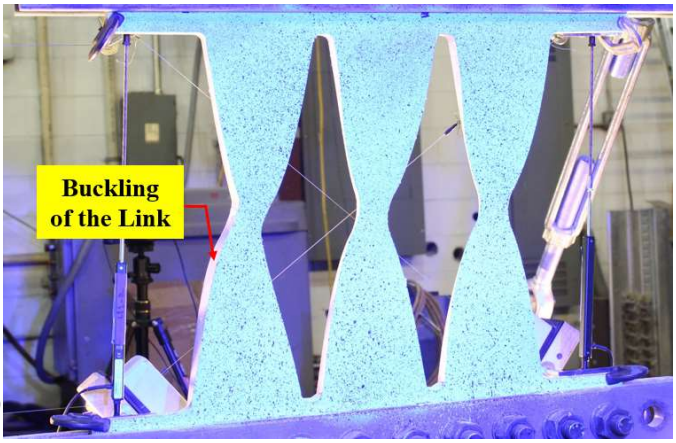

(f) Picture of HG3 at point b

Fig. 6. Hysteretic Behavior and Pictures of Key Stages for Hourglass Shaped Link Specimens

Fig. 6(c) illustrates the load-deformation curve and summarizes the remarkable events for Specimen HG2. First yielding was observed on the three links at the narrow sections as visually observable by the whitewash flaking off (at approximately 0.6% shear angle). It is worth mentioning that inelastic deformations also spread out along the link length as some small areas of whitewash also flaked off at the edges of the links. This specimen was able to maintain a stable hysteretic behavior up to approximately 14% shear angle prior to a loss of strength and stiffness due to a first fracture at the left link. Due to excessive inelastic deformations, this was followed by the second and third fractures at the right and middle links, respectively. This indicates that the

specimen failed due to shear yielding at the reduced sections of the links. No out-of-plane motion or buckling was observed during the test.

Fig. 6(e) illustrates the hysteretic curve and summary of remarkable events for specimen HG3. First signs of yielding were observed at the shear angle of approximately 0.8% as can be seen by the areas of whitewash flaking off. Three hourglass-shaped links were observed to be fully yielded (i.e., all white wash flaked off across the full width) at approximately 17% of shear angle. This was followed by out-of-plane instabilities at approximately 21% shear angle, as shown in Fig. 6(f), resulting in the pinching in the hysteretic response. Buckling of the specimen continued to get severe, leading to the significant twisting of the top loading beam. Consequently, the one of the cotter pins failed at approximately 30% shear angle cycle. Nevertheless, the specimen showed a remarkable fracture resistance as no fracture was observed yet.

Fig. 7(a) presents the summary of behavior for Specimen EL1. The whitewash started flaking off on the links at approximately 0.7% shear angle, indicating the locations of flexural yielding at approximately midway between the link ends and reduced section of the links. Stable hysteretic response was maintained up to approximately 20% shear angle, prior to out-of-plane motion, thus results in a slight loss of strength. Due to the combination of buckling and inelastic deformations, first fracture occurred at the upper plastic hinges of the left link, as shown in Fig. 8(b). Nevertheless, there was just a slight degradation in the peak force. In the next cycle, second and third fractures occurred at the middle and left links, as illustrated in Fig. 7(b). The specimen then showed no signs of carrying additional loads.

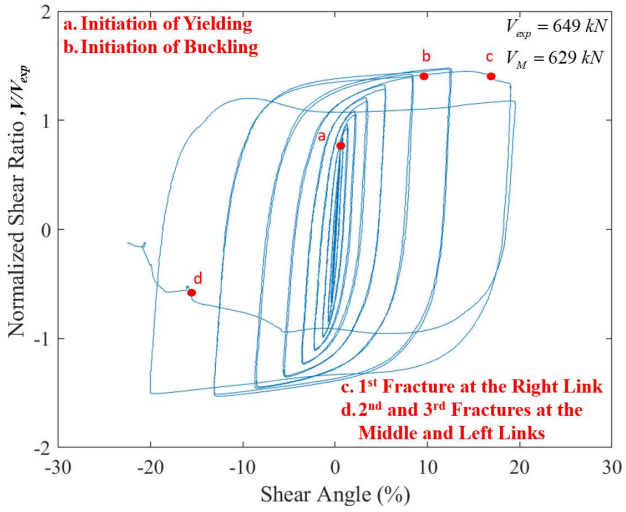

(a) Hysteretic Curve EL1

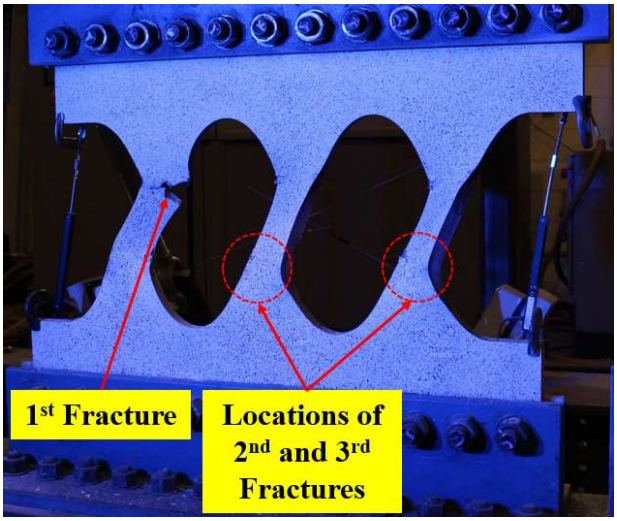

(b) Picture of EL1 at point c

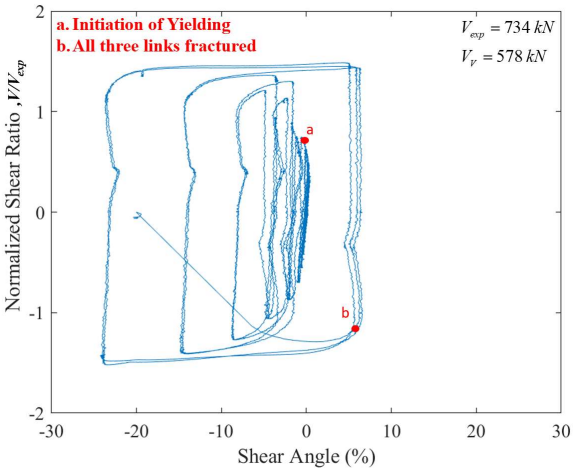

(c) Hysteretic Curve EL2

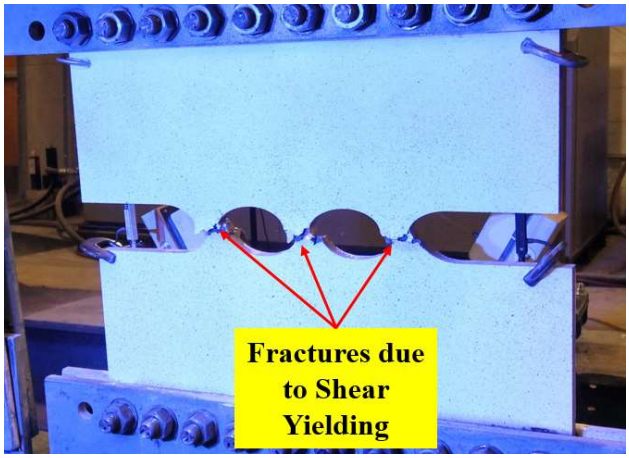

(d) Picture of EL2 at point b

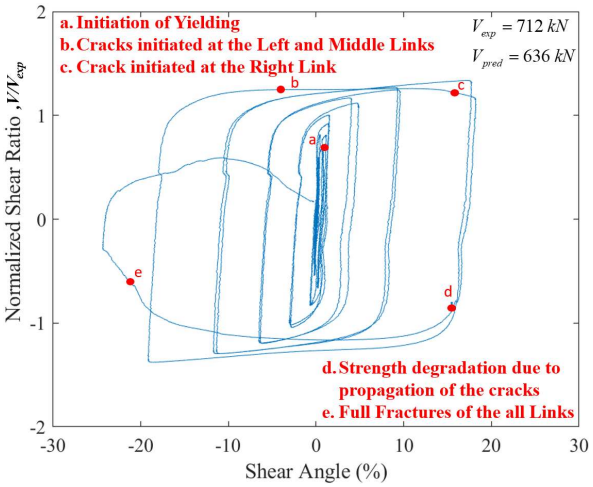

(e) Hysteretic Curve EL3

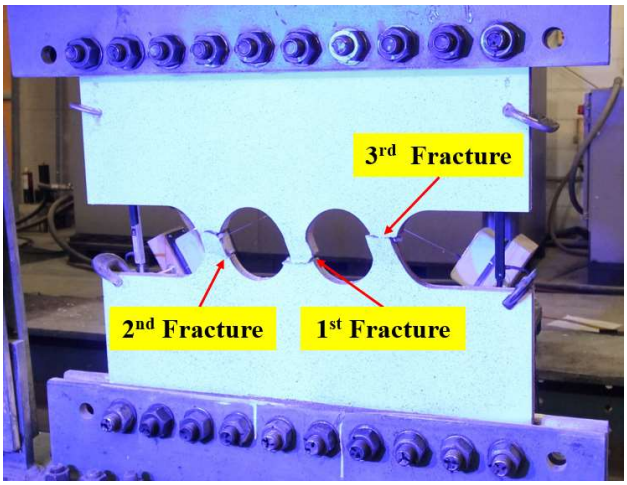

(f) Picture of EL3 at point e

Fig. 7. Hysteretic Behavior and Pictures of Key Stages for Elliptical Hole Specimens

Fig. 7(c) illustrates the hysteretic response for Specimen EL2. First signs of yielding was observed by the whitewash flaking off at approximately 0.7% shear angle. This indicates the locations of shear yielding at the middle of the links. It is noticed that whitewash started flaking off on the outside links, and then the interior link. This is likely due to axial forces acting the exterior links. The specimen rotated at the bottom as the bolts slipped between the specimen and angles. Due to excessive inelastic deformations, the specimen failed due to the fractures at three links at the same time, as illustrated in Fig. 7(d).

Hysteretic response and summary of remarkable events for Specimen EL3 are presented in Fig. 7(e). First signs of yielding was observed by the areas of whitewash flaking off at approximately 0.7% shear angle. This indicates the locations of yielding at (1) reduced section, (2) approximately midway between the link ends and reduced section, for each link. Inelastic deformations continued to spread out along the link length, resulting in the full flaking off of the whitewash, thus indicates the full yielding of the links at approximately 10% shear angle. This specimen was able to have full hysteretic behavior up to approximately 20% shear angle, prior to a slight strength degradation due to the initiation of fracture at the three links. This verifies the locations of plastic hinges, as shown in Fig. 7(f). Eventually, all three links fully fractured due to excessive inelastic deformations. No out-of-plane instability was observed for this specimen during the test.

Comparison of Specimen Behavior

Specimen behavior is summarized in Table 4. Predicted shear strength, V_M or V_V , is computed from generalized equation listed in Table 1 while measured shear strength, V_{exp}, is obtained from hysteretic curve, taken as the shear force at the intersection of initial stiffness and line tangent to the hysteresis curve at positive 4% shear angle. Yielding mechanism, the

evaluations of the prediction equations, buckling and fracture resistance are discussed in this section.

Table 4. Summary of specimen behavior

Specimen	Measured Shear Strength, V_{exp} (kN)	Predicted Shear Strength, V_M or V_V (kN)	Initial Stiffness (kN/mm)	Shear Angle at Buckling (%)	Shear Angle at 1st Fracture (%)	Accuracy of Predicted Equation
HG1	614	655	154	14	30	1.07
HG2	600	525	163	N/A	14	0.88
HG3	649	655	156	21	N/A	1.00
EL1	649	629	253	20	20	0.97
EL2	734	578	950	N/A	10	0.79
EL3	712	636	1030	N/A	20	0.90

Yielding Mechanism

This section discusses the yielding mechanism, locations of yielding of the test specimens, thus verifies the criteria to define controlling limit state listed in Table 1. While Fig. 8 represents the whitewash flaking at the back side of the specimens, Fig. 9 illustrates the effective strain field at the front side of the specimens (which is taken at approximately 10% shear angle).

For specimens with hourglass-shaped links, Specimen HG1, Specimen HG2, Specimen HG3, two geometrical parameters, b and L, are kept unchanged, resulting in a constant non-dimensional parameter $(\sqrt{3}/2)\,(b/L)$ for all three specimens while width at the narrow section, a, varies, leading to the varying ratio, a/b. Different controlling limit states (i.e flexural yielding, shear yielding and transition between the limit states of shear yielding and flexural yielding) were obtained as shown in Fig. 8(a), (b), (c). More specifically, for flexural yielding limit state (i.e Specimen HG1), yielding evenly distributes along the link length, as shown in Fig. 8(a) while inelasticity concentrates at the middle sections at links for the limit state of shear yielding (i.e Specimen HG2), as presented in Fig. 8(b). This is further confirmed by the effective strain fields

shown in Fig. 9 (a), (b). For specimen undergoing both flexural yielding and shear yielding, Specimen HG3, inelastic deformations occur both along the link length and narrow sections of the link, as evidenced in Fig. 8(c) and Fig. 9(c). The above discussions (1) confirm that hourglass configuration of the link encourages yielding to distribute over the link length, thus promotes inelastic deformations, (2) validate the criteria for each limit state of the hourglass-shaped link structural fuses listed in Table 1.

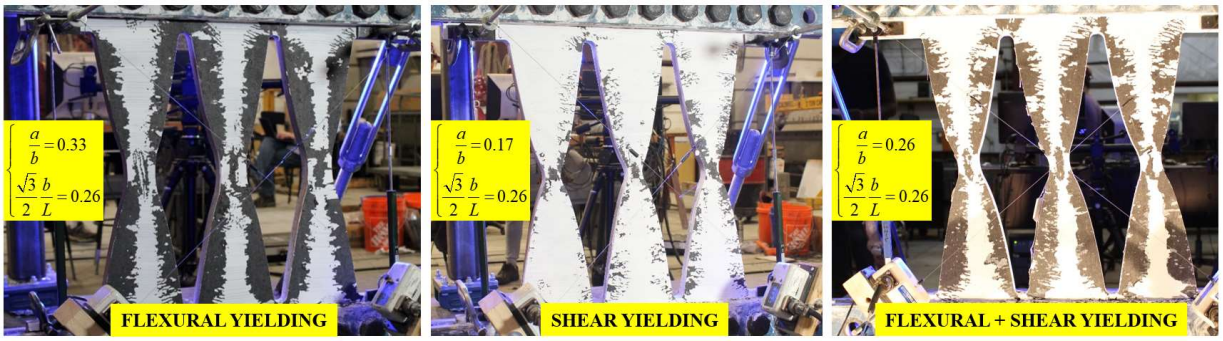

(a) HG1 (b) HG2 (c) HG3

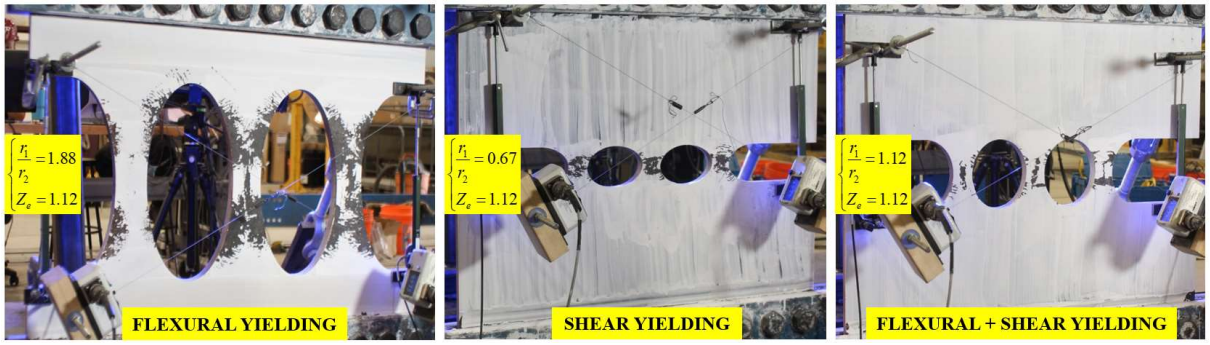

(d) EL1 (e) EL2 (f) EL3

Fig. 8. Yielding Pattern and Limit State of Test Specimens

Fig. 8(d), (e), (f) illustrate the yielding pattern for each limit state of the specimen with elliptical holes, Specimen EL1, Specimen EL2 and Specimen EL3. Values of two non-dimensional parameters, r_1/r_2 and Z_e, are also included with the purposes of validating the criteria

to define controlling limit state, listed in Table 1. While the parameter r_1/r_2 corresponds to the configuration of the elliptical hole, Z_e is a function of $k=a/r_2$ (i.e which is the ratio of width at reduced section to radius of the ellipse in the x-direction). As can be seen in Fig. 8(d), (e), (f), Z_e was kept constant (i.e equals 1.12), the geometries of the elliptical holes were changed by varying the ratio r_1/r_2, thus results in different yielding mechanism. More specifically, Specimen EL1 designed to undergo flexural yielding (i.e $r_1/r_2 > Z_e$) has shown that yielding initiated approximately midway between the reduced sections and link ends, as illustrated in Fig. 8(d). Fig. 9(d) further verified the locations of plastic hinging. It is noted that uneven areas of whitewash flaking off were observed on the three links, as shown in Fig. 8(d), likely due to non-symmetric applied displacements (i.e displacement in the positive direction was less than that of in the negative direction). Conversely, for Specimen EL2 designed to experience shear yielding limit state, the concentration of elasticities was visually observed at the reduced sections by the areas of whitewash flaking off, as illustrated in Fig. 8(e). Fig. 9(e) also verifies that plastic hinging occurred at the middle section of the links. Regarding Specimen EL3, which was designed to explore the transition between limit states of shear yielding and flexural yielding, Fig. 8(f) shows the inelasticity deformations concentrated at both the reduced sections and intermediate sections between link ends and reduced sections. The contour plot of effective strain for Specimen EL3 shown in Fig. 9(f) clearly illustrates three discrete areas of inelasticity, verifying locations of plastic hinging. To conclude, the above discussions validate (1) the yielding mechanism, and (2) criteria to define each limit state of structural fuses with elliptical holes listed in Table 1.

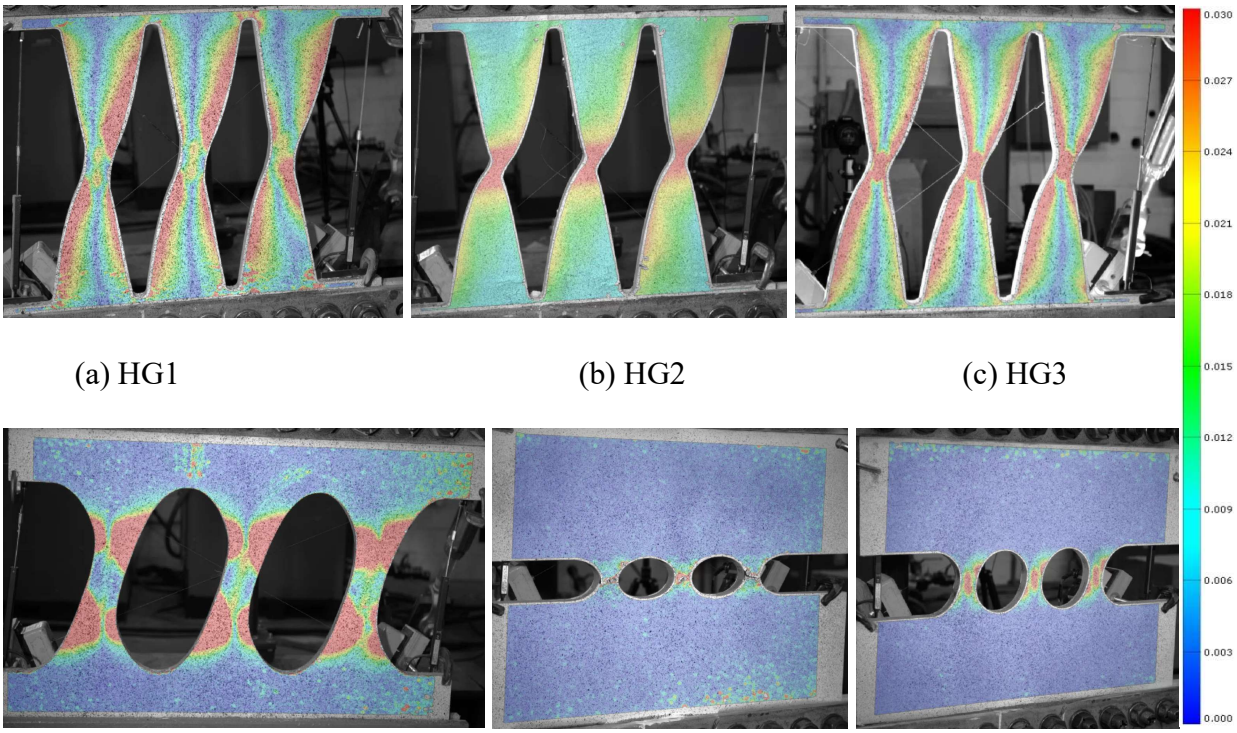

(a) HG1 (b) HG2 (c) HG3

(d) EL1 (e) EL2 (f) EL3

Fig. 9. Effective Strain of Test Specimens Obtained from DIC

Accuracy of Prediction Equations

The accuracy of the predicted equation is expressed in terms of the ratio of the predicted strength (i.e V_M or V_V, as applicable) divided to the measured strength, V_{exp}. This ratio being greater than unity implies that the predicted shear strength is greater than measured shear strength, or overestimation while this ratio being less than unity corresponds to the underestimation of the predicted equation. Table 4 reveals that the equations listed in Table 1 are relatively good in predicting the shear strength of the specimens as measured predicted strength-to- measured strength ratios are close to unity. However, for some specimens associated with shear yielding limit state or short links (i.e less than L=508 mm) such as Specimen EL2 (L=76 mm) and EL3 (L=127 mm), the predicted equations are less accurate as they underestimated the actual shear

strength of these specimens. This can be explained that the connection regions above the links rotated during the tests. This finding suggests that structural fuses should be designed such that the applied shear forces/displacements should be close to the links to exclude the effects of the rotation of the connection regions.

Buckling Resistance

For the purposes of this study, buckling resistance of the specimen is quantified by the peak shear angle of buckling. For hourglass-shaped specimens, Specimen HG3 has shown the best buckling resistance as it maintained full hysteretic up to 21% shear angle. Similarly, Specimen HG1 also demonstrated a relatively good in controlling out-of-plane instabilities as no strength and stiffness degradation due to buckling were visually observable until approximately 14% shear angle. Regarding the specimens with elliptical holes, specimens with flexural yielding including EL1 and EL3 initiated out-of-plane instabilities at approximately 20% shear angle while no buckling was observed for specimens undergoing shear yielding, HG2 and EL2.

Fracture Resistance

In this section, fracture resistance of the specimen is evaluated by the peak shear angle at first fracture. In general, specimens undergoing flexural yielding consisting of Specimen HG1, Specimen HG3, Specimen EL1 and Specimen EL3 exhibited good fracture resistance as the minimum shear angle associated with first fracture is about 20%. Especially, Specimen HG1 displayed an excellent fracture resistance since no fracture was found until the shear angle of 30% In addition, this specimen was able to carry additional load until the shear angle of 40%. Nevertheless, specimens experiencing shear yielding including Specimen HG2 and Specimen EL2, were less resistant to fracture as first fracture occurred at approximately 10% shear angle.

CONCLUSION

Study on structural fuses with hourglass-shaped links and elliptical holes was presented in this research. Design equation associated with each limit state (i.e flexural yielding, shear yielding, and the transition between limit states of flexural yielding and shear yielding) was derived for each configuration of these two seismic fuse shapes. A full-scale testing program was conducted to validate the effectiveness of using structural fuses with hourglass-shaped links and elliptical holes. More specifically, six specimens, three specimens with hourglass-shaped links and three specimens with elliptical holes, were tested to examine structural behavior associated with each limit state.

The main findings of this study can be summarized as follows:

(1) Yielding mechanism, locations of yielding were observed by the whitewash flaking off and then further validated by the DIC. Thus, this verifies the accuracy of closed-form design equation and criteria for each limit state listed in Table 1.

(2) The concept of using hourglass-shaped links for even distribution of yielding over the link length, thus promotes ductility, was verified. The experiment showed that specimen with hourglass-shaped links undergoing flexural yielding was capable to resist fracture up to 30% shear angle (i.e Specimen HG1).

(3) Structural fuses with elliptical holes have no sharp corners, thus also exhibited a good fracture resistance as the peak shear angle associated with first fracture was approximately 20% (i.e Specimen EL1 and Specimen EL3).

(4) This experimental program also validated the effectiveness of using structural fuses undergoing the transition between the limit states of shear yielding and flexural yielding. Two representative specimens, Specimen HG3 and Specimen EL3, have demonstrated good structural

behavior during load reversals as they were able to maintain full hysteretic behavior up to minimum 20% shear angle, indicating a stable energy dissipation capacity.

(5) Overall, specimens undergoing flexural yielding have shown to have a good buckling and fracture resistance while specimens with shear yielding exhibited high strength and stiffness, as listed in Table 4. The experimental results suggested that applied displacements should be close to the links of structural fuses with short links to exclude the additional moment due to eccentricity and undesired effect of the rotation of the connection region above the links.

ACKNOWLEDGEMENTS

This work was supported by the National Science Foundation under Grant No. CMMI-1453960. In-kind funding was provided by AISC and INFRA-METALS. Any opinions, findings, and conclusions or recommendations expressed in this material are those of the authors and do not necessarily reflect the views of the National Science Foundation or other sponsors.

REFERENCES

AISC. 2016. Seismic provision for structural steel buildings. ANSI/AISC 341-1. Chicago, IL: AISC.

ASTM Standard A370-07a. Standard test methods and definitions for mechanical testing of steel products. West Conshohocken, PA: American Standards for Testing and Materials International (ASTM); 2007.

Aschheim M.and Halterman A. (2002), "Reduced Web Section Beams: Phase One Experimental Findings And Design Implications". The Earthquake Engineering Online Archive, NISEE e-Library.

Cortes, G., and J. Liu (2011). "Experimental evaluation of steel slit panel–frames for seismic resistance." J. Constr. Steel Res. 67 (2): 181–191.

Egorova, N., Eatherton, M. R. and Maurya, A. (2014). "Experimental study of ring-shaped steel plate shear walls." Journal of Constructional Steel Research, 103, 179-189.

Hitaka T., and Matsui C. (2003), "Experimental Study on Steel Shear Wall with Slits". Journal of Structural Engineering, 129(5).

Kelly, J.M., Skinner, R.I. and Heine, A.J. (1972). Mechanisms of Energy Absorption in Special Devices for Use in Earthquake Resistant Structures, Bulletin of N.Z. Society for Earthquake Engineering 5:3,

Koppal and Eatherton (2013), "Perforated Steel Plate Shear Walls for Tunable Seismic Resistance", Structure Congress.

Lee C., K. Ju Y., Min J., Lho S., and Kim S. (2015), "Non-uniform steel strip dampers subjected to cyclic loadings", Engineering Structures, 99 (2015), pp. 192–204.

Lee C., Lho S., Kim D., Oh J., and K. Ju Y. (2015), “Hourglass-shaped strip damper subjected to monotonic and cyclic loadings”, Engineering Structures, 119 (2016), pp. 122–134.

Lee C., Woo S., K. Ju Y., Lee D., Oh J., Kim S. (2014), “Modified Fatigue Model for Hourglass-Shaped Steel Strip Damper Subjected to Cyclic Loadings”, Journal of Structural Engineering, 141 (8).

Lemaitre, J., & Chaboche, J. L. (1990). Mechanics of Solid Materials: Cambridge University Press.

Lopes A.P., Dusicka P., and W. Berman J. (2012), “Design of the Linked Column Frame structural system”, Taylor & Francis Group, Stessa.

LS-DYNA. 2011-2018 LSTC.

Ma, X., Borchers, E., Pena, A., Krawinkler, H. and Deierlein, G. (2010). “Design and behavior of steel shear plates with openings as energy-dissipating fuses.” John A. Blume Earthquake Engineering Center Technical Report, (173).

Nguyen, T.N. (2022). “Computational and Experimental Investigation of Seismic Structural Fuse Shapes for Resilient Structural Systems.” PhD Dissertation. Dept. of Civil Engineering, Virginia Polytechnic Institute and State Univ.

Plaut, R. and Eatherton, M. (2017) "Lateral-Torsional Buckling of Butterfly-Shaped Beams with Rectangular Cross Section" Engineering Structures, v.136 , 2017 , p.210

Popov, E. P., and M. D. Engelhardt. 1988. “Seismic eccentrically braced frames.” J. Constr. Steel Res. 10 (Jan): 321–354.

Teruna D, Majid TA, Budiono B. Experimental study of hysteretic steel damper for energy dissipation capacity. Adv Civ Eng 2015. Hindawi Publishing Corporation.

Vian, D., M. Bruneau, and R. Purba. 2009. “Special perforated steel plate shear walls with reduced beam section anchor beams. II: Analysis and design recommendations.” J. Struct. Eng. 135 (3): 221–228

Zhu, B, Wang, T, Zhang, L (2018) Quasi-static test of assembled steel shear panel dampers with optimized shapes. Engineering Structures 172: 346–357.

7. CONCLUSIONS

7.1 OVERALL

Structural fuses are ductile elements of a structure that are designed to yield and protect the surrounding members from damage, and then be replaceable after a major seismic event. There have been several studies on various cutout patterns for shear-acting structural fuses including butterfly-shaped links, hourglass-shaped links, elliptical holes, and link shapes obtained from topology optimization. However, thorough studies on different limit states of these structural fuse shapes have not been previously examined. In addition, previous analytical findings have not been experimentally validated. Hence, the overall objective of this project is to conduct computational and experimental studies to further understand structural behavior of these structural fuse shapes. This includes analytical derivation of generalized design equations, investigation of key limit states of structural fuse shapes. Experimental program was conducted to validate related theories. Design guidelines are recommended for practical design.

Twenty full-scale experimental tests were conducted at Thomas M. Murray Structures Laboratory at Virginia Tech. This includes nineteen specimens of different shapes such as Optimized Shapes, Tied-Butterfly Shapes, Butterfly Shapes, Hourglass Shape, Elliptical Holes, and one conventional Straight Link specimen, for context. Overall dimensions of specimens are approximately 762 mm x 711 mm and these specimens are subjected to cyclic shear displacement histories up to failure. Chapter 1 provides a description of the test specimens and test matrix. The actuator force, shear angle and other related axial forces were recorded for each test using the internal actuator sensor, string potentiometers and strain gages. In addition, Digital Image Correlation (DIC) system was used to get the, displacement field, strain field, etc. for each specimen.

There are totally 5 configurations to be examined which can be categorized into 4 groups associated with 4 journal manuscripts.

(a) Chapter 3 provides investigation about optimized shape structural fuses. First, experimental study is conducted to evaluate seismic performance of previously studied optimized shapes. Straight link is also included for the purpose of comparison. Finite element models are then validated against the experimental results and used to further understand the experimental behavior. Second, parameterization of one of the optimized is implemented for practical design situations with specified needs for strength, stiffness or deformation capacity, followed by the computational parametric study to further investigate the effect of varying key design parameters on cyclic behavior of the optimized shape.

(b) Chapter 4 describes the development of the new configuration, so-called Tied Butterfly Shape structural fuse. This consists of the analytical derivation of generalized equation for shear strength assuming flexural plastic hinging. Computational parametric study is conducted to find the optimum configurations of this new shape. Three configurations of this Tied Butterfly Shape resulted from the parametric study are then selected for the experimental investigation. Straight link is also included for the purpose of comparison. Nonlinear finite element models are created to validate against experimental results. Design guidelines are recommended for practical design.

(c) Chapter 5 evaluates the structural behavior of butterfly-shaped structural fuses. This consists of the investigation of key limit states including shear yielding, flexural yielding, transition between limit states of shear yielding and flexural yielding, and lateral torsional buckling. Design equation associated with each limit state is derived. Experimental program is conducted to test 8 specimens to evaluate seismic performance of the butterfly-shaped structural fuses. The design recommendations are also included.

(d) Chapter 6 investigates seismic performance of structural fuses with hourglass-shaped links and elliptical holes. This work focuses on two limit states including shear dominated, flexural dominated, and transition between shear and flexural dominated limit states. Generalized design equations are derived. Six specimens of these shapes are tested to evaluated the behavior of these two shapes. Design guidelines for each shape are recommended for design.

The following sections summarize the conclusions of this research work.

7.2 SUMMARY OF THE STUDY ON OPTIMIZED SHAPES

The objective of this study is to create an experimentally validated design approach around the selected optimized topologies created by Avecillas and Eatherton (2020). First, parameterization was introduced to make the optimized topology practical for design. Second, plastic mechanism analysis was used to derive a generalized equation for the shear strength of the parameterized configuration. Then, three experiments were conducted on specimens that were 711 mm x 762 mm x 25 mm thick to investigate the cyclic load-deformation behavior for these shapes. FE models were then validated against the experimental results and used to conduct a computational parametric study to evaluate the effect of the design variables on the cyclic behavior of the topology such as strength, stiffness, maximum out-of-plane displacement, maximum equivalent plastic strain. Lastly, based on the results of the experiments, FEM validation and parametric study, design recommendation are provided for practical design.

The main findings of this study can be summarized as follows:

(1) The experiment has shown that one of the two selected topologies, referred to as OPT1 was capable maintaining a full hysteretic behavior up to 10% shear angle before the ties fractured, after which there was a stable reserve strength through 20% shear angle. These characteristics are considerably better than the other optimized shape (i.e Specimen OPT2) or the straight link

specimen (i.e Specimen STL) which fractured after 6% shear angle and then suffered uncontrolled degradation in shear strength.

(2) The optimized configuration, OPT1, can be uniquely defined using five geometric parameters, allowing new structural fuse shape adapt to different design situations such as specific need for strength, stiffness and deformation capacity. Subsequently, a parametric computational finite element study was conducted to evaluate effect of the five geometric parameters on strength, stiffness, energy dissipation, out of plane buckling, and effective plastic strain. Another equation for predicting the stiffness of the topology was obtained from the parametric study. Details can be found in Chapter 3.

7.3 SUMMARY OF THE STUDY ON TIED BUTTERFLY SHAPE

This study aims to develop a new structural fuse shape, named Tied Butterfly Shape, to integrate the advantages of the optimized topology (i.e good buckling resistance) and the butterfly-shape link (i.e good fracture resistance). First, analytical derivation of the design equation for shear strength using plastic mechanism analysis was presented. Then, four specimens, three Tied Butterfly Shapes and one straight link, were tested to evaluate the structural behavior of this new shape under load reversals. FE models were then validated against the experiments and used to evaluate the effect of the geometric parameter of the Tied Butterfly Shape on strength, stiffness, maximum out-of-plane displacement, maximum equivalent plastic strain, through a parametric study. Lastly, based on the results of the experiments, FEM validation and parametric study, design recommendation are provided for practical design.

The main findings of this study can be summarized as follows:

(1) The experiment study showed that the one of the Tied Butterfly Shapes (i.e TBF1) possessed a good balance between buckling resistance and fracture resistance reaching

approximately 23% shear angle without either. The other Tied Butterfly Shapes, TBF2 and TBF3, also offered a substantial energy dissipation and ductility as they were shown to maintain stable hysteretic behavior up to approximately 12% and 17%, respectively which are a good target for the design earthquake hazard level.

(2) A parametric study was conducted to extend the results of the experiments and support use in practical design as another equation to predict stiffness was obtained based on the results of this study. The effect of the five geometric parameters on strength, stiffness, energy dissipation, out of plane buckling, and effective plastic strain were evaluated and ranges of variables for which behavior was not adversely affected were determined. Details can be found in Chapter 4.

7.4 SUMMARY OF THE STUDY ON BUTTERFLY SHAPED LINK

This study investigates the key limit states of the Butterfly Shaped Link Structural Fuses including flexural yielding, shear yielding, and lateral torsional buckling. Additionally, the transition between the flexural dominated and shear dominated limit states was also examined. First, design equation and criteria associated with each limit state were analytically derived. This includes the discussion about the yielding mechanism and locations of yielding. Then experimental program was conducted to test 8 specimens to understand the cyclic load-deformation behavior and validate the related theories associated with each limit state. Next, nonlinear finite element program was implemented to further understand behaviors which were not obvious during the tests. Lastly, design guidelines are provided for practical design.

The main findings of this study can be summarized as follows:

(1) The experiment validated the yielding mechanism of the BF links for each limit state. This includes the evaluation of the design equations, criteria to define controlling limit state.

(2) The experiment revealed that specimen undergoing flexural yielding offered substantial fracture and buckling resistance as they were shown to maintain a relatively stable hysteretic up to approximately 20%, after which there was a stable reserve strength through 30% shear angle before strength degradation due to buckling and fracture

(3) Regarding specimen undergoing shear yielding, this specimen displayed a substantial strength and stiffness. Nevertheless, the amount of dissipated energy was limited as it suffered from brittle fracture at approximately 10% shear angle cycles before full loss of strength in the next cycle. The experimental results also suggested short links are not recommended in practical design as they can cause unexpected behavior (i.e rotation of the connection regions)

(4) Specimen undergoing the transition between the limit states of shear yielding and flexural yielding was shown to be promising for practical design as it was capable of maintaining full hysteretic behavior up to 20% shear angle, indicating an excellent energy dissipation.

(5) Specimens undergoing lateral torsional buckling were shown to have early initiation of buckling, as expected. However, they demonstrated a significant fracture resistance as the shear angle associated with first fracture was up to approximately 30%. These characteristics can be considered advantageous as strength degradation due to buckling means less resistance against restoring force for applications in a self-centering system.

7.4 SUMMARY OF THE STUDY ON STRUCTURAL FUSES WITH HOURGLASS SHAPED LINKS AND ELLIPTICAL HOLES

This study explores the concept of using Hourglass Shaped links and Elliptical Holes for structural fuses. The Hourglass Shaped link was designed to spread inelasticity over the entire link length while the structural fuse with elliptical holes has no sharp corners, thus is expected to have good fracture resistance. First, analytical derivation of the prediction equation for shear strength was presented. This included the discussion of the criteria for each limit state of the two shapes. Second, experimental study was conducted to (1) evaluate the cyclic behavior of each shape, (2) validate related theories. In addition, the yielding pattern and location of plastic hinging associated with each limit state were verified by the whitewash flaking off and DIC system. Next, FE validation using nonlinear finite element program was implemented to understand behavior that was not obvious during the test. Lastly, based on the experimental and computational results, design recommendations were provided.

The main findings of this study can be summarized as follows:

(1) The experimental results verified the generalize design equation and criteria to define controlling limit state for each of the shapes.

(2) It was confirmed by the experiments that the Hourglass Shaped link encourages the distribution of yielding over the entire link length. Specimen with Hourglass Shaped links undergoing flexural yielding was capable to resist fracture up to 30% shear angle (i.e Specimen HG1).

(3) The experimental results showed that structural fuses with Elliptical Holes offered a good fracture resistance as the peak shear angle associated with first fracture was approximately 20% (i.e Specimen EL1 and Specimen EL3).

(4) Using structural fuses undergoing the transition between the limit states of shear yielding and flexural yielding is promising in practical design. Two representative specimens, Specimen HG3 and Specimen EL3, have demonstrated good structural behavior during load reversals as they were able to maintain full hysteretic behavior up to minimum 20% shear angle, indicating a stable energy dissipation capacity.

(5) The experiment suggested that applied displacements should be close to the links of structural fuses with short links to exclude any undesirable behaviors due to the rotation of the connection regions above the links

7.4 CONCLUDING REMARKS AND RECOMMENDATIONS FOR FUTURE STUDIES

This research work studied the four groups of structural fuse shapes including (1) Optimized Shapes to resist buckling, (2) a new shape, called Tied Butterfly Shape, for improved buckling and fracture resistance, (3) Butterfly Shaped Link, (4) Hourglass Shaped Link and Elliptical Holes. The computational and experimental studies reported in this dissertation demonstrate that these structural fuse shapes are capable of improving the seismic performance of the structural systems. In addition, the presented design guidelines allow these shapes to be usable for general seismic design. Some recommendations for practical design are listed as follows:

(1) The presented experimental results on the optimized topologies allow designers and researchers to continue to explore these shapes.

(2) The new shape, Tied Butterfly Shape, was shown to be a very promising shape for practical use as it possesses a good balance between buckling resistance and fracture resistance.

(3) In most cases, the flexural yielding limit state is desirable for the use of the structural fuses with butterfly shape links, hourglass shaped links and elliptical holes.

Some recommendations for future studies are as follows:

(1) The effect of axial forces on the behavior of these shapes is recommended for future studies as this may lead to early buckling or unexpected effects on the structural fuse.

(2) The computational and experimental studies of these shapes as part of an entire structural system are recommended (i.e single-story building or multi-story building). This includes the nonlinear response history analysis and full-scale testing on prototype building of these structural fuse shapes.

(3) A comprehensive design methodology of all these shapes considering yielding, buckling and fracture limit states is necessary for general seismic design.

REFERENCES

AISC. 2016. Seismic provision for structural steel buildings. ANSI/AISC 341-1. Chicago, IL: AISC.

ASTM Standard A370-07a. Standard test methods and definitions for mechanical testing of steel products. West Conshohocken, PA: American Standards for Testing and Materials International (ASTM); 2007.

Aschheim M.and Halterman A. (2002), "Reduced Web Section Beams: Phase One Experimental Findings and Design Implications". The Earthquake Engineering Online Archive, NISEE e-Library.

Avecillas, J. (2019) "Topology optimization of steel shear fuses to resist buckling." M.Sc. thesis, Dept. of Civil Engineering, Virginia Polytechnic Institute and State Univ.

Avecillas, J.A., Eatherton, M.R. (2020). Controlling Out-of-Plane Buckling in Shear-Acting Structural Fuses through Topology Optimization. Journal of Structural Engineering. 146. 10.1061/(ASCE)ST.1943-541X.0002692.

Basler, K. 1961. "Strength of Plate Girders in Shear." Journal of the Structural Division, ASCE, vol. 87, no. 7, 150–180.

Bergman, DM, Goel, SC (1987) Evaluation of cyclic testing of steel plate devices for added damping and stiffness. Report UMCE87-10. Ann Arbor, MI: University of Michigan.

Berman, J.W., and M. Bruneau (2005). "Experimental investigation of light gauge steel plate shear walls." J. Struct. Eng. 131 (2): 259–267.

Berman, J., and M. Bruneau. 2003. "Plastic analysis and design of steel plate shear walls." J. Struct. Eng. 129 (11): 1448–1456.

Black, C. J., N. Makris, and I. D. Aiken. (2004) "Component testing, seismic evaluation and characterization of buckling-restrained braces." J. Struct.Eng. 130 (6): 880–894.

Boardman, P. R., Wood, B. J., and Carr, A. J. 1983. "Union House–a Cross-Braced Structure with Energy Dissipators." Bulletin of the New Zealand National Society for Earthquake Engineering, vol. 16, no. 2, 83–97.

Borello, D. and Fahnestock, L. (2011). Design and testing of coupled steel plate shear walls." Proceedings of the ASCE Structures Congress, Las Vegas, NV.

Borello, D. and Fahnestock, L. (2012). Seismic design and analysis of steel plate shear walls with coupling." Journal of Structural Engineering, Vol. 139, Issue 8.

Bruneau, M., Cliffton, C., MacRae, G., Leon, R., and Fussel, A. (2014) Steel Structures Damage from the Christchurch Earthquake of February 22, 2011, NZST, Bulletin of the New Zealand Society of Earthquake Engineering, Vol. 44, No. 4, p. 297-318.

Cortes, G., and J. Liu (2011). “Experimental evaluation of steel slit panel–frames for seismic resistance.” J. Constr. Steel Res. 67 (2): 181–191.

Deng, K., Pan, P., Li, W. and Xue, Y. (2015). “Development of a buckling restrained shear panel damper.” Journal of Constructional Steel Research, 106(1), 311-321.

Driver, R. G., Kulak, G. L., Kennedy, D. J., and Elwi, A. E. (1998b). Cyclic test of four-story steel plate shear wall” Journal of Structural Engineering, 124(2), 112-120.

Eatherton, M. R., X. Ma, H. Krawinkler, D. Mar, S. Billington, J. F. Hajjar, and G. G. Deierlein (2014). “Design concepts for controlled rocking of self-centering steel-braced frames.” J. Struct. Eng. 140 (11): 04014082.

Egorova, N., Eatherton, M. R. and Maurya, A. (2014). “Experimental study of ring-shaped steel plate shear walls.” Journal of Constructional Steel Research, 103, 179-189.

El-Bahey S, Bruneau M. Bridge piers with structural fuses and Bi-steel columns. I: Experimental Testing. J Bridge Eng 2012;17(1).

El-Bahey S, Bruneau M. Bridge piers with structural fuses and Bi-steel columns. II: Analytical Investigation. J Bridge Eng 2012;17(1).

Farzampour A. and Eatherton M. (2019), “Yielding and lateral torsional buckling limit states for butterfly-shaped shear links “, Engineering Structures, vol. 180, pp. 442-451.

FEMA 461. Interim testing protocol for determining the seismic performance characteristics of structural and nonstructural components. Washington, DC (USA): Federal Emergency Management Agency; 2007.

Fujimoto, M., Aoyagi, T., Ukai, K., Wada, A., and Saito, K. 1972. “Structural Characteristics of Eccentric K-Braced Frames.” Trans.AIJ, no. 195, 39–49, May.

Ghabraie, K., Chan, R., Huang, X. and Xie, Y. M. (2010). “Shape optimization of metallic yielding devices for passive mitigation of seismic energy.” Engineering Structures, 32(8), 2258-2267.

He, H., Wang, X. and Zhang, X. (2016). Energy-dissipation performance of combined low yield point steel plate damper based on topology optimization and its application in structural control." Advances in Materials Science and Engineering, 2016.

Hitaka T., and Matsui C. (2003), “Experimental Study on Steel Shear Wall with Slits”. Journal of Structural Engineering, 129(5).

Hjelmstad, K. D., and Popov, E. P. 1983. “Cyclic Behavior and Design of Link Beams.” Journal of Structural Engineering, ASCE, vol. 109, no. 10, 2387–2403.

Huang, Y., and Mahin, S. A. (2010). PEER 2010/104 Simulating the inelastic seismic behavior of steel braced frames including the effects of low-cycle fatigue. Berkeley, CA.

Kasai, K., and Popov, E. P. 1986a. “Cyclic Web Buckling Control for Shear Link Beams.” Journal of Structural Engineering, ASCE, vol. 112, no. 3, 505–523.

Kelly, J.M., Skinner, R.I. and Heine, A.J. (1972). Mechanisms of Energy Absorption in Special Devices for Use in Earthquake Resistant Structures, Bulletin of N.Z. Society for Earthquake Engineering 5:3,

Kobori T, Miura Y, Fukuzawa E, Yamanda T, Arita T, Takenaka Y, Miyagwa N, Tanaka N, Fukumoto T (1992). Development and application of hysteresis steel dampers. In: Earthquake Engineering the 10th Conference. Rotterdam: Belkema, 1992.

Koppal and Eatherton (2013), "Perforated Steel Plate Shear Walls for Tunable Seismic Resistance", Structure Congress.

Kurokawa Y, Sakamoto M, Yamada T, Kurino H, Kunisue A. Seismic design of a tall building with energy dissipation damper for the attenuation of torsional vibration. Struct Des Tall Buil 1998;7:21–32.

Lee C., K. Ju Y., Min J., Lho S., and Kim S. (2015), "Non-uniform steel strip dampers subjected to cyclic loadings", Engineering Structures, 99 (2015), pp. 192–204.

Lee C., Lho S., Kim D., Oh J., and K. Ju Y. (2015), "Hourglass-shaped strip damper subjected to monotonic and cyclic loadings", Engineering Structures, 119 (2016), pp. 122–134.

Lee C., Woo S., K. Ju Y., Lee D., Oh J., Kim S. (2014), "Modified Fatigue Model for Hourglass-Shaped Steel Strip Damper Subjected to Cyclic Loadings", Journal of Structural Engineering, 141 (8).

Li, H. N. and Li, G. (2007). "Experimental study of structure with "dual function" metallic dampers." Engineering Structures, 29, pp.1917–1928.

Lemaitre, J., & Chaboche, J. L. (1990). Mechanics of Solid Materials: Cambridge University Press.

Liu, Y., and M. Shimoda. (2013). "Shape optimization of shear panel damper for improving the deformation ability under cyclic loading." Struct. Multidiscip. Optim. 48 (2): 427–435.

Lopes A.P., Dusicka P., and W. Berman J. (2012), "Design of the Linked Column Frame structural system", Taylor & Francis Group, Stessa.

LS-DYNA. 2011-2018 LSTC.

Luth GP, Sargunuraj S, Krawinkler H, McDonald B. USC school of cinema an example of reparable performance based design. SEAOC Convention Proceedings. 2008.

Lynch JP. Active structural control research at Kajima Corporation. Stanford, CA:National Science Foundation's Summer Institute in Japan Program, Stanford Univ.;1998.

Ma, X., Borchers, E., Pena, A., Krawinkler, H. and Deierlein, G. (2010). "Design and behavior of steel shear plates with openings as energy-dissipating fuses." John A. Blume Earthquake Engineering Center Technical Report, (173).

Martinez-Romero, E. 1993. "Experiences on the Use of Supplementary Energy Dissipators on Building Structures." Earthquake Spectra, vol. 9, no. 3, 581–625.

Michael Bruneau, Chia-Ming Uang, Rafael Sabelli (2011). Ductile Design of Steel Structures, 2nd Edition, McGraw Hill.

Nguyen, T.N. (2022). “Computational and Experimental Investigation of Seismic Structural Fuse Shapes for Structural Systems.” PhD Dissertation. Dept. of Civil Engineering, Virginia Polytechnic Institute and State Univ.

Okazaki, T., Arce, G., Ryu, H.-C., and Engelhardt, M. D. 2004. “Recent Research on Link Performance in Steel Eccentrically Braced Frames.” Proceedings of the 13th World Conference on Earthquake Engineering, IAEE.

Phillips, A.R., and M. R. Eatherton (2018). “Large-scale experimental study of ring shaped–steel plate shear walls.” J. Struct. Eng. 144 (8):04018106.

Phillips, A. R. 2016. “Large-scale testing and development of Ring-shaped steel plate shear walls for improved seismic performance of buildings.” Ph.D. thesis, Virginia Tech.

Plaut, R. and Eatherton, M. (2017) "Lateral-Torsional Buckling of Butterfly-Shaped Beams with Rectangular Cross Section" Engineering Structures, v.136, 2017 , p.210

Popov, E. P., and M. D. Engelhardt. 1988. “Seismic eccentrically braced frames.” J. Constr. Steel Res. 10 (Jan): 321–354.

Sarraf, M., and Bruneau, M. 1998a. “Ductile Seismic Retrofit of Steel Deck-Truss Bridges. I: Strategy and Modeling.” ASCE Journal of Structural Engineering,vol. 124, no. 11, 1253–1262.

Sarraf, M., and Bruneau, M. 1998b. “Ductile Seismic Retrofit of Steel Deck-Truss Bridges. II: Design Applications.” ASCE Journal of Structural Engineering,vol. 124, no. 11, 1263–1271.

Seilie, I. F. and Hooper, J. D. (2005). “Steel plate shear walls - practical design and construction.” Modern Steel Construction (AISC, Chicago, IL).

Roeder, C. W., and Popov, E. P. 1978. “Eccentrically Braced Steel Frames for Earthquakes.” Journal of the Structural Division, ASCE, vol. 104, no. ST3, 391–411.

Shin M., Kim S., Halterman A., and Aschheim M. (2017), “Seismic toughness and failure mechanisms of reduced web-section beams: Phase 1 tests”. Engineering Structures. 141 (15), pp. 198–216

Tanabashi, R., Naneta, K., and Ishida, T. 1974. “On the Rigidity and Ductility of Steel Bracing Assemblage,” Proceedings of the 5th World Conference on Earthquake Engineering, Rome, IAEE. vol. 1, 834–840.

Teruna D, Majid TA, Budiono B. Experimental study of hysteretic steel damper for energy dissipation capacity. Adv Civ Eng 2015. Hindawi Publishing Corporation.

Timler P. A., and Kulak, G. L. 1983. “Experimental Study of Steel Plate Shear Walls,” Structural Engineering Report No. 114. Edmonton, AB, Canada: Department of Civil Engineering, University of Alberta.

Thorburn, L. J., Kulak, G. L., and Montgomery, C. J. 1983. “Analysis of Steel Plate Shear Walls,” Structural Engineering Report No. 107. Edmonton, AB, Canada: Department of Civil Engineering, University of Alberta.

Tsai, K. C., H. W. Chen, C. P. Hong, and Y. F. Su. 1993. “Design of steel triangular plate energy absorbers for seismic resistant construction.” Earthquake Spectra 9 (3): 505–528.

Vian, D., M. Bruneau, and R. Purba. 2009. “Special perforated steel plate shear walls with reduced beam section anchor beams. II: Analysis and design recommendations.” J. Struct. Eng. 135 (3): 221–228

Wagner, H. 1931. “Flat Sheet Metal Girders with Very Thin Metal Webs. Part I General Theories and Assumptions, and Part III: Sheet Metal Girders with Spars Resistant to Bending—The Stress in Uprights—Diagonal Tension Fields.” Technical Memorandum Nos. 604 and 606, National Advisory Committee for Aeronautics, Washington, D.C.

Whittaker, A. S., Bertero, V. V., Thompson, C. L., and Alonso, L. J. 1989. “Earthquake Simulator Testing of Steel Plate Added Damping and Stiffness Elements.” Report No. UCB/EERC-89/02. Berkeley, CA: Earthquake Engineering Research Center, University of California.

Whittaker, A. S., Bertero, V. V., Thompson, C. L., and Alonso, L. J. 1991. “Seismic Testing of Steel Plate Energy Dissipation Devices.” Earthquake Spectra, vol. 7, no. 4, 563–604.

Zahrai, S. M., and Bruneau, M. 1999a. “Cyclic Testing of Ductile End-Diaphragms for Slab-on-Girder Steel Bridges.” ASCE Journal of Structural Engineering, vol. 125, no. 9, 987–996.

Zahrai, S. M., and Bruneau, M. 1999b. “Ductile End-Diaphragms for the Seismic Retrofit of Slab-on-Girder Steel Bridges.” ASCE Journal of Structural Engineering, vol. 125, no. 1, 71–80.

Zhu, B, Wang, T, Zhang, L (2018) Quasi-static test of assembled steel shear panel dampers with optimized shapes. Engineering Structures 172: 346–357.

APPENDIX A

DETAILS ABOUT EXPERIMENTAL PROGRAM

This appendix presents more details about the experimental program. This includes the details about the test specimens, test setup, displacement protocol, etc.

A1. DRAWINGS OF TEST SETUP, TEST SPECIMEN AND MILL CERTS

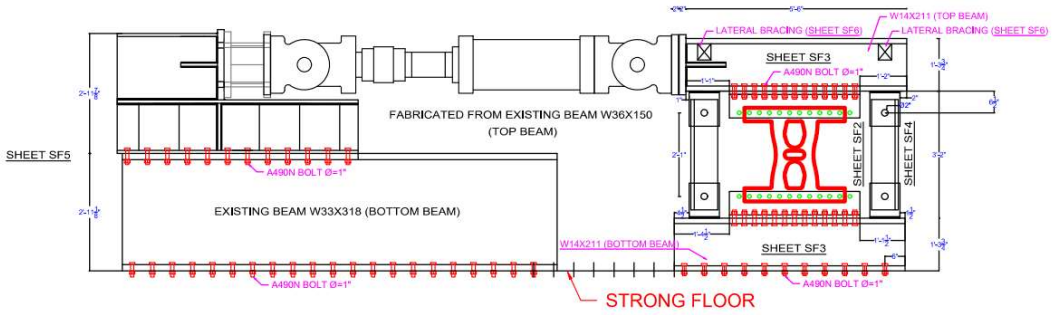

VIRGINIA TECH	OVERALL TEST SETUP		
PROJECT: STRUCTURAL FUSES	DRAWN BY: TN	DATE: 06/08/20	SHEET SF1

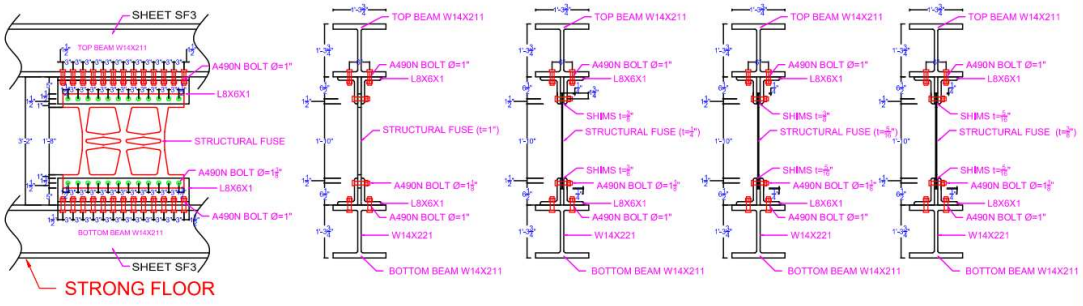

VIRGINIA TECH	LOAD FRAME		
PROJECT: STRUCTURAL FUSES	DRAWN BY: TN	DATE: 06/08/20	SHEET SF2

TOP BEAM

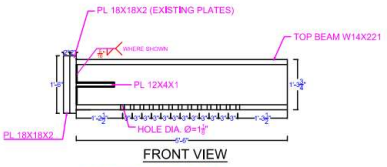

FRONT VIEW

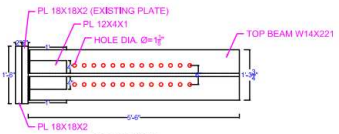

TOP VIEW

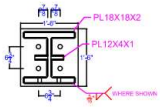

CROSS-SECTION

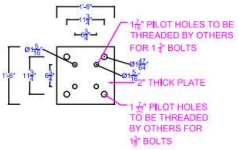

ACTUATOR SWIVEL HEAD END PLATE

(EXISTING PLATE)

BOTTOM BEAM

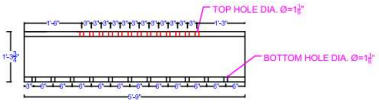

FRONT VIEW

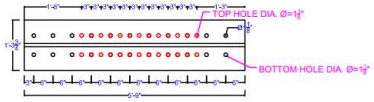

TOP VIEW

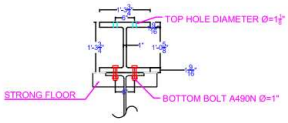

CROSS-SECTION

VIRGINIA TECH	LOADING BEAMS		
PROJECT: STRUCTURAL FUSES	DRAWN BY: TN	DATE: 06/08/20	SHEET SF3

LEFT STRUT

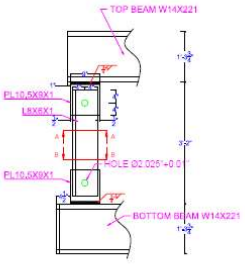

FRONT VIEW

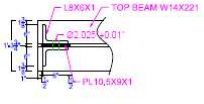

SECTION A-A

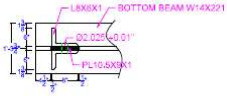

SECTION B-B

RIGHT STRUT

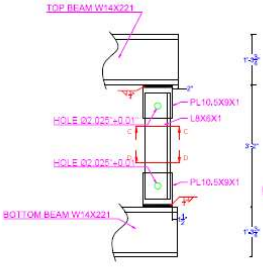

FRONT VIEW

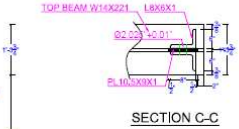

SECTION C-C

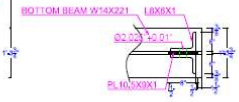

SECTION D-D

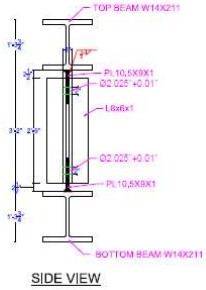

SIDE VIEW

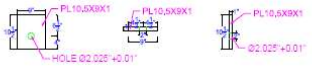

PLATE

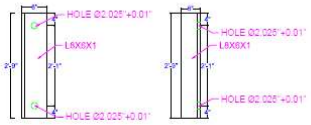

ANGLE

VIRGINIA TECH	STRUTS		
PROJECT: STRUCTURAL FUSES	DRAWN BY: TN	DATE: 06/08/20	SHEET SF4

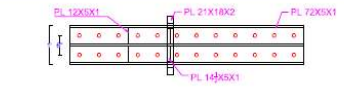

TOP BEAM W36X150 (FABRICATED FROM EXISTING BEAM)

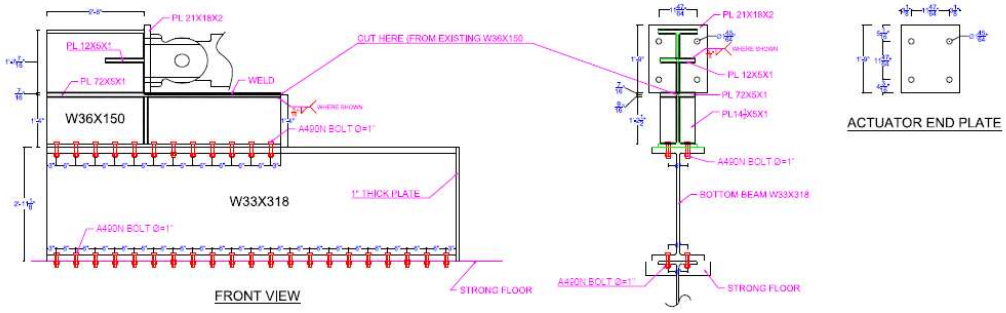

FRONT VIEW

LEFT SIDE VIEW

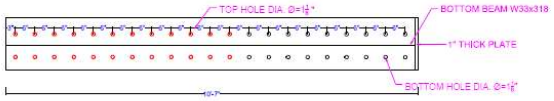

BOTTOM BEAM 33X318 (FABRICATED FROM EXISTING BEAM)

VIRGINIA TECH	REACTION BEAMS		
PROJECT: STRUCTURAL FUSES	DRAWN BY: TN	DATE: 06/08/20	SHEET SF5

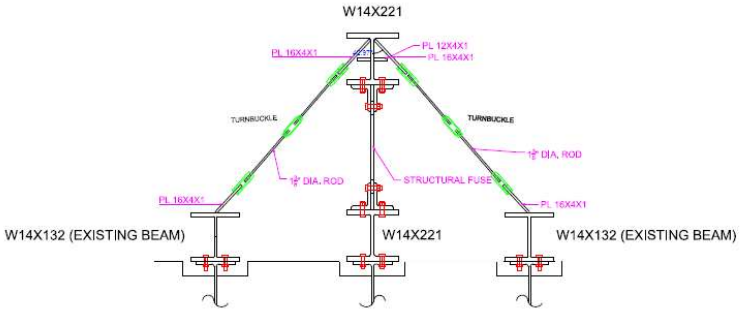

SIDE VIEW

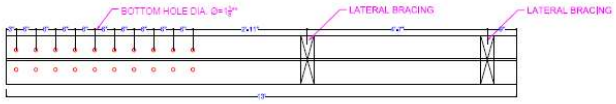

LATERAL BRACING BEAM (FABRICATED FROM EXISTING BEAM W14X132)

VIRGINIA TECH	LATERAL BRACING		
PROJECT: STRUCTURAL FUSES	DRAWN BY: TN	DATE: 06/08/20	SHEET SF6

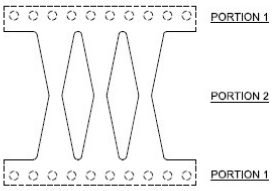

- PORTION 1 (DASHED LINES) TO BE WATER CUT WITH LOWEST LEVEL OF QUALITY.
- PORTION 2 (SOLID LINES) TO BE WATER CUT WITH HIGHEST LEVEL OF QUALITY.

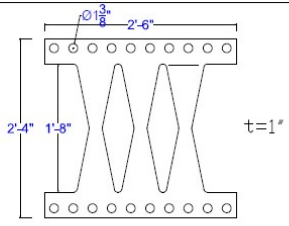

BF1
(QUANTITY=1)

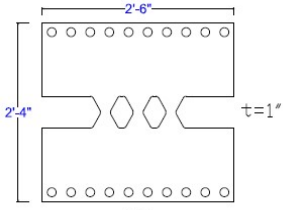

BF2
(QUANTITY=1)

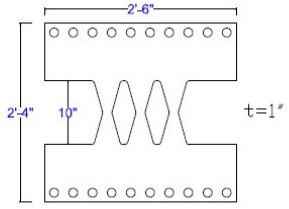

BF3
(QUANTITY=1)

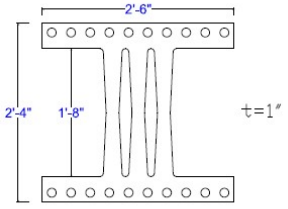

BF4
(QUANTITY=1)

NOTES:

1. ALL SPECIMENS TO BE WATER CUT WITH EXACT DIMENSIONS AS MEASURED FROM AUTOCAD.

TITLE: STRUCTURAL FUSES	DRAWN BY: TN	DATE: 01/24/20	SHEET 1

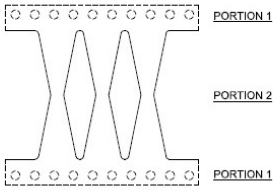

- PORTION 1 (DASHED LINES) TO BE WATER CUT WITH LOWEST LEVEL OF QUALITY.
- PORTION 2 (SOLID LINES) TO BE WATER CUT WITH HIGHEST LEVEL OF QUALITY.

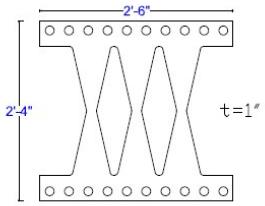

BF5
(QUANTITY=1)

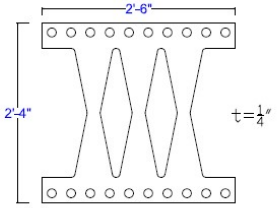

BF6
(QUANTITY=1)

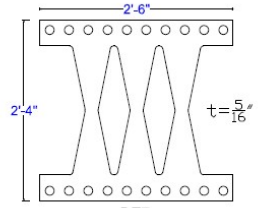

BF7
(QUANTITY=1)

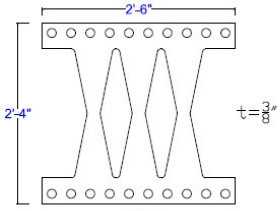

BF8
(QUANTITY=1)

NOTES:

1. ALL SPECIMENS TO BE WATER CUT WITH EXACT DIMENSIONS AS MEASURED FROM AUTOCAD.

TITLE: STRUCTURAL FUSES	DRAWN BY: TN	DATE: 01/24/20	SHEET 2

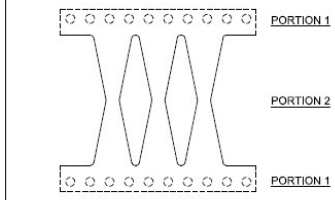

- PORTION 1 (DASHED LINES) TO BE WATER CUT WITH LOWEST LEVEL OF QUALITY.
- PORTION 2 (SOLID LINES) TO BE WATER CUT WITH HIGHEST LEVEL OF QUALITY.

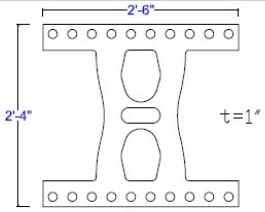

OPT1
(QUANTITY=1)

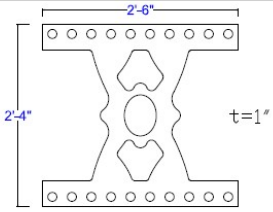

OPT2
(QUANTITY=1)

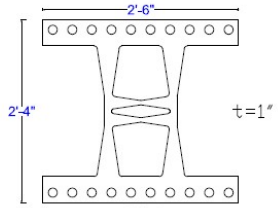

NS1
(QUANTITY=1)

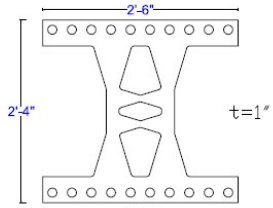

NS2
(QUANTITY=1)

NOTES:

1. ALL SPECIMENS TO BE WATER CUT WITH EXACT DIMENSIONS AS MEASURED FROM AUTOCAD.

TITLE: STRUCTURAL FUSES	DRAWN BY: TN	DATE: 01/24/20	SHEET 3

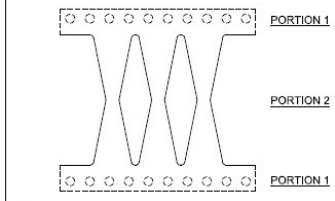

- PORTION 1 (DASHED LINES) TO BE WATER CUT WITH LOWEST LEVEL OF QUALITY.
- PORTION 2 (SOLID LINES) TO BE WATER CUT WITH HIGHEST LEVEL OF QUALITY.

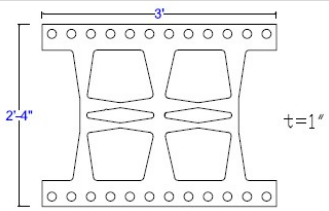

NS3
(QUANTITY=1)

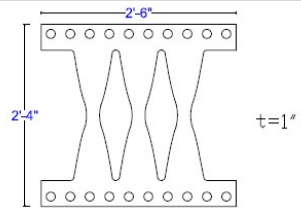

HG1
(QUANTITY=1)

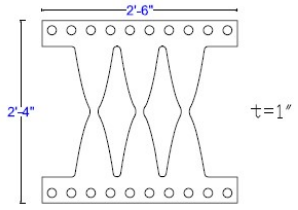

HG2
(QUANTITY=1)

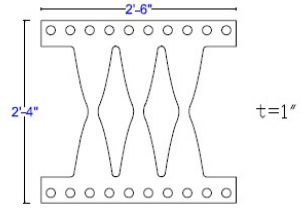

HG3
(QUANTITY=1)

NOTES:

1. ALL SPECIMENS TO BE WATER CUT WITH EXACT DIMENSIONS AS MEASURED FROM AUTOCAD.

TITLE: STRUCTURAL FUSES	DRAWN BY: TN	DATE: 01/24/20	SHEET 4

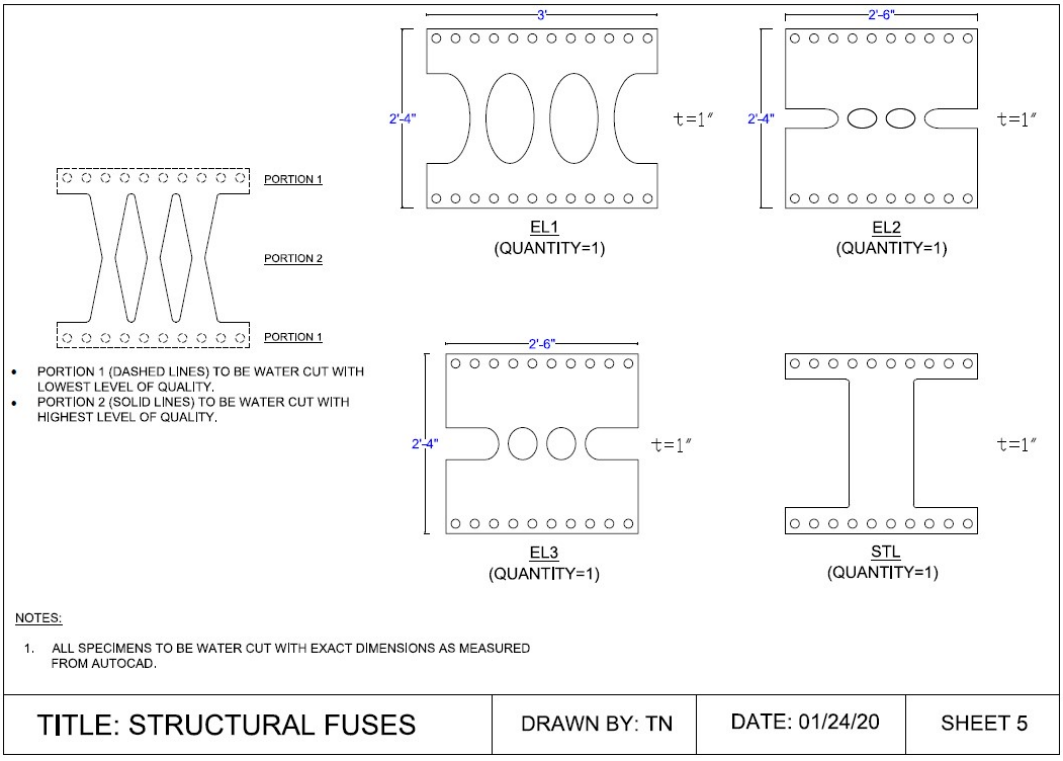

- PORTION 1 (DASHED LINES) TO BE WATER CUT WITH LOWEST LEVEL OF QUALITY.
- PORTION 2 (SOLID LINES) TO BE WATER CUT WITH HIGHEST LEVEL OF QUALITY.

NOTES:

1. ALL SPECIMENS TO BE WATER CUT WITH EXACT DIMENSIONS AS MEASURED FROM AUTOCAD.

TITLE: STRUCTURAL FUSES	DRAWN BY: TN	DATE: 01/24/20	SHEET 5

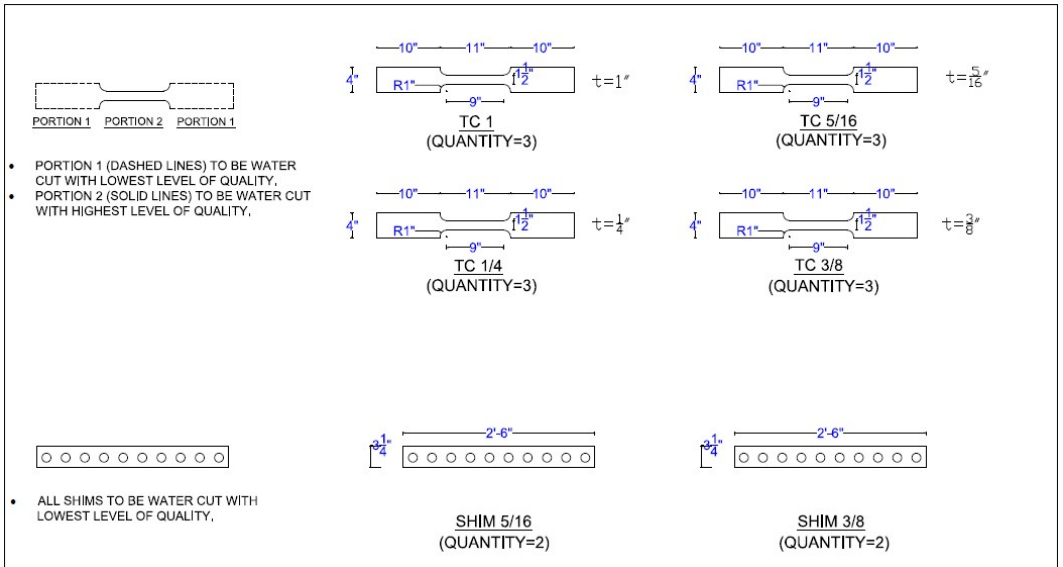

- PORTION 1 (DASHED LINES) TO BE WATER CUT WITH LOWEST LEVEL OF QUALITY.
- PORTION 2 (SOLID LINES) TO BE WATER CUT WITH HIGHEST LEVEL OF QUALITY.
- ALL SHIMS TO BE WATER CUT WITH LOWEST LEVEL OF QUALITY.

NOTES:

1. ALL SPECIMENS TO BE WATER CUT WITH EXACT DIMENSIONS AS MEASURED FROM AUTOCAD.

TITLE: STRUCTURAL FUSES	DRAWN BY: TN	DATE: 01/24/20	SHEET 6

PIECE MARK	THICKNESS	OVERALL DIMENSION	QUANTITY
BF1	1"	30" X 28"	1
BF2	1"	30" X 28"	1
BF3	1"	30" X 28"	1
BF4	1"	30" X 28"	1
BF5	1"	30" X 28"	1
BF6	$\frac{1}{4}$"	30" X 28"	1
BF7	$\frac{5}{16}$"	30" X 28"	1
BF8	$\frac{3}{8}$"	30" X 28"	1
OPT1	1"	30" X 28"	1
OPT2	1"	30" X 28"	1
NS1	1"	30" X 28"	1
NS2	1"	30" X 28"	1
NS3	1"	36" X 28"	1
HG1	1"	30" X 28"	1
HG2	1"	30" X 28"	1
HG3	1"	30" X 28"	1
EL1	1"	36" X 28"	1
EL2	1"	30" X 28"	1
EL3	1"	30" X 28"	1
STL	1"	30" X 28"	1
TC 1	1"	31" X 4"	3
TC 1/4	$\frac{1}{4}$"	31" X 4"	3
TC 5/16	$\frac{5}{16}$"	31" X 4"	3
TC 3/8	$\frac{3}{8}$"	31" X 4"	3
SHIM 5/16	$\frac{5}{16}$"	30" X $3\frac{1}{2}$"	2
SIM 3/8	$\frac{3}{8}$"	30" X $3\frac{1}{2}$"	2

TITLE: STRUCTURAL FUSES	DRAWN BY: TN	DATE: 01/24/20	SHEET 7

STRAIGHT BILL OF LADING - SHORT FORM
ORIGINAL - NOT NEGOTIABLE

Trailer No: TYLER-4506
Load No: 885534
BOL No: 874515

Carrier: Our Truck

RECEIVED, Subject to the classifications and tariffs in effect on the date of the issue of this Bill of Lading.

From: Infra-Metals Co. - PETERSBURG
1900 Bessemer Rd
PETERSBURG, VA 23805
Phone: 800-435-0850

Date:12/14/2019
Page 1 of 1

The property described below in apparent good order, except as noted (contents and condition of contents of packages unknown) marked consigned, and destined as indicated below, which said carrier (the word carrier being understood throughout this contract as meaning any person or corporation in possession of the property under the contract) agrees to carry to its usual place of delivery to said destination if on its route, otherwise to deliver to another carrier on the route to said destination. It is mutually agreed, as to each carrier of all or any of said property that every service to be performed hereunder shall be subject to all the terms and conditions of the Uniform Domestic Straight Bill of Lading set forth in (1) in Official Southern, Western and Illinois Freight Classifications in effect on the date hereof. If this is a rail or a rail-water shipment, or (2) in the applicable motor carrier classification or tariff if this is a motor carrier shipment. Shipper hereby certifies that he is familiar with all terms and conditions of the said bill of lading, including those on the back thereof, set forth in the classification or tariff which governs the transportation of this shipment, and the said terms and conditions are hereby agreed to by the shipper and accepted for himself and his assigns.

Sold To: AMERICAN INSTITUTE OF STEEL CONSTRUCTION
130 EAST RANDOLPH ST SUITE 2000
ATTN: ACCOUNTS PAYABLE
CHICAGO, IL 60601

Phone: 312-670-2400
Contact:

Ship To: AMERICAN INSTITUE OF STEEL CONSTRUCTION
255 INVENTIVE LANE
BLACKSBURG, VA 24060

Phone: 312-670-2400

1619107

Quantity	Description	Width	Length	Weight
Cust PO: ENG12112019A	Sales Order: 1586602	Inside Salesperson: Carey Scott		
3	PLATE 1 ASTM - A572 GR 50 Heat Numbers: 813K63470(1) 813K63490(2)	96"	240"	19,603
				Net Wt.: 19,603

Shipping Instructions:
Receiving Hours:
Max Bundle Weight: 0
Spacers:

Sales Order Total 19,603

Messages:
**** SHIP TO: Virginia Tech Structural Engineering Lab ***
*** 255 Inventive Lane Blacksburg, VA 24060 ***

Lab phone number for deliveries: 540-231-4211
They can take delivery M-F, 7:30 AM to 4:00 PM, except between 12-1 pm.
The material would be to the attention of Matt Eatherton!

3 **Grand Total Ship To:** 19,603

19,603

*****VERIFY LOAD, YOU ARE RESPONSIBLE FOR WHAT YOU SIGN FOR.*****
*****All discrepencies MUST be reported within 24 hours*****

Date 12.16.19 Driver Sig _____ Consignee Sig Brett N. Farmer
Print _____ Print Brett N. Farmer

These items are controlled by the U.S. Government and authorized for export only to the country of ultimate destination for use by the ultimate consignee or end-user(s) herein identified. They may not be resold, transferred, or otherwise disposed of, to any other country or to any person other than the authorized ultimate consignee or end-user(s), either in their original form or after being incorporated into other items, without first obtaining approval from the U.S. Government or as otherwise authorized by U.S. law and regulations. A copy of the AES Filing must be sent to export@infra-metals.com as soon as filed. This is a requirement of part 762 of U.S. Export Administration Regulations.

Trailer No: TYLER-4506 *Load No: 885534* *BOL No: 874515*

Comments:

Customer Name	Customer PO#	Invoice No	Shipper No	Heat Number
AMERICAN INSTITUTE OF STEEL	ENG12112019A	1619107	1586602	813K63470

ArcelorMittal Burns Harbor Plate

QUALITY ASSURANCE
REPORT OF TEST AND ANALYSES

US HWY 12 Burns Harbor, Indiana

SHIPMENT NO.	DATE SHIPPED	CAR OR VEHICLE NO		
803-54226	11-26-19	CSS-CHGO-CSXT	LMIC 007095	PAGE 2

SOLD TO
INFRA-METALS CO
1900 BESSEMER RD
PETERSBURG VA 23805-1112

SHIP TO
INFRA-METALS CO
THEIR SIDING
1900 BESSEMER RD
PETERSBURG VA 23805

NOTE	SERIAL NUMBER	PAT NO	HEAT NUMBER	NO. PCS.	SIZE AND QUANTITY: THICKNESS	WIDTH OR DIA.	LENGTH	WEIGHT	YIELD POINT	TENSILE STRENGTH	AF FRAC ELONG	RED
					INCHES	INCHES	INCHES	POUNDS	PSI	PSI	IN	% %

QUALITY STEEL MELTED & MANUFACTURED IN THE U. S. A.
PLATES - ASTM A572-18 GR 50 KLD FINE GRAIN
PRAC TYPE 2, CH-V A673 FREQ (H) L
15/10 FTLBS AT +40F
MFST - MFST MILL SERIAL# & PATTERN# MFST PPI 0082671-
0001 LIFT MAX 10 TON UNLDG FORK LIFT-SIDE
CO# VA-582162 GH 402-2245G

813K63510	6	3/4	96	240	29406	57400	82400	8	23
						58200	81700	8	25

PLATES - ASTM A572-18 GR 50 KLD FINE GRAIN
PRAC TYPE 2, CH-V A673 FREQ (H) L
15/10 FTLBS AT +40F
MFST - MFST MILL SERIAL# & PATTERN# MFST PPI 0082671-
0001 LIFT MAX 10 TON UNLDG FORK LIFT-SIDE
CO# VA-582162 GH 402-2245J

813K63470	2	1	96	240	13068	53400	79800	8	24
813K63490	2	1	96	240	13068	55000	81500	8	24

Q-QUENCH TEMPERATURE T-TEMPER TEMPERATURE N-NORMALIZE TEMPERATURE

SERIAL NUMBER	PAT NO	HEAT NUMBER	HARD BHN	BEND	THICKNESS	TYPE	SIZE	DIR	TEST TEMP °F	CHARPY IMPACT ENERGY FT LBS 1	2	3	SHEAR(%) 1	2	3	LAT EXP MILS 1	2	3
					INCHES													
		813K63510			.750	V	FULL	L	+40	118	118	117						
		813K63470			1.000	V	FULL	L	+40	132	122	106						
		813K63490			1.000	V	FULL	L	+40	108	109	114						

HEAT NUMBER	CHEMICAL ANALYSIS C	Mn	P	S	Si	Cu	Ni	Cr	Mo	V	Ti	Al	B	Cb	N	Sn	MQUAD GRAIN SIZE
813K63510	.18	1.20	.014	.006	.272	.037	.03	.03	.008	.058	.002	.031	.0002	.002	.006	.002	
813K63470	.18	1.20	.013	.005	.279	.015	.01	.02	.004	.060	.002	.039	.0002	.002	.003	.002	
813K63490	.18	1.21	.014	.006	.274	.019	.01	.02	.006	.061	.002	.040	.0002	.002	.003	.002	

I certify that the above results are a true and correct copy of actual results contained in records maintained by ArcelorMittal Burns Harbor and are in full compliance with the requirements of the specification cited above. This test report cannot be altered and must be transmitted intact with any subsequent third party test reports, if required.

ANDREW SMITH PER ELJ

BHPLTRPT.TIF SUPV. QUALITY ASSURANCE

Customer Name	Customer PO#	Invoice No	Shipper No	Heat Number
AMERICAN INSTITUTE OF STEEL	ENG12112019A	1619107	1586602	813K63490

ArcelorMittal Burns Harbor Plate

QUALITY ASSURANCE
REPORT OF TEST AND ANAYLSES

US HWY 12 Burns Harbor, Indiana

SHIPMENT NO.	DATE SHIPPED	CAR OR VEHICLE NO		
803-54226	11-26-19	CSS-CHGO-CSXT	LMIC 007095	PAGE 2

SOLD TO
INFRA-METALS CO
1900 BESSEMER RD
PETERSBURG VA 23805-1112

SHIP TO
INFRA-METALS CO
THEIR SIDING
1900 BESSEMER RD
PETERSBURG VA 23805

NOTE	SERIAL NUMBER	PAT NO	HEAT NUMBER	NO. PCS.	SIZE AND QUANTITY THICKNESS	WIDTH OR DIA.	LENGTH	WEIGHT	YIELD POINT	TENSILE STRENGTH	AF FRAC ELONG	RED
					INCHES	INCHES	INCHES	POUNDS	PSI	PSI	IN	% %

QUALITY STEEL MELTED & MANUFACTURED IN THE U. S. A.
PLATES - ASTM A572-18 GR 50 KLD FINE GRAIN
PRAC TYPE 2, CH-V A673 FREQ (H) L
15/10 FTLBS AT +40F
MFST - MFST MILL SERIAL# & PATTERN# MFST PPI 0082671-
0001 LIFT MAX 10 TON UNLDG FORK LIFT-SIDE
CO# VA-582162 GH 402-2245G

813K63510	6	3/4	96	240	29406	57400	82400	8	23		
						58200	81700	8	25		

PLATES - ASTM A572-18 GR 50 KLD FINE GRAIN
PRAC TYPE 2, CH-V A673 FREQ (H) L
15/10 FTLBS AT +40F
MFST - MFST MILL SERIAL# & PATTERN# MFST PPI 0082671-
0001 LIFT MAX 10 TON UNLDG FORK LIFT-SIDE
CO# VA-582162 GH 402-2245J

813K63470	2	1	96	240	13068	53400	79800	8	24		
813K63490	2	1	96	240	13068	55000	81500	8	24		

Q-QUENCH TEMPERATURE T-TEMPER TEMPERATURE N-NORMALIZE TEMPERATURE

SERIAL NUMBER	PAT NO	HEAT NUMBER	HARD BHN	BEND	THICKNESS INCHES	TYPE	SIZE	DIR	TEST T&MP F	CHARPY IMPACT ENERGY FT LBS 1	2	3	SHEAR(%) 1	2	3	LAT EXP MILS 1	2	3
		813K63510			.750	V	FULL	L	+40	118	118	117						
		813K63470			1.000	V	FULL	L	+40	132	122	106						
		813K63490			1.000	V	FULL	L	+40	108	109	114						

HEAT NUMBER	CHEMICAL ANALYSIS C	Mn	P	S	Si	Cu	Ni	Cr	Mo	V	Ti	Al	B	Cb	N	Sn	MQUAID GRAIN SIZE
813K63510	.18	1.20	.014	.006	.272	.037	.03	.03	.058	.002	.031	.0002	.002	.006	.002		
813K63470	.18	1.20	.013	.005	.279	.015	.01	.02	.004	.060	.002	.039	.0002	.002	.003	.002	
813K63490	.18	1.21	.014	.006	.274	.019	.01	.02	.006	.061	.002	.040	.0002	.002	.003	.002	

I certify that the above results are a true and correct copy of actual results contained in records maintained by ArcelorMittal Burns Harbor and are in full compliance with the requirements of the specification cited above. This test report cannot be altered and must be transmitted intact with any subsequent third party test reports, if required.

ANDREW SMITH PER ELJ

BHPLTRPT TIF

SUPV QUALITY ASSURANCE

Virginia Tech P3705074

QLHRJ196245

SSAB

Test Certificate

1770 Bill Sharp Boulevard, Muscatine, IA 52761-9412, US

Form TC1: Revision 2: Date 23 Apr 2014

Customer:

VA TECH 3705074

ACE 215157

Customer P.O.No.:JCR-8922 | Mill Order No. 41-479701-03 | Shipping Manifest: MR297901

Product Description: ASTM A572-50/M345(15)/A709-50/M345(16A)
AASHTO M270(15) 50/345; REDUCTION RATIO
LCVN 15 FT-LBS @ +25F / A673-H

Ship Date: 17 Oct 16
Cert Date: 17 Oct 16

Cert No: 061604231
(Page 1 of 1)

Size: 0.313 X 96.00 X 240.0 (IN)

Tested Pieces: / **Tensiles:** / **Charpy Impact Tests**

	Heat Id	Piece Id	Tested Thickness	Tst Loc	YS (KSI)	UTS (KSI)	%RA	Elong % 2in 8in	Tst Dir	Hardness	Abs. Energy(FTLB) 1 2 3 Avg	% Shear 1 2 3 Avg	Tst Tmp	Tst Dir	Tst Siz (mm)	BDWTT Tmp %Shr
*	A6J141	A25	0.309 (DISCRT)	L	54	72		32	T		127 118 139 128		25F	L	6.7	
	B6J609	A18	0.309 (DISCRT)	L	56	76		32	T		64 61 70 65		25F	L	6.7	

Chemical Analysis

Heat Id	C	Mn	P	S	Si	Tot Al	Sol Al	Cu	Ni	Cr	Mo	Cb	V	Ti	ORGN
A6J141	15	.85	.011	.002	.04	.029	.025	.26	.14	.14	.05	.001	.019	.006	USA
B6J609	16	.86	.013	.003	.04	.030	.028	.30	.16	.13	.06	.001	.021	.006	USA

KILLED STEEL
MERCURY IS NOT A METALLURGICAL COMPONENT OF THE STEEL AND NO MERCURY WAS INTENTIONALLY ADDED DURING THE MANUFACTURE OF THIS PRODUCT.
KILLED STEEL, PRODUCED TO A FINE GRAIN PRACTICE
MTR EN 10204:2004 INSPECTION CERTIFICATE 3.1 COMPLIANT
100% MELTED AND MANUFACTURED IN THE USA.
CHARPY FULL SIZE EQUIVALENT = ABSORBED ENERGY AVG X 10 / TEST SIZE IN MM
STRAND CAST; REDUCTION RATIO = 19.2 : 1
PRODUCTS SHIPPED:
B6J609 A18 PCES: 26, LBS: 53170 A6J141 A25 PCES: 8, LBS: 16360

(P) Cust Part #:

WE HEREBY CERTIFY THAT THIS MATERIAL WAS TESTED IN ACCORDANCE WITH, AND MEETS THE REQUIREMENTS OF, THE APPROPRIATE SPECIFICATION

Brian Wales
SENIOR METALLURGIST - PRODUCT

Virginia Tech - P3705074

QLHR3196245 ACE 215157

SSAB

Test Certificate

1770 Bill Sharp Boulevard, Muscatine, IA 52761-9412, US

Form TC1: Revision 2: Date 23 Apr 2014

Customer:
WARREN FABRICATING & MACHINING CORP.
PO BOX 1032
3240 MAHONING AVENUE
WARREN
OH 44482

Customer P.O.No.: JCR-8922 | **Mill Order No.** 41-479701-03 | **Shipping Manifest:** MR297901

Product Description: ASTM A572-50/M345(15)/A709-50/M345(16A)
AASHTO M270(15) 50/345; REDUCTION RATIO
LCVN 15 FT-LBS @ +25F / A673-H

Ship Date: 17 Oct 16 | **Cert Date:** 17 Oct 16 | **Cert No:** 061604231 (Page 1 of 1)

Size: 0.313 X 96.00 X 240.0 (IN)

Tested Pieces:

Heat Id	Piece Id	Tested Thickness	Tst Loc	YS (KSI)	UTS (KSI)	%RA	Elong % 2in 8in	Tst Dir	Hardness	Tensiles: Abs. Energy(FTLB) 1 2 3 Avg	% Shear 1 2 3 Avg	Tst Tmp	Tst Dir	Tst Siz (mm)	BDWTT Tmp %Shr
A6J141	A25	0.309 (DISCRT)	L	54	72		32	T		127 118 139 129		25F	L	6.7	
* B6J609	A18	0.309 (DISCRT)	L	56	76		32	T		64 61 70 65		25F	L	6.7	

Chemical Analysis

Heat Id	C	Mn	P	S	Si	Tot Al	Sol Al	Cu	Ni	Cr	Mo	Cb	V	Ti	ORGN
A6J141	.15	.85	011	002	.04	.029	.025	.26	.14	.14	.05	.001	.019	.006	USA
B6J609	.16	.86	013	003	.04	.030	.028	.30	.16	.13	.06	.001	.021	006	USA

KILLED STEEL
MERCURY IS NOT A METALLURGICAL COMPONENT OF THE STEEL AND NO MERCURY WAS INTENTIONALLY ADDED DURING THE MANUFACTURE OF THIS PRODUCT.
KILLED STEEL, PRODUCED TO A FINE GRAIN PRACTICE
MTR EN 10204:2004 INSPECTION CERTIFICATE 3.1 COMPLIANT
100% MELTED AND MANUFACTURED IN THE USA.
CHARPY FULL SIZE EQUIVALENT = ABSORBED ENERGY AVG X 10 / TEST SIZE IN MM
STRAND CAST; REDUCTION RATIO = 19.2 : 1
PRODUCTS SHIPPED:
B6J609 A18 PCES: 26, LBS: 53170 A6J141 A25 PCES: 8, LBS: 16360

(P) Cust Part #:

WE HEREBY CERTIFY THAT THIS MATERIAL WAS TESTED IN ACCORDANCE WITH, AND MEETS THE REQUIREMENTS OF, THE APPROPRIATE SPECIFICATION

Brian Wales
SENIOR METALLURGIST - PRODUCT

Virginia Tech - P37050074
ACE - 215157

NUCOR®

NUCOR STEEL TUSCALOOSA, INC.

QLHR2580

MILL TEST CERTIFICATE

Nucor Steel Tuscaloosa, Inc.
1700 HOLT RD N.E.
Tuscaloosa, AL 35404-1000
800 800-8204
customerservice@nucortusk.com

Load Number	Tally	Mill Order Number	PO NO / Line NO.	Part Number	Certificate Number	Prepared
R213600	0000000848132	N-171928-001	JCR9873 01		S84813201-1	03/25/2019 05:22
Grade						

Order Description:
Hot Roll Plate From Coil
A572 50, 0.2500 IN x 96.000 IN x 240.000 IN
Quality Plan Description:
A572S0/IMP T1: ASTM A572-50-15/A70950/M27050/CSA50W T2 IMPACTS

Customer:
Sold TO:
WARREN FAB AND MACHINING WARREN OH
Ship TO:
WARREN FABRICATING & MACHINING Hubbard OH
Sent TO:

Shipped Item	Heat/Slab Number	Certified By	C	Mn	P	S	Si	Cu	Ni	Cr	Mo	Cb	V	Al	Ti	N2	B	Ca	Sn	CEV	ACI
9C2571B	A9P1351-04 ***	A9P1351	0.07	1.12	0.012	0.002	0.20	0.18	0.07	0.08	0.017	0.022	0.007	0.033	0.012	0.010	0.0002	0.0012		0.29	
9C2571C	A9P1351-04 ***	A9P1351	0.07	1.12	0.012	0.002	0.20	0.18	0.07	0.08	0.017	0.022	0.007	0.033	0.012	0.010	0.0002	0.0012		0.29	
9C2571D	A9P1351-04 ***	A9P1351	0.07	1.12	0.012	0.002	0.20	0.18	0.07	0.08	0.017	0.022	0.007	0.033	0.012	0.010	0.0002	0.0012		0.29	
* 9C2572B	A9P1351-03 ***	A9P1351	0.07	1.12	0.012	0.002	0.20	0.18	0.07	0.08	0.017	0.022	0.007	0.033	0.012	0.010	0.0002	0.0012		0.29	
9C2572C	A9P1351-03 ***	A9P1351	0.07	1.12	0.012	0.002	0.20	0.18	0.07	0.08	0.017	0.022	0.007	0.033	0.012	0.010	0.0002	0.0012		0.29	
9C2572D	A9P1351-03 ***	A9P1351	0.07	1.12	0.012	0.002	0.20	0.18	0.07	0.08	0.017	0.022	0.007	0.033	0.012	0.010	0.0002	0.0012		0.29	
9C2574B	A9P1352-01 ***	A9P1352	0.07	1.13	0.012	0.002	0.20	0.18	0.06	0.07	0.016	0.024	0.006	0.031	0.012	0.010	0.0002	0.0014		0.29	

Mercury has not come in contact with this product during the manufacturing process nor has any mercury been used by the manufacturing process. Certified in accordance with EN 10204 3.1. No weld repair has been performed on this material. Yield strength is determined by the 0.2% offset method unless otherwise noted. Manufactured to a fully killed fine grain practice.
NUTEMPER TEMPER PASSED plate from coil
ISO 9001:2015 Registered. PED Certified

*** indicates Heats melted and Manufactured in the U.S.A.

We hereby certify that the product described above passed all of the tests required by the specifications.

Dr. Qulin Yu - Metallurgist

NUCOR®

NUCOR STEEL TUSCALOOSA, INC.

MILL TEST CERTIFICATE

Nucor Steel Tuscaloosa, Inc.
1700 HOLT RD N.E.
Tuscaloosa, AL 35404-1000
800 800-8204
customerservice@nucortusk.com

Load Number	Tally	Mill Order Number	PO NO / Line NO	Part Number	Certificate Number	Prepared
R213600	00000000848132	N-171928-001	JCR9873 01		S84813201-1	03/25/2019 05:22
Grade						

Order Description:
Hot Roll Plate From Coil
A572 50, 0.2500 IN x 96.000 IN x 240.000 IN
Quality Plan Description:
A57250/IMP T1: ASTM A572-50-15/A70950/M27050/CSA50W T2 IMPACTS

Customer:
Sold TO:
WARREN FAB AND MACHINING WARREN OH
Ship TO:
WARREN FABRICATING & MACHINING Hubbard OH
Sent TO:

Shipped Item	Certified By	Heat/Slab Number	Yield ksi	Tensile ksi	Y/T %	ELONGATION % 2"	8"	Bend OK?	Hard HB	Charpy Impacts (ft-lbs) Size	1	2	3	Avg	Shear % 1	2	3	Avg	Test Temp
9C2571B	S9C2571FTT	A9P1351-04 ***	69.6	79.6	87.4	21.6													
9C2571B	S9C2571BLI	A9P1351-04 ***								5.0	106	90	96	97.3					40 F
9C2571B	S9C2571FLI	A9P1351-04 ***								5.0	92	91	97	93.3					40 F
9C2571B	S9C2571MLI	A9P1351-04 ***								5.0	85	106	98	96.3					40 F
9C2571B	S9C2571MTT	A9P1351-04 ***	70.7	79.8	88.6	21.3													
9C2571C	S9C2571FTT	A9P1351-04 ***	69.6	79.6	87.4	21.6													
9C2571C	S9C2571BLI	A9P1351-04 ***								5.0	106	90	96	97.3					40 F
9C2571C	S9C2571FLI	A9P1351-04 ***								5.0	92	91	97	93.3					40 F
9C2571C	S9C2571MLI	A9P1351-04 ***								5.0	85	106	98	96.3					40 F
9C2571C	S9C2571MTT	A9P1351-04 ***	70.7	79.8	88.6	21.3													
9C2571D	S9C2571FTT	A9P1351-04 ***	69.6	79.6	87.4	21.6													
9C2571D	S9C2571BLI	A9P1351-04 ***								5.0	106	90	96	97.3					40 F
9C2571D	S9C2571FLI	A9P1351-04 ***								5.0	92	91	97	93.3					40 F
9C2571D	S9C2571MLI	A9P1351-04 ***								5.0	85	106	98	96.3					40 F
9C2571D	S9C2571MTT	A9P1351-04 ***	70.7	79.8	88.6	21.3													
9C2572B	S9C2570FTT	A9P1351-03 ***	72.8	80.4	90.5	22.7													
9C2572B	S9C2571FTT	A9P1351-03 ***	69.6	79.6	87.4	21.6													
9C2572B	S9C2570BLI	A9P1351-03 ***								6.7	174	171	176	173.7					40 F

Mercury has not come in contact with this product during the manufacturing process nor has any mercury been used by the manufacturing process. Certified in accordance with EN 10204 3.1. No weld repair has been performed on this material. Yield strength is determined by the 0.2% offset method unless otherwise noted. Manufactured to a fully killed fine grain practice.
NUTEMPER TEMPER PASSED plate from coil
ISO 9001:2015 Registered, PED Certified

"***" Indicates Heats melted and Manufactured in the U.S.A.

We hereby certify that the product described above passed all of the tests required by the specifications.

Dr. Quilin Yu - Metallurgist

NUCOR®

NUCOR STEEL TUSCALOOSA, INC.

MILL TEST CERTIFICATE

Nucor Steel Tuscaloosa, Inc.
1700 HOLT RD N.E.
Tuscaloosa, AL 35404-1000
800 800-8204
customerservice@nucortusk.com

Load Number	Tally	MTI Order Number	PO NO | Line NO	Part Number	Certificate Number	Prepared
R213600	00030000848132	N-171928-001	JCR9873 01		S84813201-1	03/25/2019 05:22

Grade

Order Description:
Hot Roll Plate From Coil
A572 50, 0.2500 IN x 96.000 IN x 240.000 IN
Quality Plan Description:
A57250/IMP T1: ASTM A572-50-15/A709S0/M27050/CSA50W T2 IMPACTS

Customer:
Sold TO:
WARREN FAB AND MACHINING WARREN OH
Ship TO:
WARREN FABRICATING & MACHINING Hubbard OH
Sent TO:

Shipped Item	Certified By	Heat/Slab Number	Yield ksi	Tensile ksi	Y/T %	ELONGATION % 2"	8"	Weld OK?	Hard HB	Charpy Impacts (ft-lbs) Size	1	2	3	Avg	Shear % 1	2	3	Avg	Test Temp
9C2572B	S9C2571BLI	A9P1351-03 ***								5.0	106	90	96	97.3					40 F
9C2572B	S9C2570FLI	A9P1351-03 ***								6.7	191	185	178	184.7					40 F
9C2572B	S9C2571FLI	A9P1351-03 ***								5.0	92	91	97	93.3					40 F
9C2572B	S9C2570MLI	A9P1351-03 ***								6.7	173	180	176	176.3					40 F
9C2572B	S9C2571MLI	A9P1351-03 ***								5.0	85	106	98	96.3					40 F
9C2572B	S9C2570MTT	A9P1351-03 ***	71.1	79.3	89.7	21.5													
9C2572B	S9C2571MTT	A9P1351-03 ***	70.7	79.8	88.6	21.3													
9C2572C	S9C2570FTT	A9P1351-03 ***	72.8	80.4	90.5	22.7													
9C2572C	S9C2571FTT	A9P1351-03 ***	69.6	79.6	87.4	21.6													
9C2572C	S9C2570BLI	A9P1351-03 ***								6.7	174	171	176	173.7					40 F
9C2572C	S9C2571BLI	A9P1351-03 ***								5.0	106	90	96	97.3					40 F
9C2572C	S9C2570FLI	A9P1351-03 ***								6.7	191	185	178	184.7					40 F
9C2572C	S9C2571FLI	A9P1351-03 ***								5.0	92	91	97	93.3					40 F
9C2572C	S9C2570MLI	A9P1351-03 ***								6.7	173	180	176	176.3					40 F
9C2572C	S9C2571MLI	A9P1351-03 ***								5.0	85	106	98	96.3					40 F
9C2572C	S9C2570MTT	A9P1351-03 ***	71.1	79.3	89.7	21.5													
9C2572C	S9C2571MTT	A9P1351-03 ***	70.7	79.8	88.6	21.3													
9C2572D	S9C2570FTT	A9P1351-03 ***	72.8	80.4	90.5	22.7													

Mercury has not come in contact with this product during the manufacturing process nor has any mercury been used by the manufacturing process. Certified in accordance with EN 10204 3.1. No weld repair has been performed on this material. Yield strength is determined by the 0.2% offset method unless otherwise noted. Manufactured to a fully killed fine grain practice.
NUTEMPER TEMPER PASSED plate from coil
ISO 9001:2015 Registered, PED Certified

*** indicates Heats melted and Manufactured in the U.S.A.

We hereby certify that the product described above passed all of the tests required by the specifications.

Dr. Quilin Yu - Metallurgist

NUCOR®

NUCOR STEEL TUSCALOOSA, INC.

MILL TEST CERTIFICATE

Nucor Steel Tuscaloosa, Inc.
1700 HOLT RD N.E.
Tuscaloosa, AL 35404-1000
800 800-8204
customerservice@nucortusk.com

Load Number	Tally	Mill Order Number	PO NO | Line NO	Part Number	Certificate Number	Prepared
R213600	00000000848132	N-171928-001	JCR9873 01		S84813201-1	03/25/2019 05:22

Grade

Order Description:
Hot Roll Plate From Coil
A572 50, 0.2500 IN x 96.000 IN x 240.000 IN
Quality Plan Description:
A57250/IMP T1: ASTM A572-50-15/A70950/M27050/CSA50W T2 IMPACTS

Customer:

Sold TO:
WARREN FAB AND MACHINING WARREN OH
Ship TO:
WARREN FABRICATING & MACHINING Hubbard OH
Sent TO:

Shipped Item	Certified By	Heat/Slab Number	Yield ksi	Tensile ksi	Y/T	ELONGATION % 2"	8"	Bend OK?	Hard HB	Charpy Impacts (ft-lbs) Size mm	1	2	3	Avg	Shear % 1	2	3	Avg	Test Temp
9C2572D	S9C2571FTT	A9P1351-03 ***	69.6	79.6	87.4	21.6													
9C2572D	S9C2570BLI	A9P1351-03 ***								6.7	174	171	176	173.7					40 F
9C2572D	S9C2571BLI	A9P1351-03 ***								5.0	106	90	96	97.3					40 F
9C2572D	S9C2570FLI	A9P1351-03 ***								6.7	191	185	178	184.7					40 F
9C2572D	S9C2571FLI	A9P1351-03 ***								5.0	92	91	97	93.3					40 F
9C2572D	S9C2570MLI	A9P1351-03 ***								6.7	173	180	176	176.3					40 F
9C2572D	S9C2571MLI	A9P1351-03 ***								5.0	85	106	98	96.3					40 F
9C2572D	S9C2570MTT	A9P1351-03 ***	71.1	79.3	89.7	21.5													
9C2572D	S9C2571MTT	A9P1351-03 ***	70.7	79.8	88.6	21.3													
9C2574B	S9C2574FTT	A9P1352-01 ***	64.5	75.4	85.5	24.1													
9C2574B	S9C2574BLI	A9P1352-01 ***								5.0	86	84	82	84.0					40 F
9C2574B	S9C2574FLI	A9P1352-01 ***								5.0	92	91	87	90.0					40 F
9C2574B	S9C2574MLI	A9P1352-01 ***								5.0	77	76	78	77.0					40 F
9C2574B	S9C2574MTT	A9P1352-01 ***	68.7	77.7	88.4	21.8													

Items: 7 PCS: 71 Weight: 115981 LBS

Mercury has not come in contact with this product during the manufacturing process nor has any mercury been used by the manufacturing process. Certified in accordance with EN 10204 3.1. No weld repair has been performed on this material. Yield strength is determined by the 0.2% offset method unless otherwise noted. Manufactured to a fully killed fine grain practice.
NUTEMPER TEMPER PASSED plate from coil
ISO 9001:2015 Registered, PED Certified

"***" indicates Heats melted and Manufactured in the U.S.A.

We hereby certify that the product described above passed all of the tests required by the specifications.

Dr. Quilin Yu - Metallurgist

QLHRJ76

ArcelorMittal Burns Harbor Plate

QUALITY ASSURANCE
REPORT OF TEST AND ANALYSES

US HWY 12 Burns Harbor, Indiana

SHIPMENT NO.	DATE SHIPPED	CAR OR VEHICLE NO.	PAGE
804-17261	01-09-19	AREA TRANSPORTATIONTRLR 5451	1

SOLD TO: Va Tech 3705074
ACS 21557

SHIP TO:

NOTE	SERIAL NUMBER	PAT NO.	HEAT NUMBER	NO. PCS.	SIZE AND QUANTITY: THICKNESS	WIDTH OR DIA.	LENGTH	WEIGHT	YIELD POINT	TENSILE STRENGTH	AF FRAC. EL.ONG.	RED.
					INCHES	INCHES	INCHES	POUNDS	PSI	PSI	IN	% %

QUALITY STEEL MELTED & MANUFACTURED IN THE U. S. A.
PLATES - AASHTO M-270-15 GR 50T2 KLD FINE GRAIN PRAC TYPE 2, ASTM A709-13A GR 50T2, ASTM A572-13A GR 50, ASME SA572 GR 50 2017 EDITION, CH-V A673 FREQ (H) L 15/10 FTLBS AT +40F --- TEST CERTS ARE PREPARED IN ACCORD WITH PROCEDURES OUTLINED IN EN 10204:2004 TYPE 3.1
MFST - MFST MILL SERIAL# & PATTERN# MFST PPI 0076658-0001 MFST TEST CERTS ARE PREPARED IN ACCORD WITH PROCEDURES OUTLINED IN EN MFST 10204:2004 TYPE 3.1
- LIFT MAX 5 PCS-SIZES & GRADES SEP
CO# JCR 9688 GH 403-1775B

811D07600	9	.375	96	480	44109	56300	75600	2	45
						56700	75200	8	25

(M55)MFST REF#:ITEM 003/A572-50

Q QUENCH TEMPERATURE | T-TEMPER TEMPERATURE | N-NORMALIZE TEMPERATURE

SERIAL NUMBER	PAT NO.	HEAT NUMBER	HARD BHN	BEND	THICKNESS INCHES	TYPE	SIZE	DIR	TEST TEMP F	CHARPY IMPACT ENERGY FT LBS 1	2	3	SHEAR(%) 1	2	3	LAT. EXP MILS 1	2	3
		811D07600			.375	V	3/4	L	+40	198	199	201						

HEAT NUMBER	CHEMICAL ANALYSIS C	Mn	P	S	Si	Cu	Ni	Cr	Mo	V	Ti	Al	B	Cb	N	Sn	MOLIAD GRAIN SIZE
811D07600	.12	1.19	.016	.005	.292	.029	.01	.04	.055	.002	.028	.0002		.002	.005	.004	

I certify that the above results are a true and correct copy of actual results contained in records maintained by ArcelorMittal Burns Harbor and are in full compliance with the requirements of the specification cited above. This test report cannot be altered and must be transmitted intact with any subsequent third party test reports, if required.

ANDREW SMITH PER ELJ

BHPLTRPT.TIF

SUPV. QUALITY ASSURANCE

A2. TENSION COUPON TESTS

The stress-strain curves obtained from the tension coupon tests are presented in the figures below

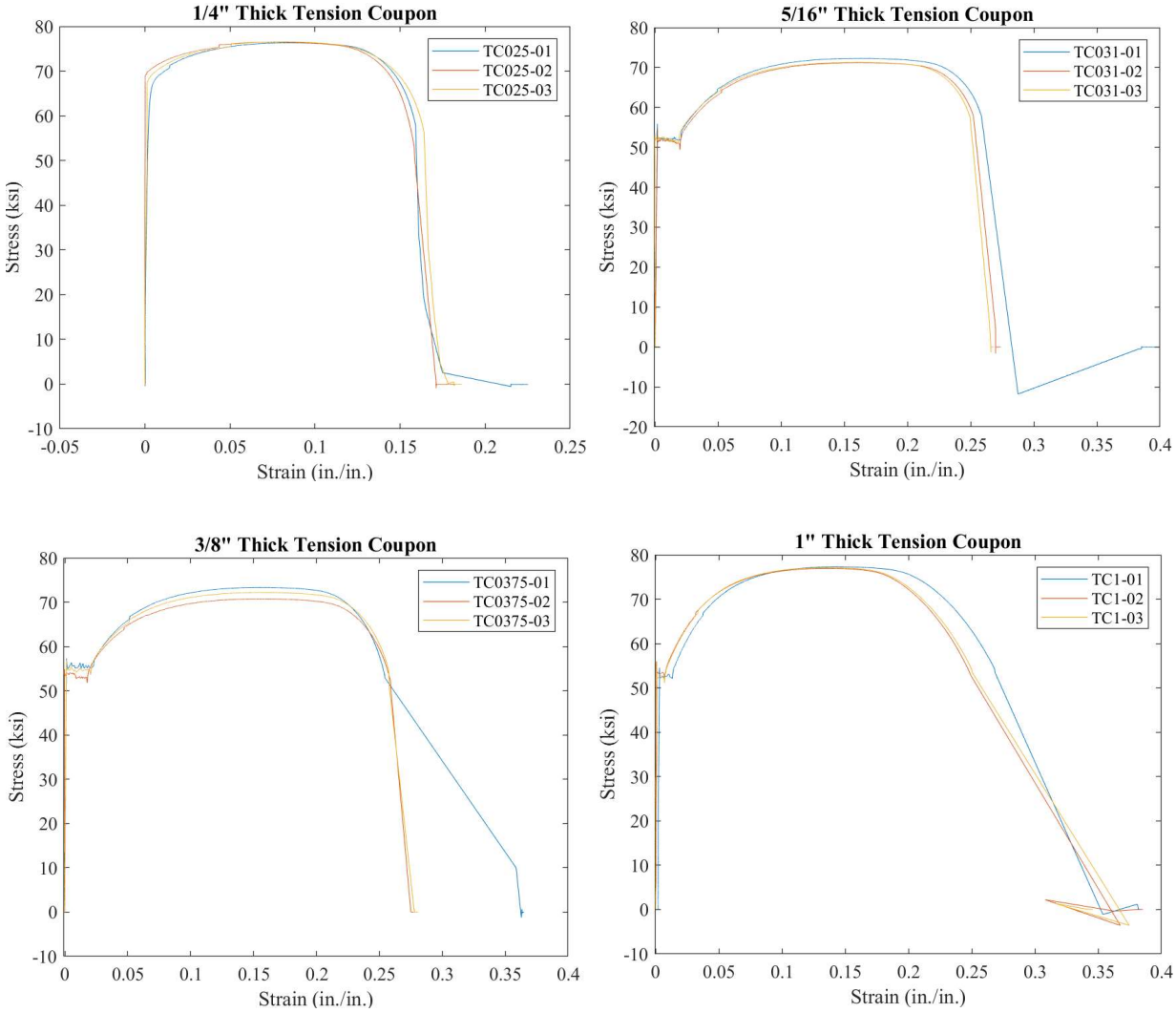

Figure A1. Tension Coupon Tests

Material model parameters of 1” thick plate used for FEM in Chapter 3 and Chapter 4

E=224,000 MPa, σ_{yo}=376 MPa, H_1= 414 MPa, β=6, H_2= 3516 MPa, γ=15, s=0.3, t=1.49, D_C=0.5.

A.3 DISPLACEMENT PROTOCOL

The FEMA 461 cyclic displacement protocol was adopted for all test specimens. The table A1 provides the general displacement protocol in terms of target shear angle (%), the target peak displacements can be calculated based on the overall link length, L, of each specimen. Example displacement protocol associated with link length of L=20 in., is provided in Table A2. The displacement steps were continued until the specimen experienced near complete loss of lateral strength.

Table A1. Displacement Protocol (FEMA 416)

Cycle	Target Shear Angle (%)	Cycle	Target Shear Angle (%)
1	0.15	21	4.3388
2		22	
3	0.21	23	6.0743
4		24	
5	0.294	25	8.5041
6		26	
7	0.4116	27	11.906
8		28	
9	0.5762	29	16.668
10		30	
11	0.8067	31	23.335
12		32	
13	1.1294	33	32.669
14		34	
15	1.5812	35	45.737
16		36	
17	2.2137	37	64.032
18		38	
19	3.0992		
20			
21	4.3388		
22			
23	6.0743		
24			

Table A2. Example Displacement Protocol (L=20 in.)

Cycle	Positive Peak (in.)	Negative Peak (in.)	Target Shear Angle (%)	Loading Rate
1	0.0300	-0.0300	0.15	0.25 in./min
2	0.0300	-0.0300		
3	0.0420	-0.0420	0.21	
4	0.0420	-0.0420		
5	0.0588	-0.0588	0.294	
6	0.0588	-0.0588		
7	0.0823	-0.0823	0.4116	
8	0.0823	-0.0823		
9	0.1152	-0.1152	0.5762	
10	0.1152	-0.1152		
11	0.1613	-0.1613	0.8067	0.5 in./min
12	0.1613	-0.1613		
13	0.2259	-0.2259	1.1294	
14	0.2259	-0.2259		
15	0.3162	-0.3162	1.5812	
16	0.3162	-0.3162		
17	0.4427	-0.4427	2.2137	1 in./min
18	0.4427	-0.4427		
19	0.6198	-0.6198	3.0992	
20	0.6198	-0.6198		
21	0.8678	-0.8678	4.3388	
22	0.8678	-0.8678		
23	1.2149	-1.2149	6.0743	2 in./min
24	1.2149	-1.2149		
25	1.7008	-1.7008	8.5041	
26	1.7008	-1.7008		
27	2.3811	-2.3811	11.906	
28	2.3811	-2.3811		
29	3.3336	-3.3336	16.668	4 in./min
30	3.3336	-3.3336		
31	4.6670	-4.6670	23.335	
32	4.6670	-4.6670		
33	6.5339	-6.5339	32.669	
34	6.5339	-6.5339		
35	9.1474	-9.1474	45.737	
36	9.1474	-9.1474		
37	12.8064	-12.8064	64.032	
38	12.8064	-12.8064		

A.4 SHEAR ANGLE CALCULATION

The shear angle of the specimen is calculated using the law of cosines, as shown in Fig. A2 and Eq. (A1), (A2), (A3).

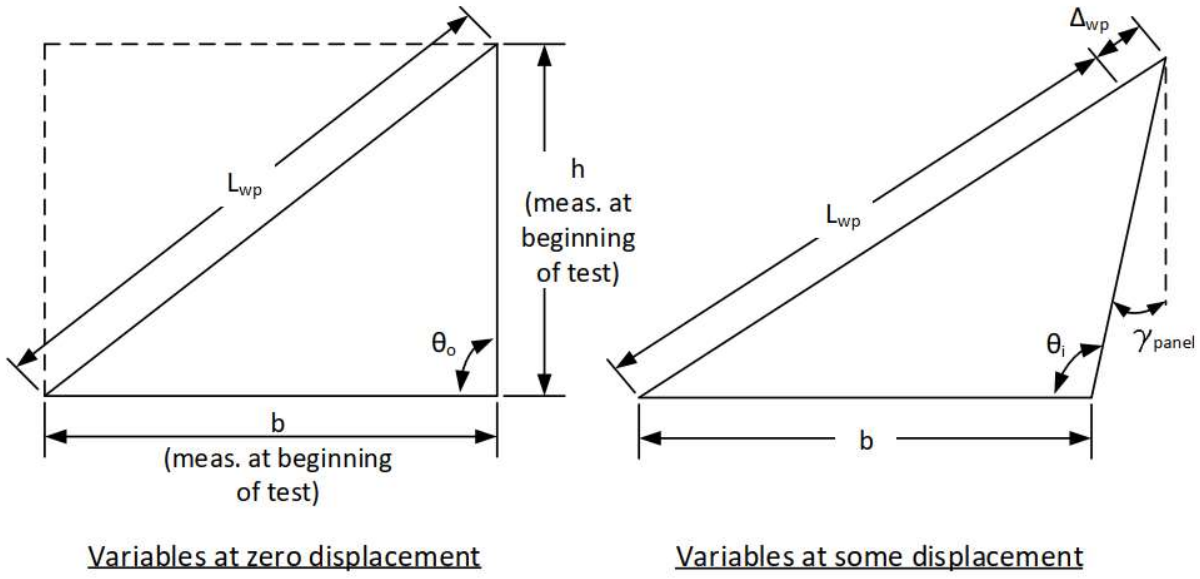

Fig. A2. Shear angle calculation using Diagonal String Potentiometer and Linear Potentiometers (from Phillips 2016)

$$\theta_0 = a\cos\left(\frac{b^2 + h^2 - L_{wp}^2}{2bh}\right) \tag{A1}$$

$$\theta_i = a\cos\left[\frac{b^2 + h^2 - \left(L_{wp} + \Delta_{wp}\right)^2}{2bh}\right] \tag{A2}$$

$$\gamma = \theta_i - \theta_0 \tag{A3}$$

APPENDIX B

DETAILS ABOUT STUDY ON THE OPTIMIZED TOLOPOGIES

This appendix provides additional information about the computational and experimental study on the Optimized Topologies, presented in Chapter 3.

B1. EXPERIMENTAL RAW DATA

This section provides experimental raw data obtained from the tests of Specimen STL, Specimen OPT1 and Specimen OPT2, respectively.

Specimen STL

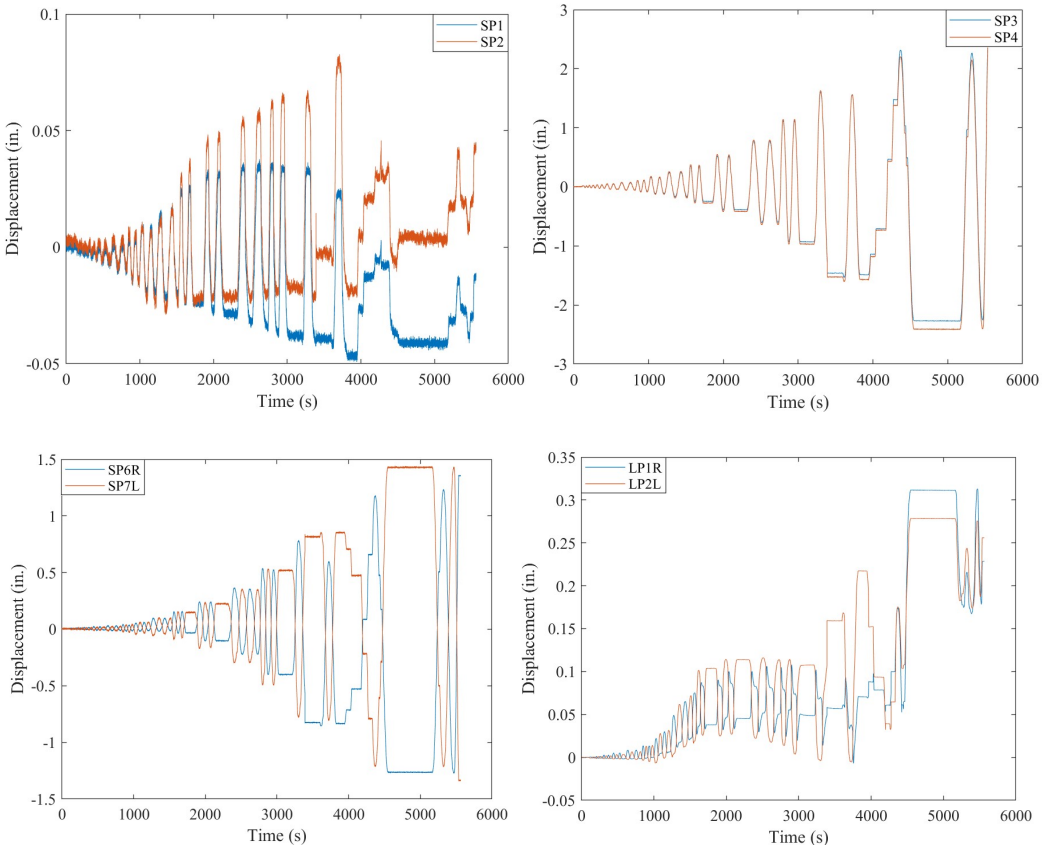

Fig. B1. Raw Displacement Measurements of Specimen STL

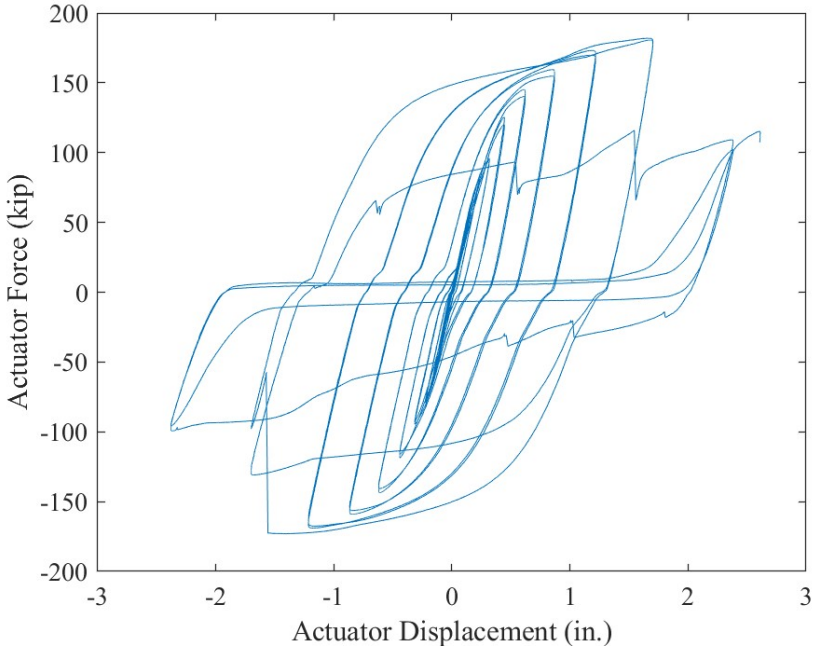

Fig. B2. Actuator Force vs. Actuator Displacement of Specimen STL

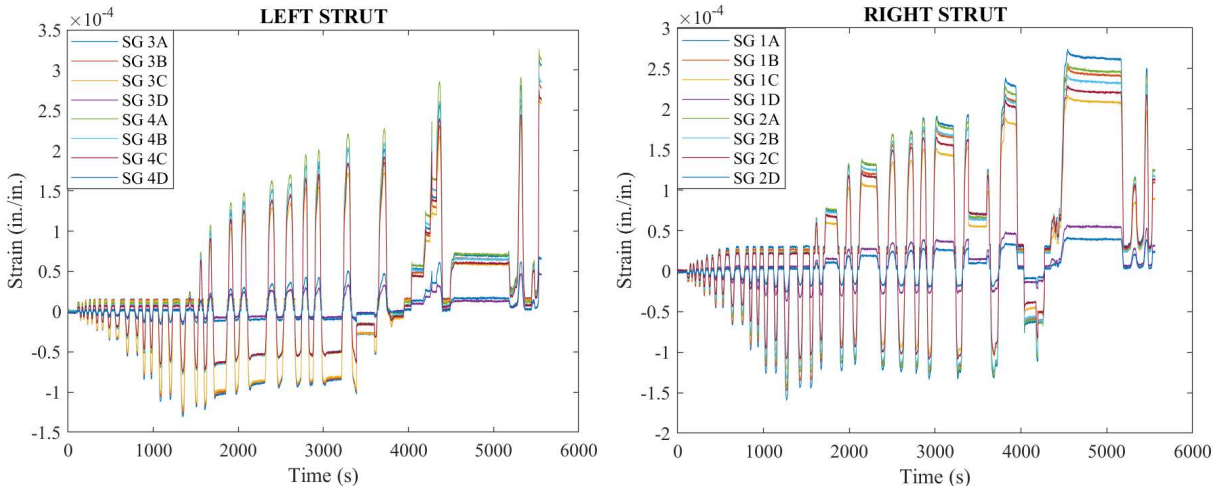

Fig. B3. Raw Strain Gage measurements of Specimen STL

Specimen OPT1

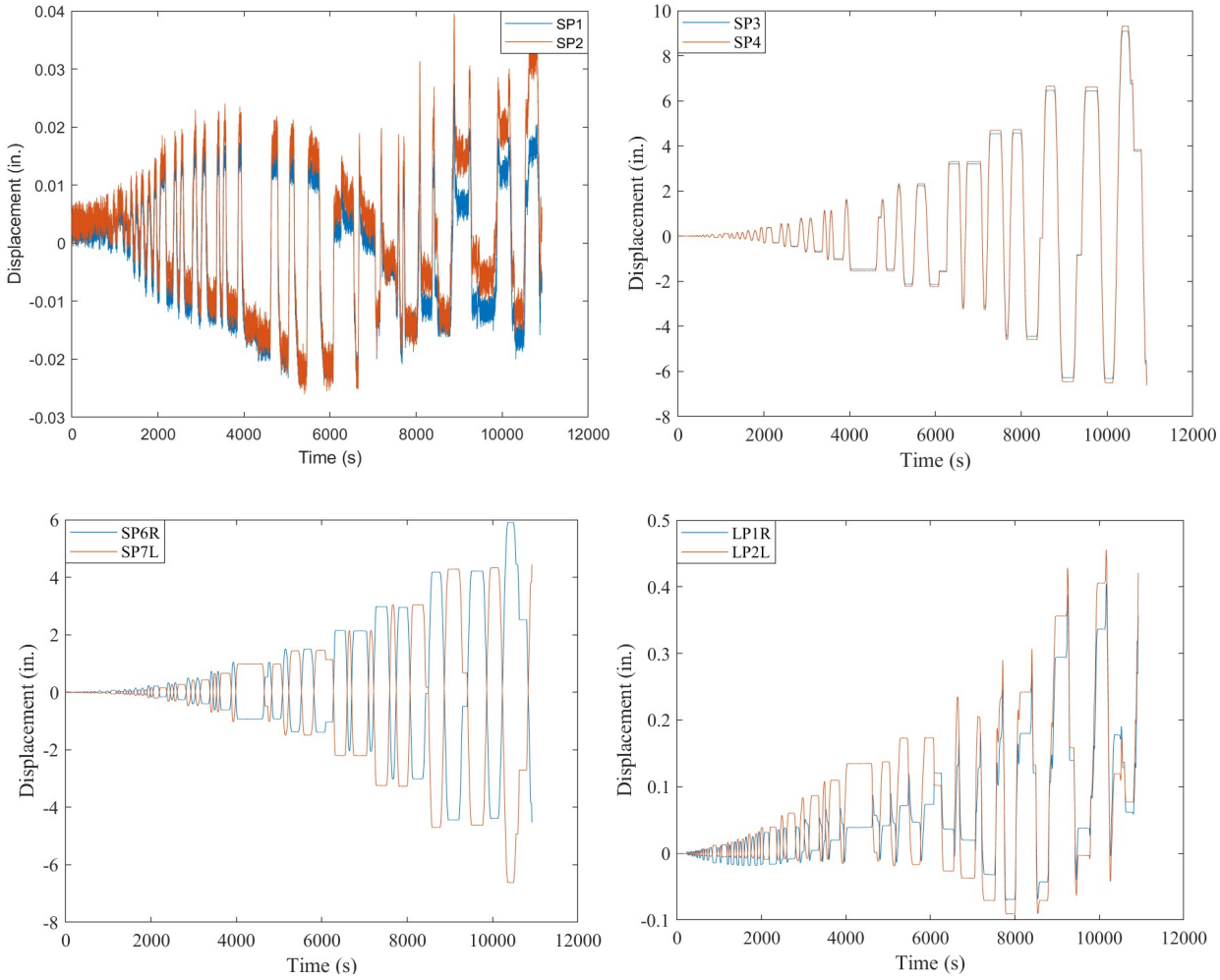

Fig. B4. Raw Displacement Measurements of Specimen OPT1

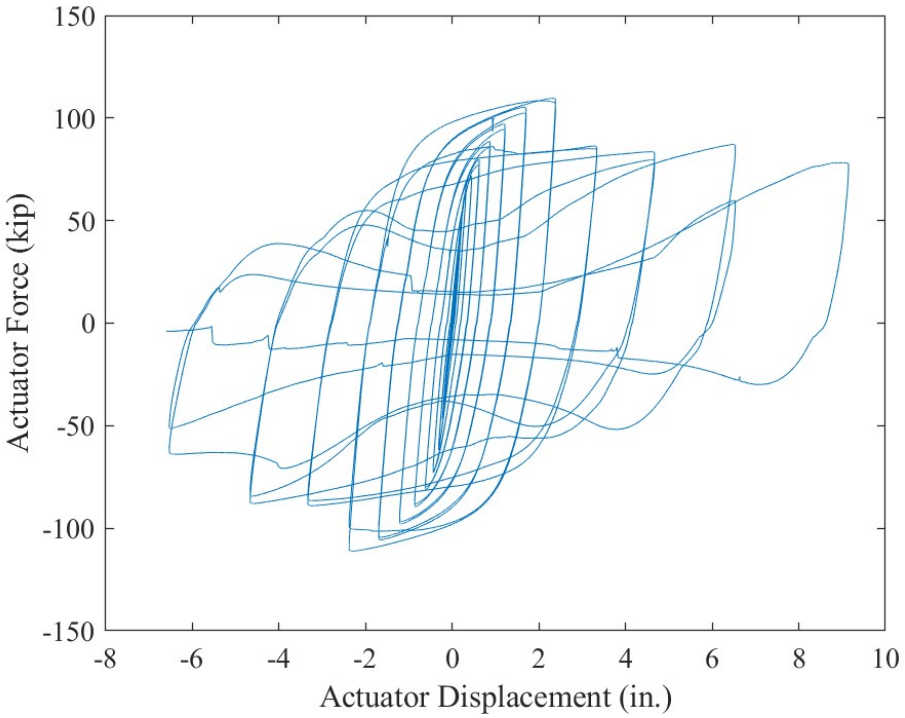

Fig. B5. Actuator Force vs. Actuator Displacement of Specimen OPT1

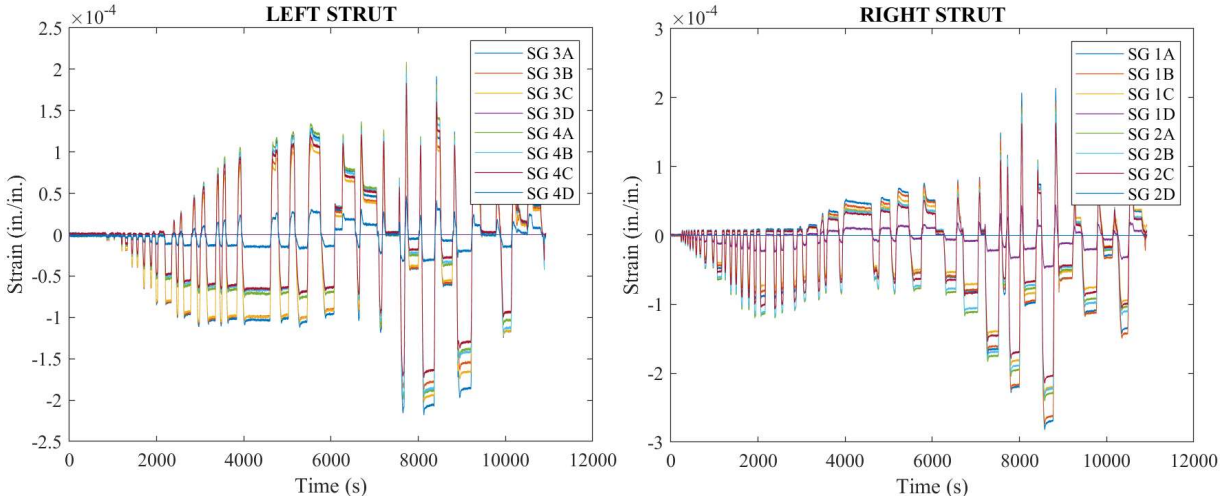

Fig. B6. Raw Strain Gage measurements of Specimen OPT1

Specimen OPT2

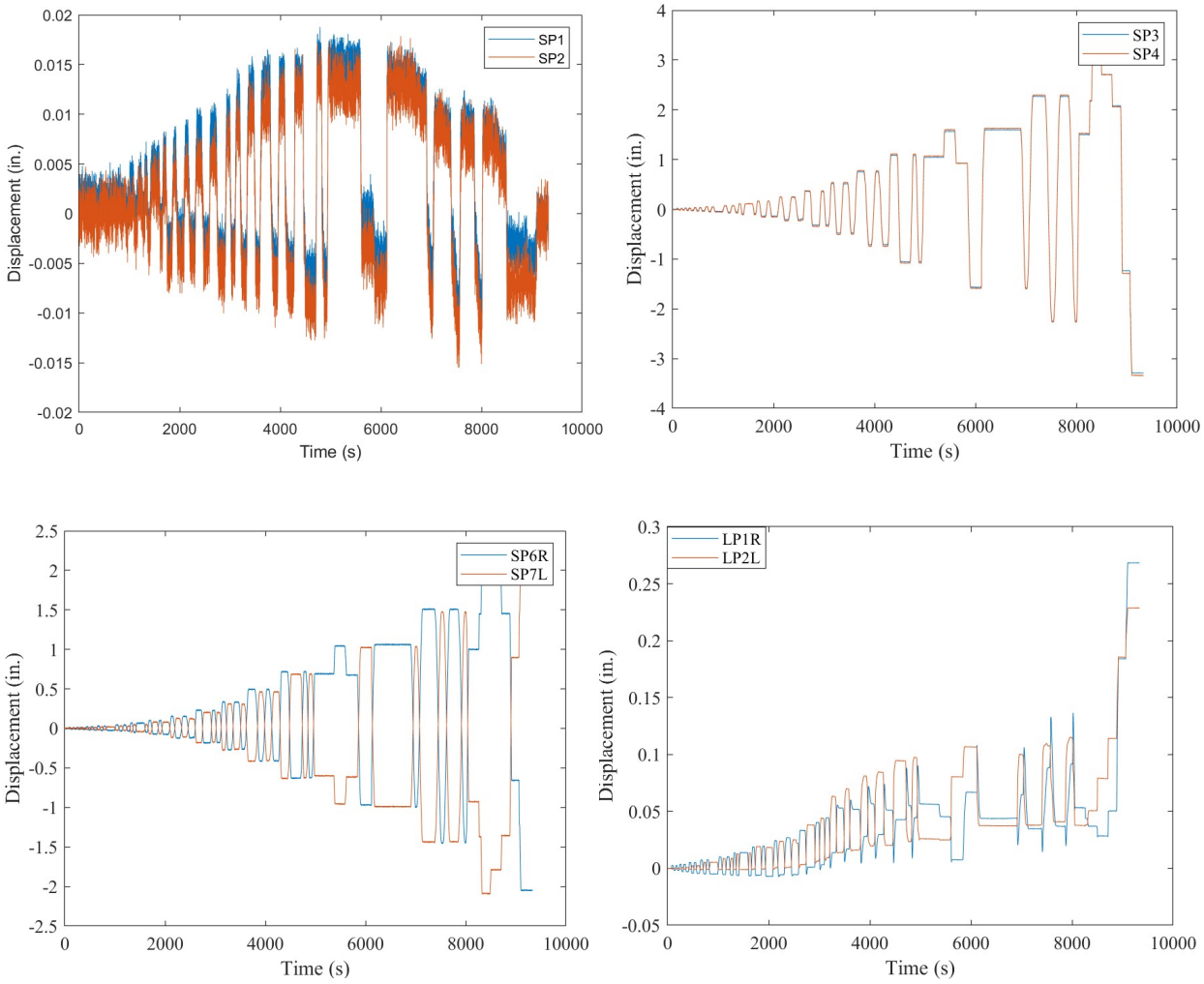

Fig. B7. Raw Displacement Measurements of Specimen OPT2

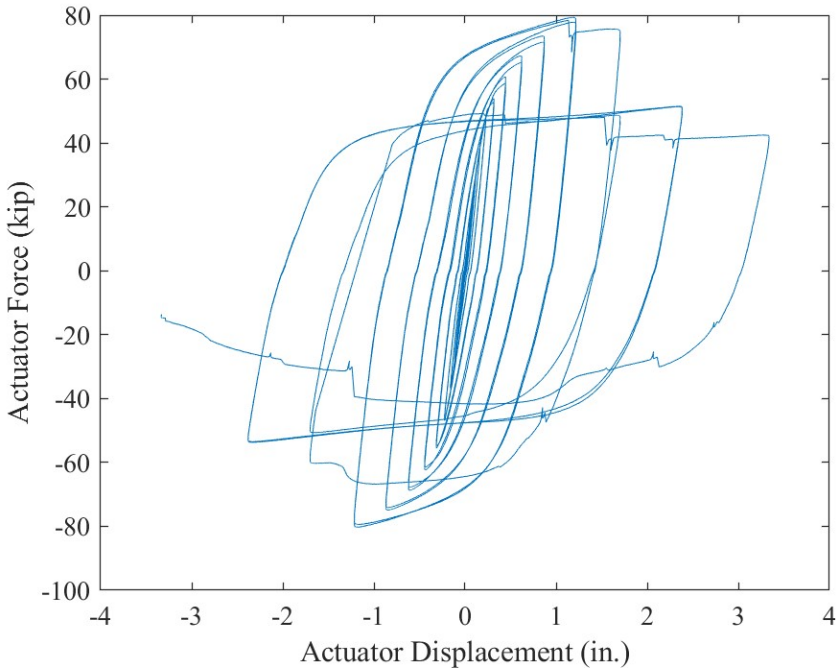

Fig. B8. Actuator Force vs. Actuator Displacement of Specimen OPT2

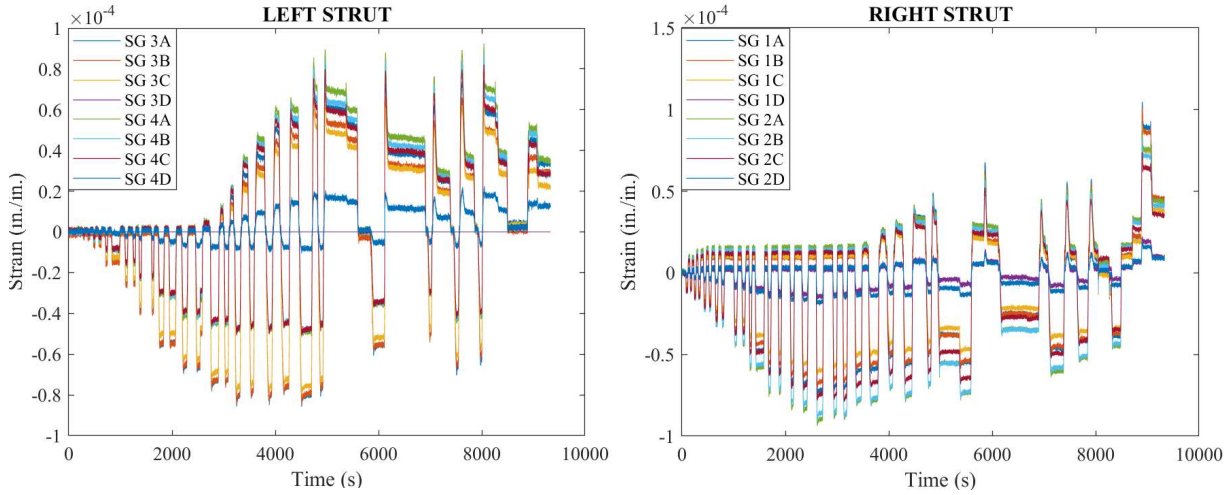

Fig. B9. Raw Strain Gage measurements of Specimen OPT2

B2. PARAMETRIC STUDY RESULTS

Displacement Protocol

The Eccentrically Braced Frame (EBF) displacement protocol in AISC 341-16 (AISC, 2016), was adopted for this parametric study, as shown in Table B1.

Table B1. Displacement Protocol for Parametric Study

Cycle	Target Shear Angle (%)
1	0.375
2	0.5
3	0.75
4	1
5	1.5
6	2
7	3
8	4
9	5
10	7
11	9

In addition, and a theoretical vertical displacement was also applied at the top of the specimens, following an arc associated with the constraint enforced by pinned struts, as shown in Fig. B10. More specifically, the vertical displacement can be calculated using Eq. (B1), as shown below, where R_{strut} is the length of the strut, which is dependents on the link length. The negative sign means downward displacement.

$$\delta_y = -\left(R_{strut} - \sqrt{R_{strut}^2 - \delta_x^2}\right) \tag{B1}$$

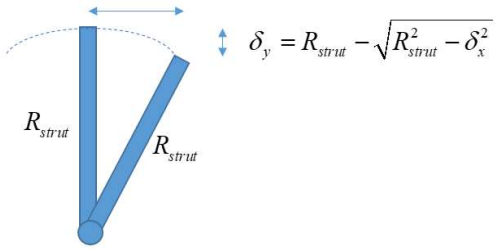

Fig. B10. Motion of the specimen during the test

Mesh Sensitivity

Three mesh sizes were considered for the mesh sensitivity analysis including e=0.1 in., e=0.15 in., e=0.2 in. Effective plastic strain, out-of-plane displacement and hysteretic behavior were considered. Considering the convergence and run time, the mesh size of *e*=0.15 in. (= 3.81 mm), is considered for the computational study.

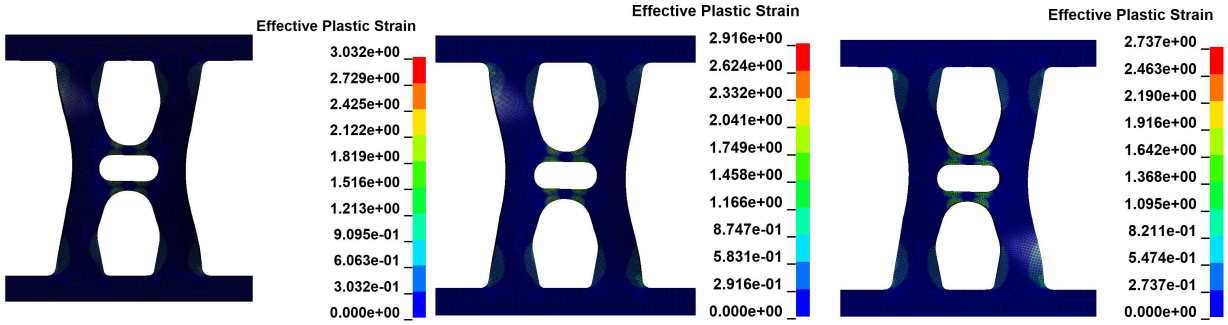

(a) *e*=0.1 in. (b) *e*=0.15 in. (c) *e*=0.2 in.

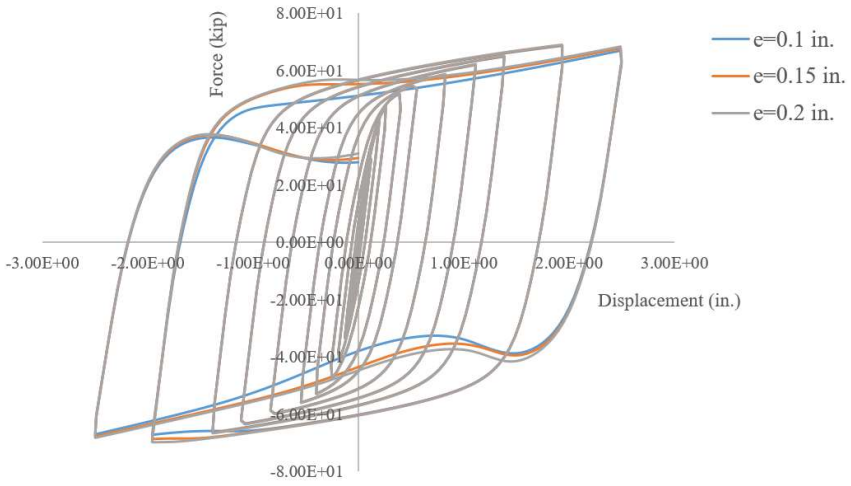

(d) Hysteretic Curve

Fig. B11. Hysteretic Behavior and Effective Plastic Strain for the Mesh Sensitivity analysis

Hysteretic Curve of Topologies from FEM

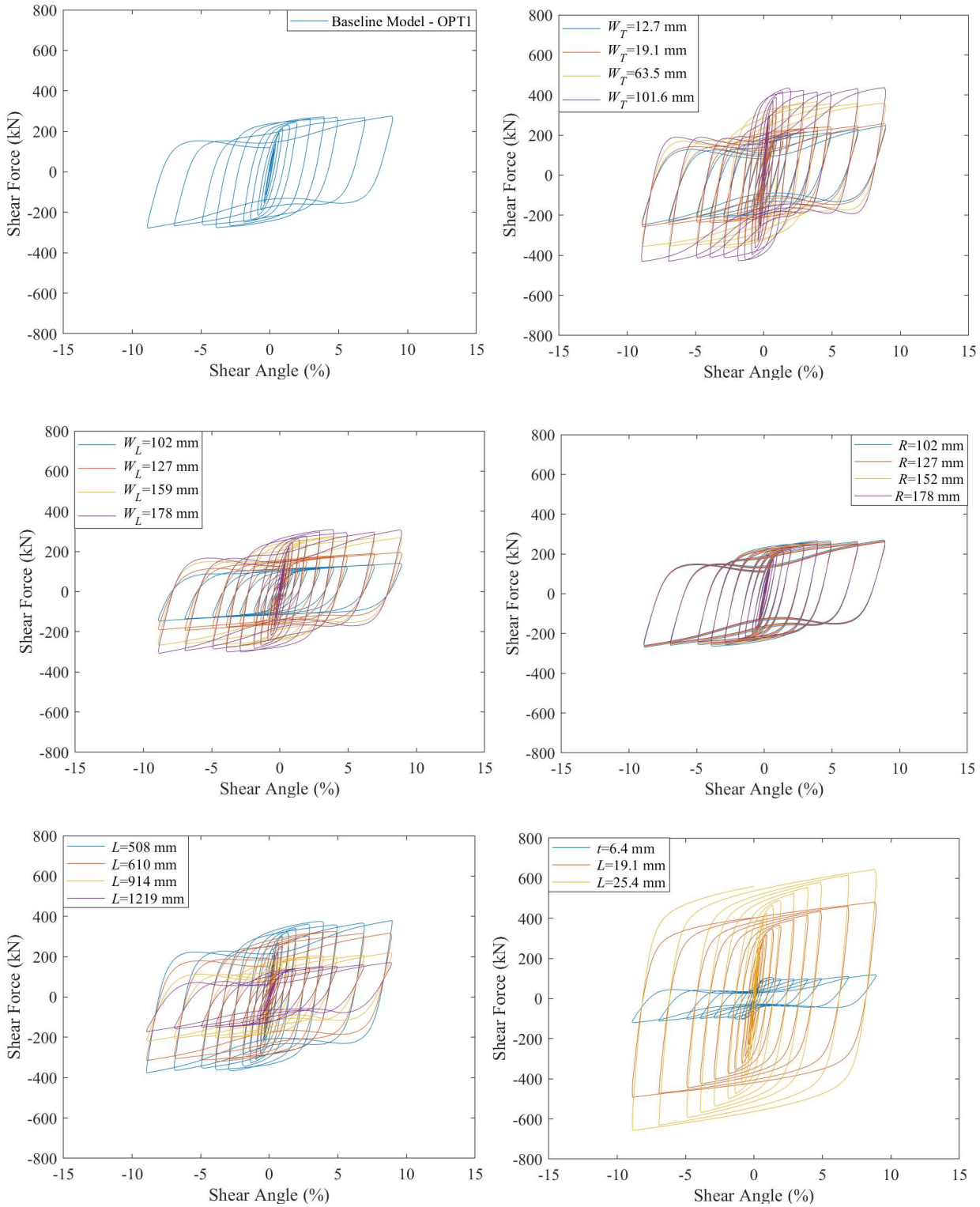

Fig. B12. Hysteretic Curve of Topologies

Maximum out-of-plane displacement and maximum effective plastic strain

Table B2. Max. Equivalent plastic strain and Out-of-plane Displacement

Model		Max. Equivalent plastic strain	Max. Out-of-plane displacement (in.)
Baseline		2.44	2.316
W_T	0.5 in.	2.134	2.16
	0.75 in.	2.281	2.252
	2.5 in.	2.122	2.832
	4 in.	1.942	3.206
R	4 in.	2.162	2.308
	5 in.	1.967	2.291
	6 in.	1.884	2.279
	7 in.	1.84	2.27
W_L	4 in.	2.491	1.284
	5 in.	2.435	1.762
	6.25 in.	2.383	2.247
	7 in.	2.222	2.47
L	20 in.	2.493	1.824
	24 in.	2.352	2.101
	36 in.	2.363	2.69
	48 in.	2.343	3.036
t	0.25 in.	1.21	3.5
	0.75 in.	3.155	0.614
	1 in.	3.147	0.07

The effect of design parameters on buckling resistance

Buckling is quantified by the maximum out-of-plane displacement (δ_z) obtained from FE models. The effect of five individual geometric parameters on buckling of topology is illustrated in Fig. B13. The *y*-axis is expressed in terms of out-of-plane displacement ratio while the *x*-axis was normalized to the maximum out-of-plane displacement of the baseline model, $dz_{baseline}$.

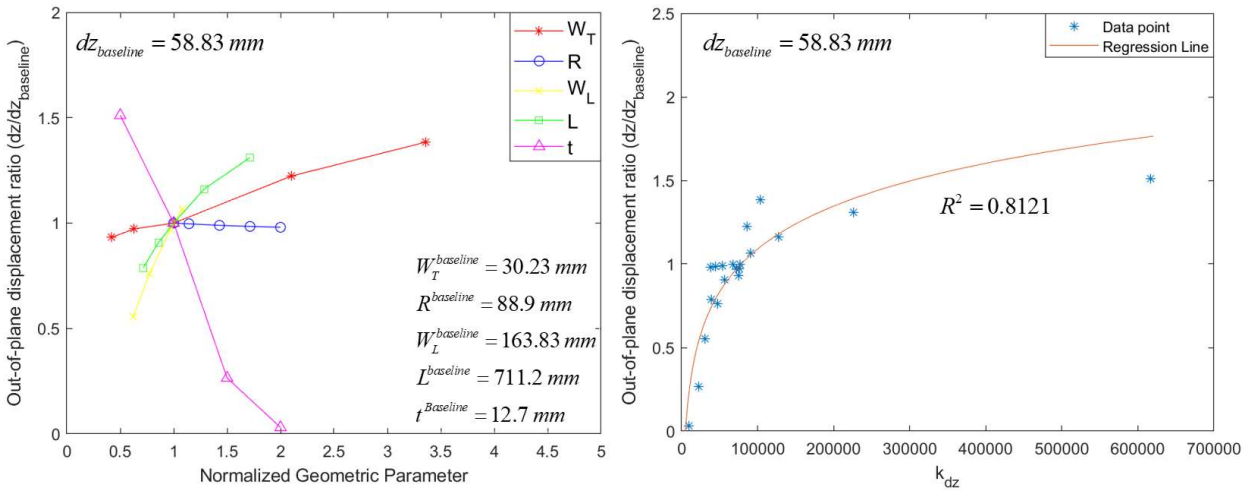

(a) Geometric Parameters (b) Non-dimensional Parameter - k_{dz}

Fig. B13. The effect of design parameters on buckling

As shown in Fig. B13(a) the greater tie width, W_T, leg width, W_L, and link length, L, are, the greater maximum out-of-plane displacement the topology has. Among these three parameters, while leg width, W_L, seems to have an important impact on the ability to resist buckling of the topology, tie width, W_T, has slight effect on controlling out-of-plane displacement. In contrast, increasing tie radius, R, or plate thickness, t, tends to increase buckling resistance capacity of the topology. This can be explained that the overall slenderness of the topology reduces as those parameters get greater. Even though tie radius, R, contributes in reducing buckling, plate thickness, t, is the main parameter in controlling buckling of the topology.

a new non-dimensional parameter believed to control the buckling of the shape, k_{dz}, is shown in Eq. (B2). This equation was introduced based on some observations illustrated in Fig. B13(a) such as (1) increasing plate thickness, t, and tie radius, R, improves buckling resistance of the topology, (2) increasing overall length, L, tie width, W_T, and leg width, W_L increases the overall slenderness of the topology, leading to more buckling. Fig. B13(b) represents the relationship between k_{dz} and out-of-plane displacement ratio. Furthermore, Eq. (B3) provides a simple way of predicting maximum out-of-plane displacement of a topology.

$$k_{dz} = \frac{(W_T^2 + W_L^2)L^2}{Rt^3} \tag{B2}$$

$$dz = dz_{Baseline}\left[0.37\ln\left(k_{dz}\right) - 3.17\right] \tag{B3}$$

The effect of design parameters on fracture resistance

Fig. B14(a) shows how each individual geometric parameter affects maximum equivalent plastic strain of the topology. It was found that tie radius, R, and plate thickness, t, and leg width, W_L, have some effect on reducing maximum equivalent plastic strain, thus controlling potential for fracture. However, plate thickness, t, is likely to be more important parameter compared to tie radius, R, or leg width, W_L, as its corresponding slope is greater than that of the tie radius and leg width. On the other hand, it is suggested that maximum equivalent plastic strain is not easy to control by other parameters including tie width, W_T, even though it was found that increase the tie width, W_T, leads to the reduce in equivalent plastic strain. However, plastic mechanism is expected to change as the width of the ties get greater and inelasticity is not concentrated at predicted plastic hinges. Hence, topologies with great values of tie width, W_T, tend to buckle more compared to those with smaller tie width, W_T as mentioned in previous section. Overall, effective plastic strain can be slightly reduced by either increasing the tie radius or reducing plate thickness.

Results observed from Fig. B14(a) also suggested a new non-dimensional parameter, k_{PL}, expressed in Eq. (B4), likely to control maximum equivalent plastic strain. More specifically, while increasing plate thickness, t, equivalent plastic strain increases while increasing tie radius, R, and leg width, W_L, is likely to minimize accumulated plastic strain. Eq. (B5) is introduced to provide an approximation of maximum equivalent plastic strain, ε, of a topology in terms of non-dimensional parameter, k_{PL}, and maximum equivalent plastic strain of baseline topology, $\varepsilon_{baseline}$.

$$k_{PL} = \frac{t^2}{(R + W_L)^2} \tag{B4}$$

$$\varepsilon = \varepsilon_{baseline}[0.3\ln(k_{PL}) + 2.7 \tag{B5}$$

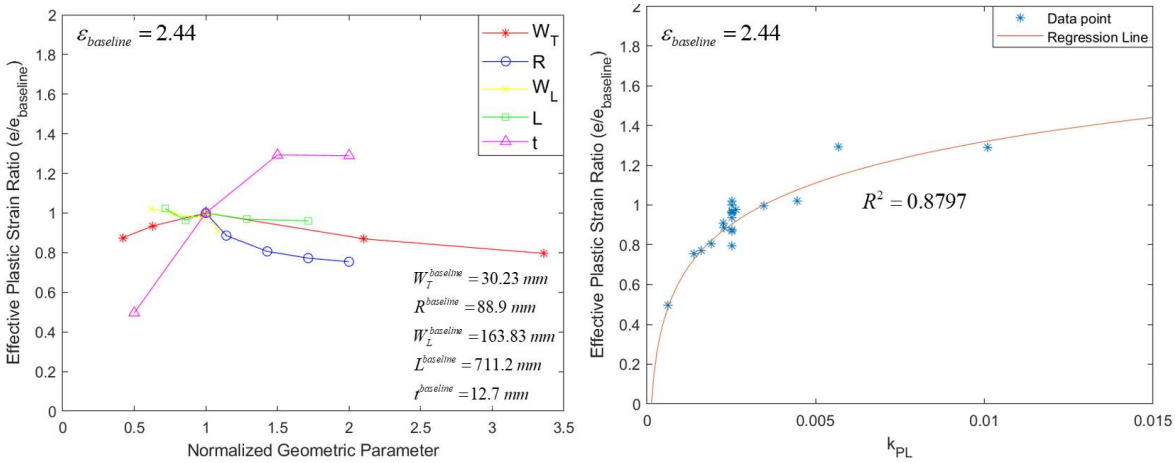

(a) Geometric Parameters (b)Non-dimensional parameter - k_{PL}

Fig. B14. The effect of design parameters on buckling

APPENDIX C

DETAILS ABOUT STUDY ON THE TIED BUTTERFLY SHAPE

This appendix provides more information about the computational and experimental study on the Tied Butterfly Shape, presented in Chapter 4.

C1. EXPERIMENTAL RAW DATA

This section provides experimental raw data obtained from the tests of Specimen STL, Specimen TBF1, Specimen TBF2, and Specimen TBF3 respectively.

Specimen STL

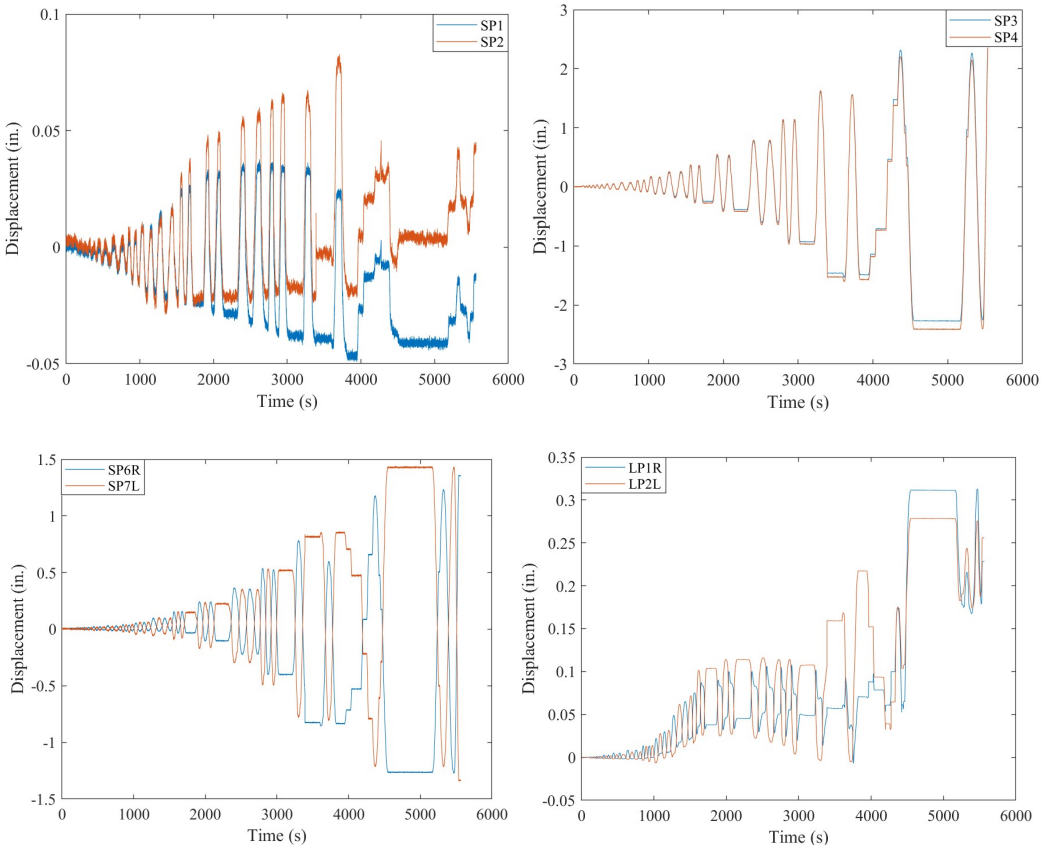

Fig. C1. Raw Displacement Measurements of Specimen STL

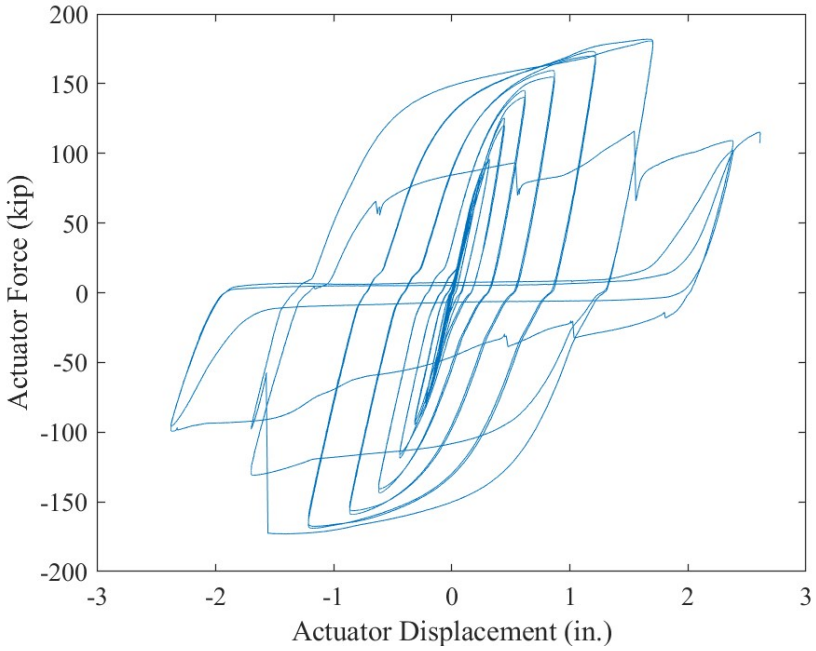

Fig. C2. Actuator Force vs. Actuator Displacement of Specimen STL

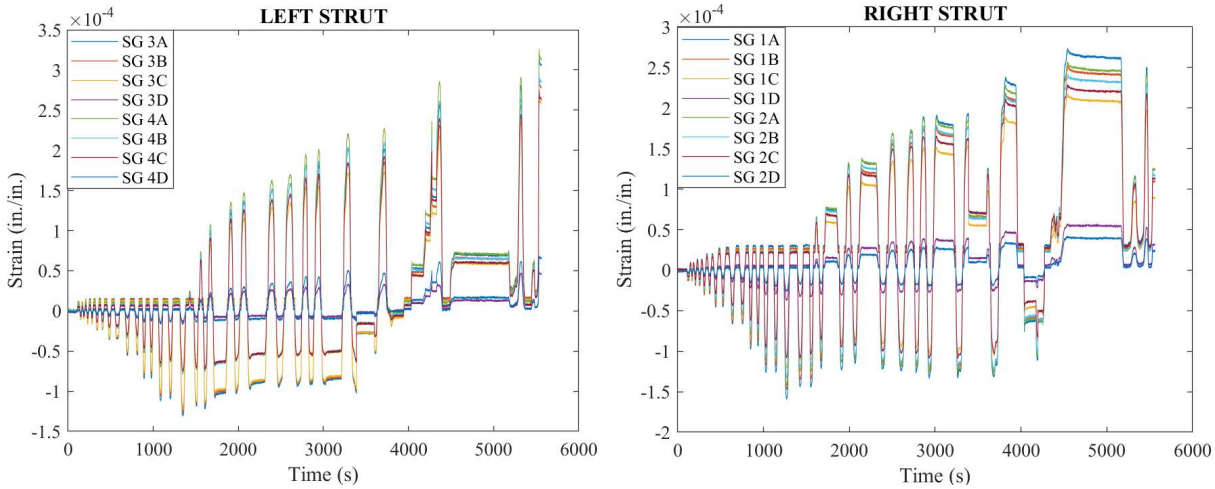

Fig. C3. Raw Strain Gage measurements of Specimen STL

Specimen TBF1

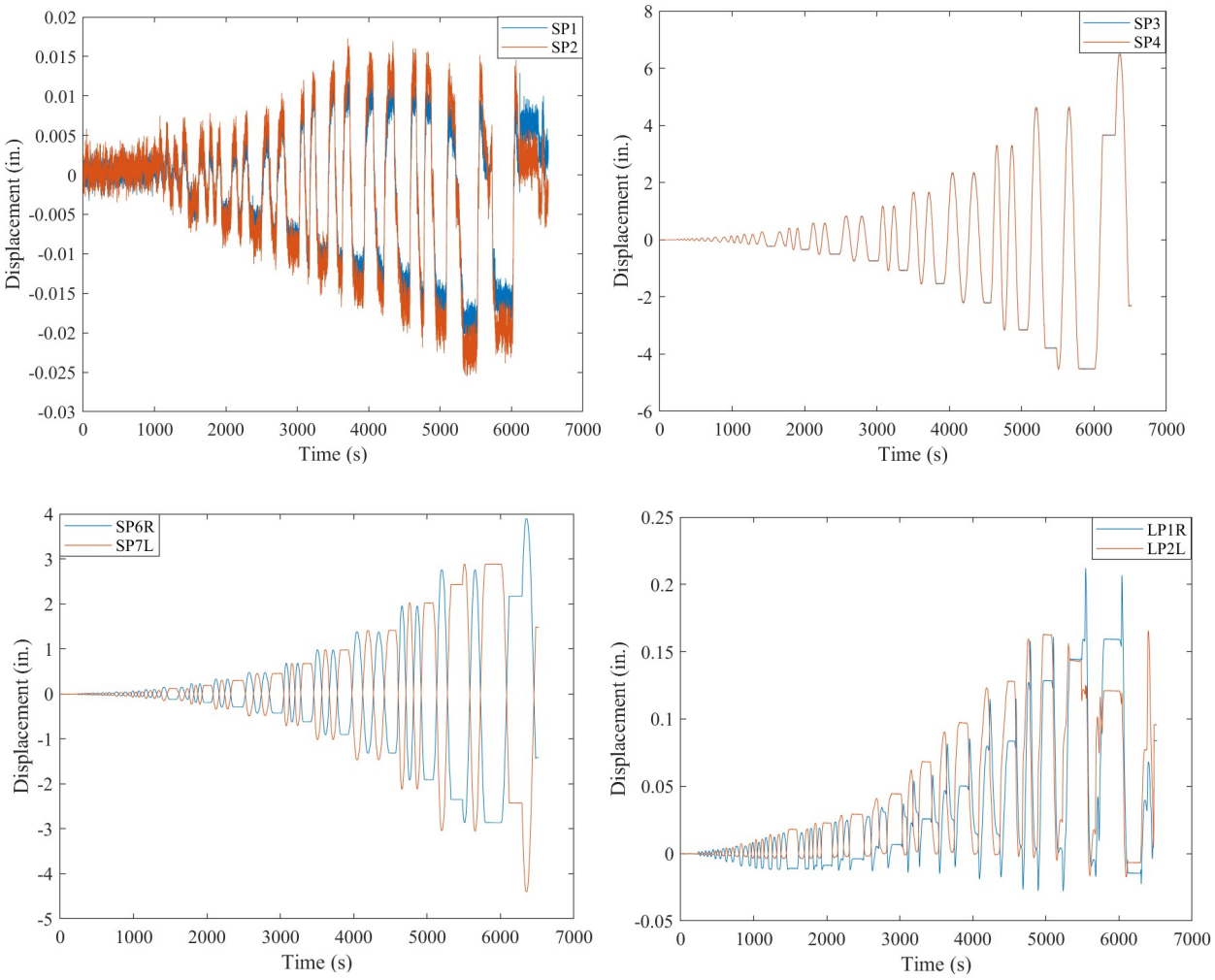

Fig. C4. Raw Displacement Measurements of Specimen TBF1

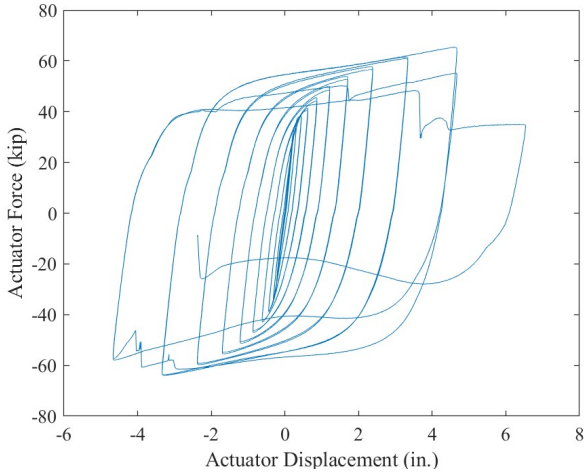

Fig. C5. Raw Displacement Measurements of Specimen TBF1

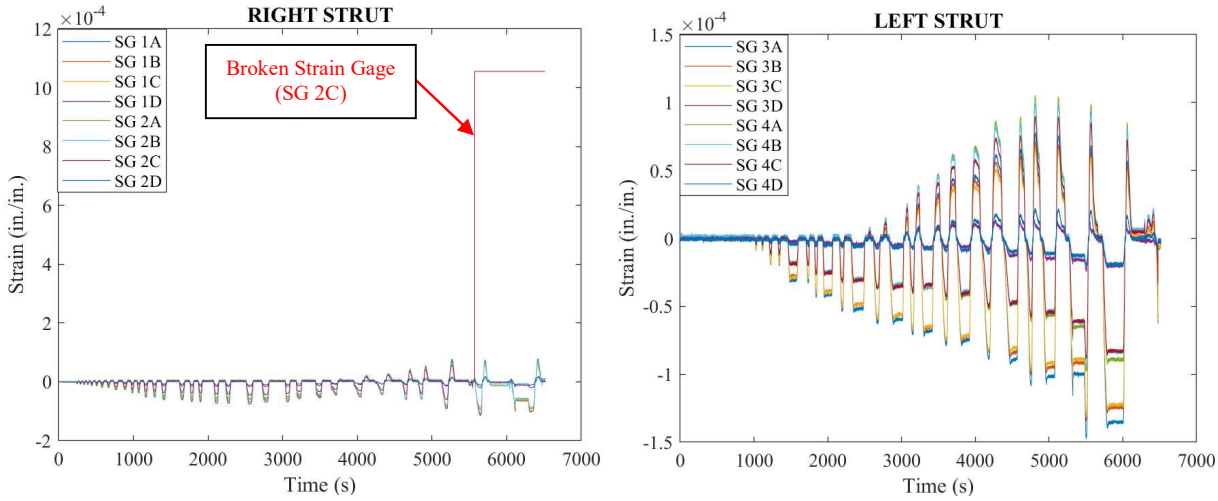

Fig. C6 Raw Strain Gage measurements of Specimen TBF1

Specimen TBF2

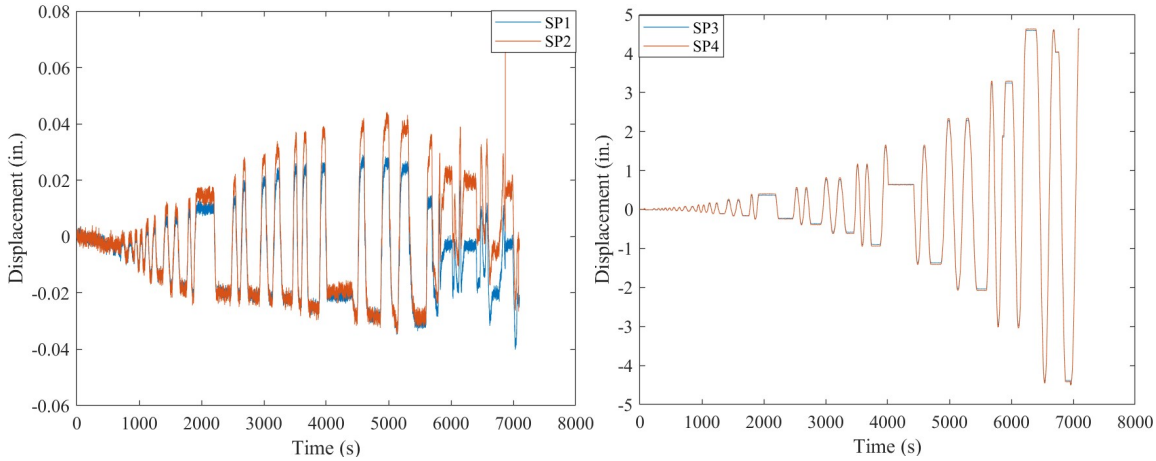

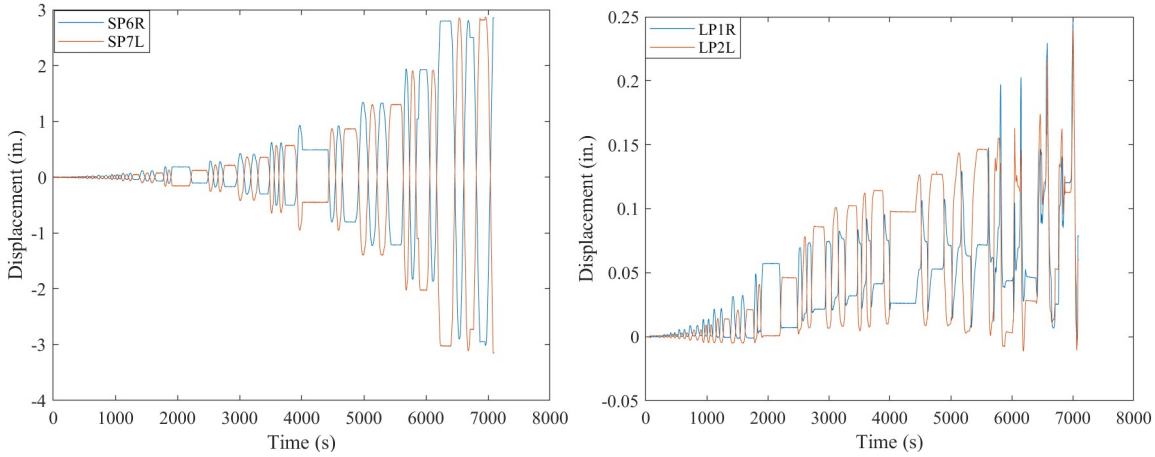

Fig. C7. Raw Displacement Measurements of Specimen TBF2

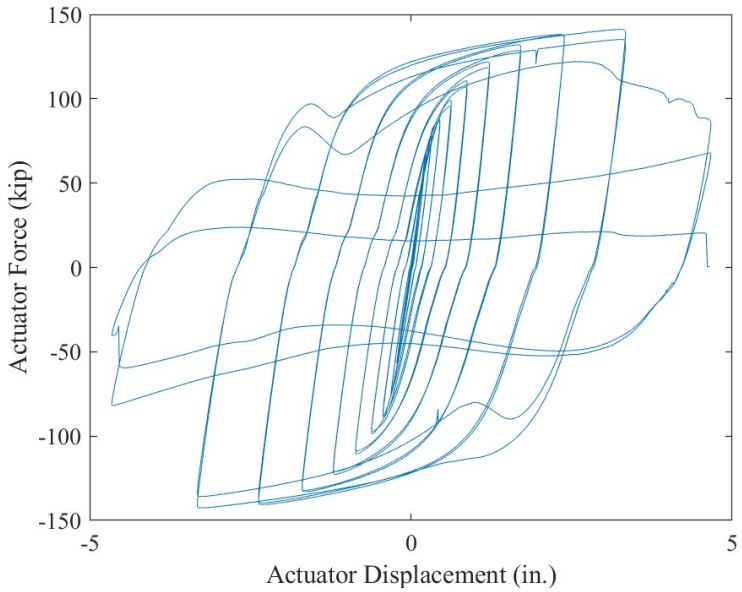

Fig. C8. Raw Displacement Measurements of Specimen TBF2

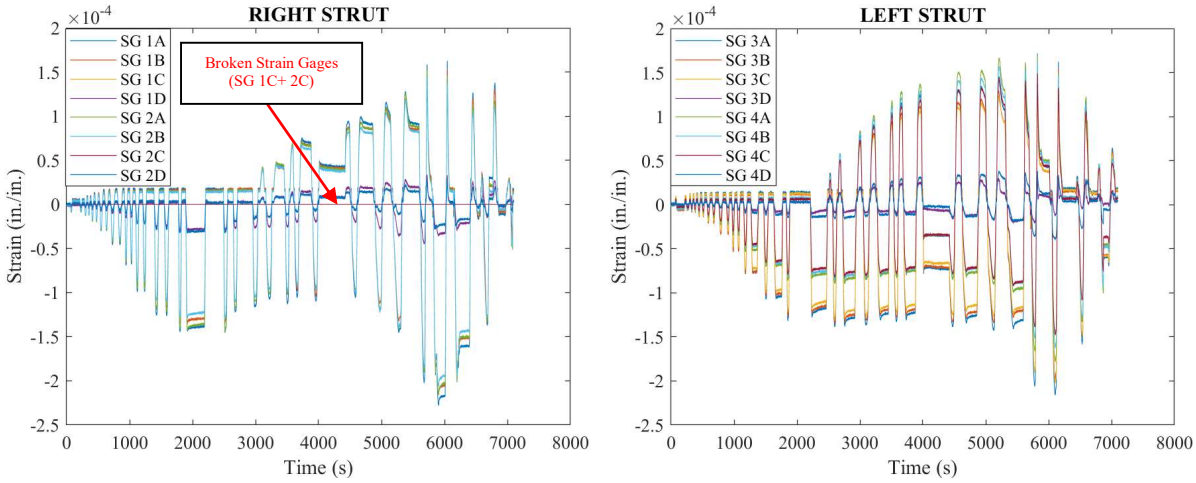

Fig. C9 Raw Strain Gage measurements of Specimen TBF2

Specimen TBF3

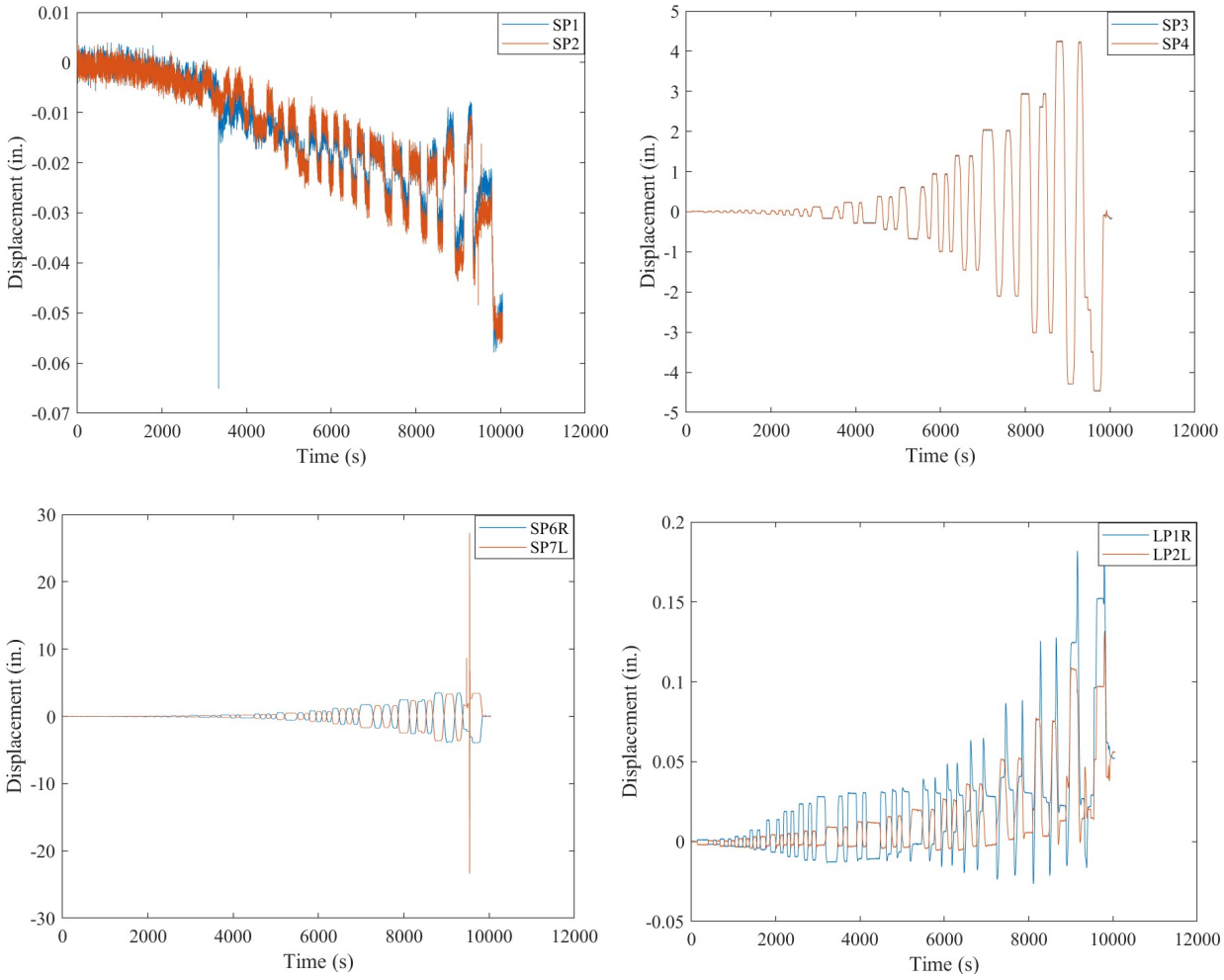

Fig. C10. Raw Displacement Measurements of Specimen TBF3

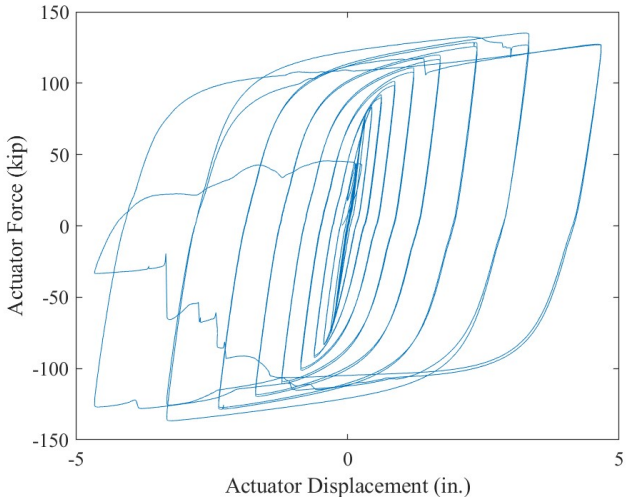

Fig. C11. Raw Displacement Measurements of Specimen TBF3

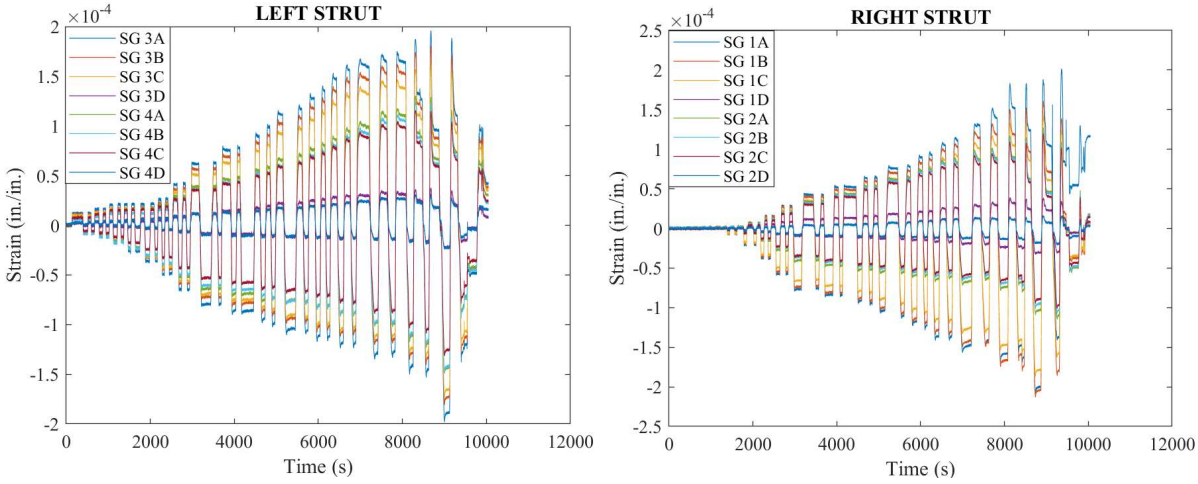

Fig. C12 Raw Strain Gage measurements of Specimen TBF3

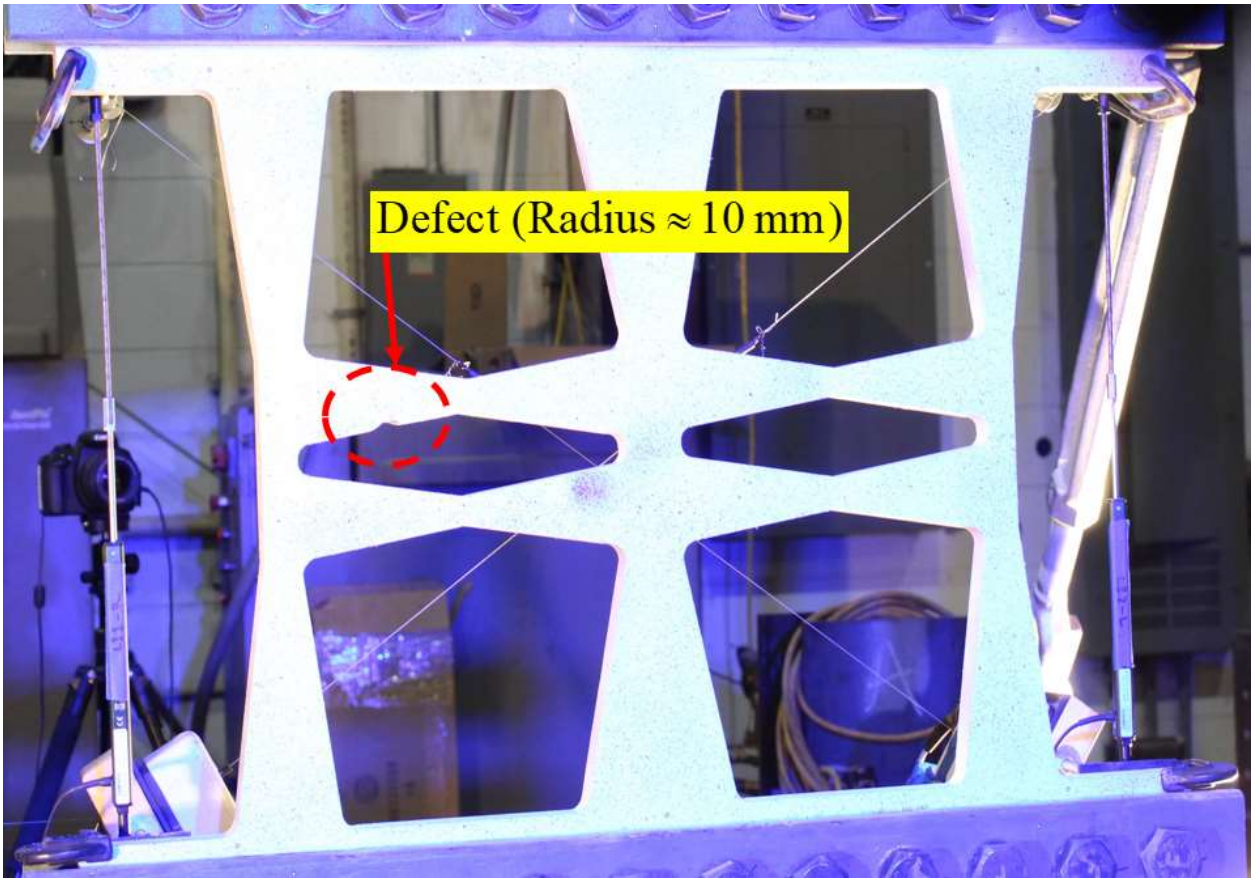

Fig. C13. Defect at the tie of Specimen TBF3

C2. PARAMETRIC STUDY RESULTS

Displacement Protocol

The Eccentrically Braced Frame (EBF) displacement protocol in AISC 341-16 (AISC, 2016), was adopted for this parametric study, as shown in Table C1.

Table C1. Displacement Protocol for Parametric Study

Cycle	Target Shear Angle (%)
1	0.375
2	0.5
3	0.75
4	1
5	1.5
6	2
7	3
8	4
9	5
10	7
11	9

In addition, and a theoretical vertical displacement was also applied at the top of the specimens, following an arc associated with the constraint enforced by pinned struts. More specifically, the vertical displacement can be calculated using Eq. (C1), as shown below, where R_{strut} is the length of the strut, which is dependents on the link length. The negative sign means downward displacement.

$$\delta_y = -\left(R_{strut} - \sqrt{R_{strut}^2 - \delta_x^2}\right) \tag{C1}$$

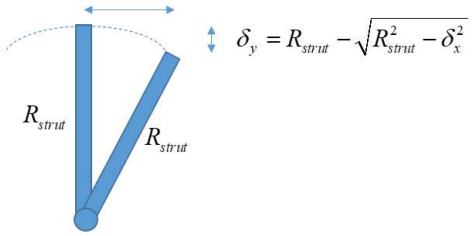

Fig. C14. Motion of the specimen during the test

Geometric Parameter of the Tied Butterfly Shape

Table C2. Geometric Parameter and Max. Out-of-plane displacements

W_T (in.)	W_L (in.)	L_L (in.)	L_T (in.)	W_T/L_T	W_L/L_L	$(W_L/W_T)^2$	dz (mm)
0.8572678	**1.0499344**	**6.9995626**	**5.7151189**	0.15	0.15	1.5	0.25019
0.8572678	**1.0499344**	**6.9995626**	**4.2863392**	0.2	0.15	1.5	0.3556
0.8572678	**1.0499344**	**6.9995626**	**3.4290713**	0.25	0.15	1.5	0.42418
0.8572678	**1.0499344**	**6.9995626**	**2.8575595**	0.3	0.15	1.5	0.470662
0.7735094	1.0939075	7.292717	5.1567296	0.15	0.15	2	0.165862
0.7735094	1.0939075	7.292717	3.8675472	0.2	0.15	2	0.199644
0.7735094	1.0939075	7.292717	3.0940378	0.25	0.15	2	3.8354
0.7735094	1.0939075	7.292717	2.5783648	0.3	0.15	2	12.954
0.6645841	**1.1510934**	**7.6739558**	**4.4305604**	0.15	0.15	3	0.197612
0.6645841	**1.1510934**	**7.6739558**	**3.3229203**	0.2	0.15	3	0.254
0.6645841	**1.1510934**	**7.6739558**	**2.6583363**	0.25	0.15	3	0.29972
0.6645841	**1.1510934**	**7.6739558**	**2.2152802**	0.3	0.15	3	0.33274
0.5940594	1.1881188	7.9207921	3.960396	0.15	0.15	4	0.21717
0.5940594	1.1881188	7.9207921	2.970297	0.2	0.15	4	0.28956
0.5940594	1.1881188	7.9207921	2.3762376	0.25	0.15	4	0.33274
0.5940594	1.1881188	7.9207921	1.980198	0.3	0.15	4	0.37846
1.0390988	**1.2726309**	**6.3631544**	**6.927325**	0.15	0.2	1.5	0.25146
1.0390988	**1.2726309**	**6.3631544**	**5.1954938**	0.2	0.2	1.5	0.3302
1.0390988	**1.2726309**	**6.3631544**	**4.156395**	0.25	0.2	1.5	0.3683
1.0390988	**1.2726309**	**6.3631544**	**3.4636625**	0.3	0.2	1.5	14.859
0.9459782	1.3378152	6.6890762	6.3065215	0.15	0.2	2	0.18288
0.9459782	1.3378152	6.6890762	4.7298911	0.2	0.2	2	0.23368
0.9459782	1.3378152	6.6890762	3.7839129	0.25	0.2	2	0.26924
0.9459782	1.3378152	6.6890762	3.1532608	0.3	0.2	2	0.29972
0.8223512	**1.4243541**	**7.1217707**	**5.4823416**	0.15	0.2	3	0.20828
0.8223512	**1.4243541**	**7.1217707**	**4.1117562**	0.2	0.2	3	0.27178
0.8223512	**1.4243541**	**7.1217707**	**3.289405**	0.25	0.2	3	0.3175
0.8223512	**1.4243541**	**7.1217707**	**2.7411708**	0.3	0.2	3	0.36068
0.7407407	1.4814815	7.4074074	4.9382716	0.15	0.2	4	0.225298
0.7407407	1.4814815	7.4074074	3.7037037	0.2	0.2	4	0.29464
0.7407407	1.4814815	7.4074074	2.962963	0.25	0.2	4	0.34798
0.7407407	1.4814815	7.4074074	2.4691358	0.3	0.2	4	0.40386
1.1906208	**1.4582068**	**5.8328271**	**7.9374723**	0.15	0.25	1.5	0.4318
1.1906208	**1.4582068**	**5.8328271**	**5.9531042**	0.2	0.25	1.5	0.5334
1.1906208	**1.4582068**	**5.8328271**	**4.7624834**	0.25	0.25	1.5	0.59182
1.1906208	**1.4582068**	**5.8328271**	**3.9687361**	0.3	0.25	1.5	6.35

1.0920781	**1.5444317**	**6.1777266**	**7.2805207**	0.15	0.25	2	0.28448
1.0920781	1.54443166	6.17772665	5.46039051	0.2	0.25	2	0.36322
1.0920781	1.54443166	6.17772665	4.3683124	0.25	0.25	2	0.4191
1.0920781	1.54443166	6.17772665	3.64026034	0.3	0.25	2	2.02184
0.958938	**1.6609293**	**6.6437171**	**6.3929198**	0.15	0.25	3	0.20828
0.958938	**1.6609293**	**6.6437171**	**4.7946898**	0.2	0.25	3	0.27432
0.958938	**1.6609293**	**6.6437171**	**3.8357519**	0.25	0.25	3	0.32512
0.958938	**1.6609293**	**6.6437171**	**3.1964599**	0.3	0.25	3	0.3683
0.86956522	1.73913043	6.95652174	5.79710145	0.15	0.25	4	0.231648
0.86956522	1.73913043	6.95652174	4.34782609	0.2	0.25	4	0.29972
0.86956522	1.73913043	6.95652174	3.47826087	0.25	0.25	4	0.3556
0.86956522	1.73913043	6.95652174	2.89855072	0.3	0.25	4	0.40894
1.3188292	**1.6152293**	**5.3840977**	**8.7921948**	0.15	0.3	1.5	0.78232
1.3188292	**1.6152293**	**5.3840977**	**6.5941461**	0.2	0.3	1.5	2.667
1.3188292	**1.6152293**	**5.3840977**	**5.2753169**	0.25	0.3	1.5	4.9276
1.3188292	**1.6152293**	**5.3840977**	**4.3960974**	0.3	0.3	1.5	4.064
1.21742695	1.7217017	5.73900568	8.11617966	0.15	0.3	2	0.4064
1.21742695	1.7217017	5.73900568	6.08713475	0.2	0.3	2	0.51816
1.21742695	1.7217017	5.73900568	4.8697078	0.25	0.3	2	0.9144
1.21742695	1.7217017	5.73900568	4.05808983	0.3	0.3	2	71.12
1.0783412	**1.8677417**	**6.2258058**	**7.1889413**	0.15	0.3	3	0.28702
1.0783412	**1.8677417**	**6.2258058**	**5.391706**	0.2	0.3	3	0.32258
1.0783412	**1.8677417**	**6.2258058**	**4.3133648**	0.25	0.3	3	0.37084
1.0783412	**1.8677417**	**6.2258058**	**3.5944707**	0.3	0.3	3	0.45212
0.98360656	1.96721311	6.55737705	6.55737705	0.15	0.3	4	0.2794
0.98360656	1.96721311	6.55737705	4.91803279	0.2	0.3	4	0.3048
0.98360656	1.96721311	6.55737705	3.93442623	0.25	0.3	4	0.3556
0.98360656	1.96721311	6.55737705	3.27868852	0.3	0.3	4	0.41402

Hysteretic Curve, Max. Out-of-Plane Displacement, and Max. Equivalent Plastic Strain

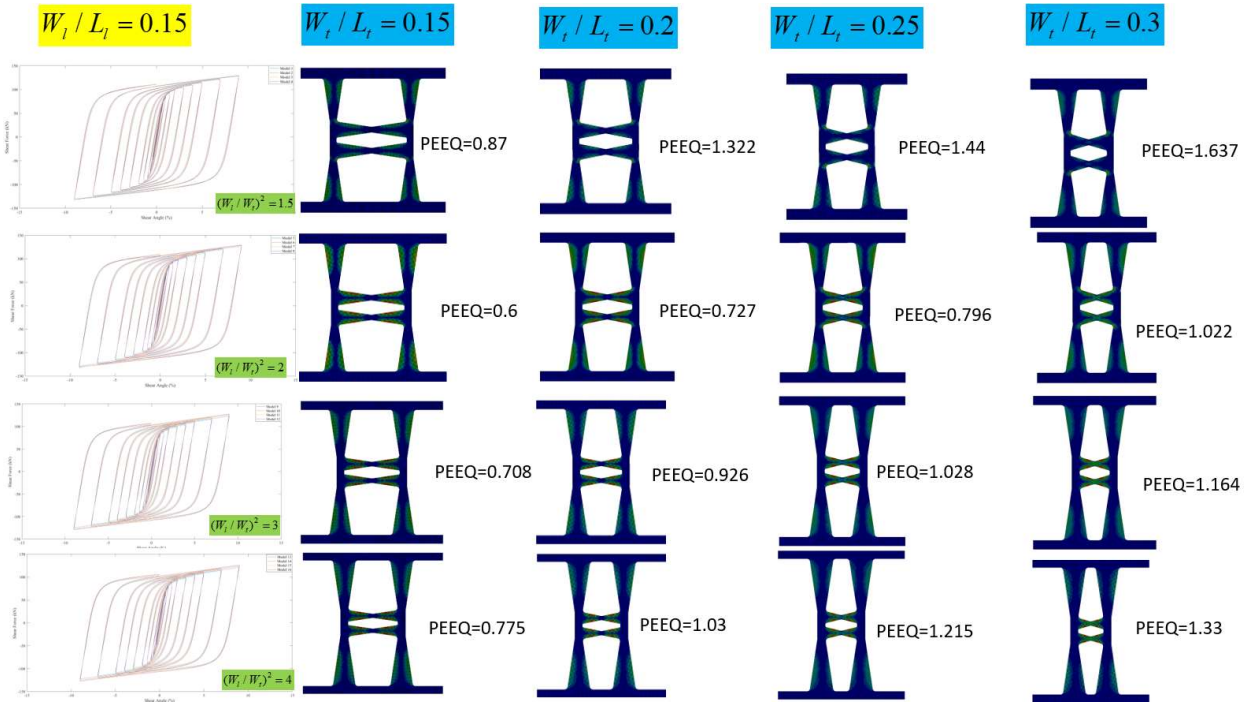

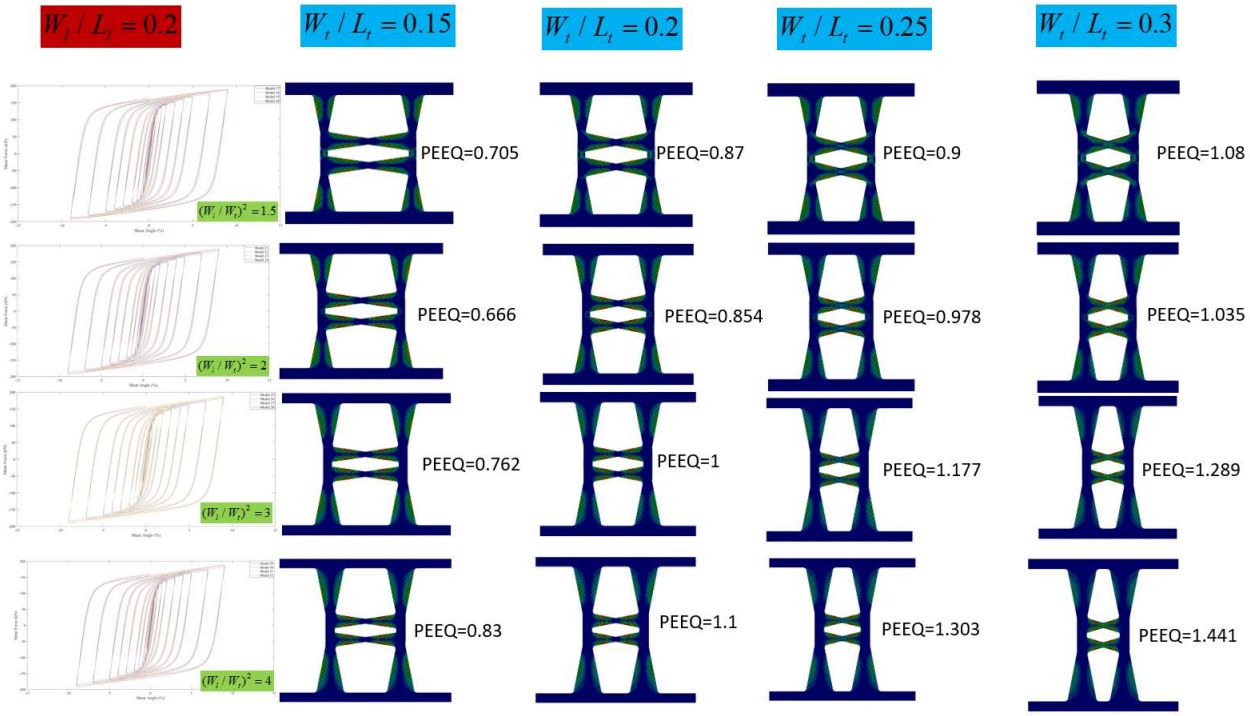

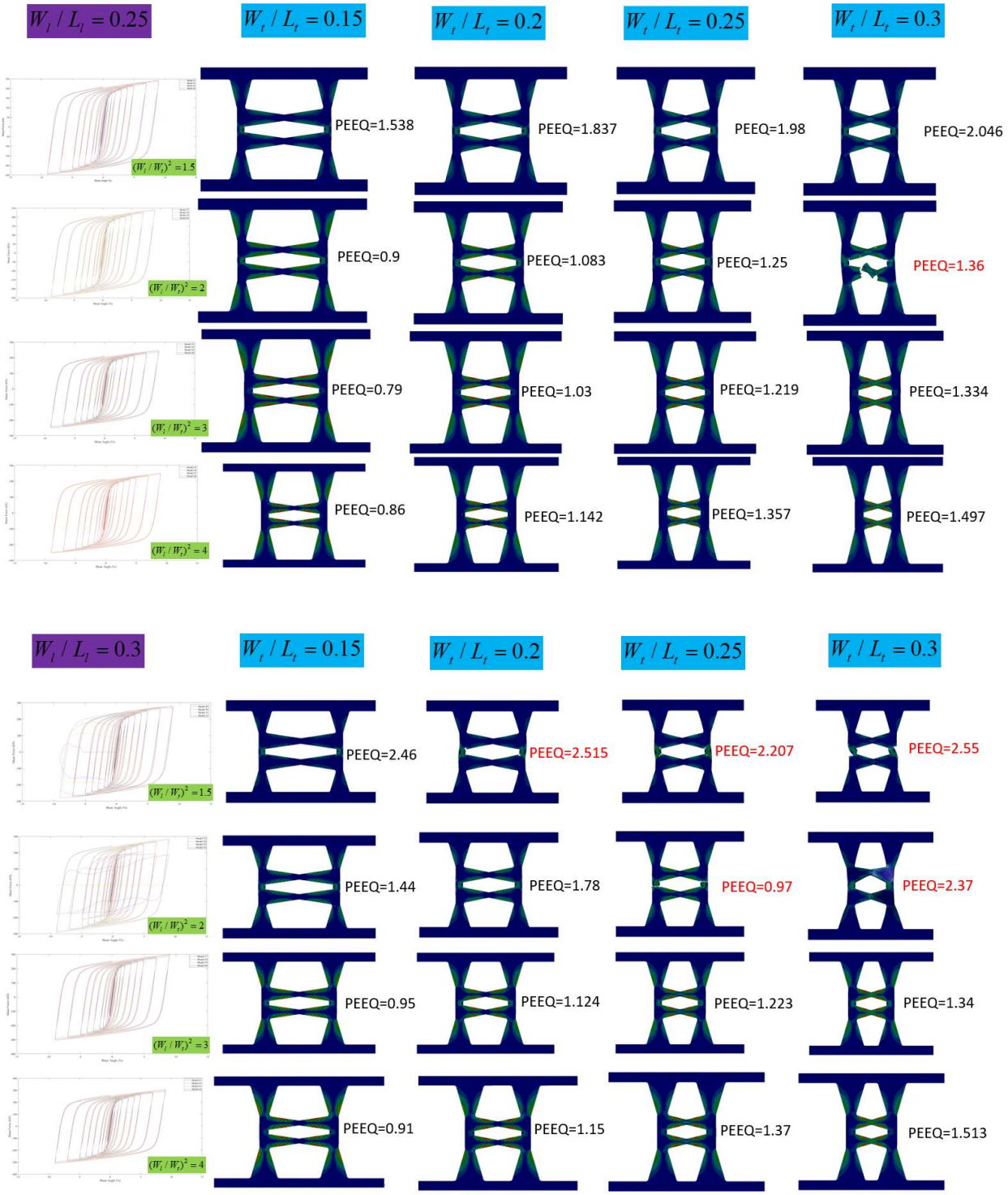
$W_l / L_l = 0.25$
$W_t / L_t = 0.15$
$W_t / L_t = 0.2$
$W_t / L_t = 0.25$
$W_t / L_t = 0.3$
$(W_l / W_t)^2 = 1.5$
$(W_l / W_t)^2 = 2$
$(W_l / W_t)^2 = 3$
$(W_l / W_t)^2 = 4$
PEEQ=1.538
PEEQ=1.837
PEEQ=1.98
PEEQ=2.046
PEEQ=0.9
PEEQ=1.083
PEEQ=1.25
PEEQ=1.36
PEEQ=0.79
PEEQ=1.03
PEEQ=1.219
PEEQ=1.334
PEEQ=0.86
PEEQ=1.142
PEEQ=1.357
PEEQ=1.497
$W_l / L_l = 0.3$
$W_t / L_t = 0.15$
$W_t / L_t = 0.2$
$W_t / L_t = 0.25$
$W_t / L_t = 0.3$
$(W_l / W_t)^2 = 1.5$
$(W_l / W_t)^2 = 2$
$(W_l / W_t)^2 = 3$
$(W_l / W_t)^2 = 4$
PEEQ=2.46
PEEQ=2.515
PEEQ=2.207
PEEQ=2.55
PEEQ=1.44
PEEQ=1.78
PEEQ=0.97
PEEQ=2.37
PEEQ=0.95
PEEQ=1.124
PEEQ=1.223
PEEQ=1.34
PEEQ=0.91
PEEQ=1.15
PEEQ=1.37
PEEQ=1.513

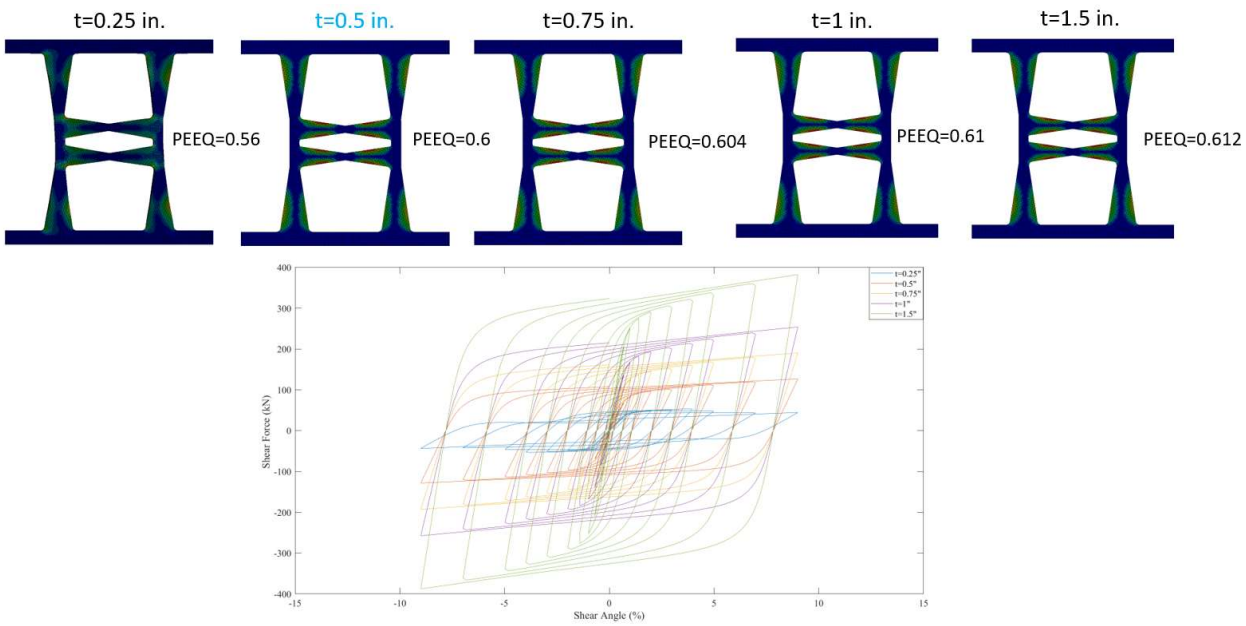

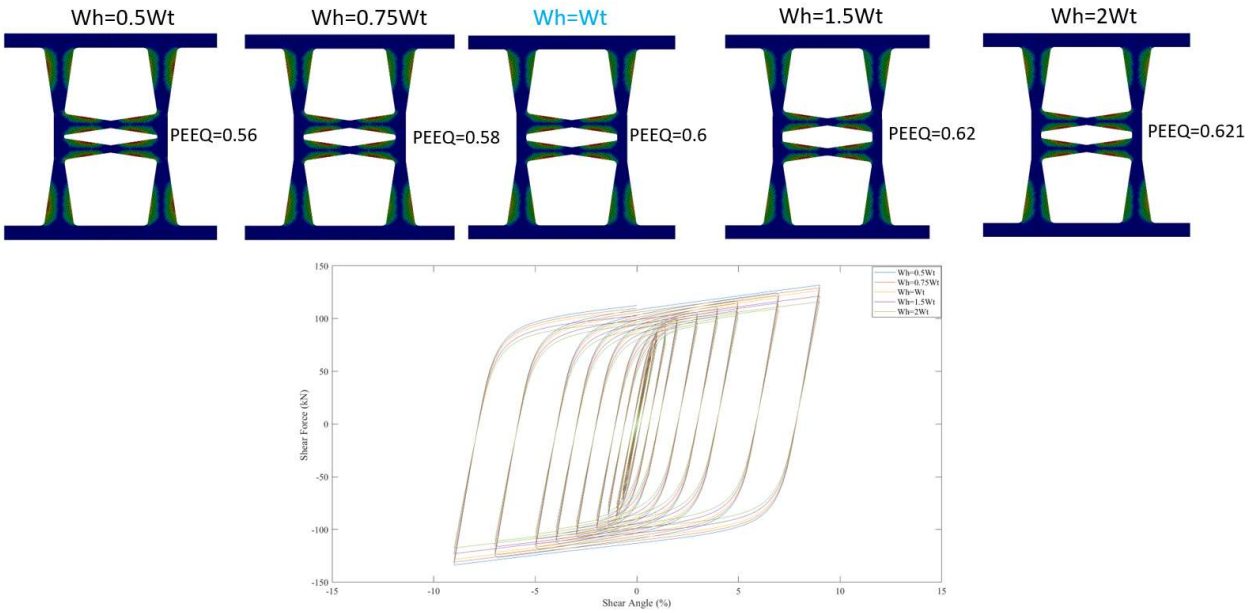

Note: *x*-axis is Shear angle (%) and *y*-axis is Shear force (kN)

Fig. C15. Hysteretic Curve and Max. Equivalent Plastic Strain

Discussion about Buckling

One non-dimensional parameter, k_{dz}, shown in Eq. (C2), is expected to control the buckling resistance of the TBF shape. This equation implies that buckling resistance of the TBF shape is a function of tie slenderness and leg slenderness. Fig. C16 represents the effect of k_{dz} on the buckling resistance of the TBF shape. This plot suggests that the TBF shape is relatively good in controlling buckling as the maximum out-of-plane of approximately 90% of the FE models ranges from 3mm to 5mm. The remaining FE models having stocky ties and legs resulted in substantial buckling.

$$k_{dz} = \frac{W_T}{L_T}\left(\frac{W_L}{L_L + 1.5W_T}\right) \qquad \text{(C2)}$$

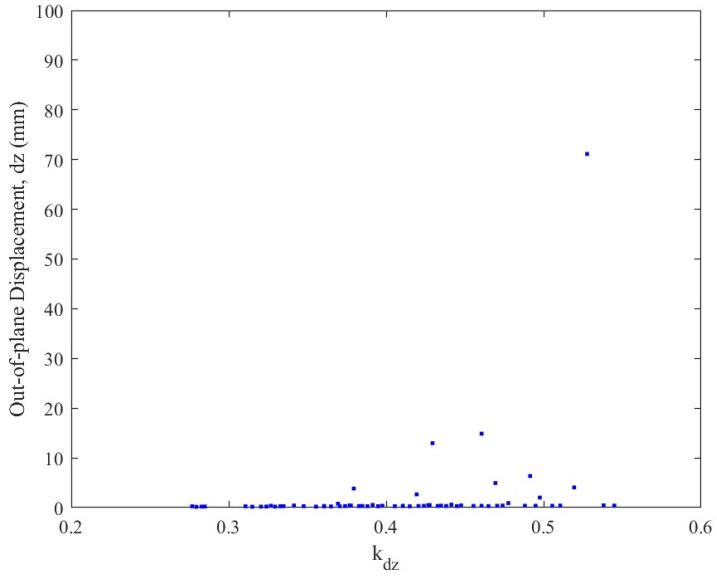

Fig. C16. The effect of k_{dz} on buckling

Discussion about Fracture

One non-dimensional parameter, k_{PL}, as shown in Eq. (C3) is likely to control the equivalent plastic strain of the TBF shape. This equation suggests that worst equivalent plastic strain of the TBF shape is dependent upon the tie slenderness and leg slenderness. Fig. C17 illustrates the effect of k_{PL} on the effective plastic strain of the TBF shape. Overall, this plot reveals that approximately 85% of the FE models have the worst equivalent plastic strain ranging from 0.5 to 1.5. The remaining models have stockier ties and legs led to large effective plastic strain.

$$k_{PL} = \frac{W_T}{L_T}\left(\frac{W_L}{L_L + 1.5W_T}\right) \qquad \text{(C3)}$$

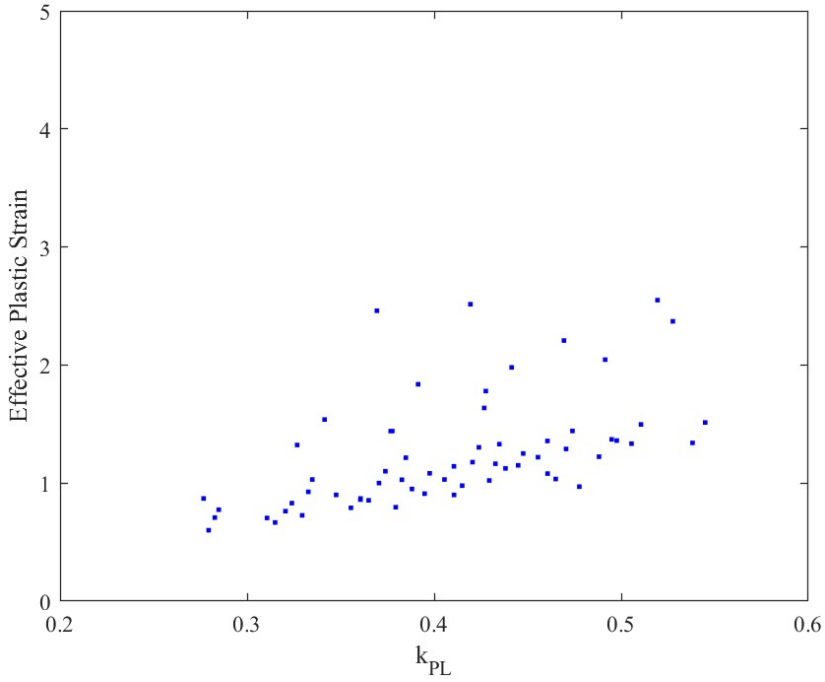

Fig. C17. The effect of k_{PL} on fracture

APPENDIX D

DETAILS ABOUT STUDY ON THE BUTTERFLY SHAPE

This appendix provides additional information about the computational and experimental study on the Butterfly Shape, presented in Chapter 5.

D1. EXPERIMENTAL RAW DATA

This section provides experimental raw data obtained from the tests of Specimen BF1, Specimen BF2, Specimen BF3, Specimen BF4, Specimen BF5, Specimen BF6, Specimen BF7, Specimen BF8, respectively.

Specimen BF1

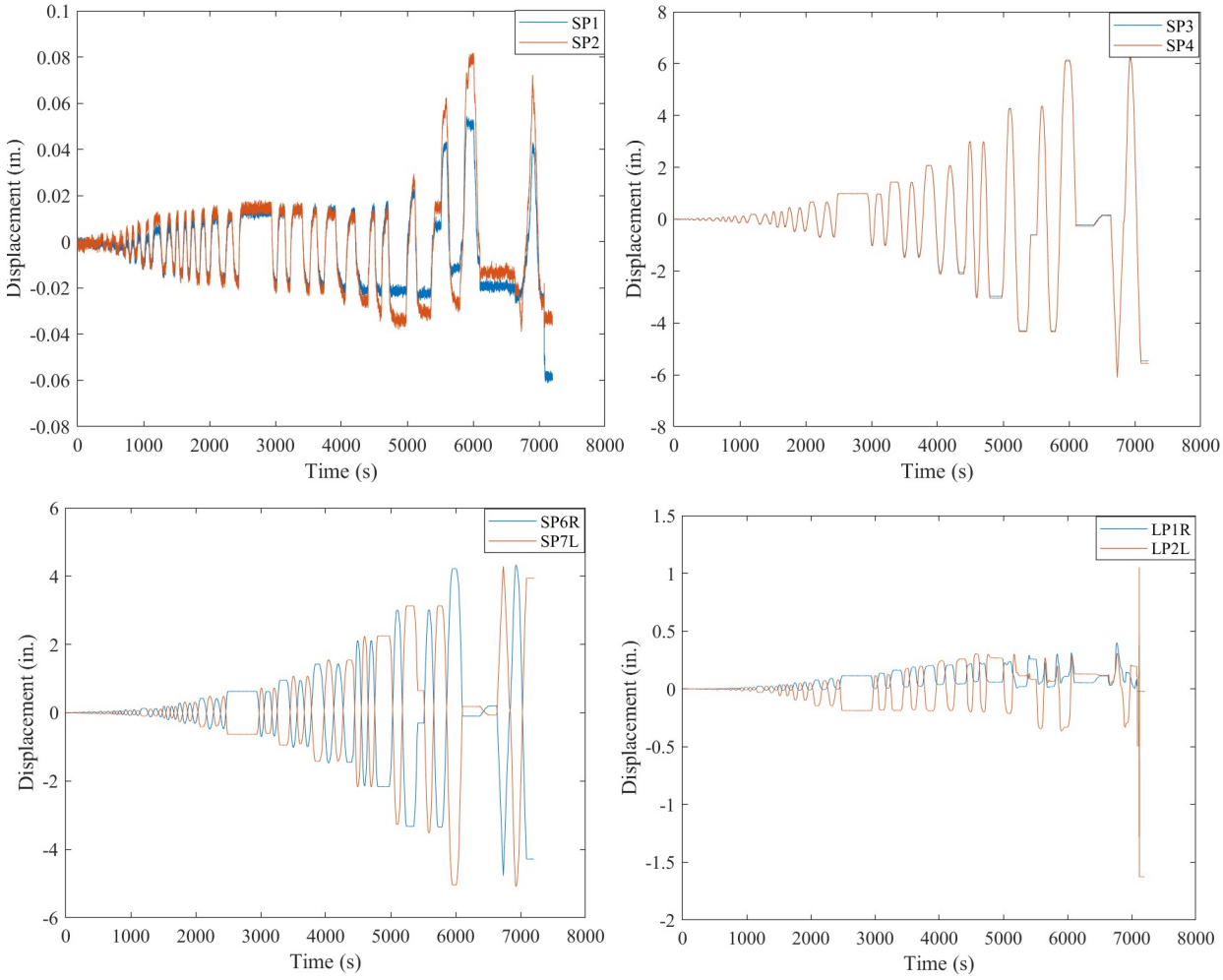

Fig. D1. Raw Displacement Measurements of Specimen BF1

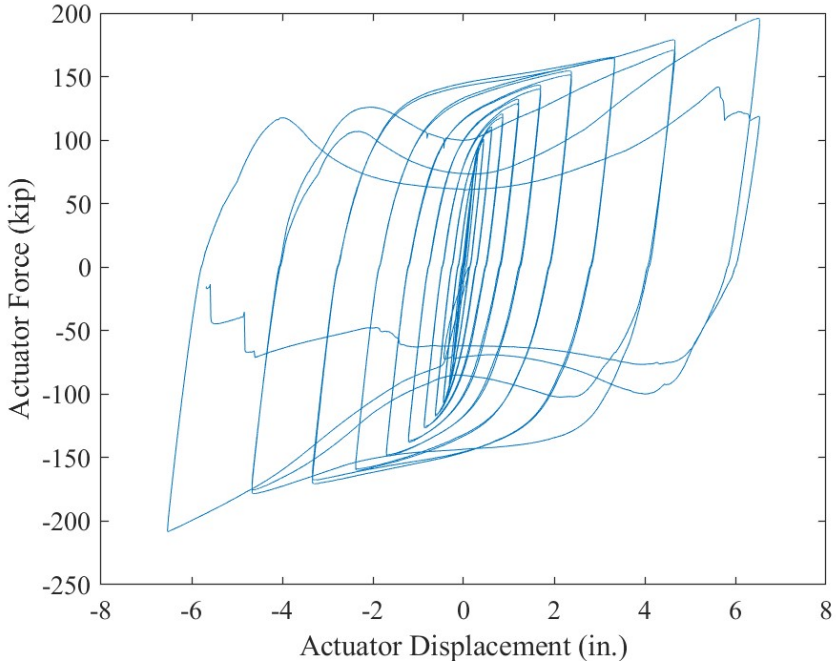

Fig. D2. Actuator Force vs. Actuator Displacement of Specimen BF1

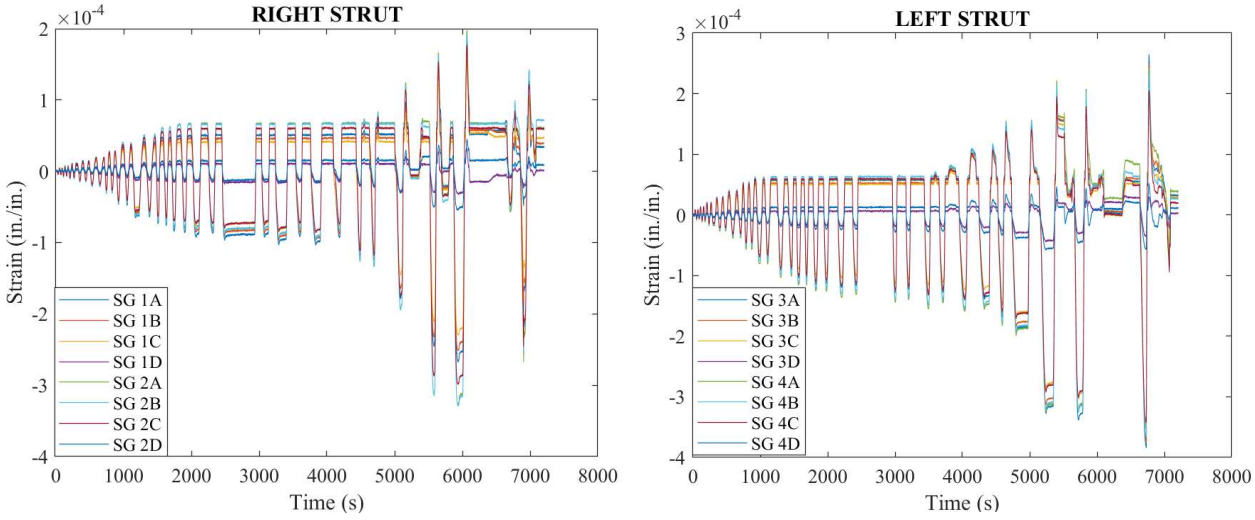

Fig. D3. Raw Strain Gage measurements of Specimen BF1

Specimen BF2

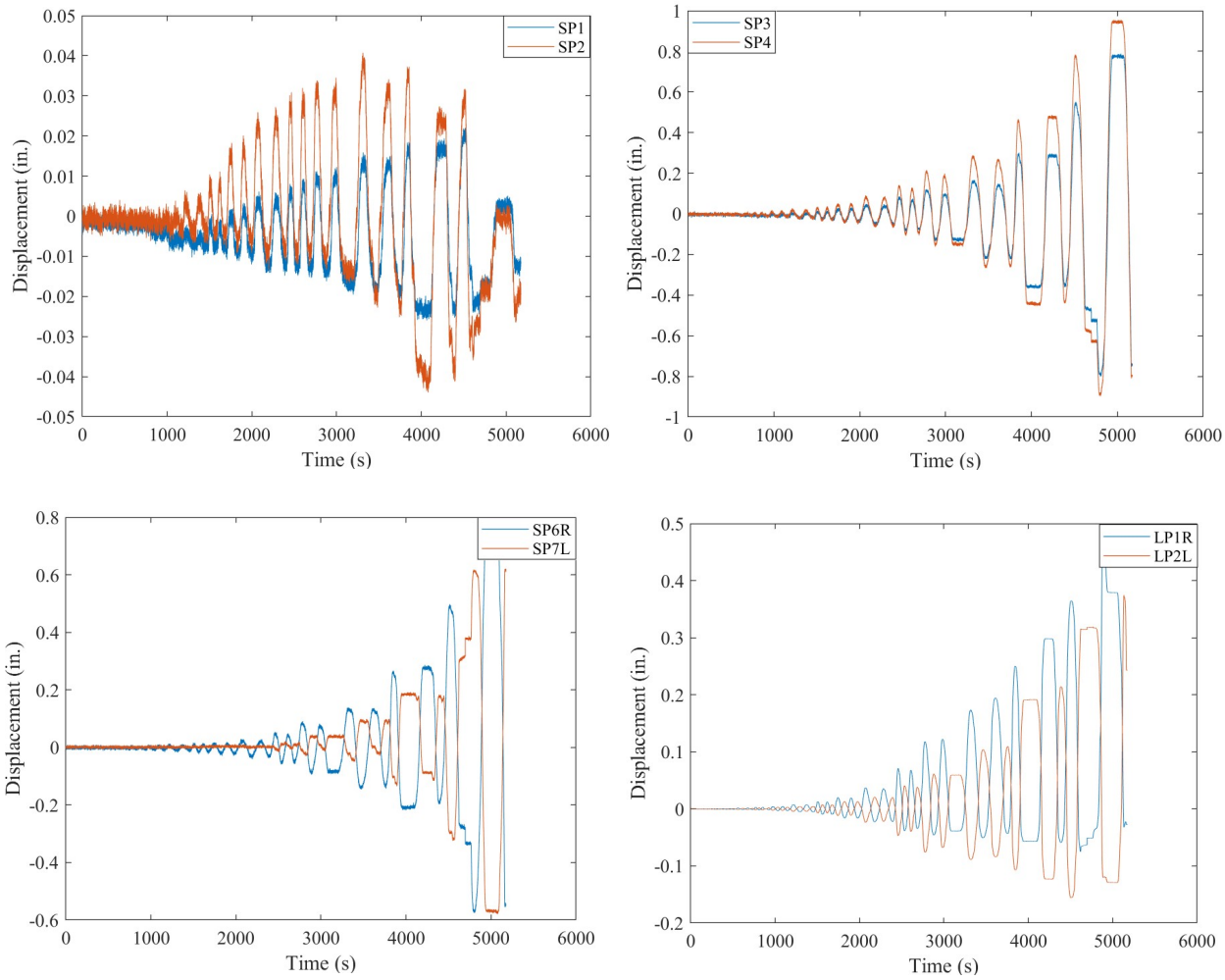

Fig. D4. Raw Displacement Measurements of Specimen BF2

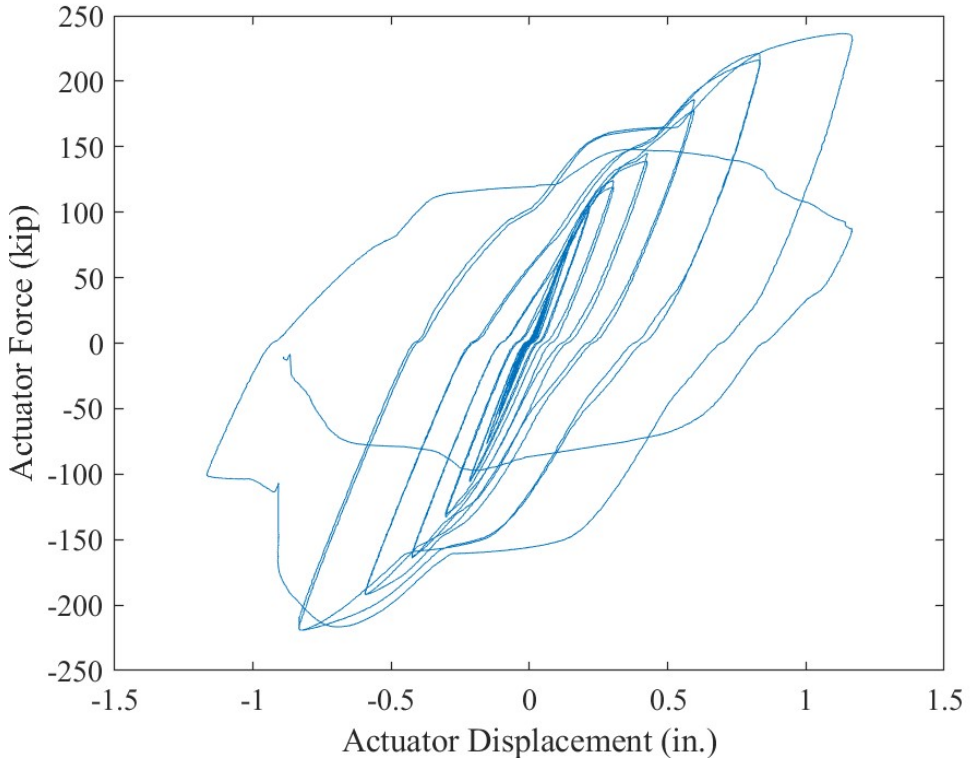

Fig. D5. Actuator Force vs. Actuator Displacement of Specimen BF2

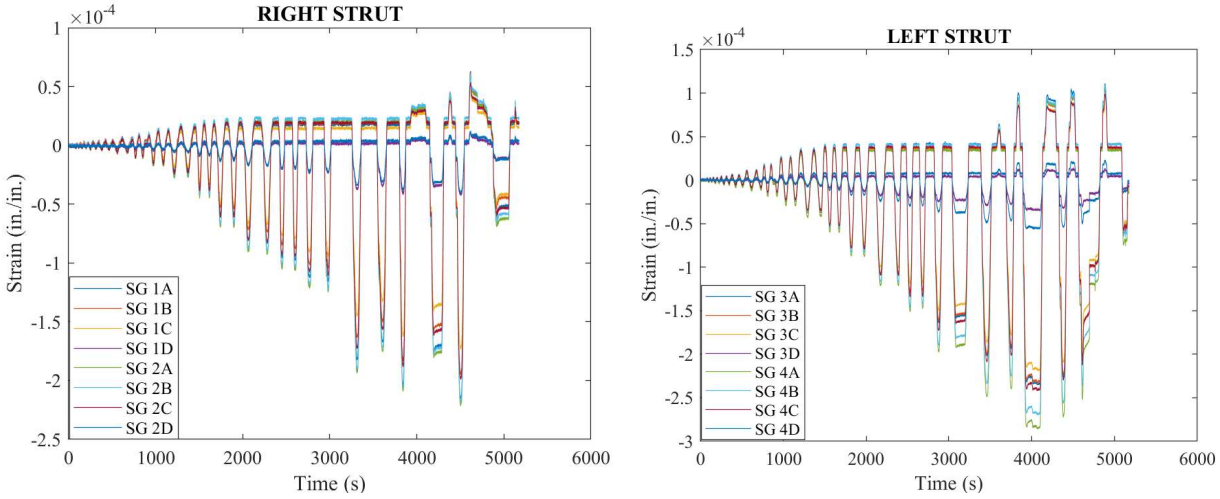

Fig. D6. Raw Strain Gage measurements of Specimen BF2

Specimen BF3

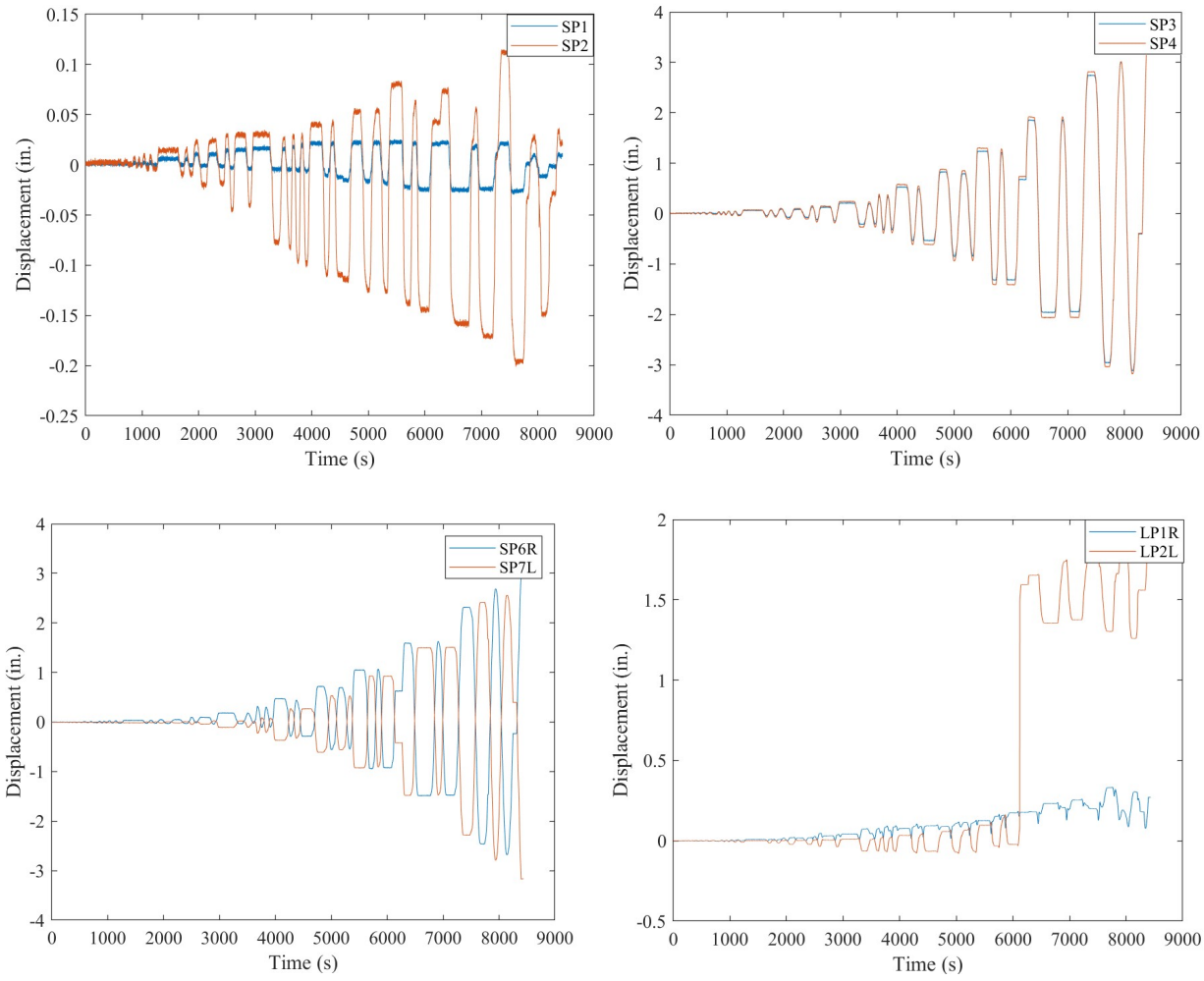

Fig. D7. Raw Displacement Measurements of Specimen BF3

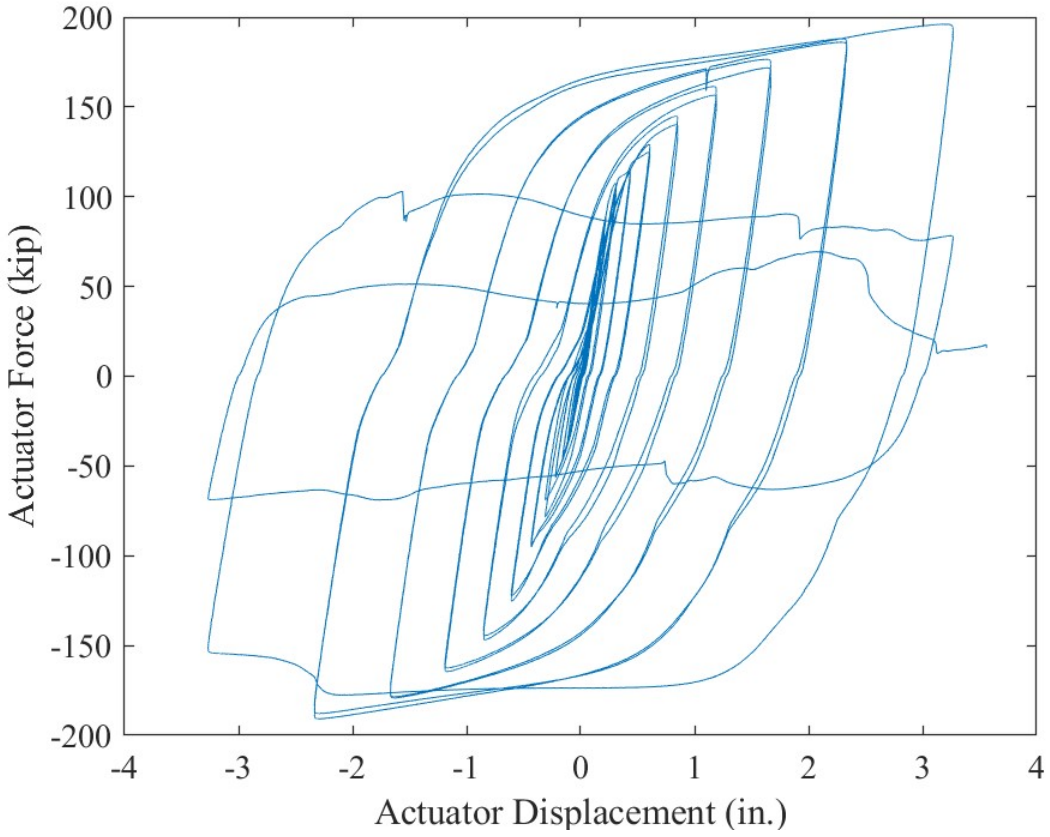

Fig. D8. Actuator Force vs. Actuator Displacement of Specimen BF3

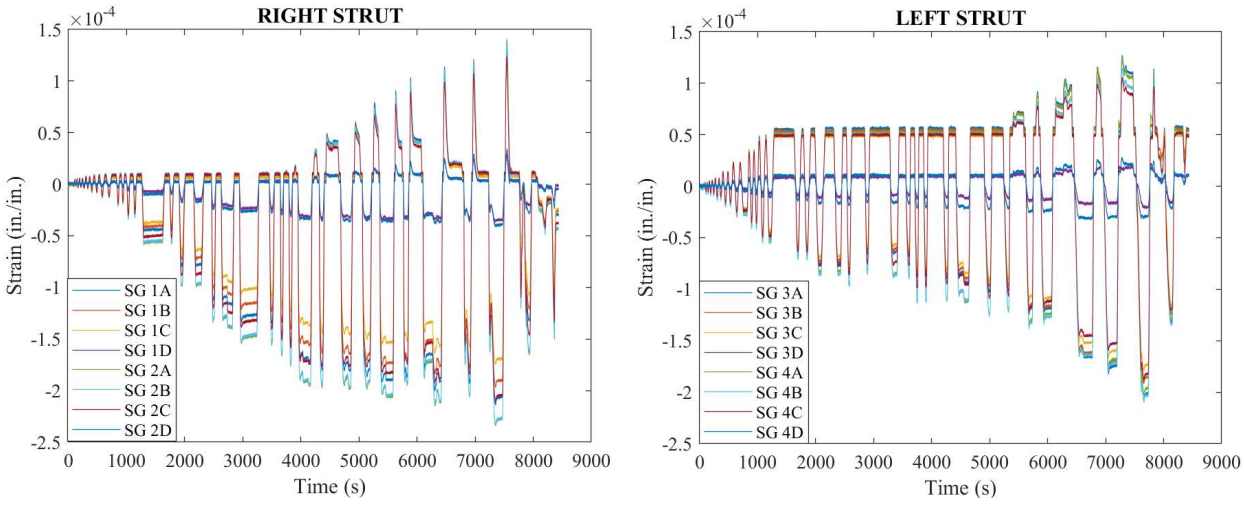

Fig. D9. Raw Strain Gage measurements of Specimen BF3

Specimen BF4

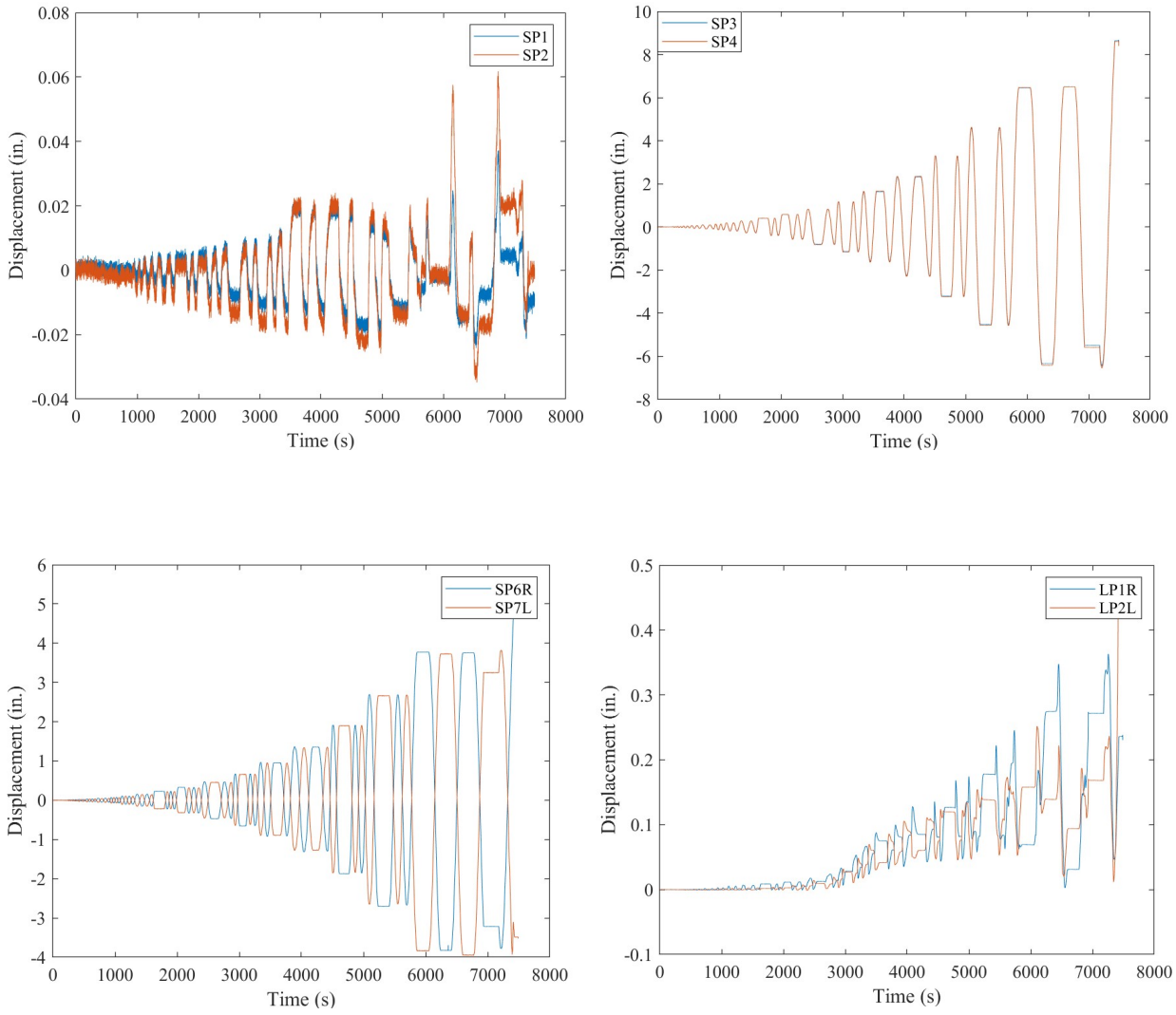

Fig. D10. Raw Displacement Measurements of Specimen BF4

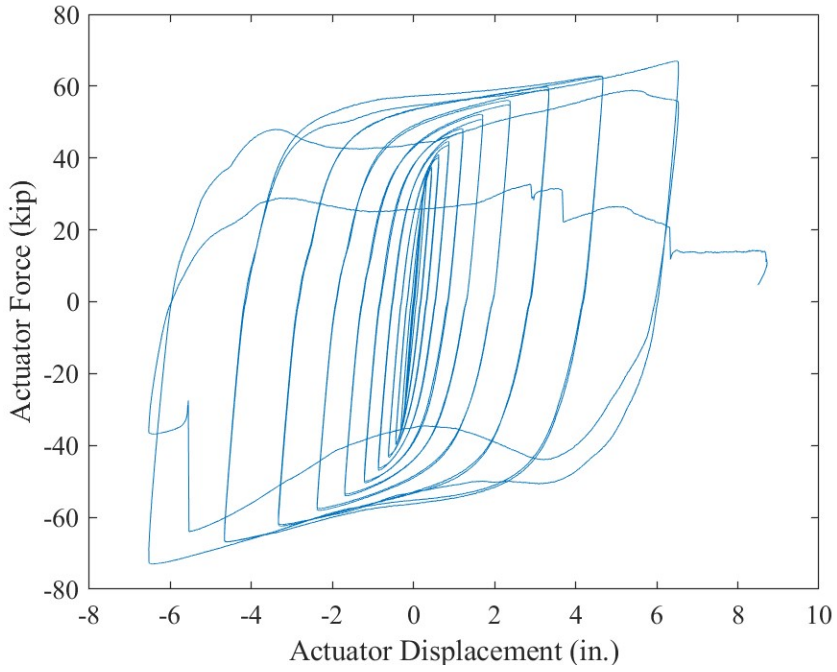

Fig. D11. Actuator Force vs. Actuator Displacement of Specimen BF4

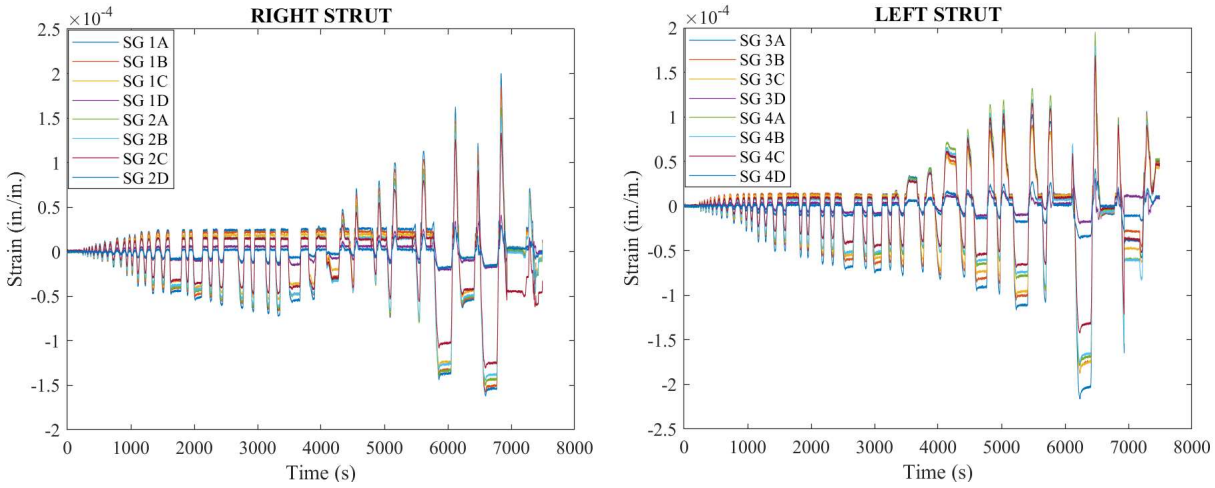

Fig. D12. Raw Strain Gage measurements of Specimen BF4

Specimen BF5

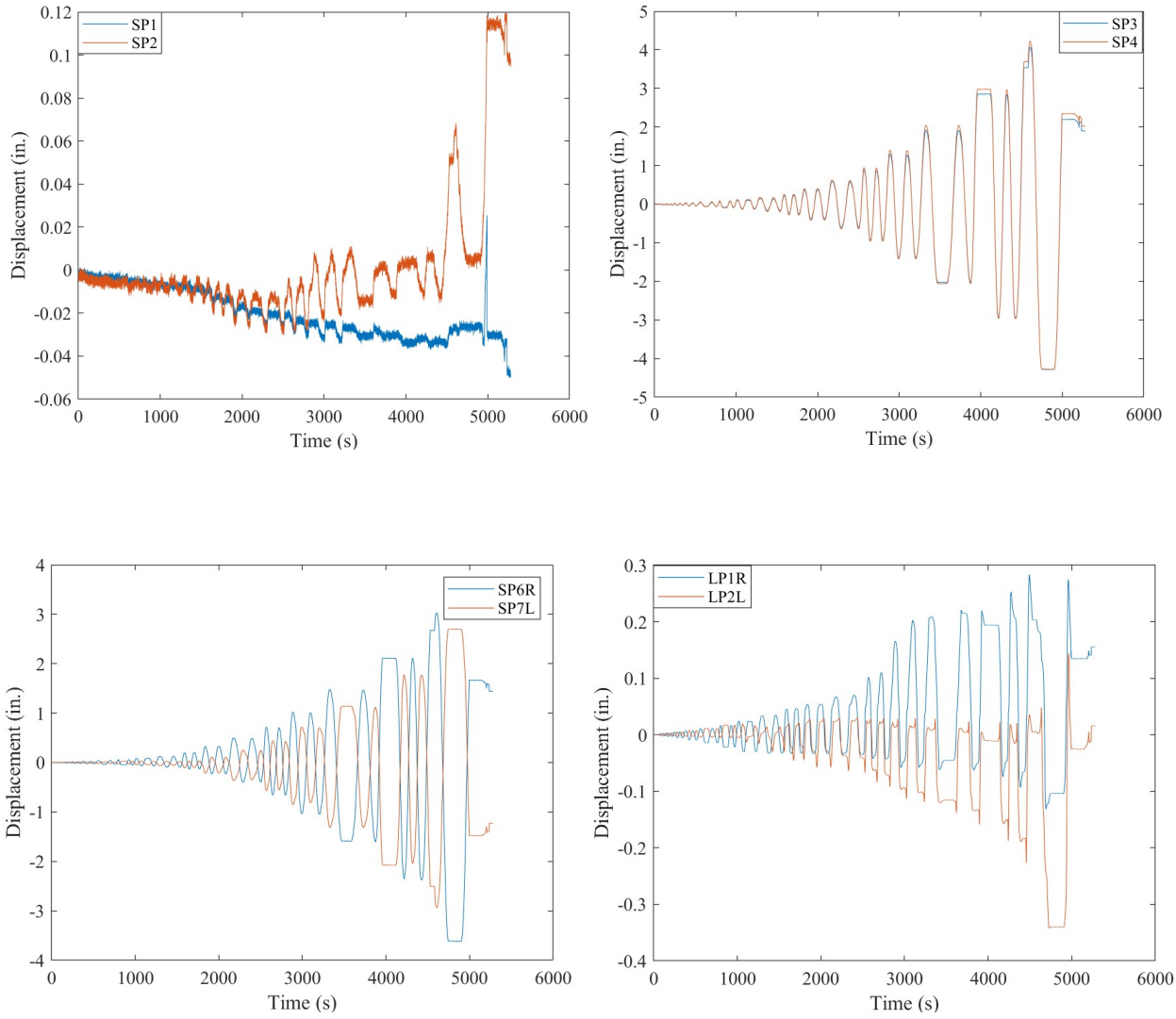

Fig. D13. Raw Displacement Measurements of Specimen BF5

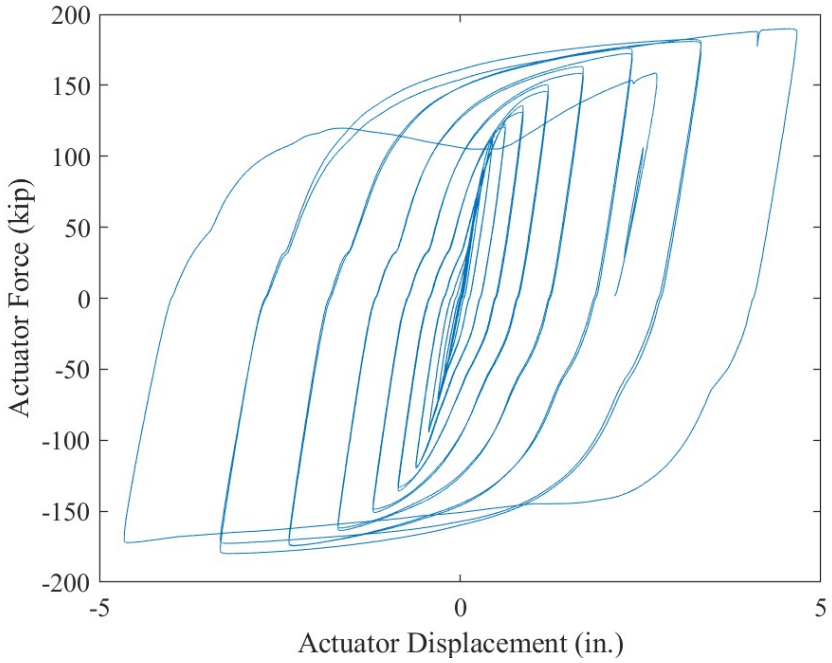

Fig. D14. Actuator Force vs. Actuator Displacement of Specimen BF5

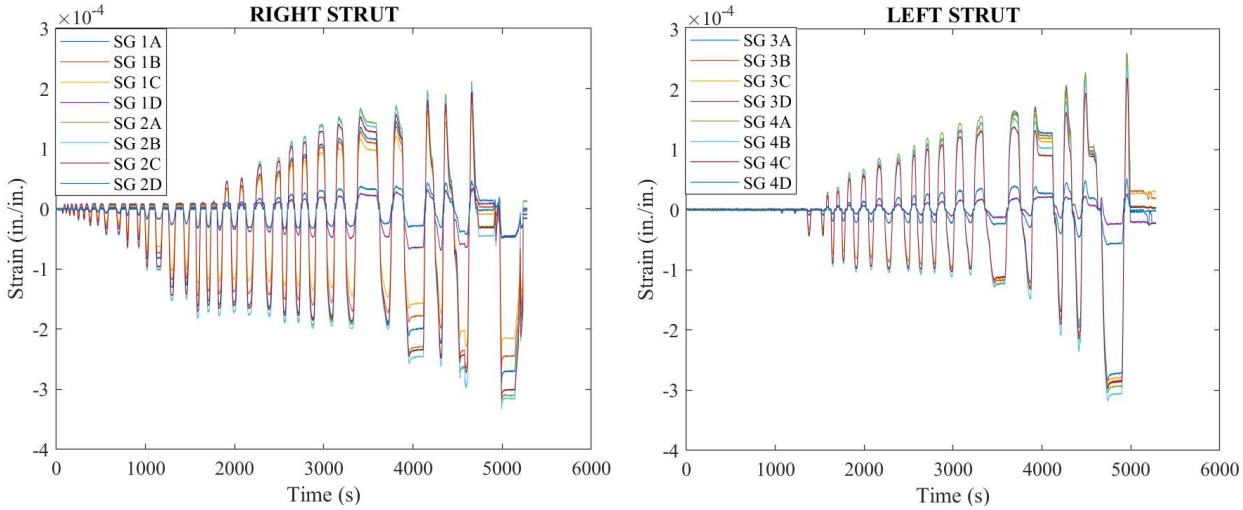

Fig. D15. Raw Strain Gage measurements of Specimen BF5

Specimen BF6

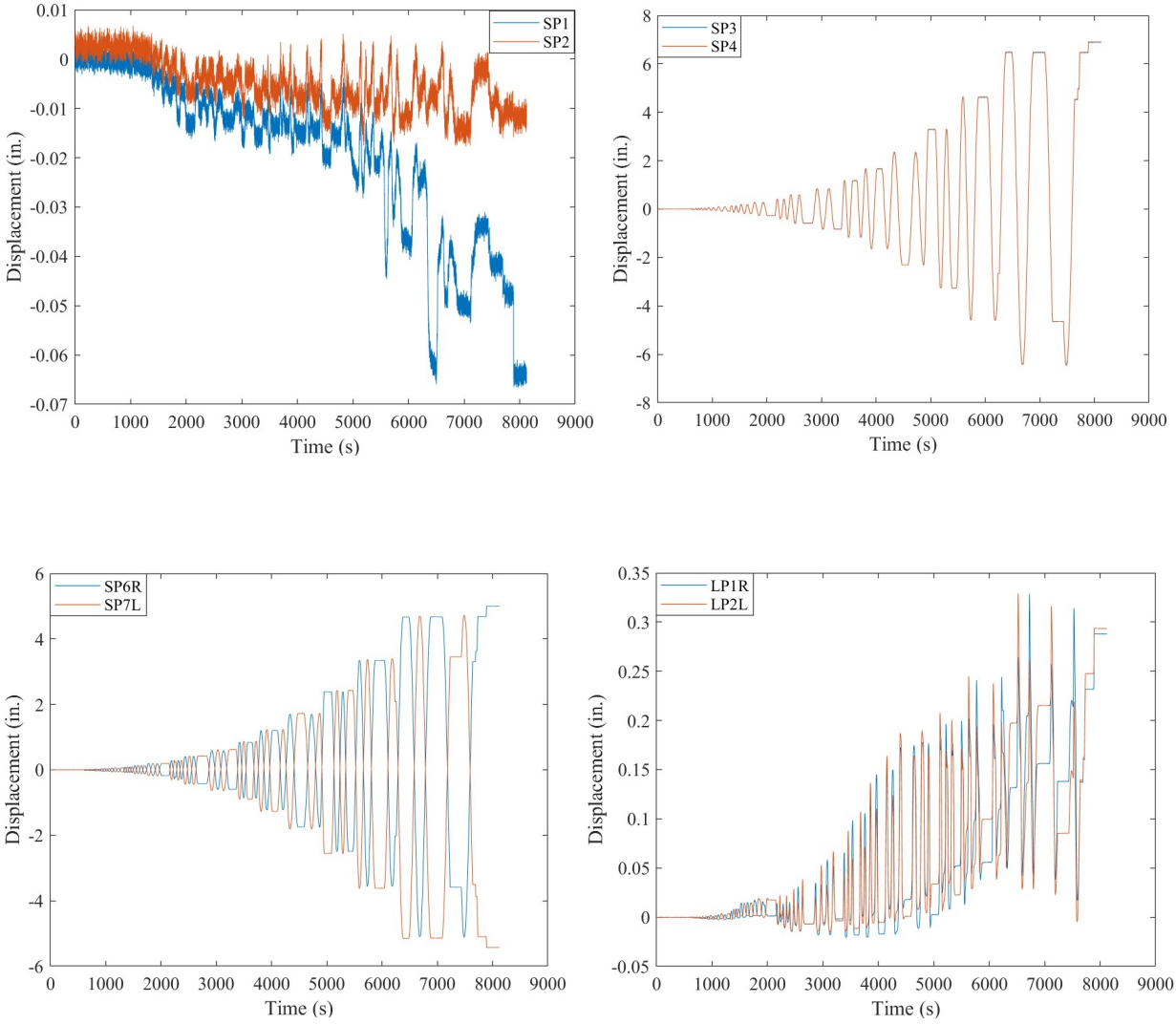

Fig. D16. Raw Displacement Measurements of Specimen BF6

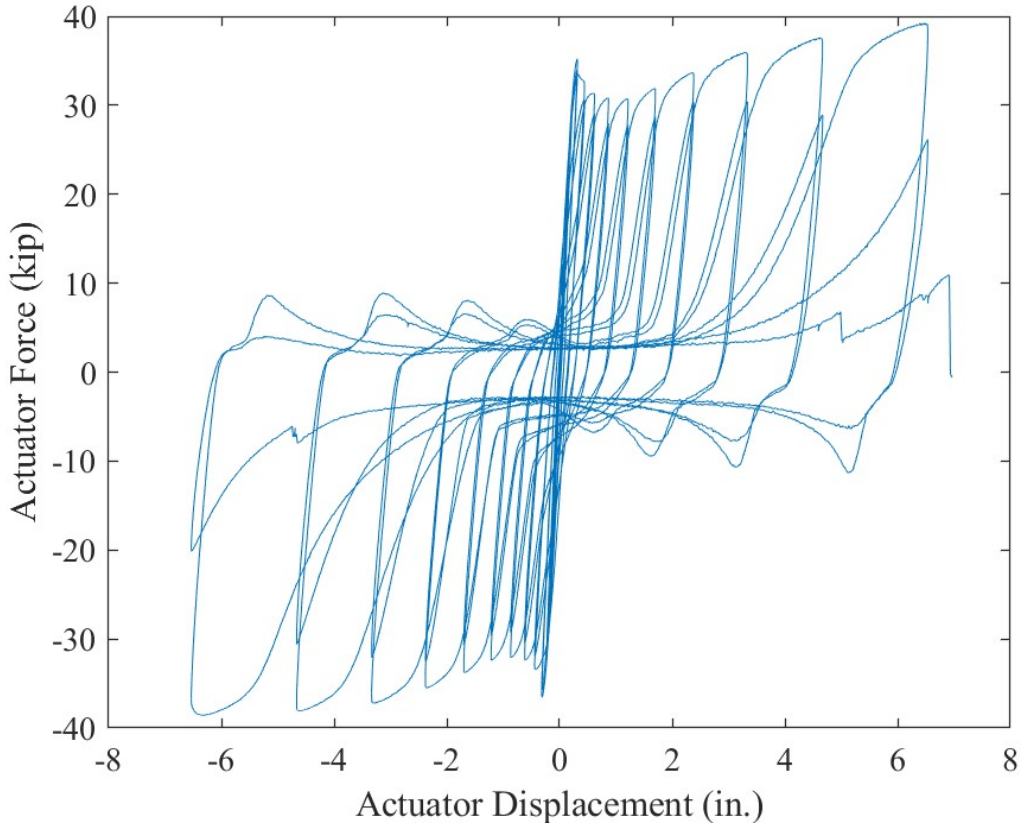

Fig. D17. Actuator Force vs. Actuator Displacement of Specimen BF6

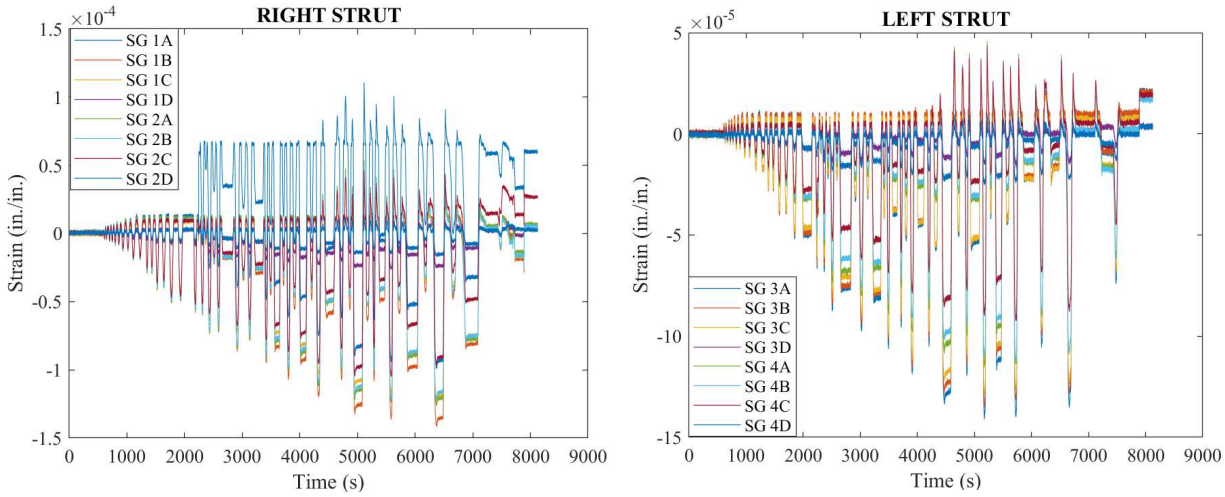

Fig. D18. Raw Strain Gage measurements of Specimen BF6

Specimen BF7

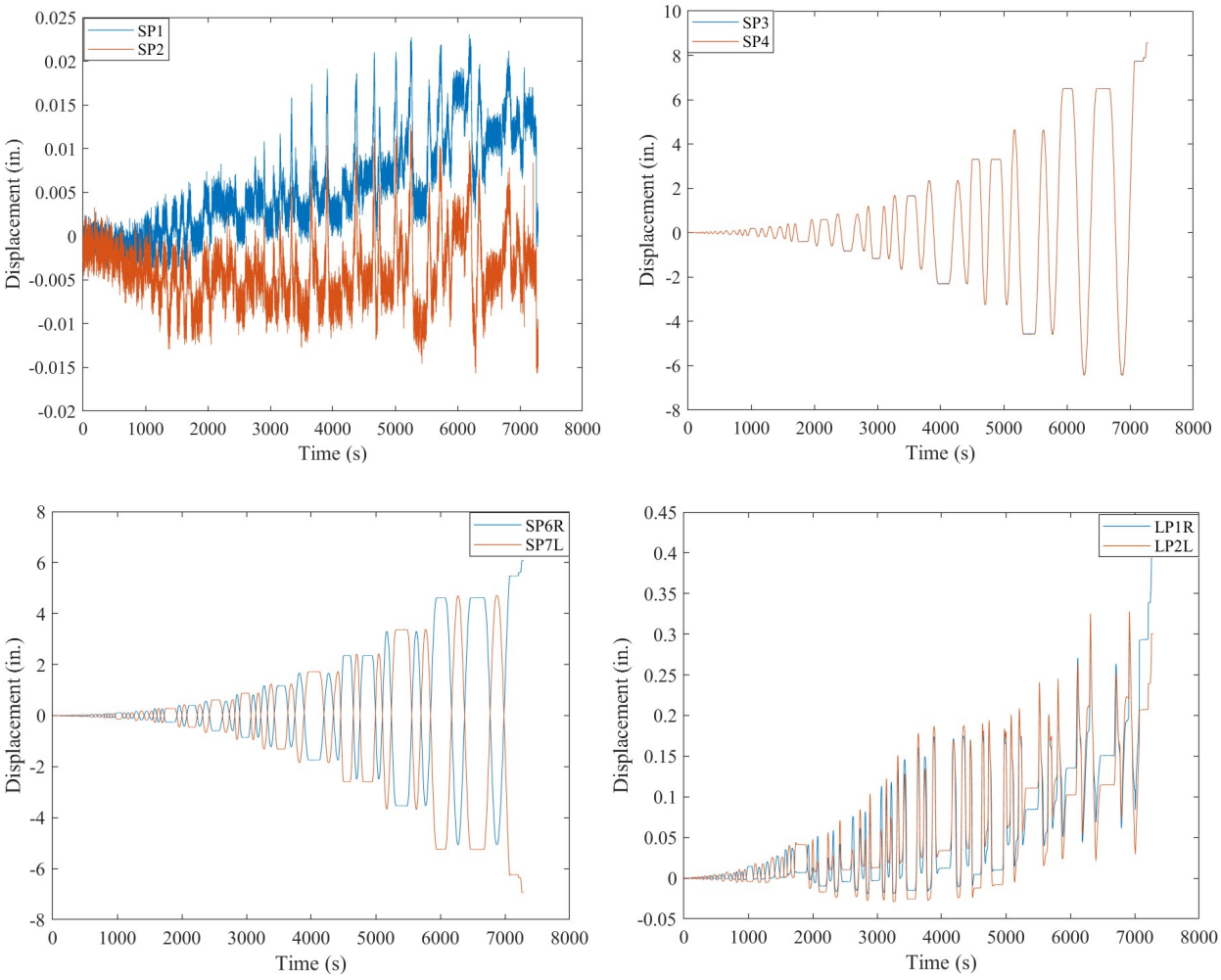

Fig. D19. Raw Displacement Measurements of Specimen BF7

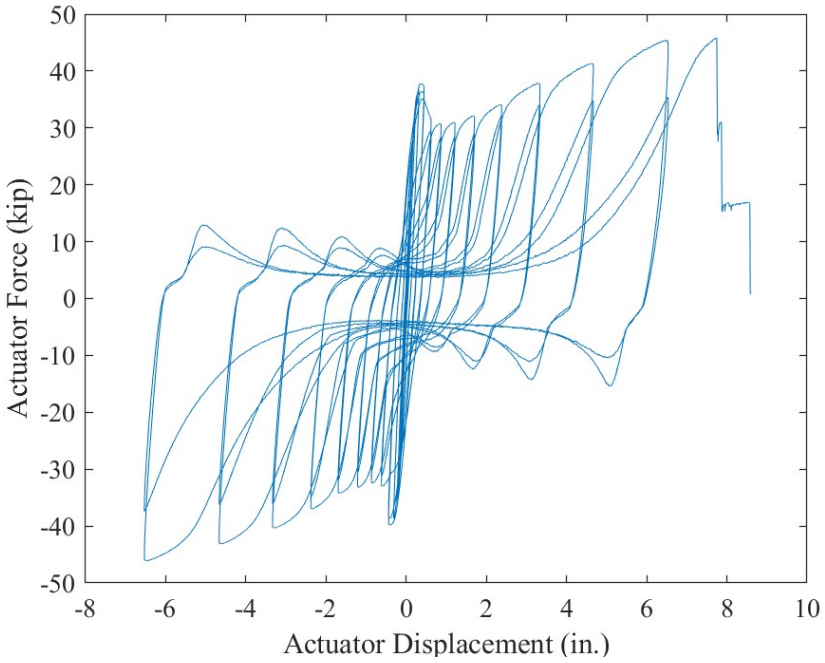

Fig. D20. Actuator Force vs. Actuator Displacement of Specimen BF7

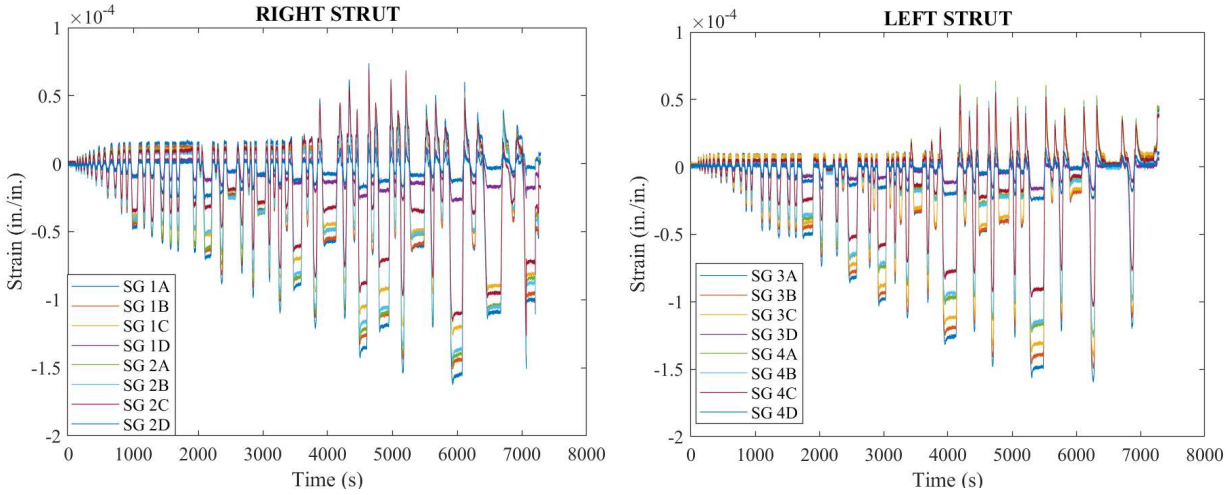

Fig. D21. Raw Strain Gage measurements of Specimen BF7

Specimen BF8

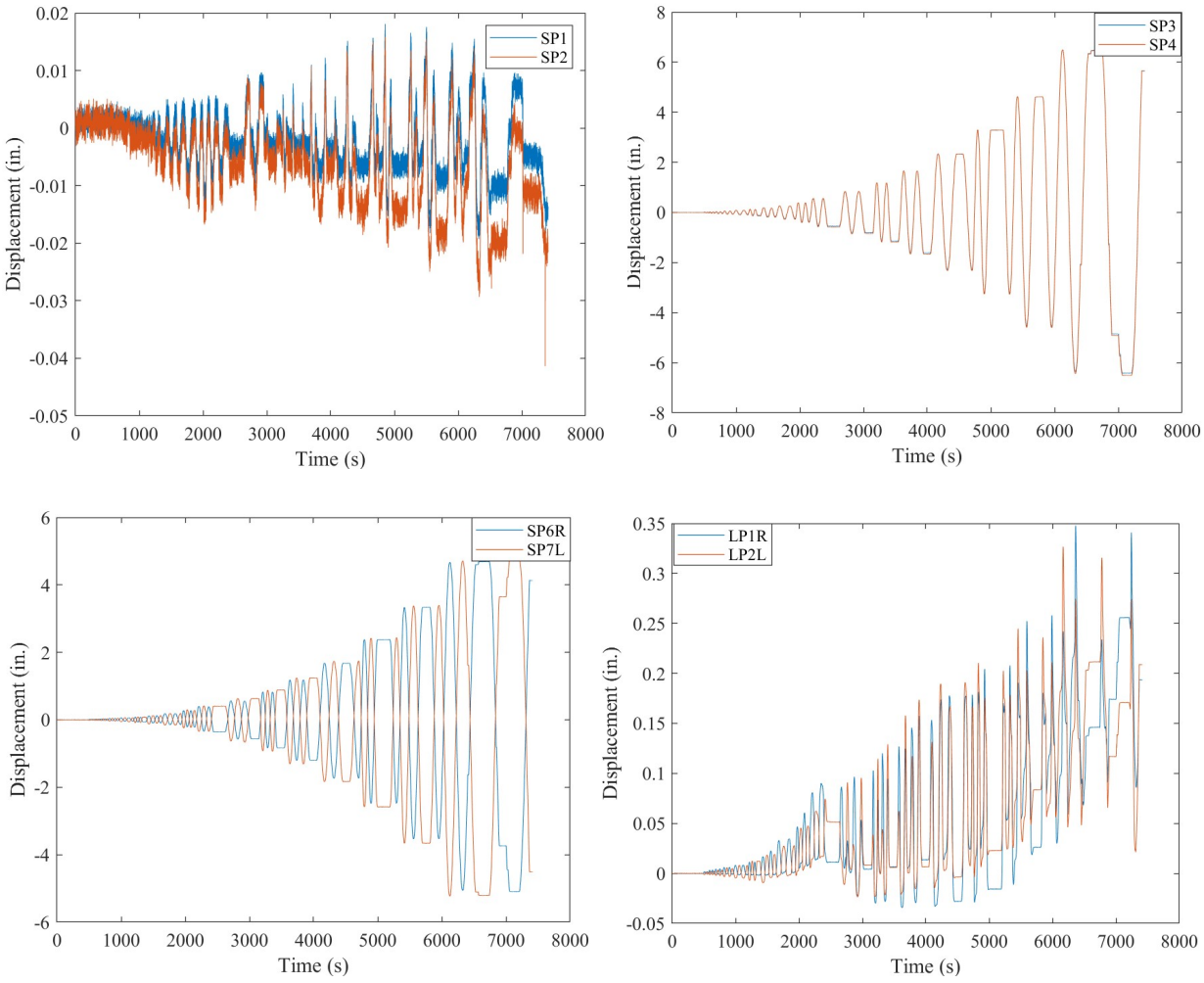

Fig. D22. Raw Displacement Measurements of Specimen BF8

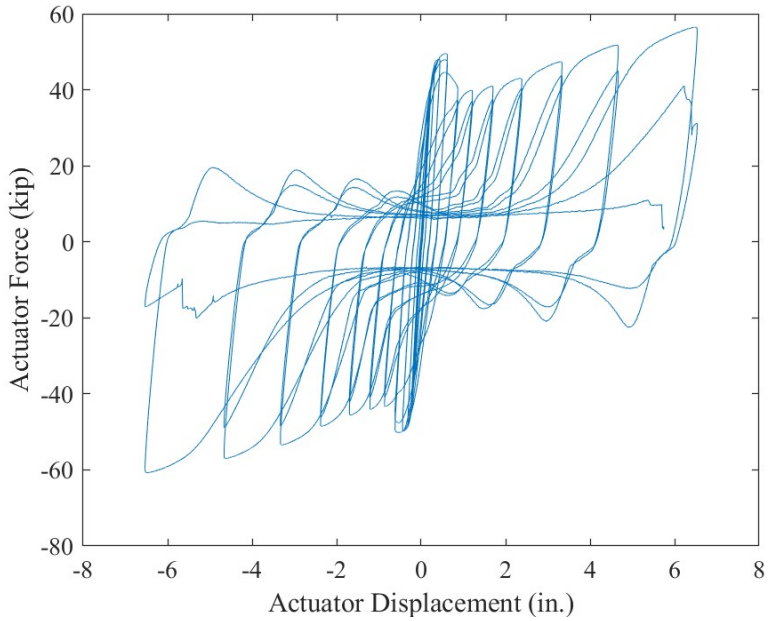

Fig. D23. Actuator Force vs. Actuator Displacement of Specimen BF8

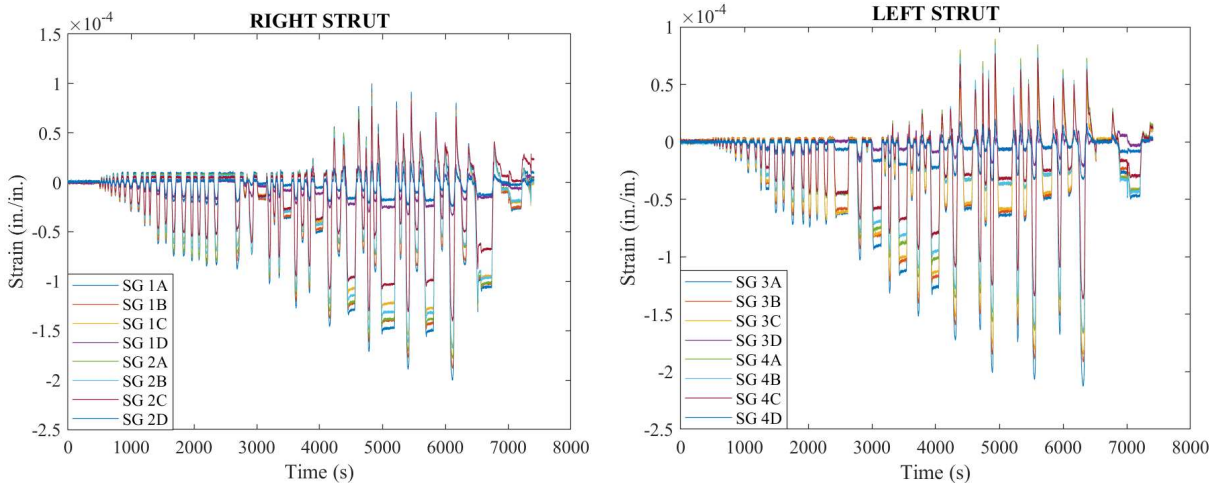

Fig. D24. Raw Strain Gage measurements of Specimen BF8

APPENDIX E

DETAILS ABOUT STUDY ON THE HOURGLASS SHAPED LINK AND ELLIPTICAL SHAPED HOLES

This appendix provides more information about the computational and experimental study on the Hourglass Shaped Link and Elliptical Shaped Holes, presented in Chapter 6.

E1. EXPERIMENTAL RAW DATA

This section provides experimental raw data obtained from the tests of Specimen HG1, Specimen HG2, Specimen HG3, Specimen EL1, Specimen EL2, Specimen EL3, respectively.

Specimen HG1

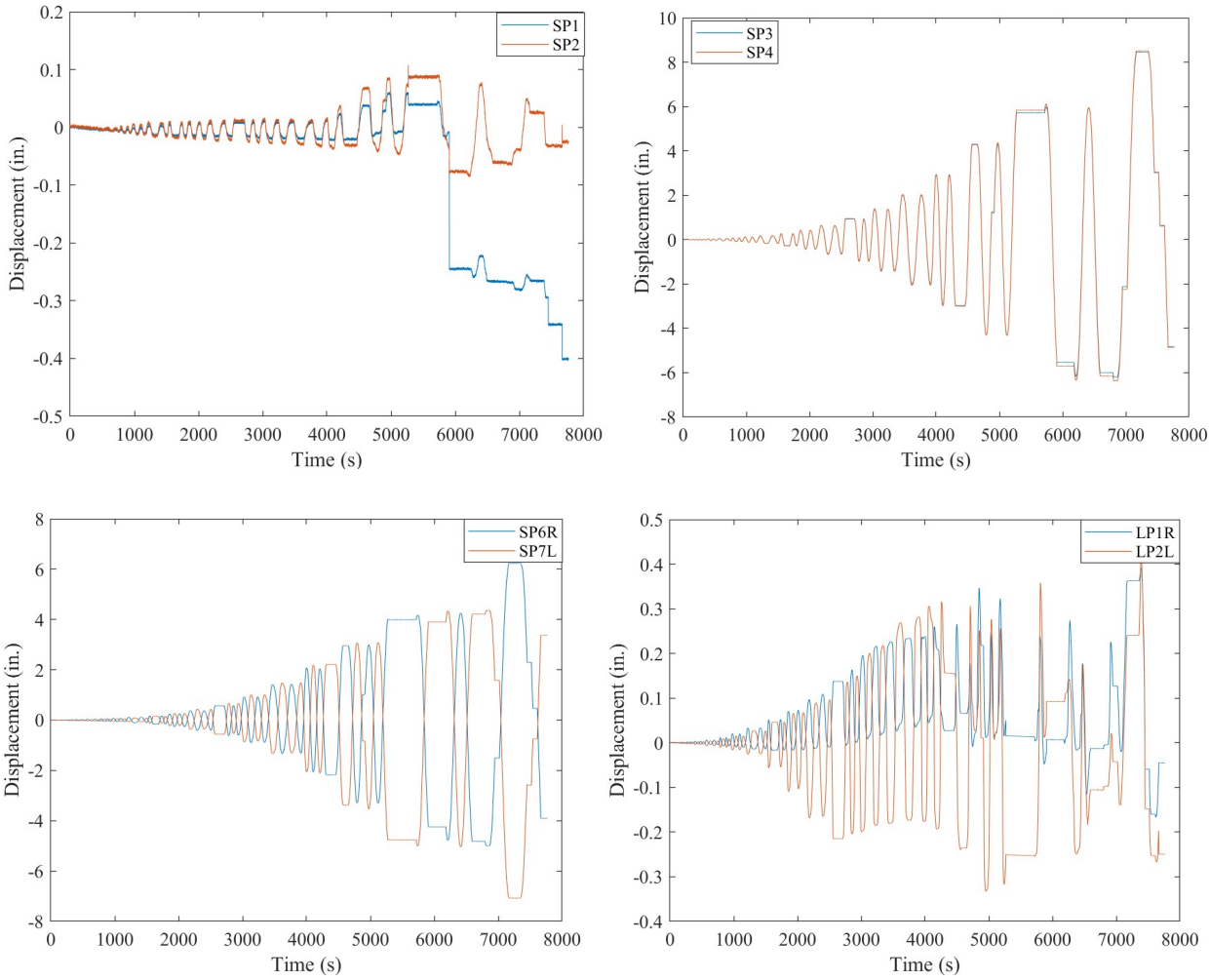

Fig. E1. Raw Displacement Measurements of Specimen HG1

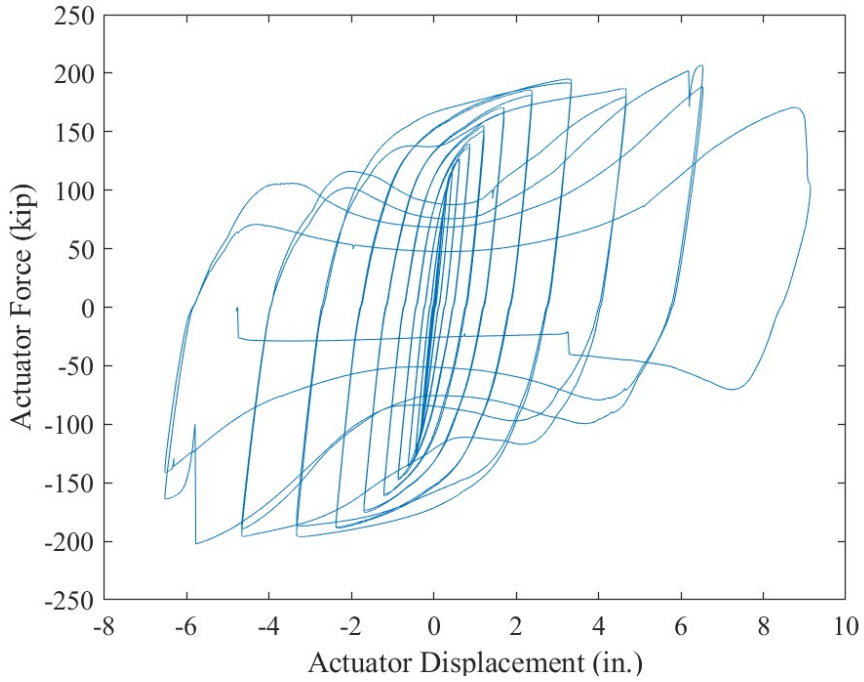

Fig. E2. Actuator Force vs. Actuator Displacement of Specimen HG1

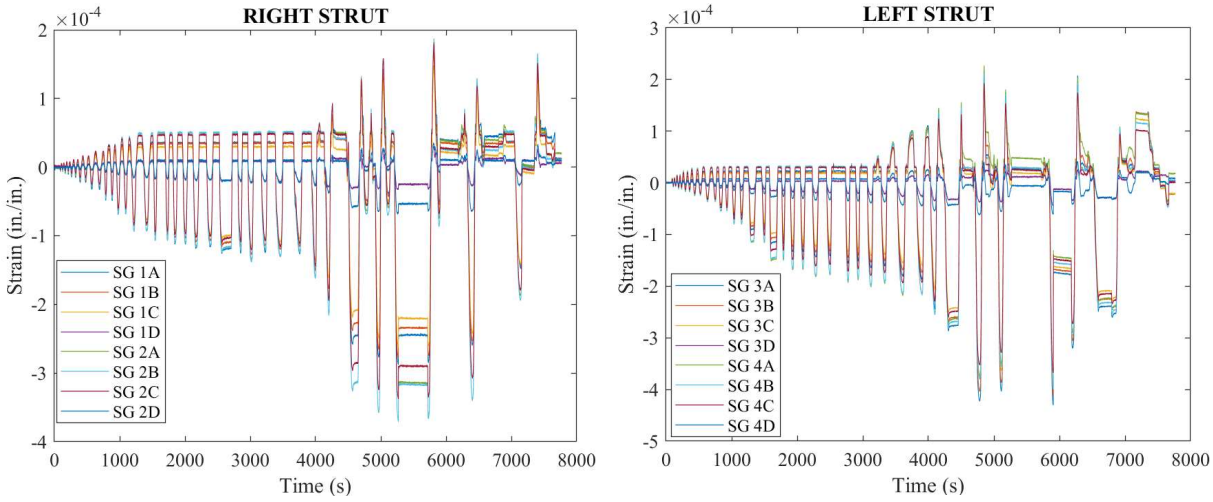

Fig. E3. Raw Strain Gage measurements of Specimen HG1

Specimen HG2

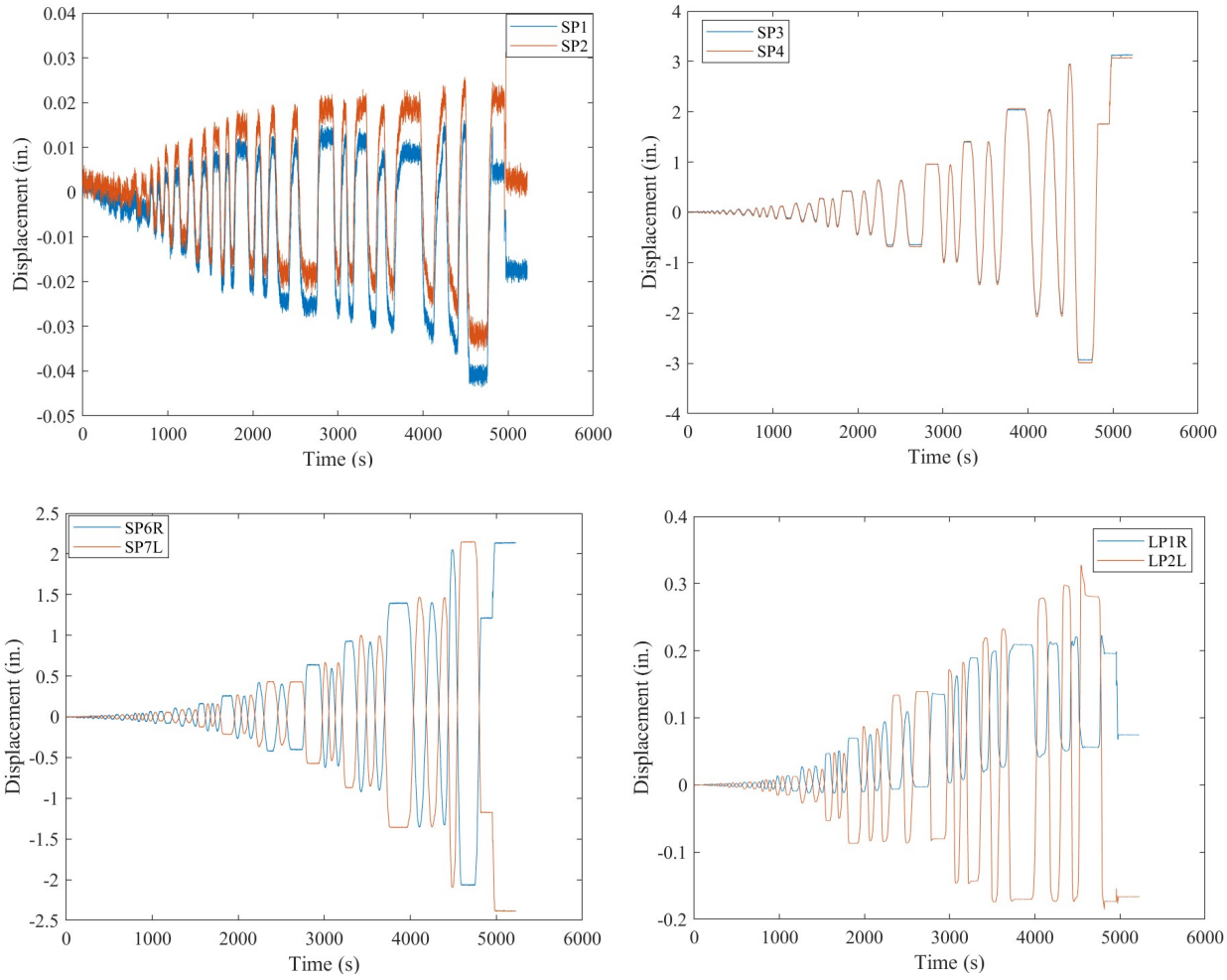

Fig. E4. Raw Displacement Measurements of Specimen HG2

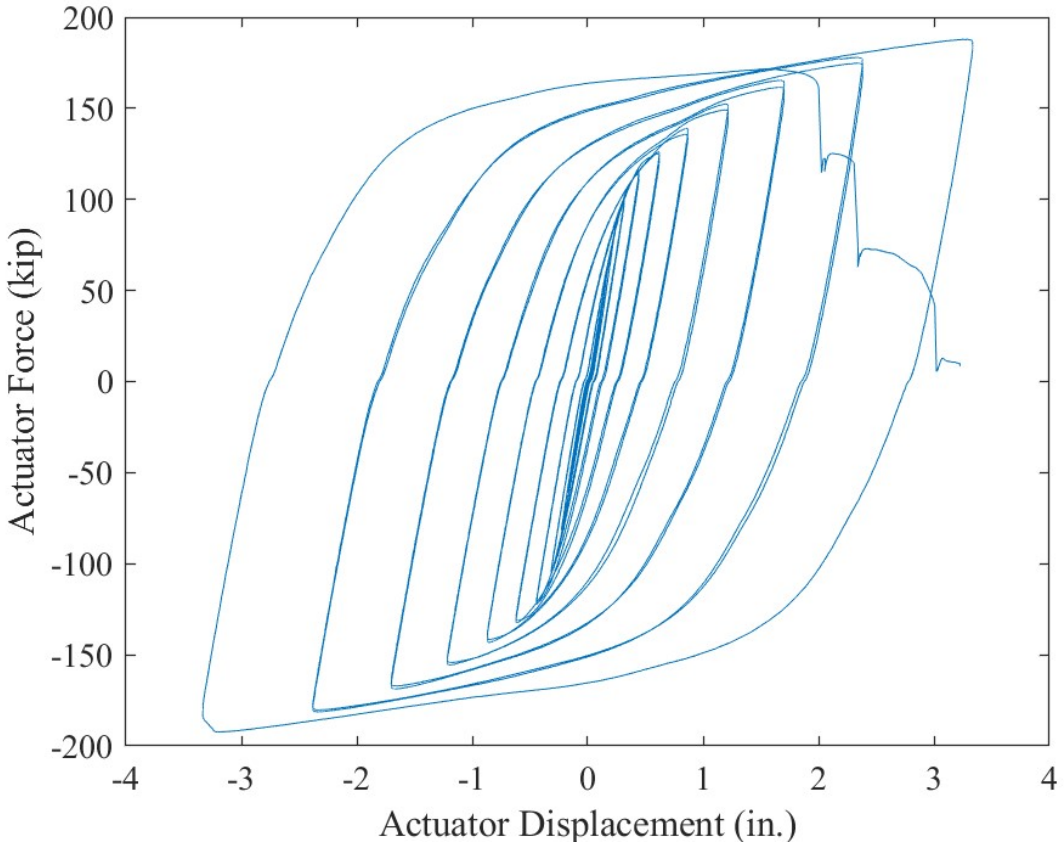

Fig. E5. Actuator Force vs. Actuator Displacement of Specimen HG2

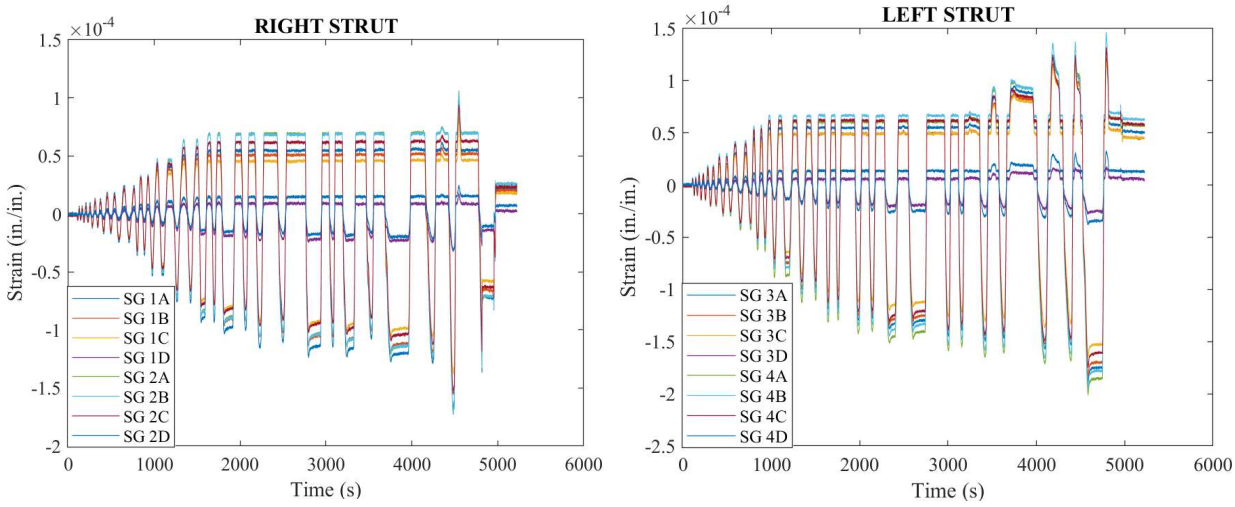

Fig. E6. Raw Strain Gage measurements of Specimen HG2

Specimen HG3

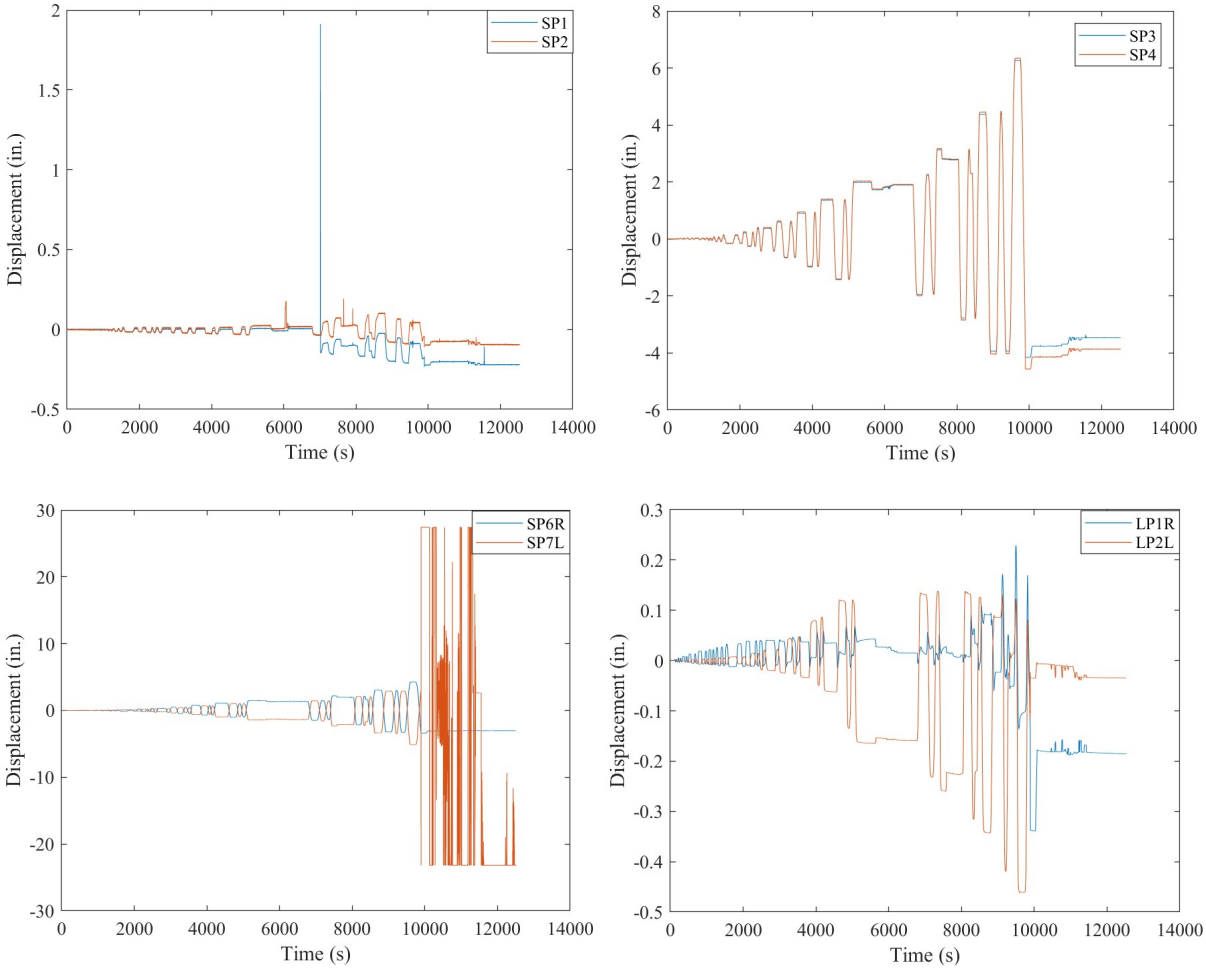

Fig. E7. Raw Displacement Measurements of Specimen HG3

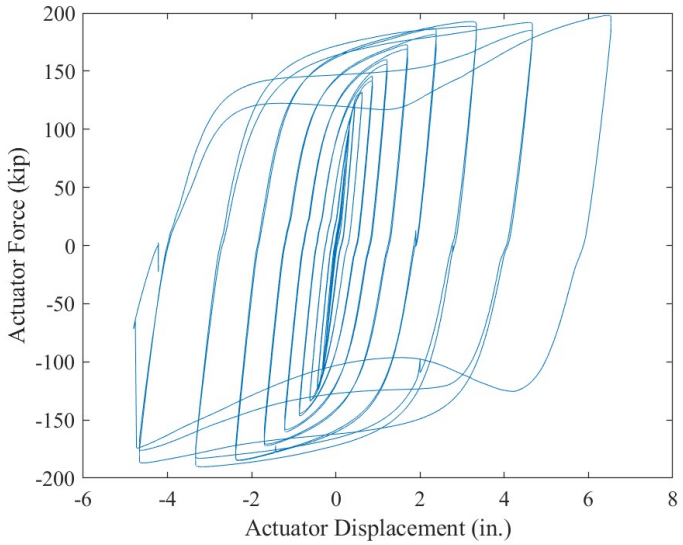

Fig. E8. Actuator Force vs. Actuator Displacement of Specimen HG3

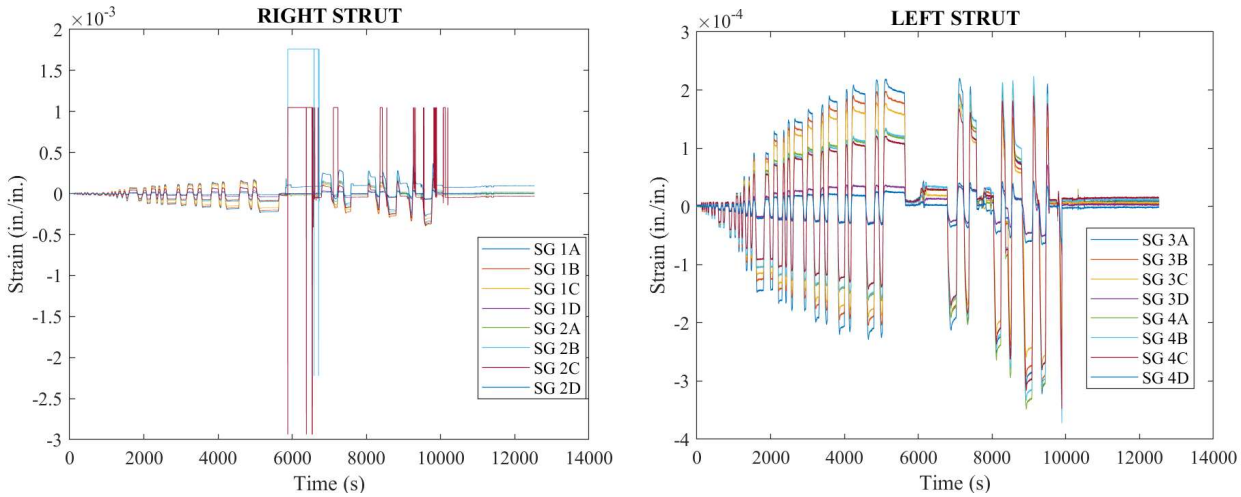

Fig. E9. Raw Strain Gage measurements of Specimen HG3

Specimen EL1

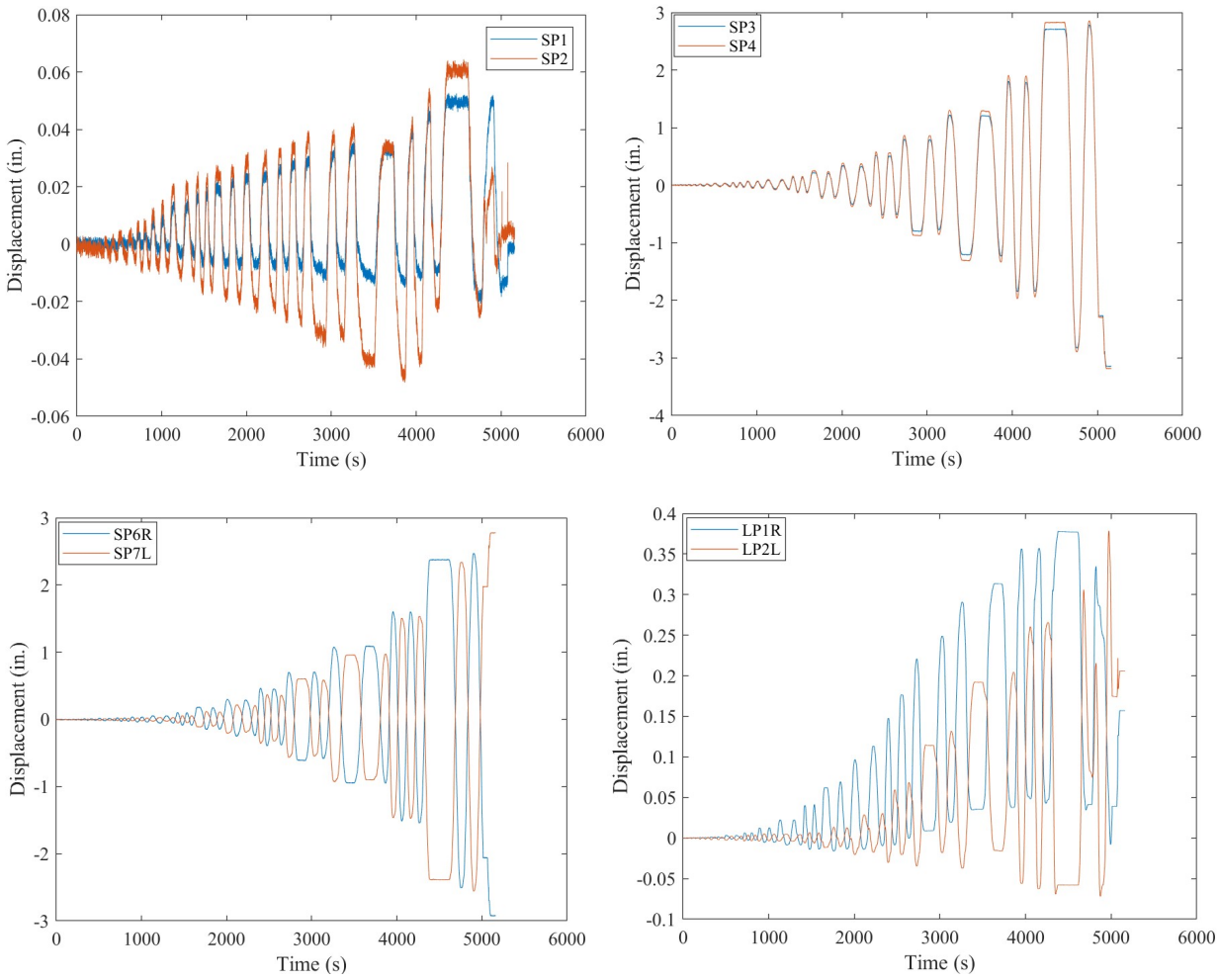

Fig. E10. Raw Displacement Measurements of Specimen EL1

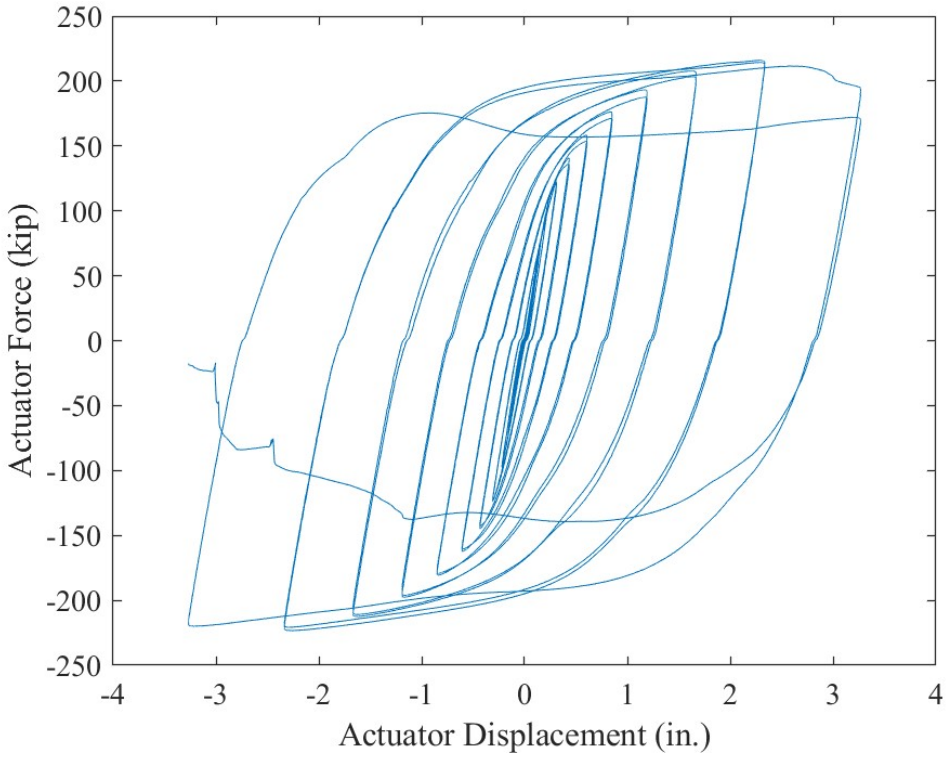

Fig. E11. Actuator Force vs. Actuator Displacement of Specimen EL1

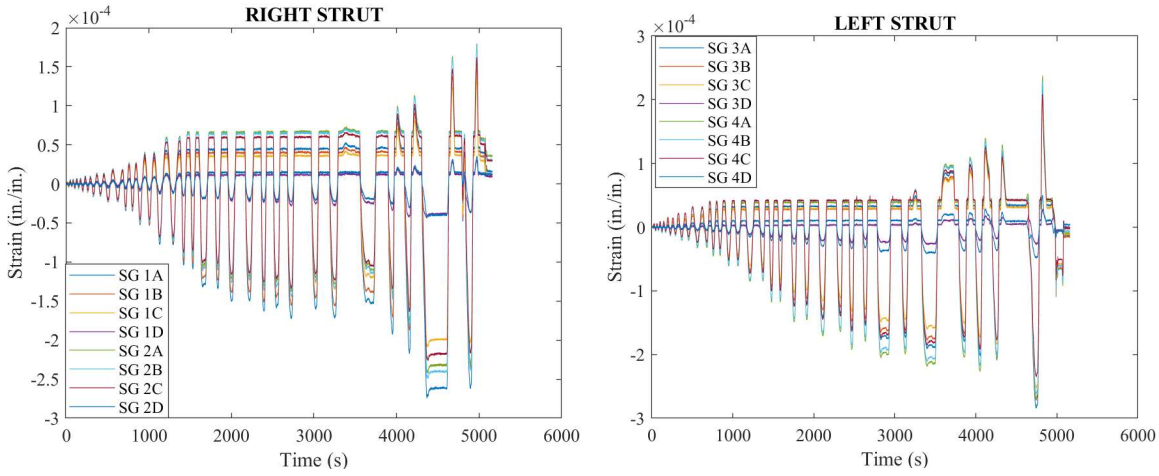

Fig. E12. Raw Strain Gage measurements of Specimen EL1

Specimen EL2

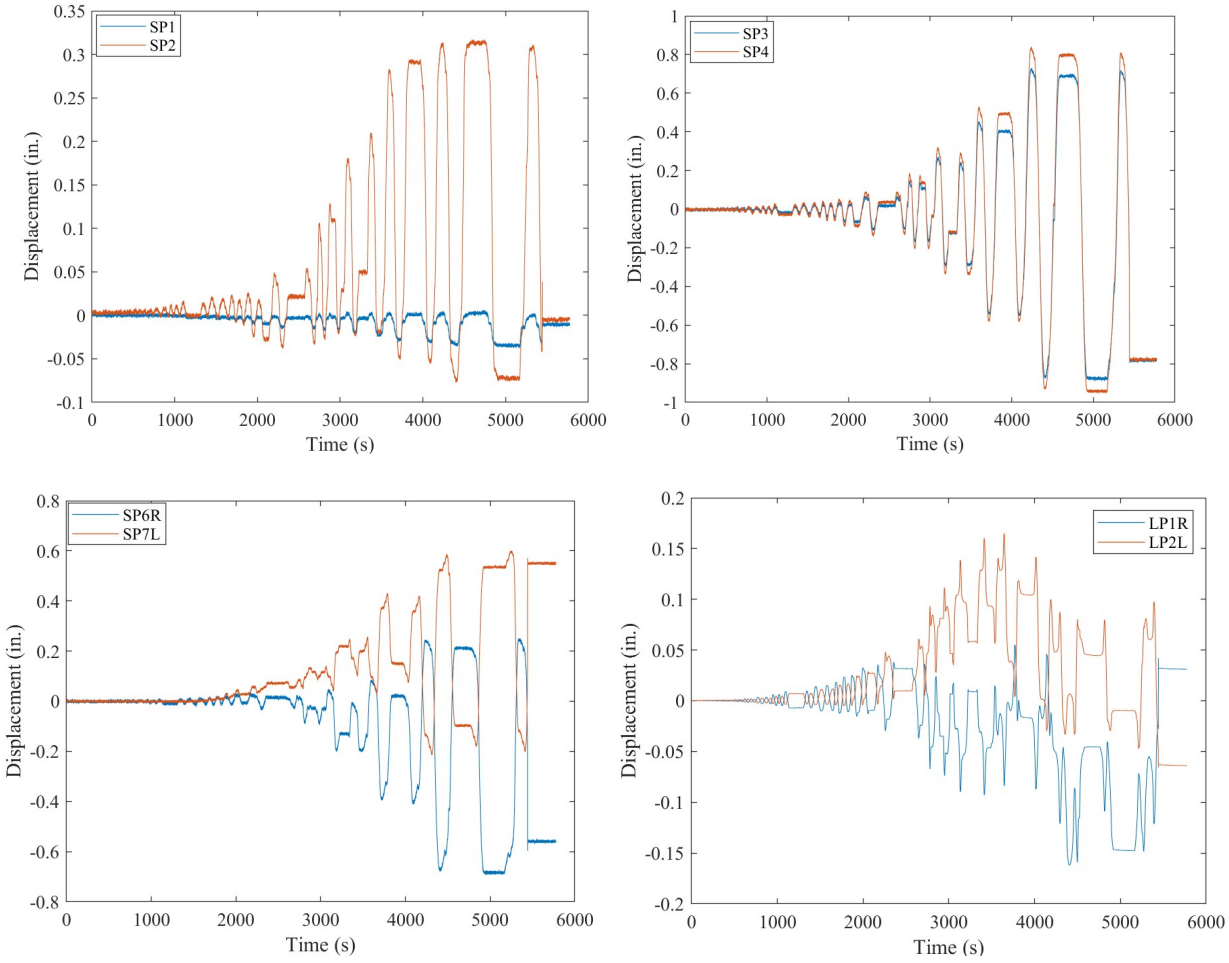

Fig. E13. Raw Displacement Measurements of Specimen EL2

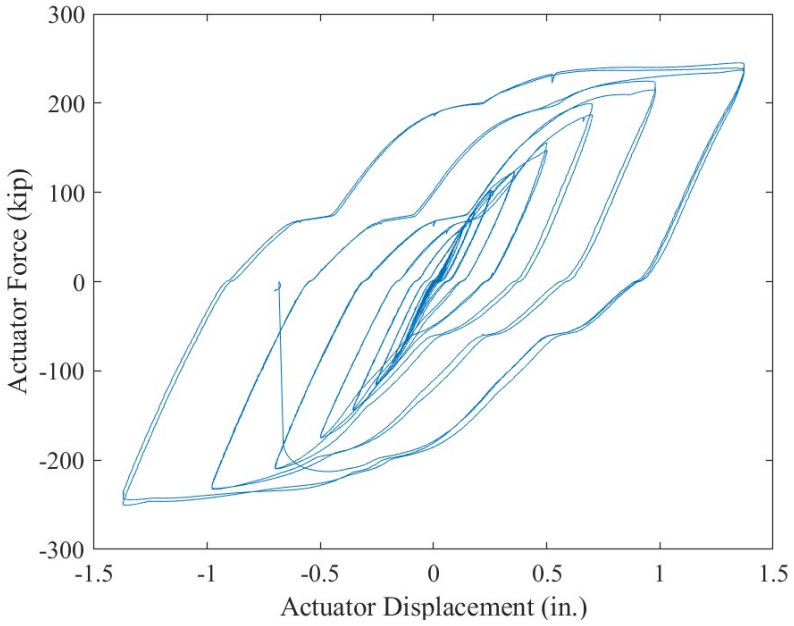

Fig. E14. Actuator Force vs. Actuator Displacement of Specimen EL2

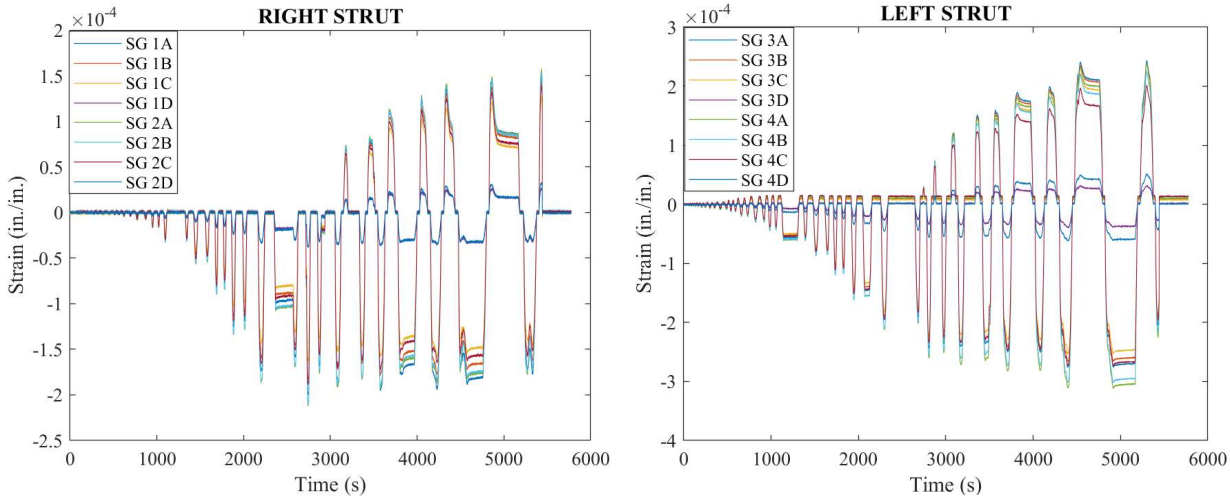

Fig. E15. Raw Strain Gage measurements of Specimen EL2

Specimen EL3

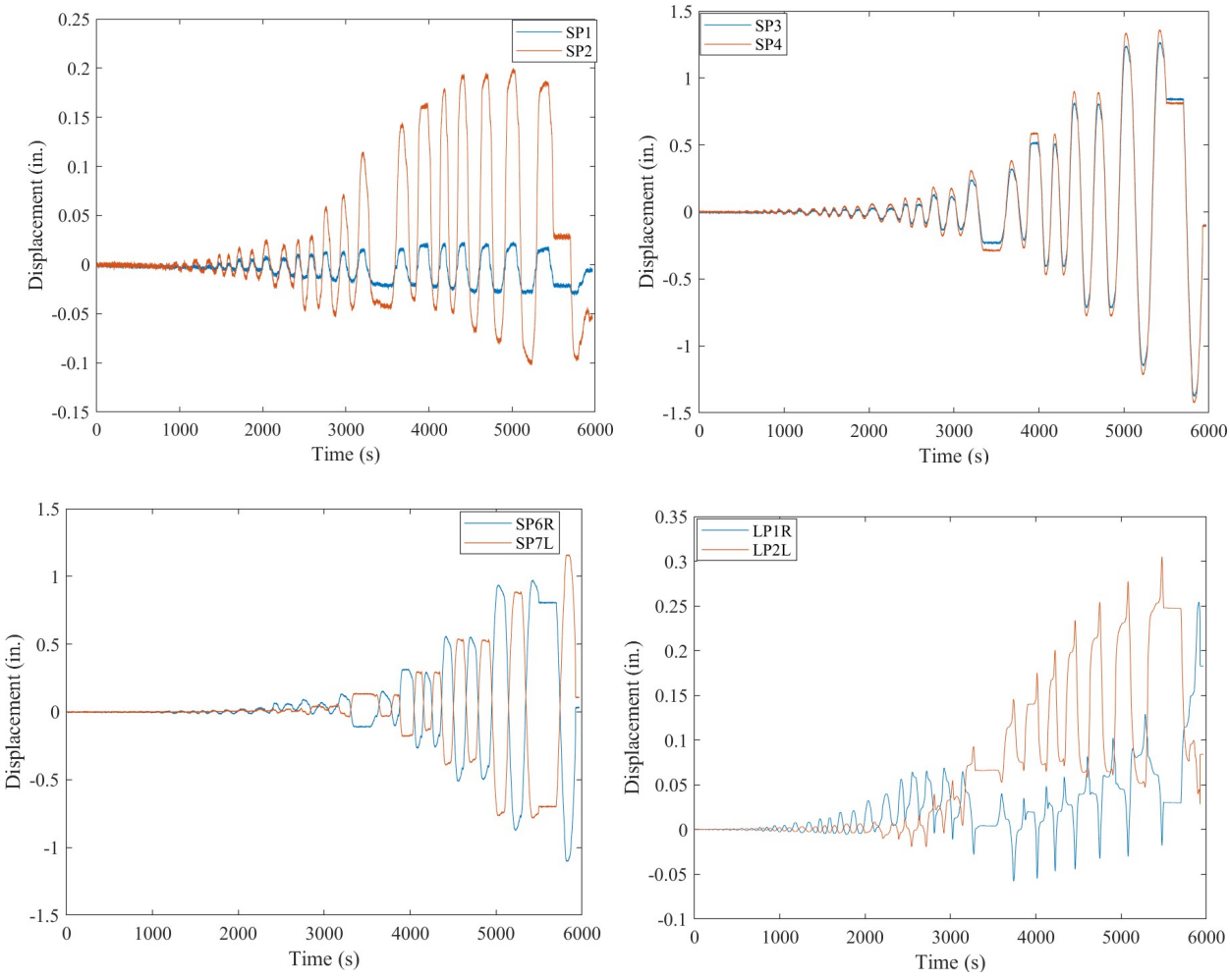

Fig. E16. Raw Displacement Measurements of Specimen EL3

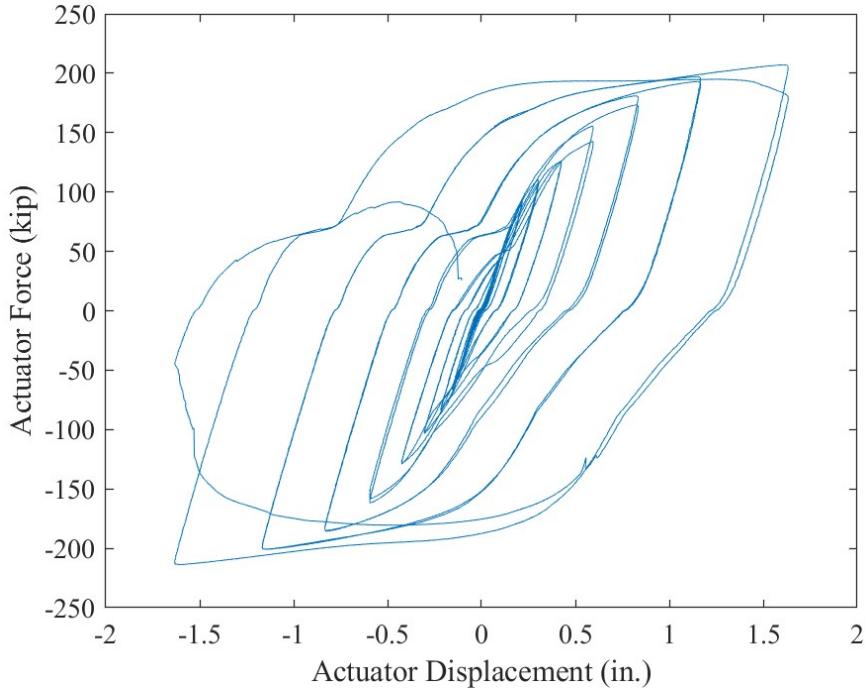

Fig. E17. Actuator Force vs. Actuator Displacement of Specimen EL3

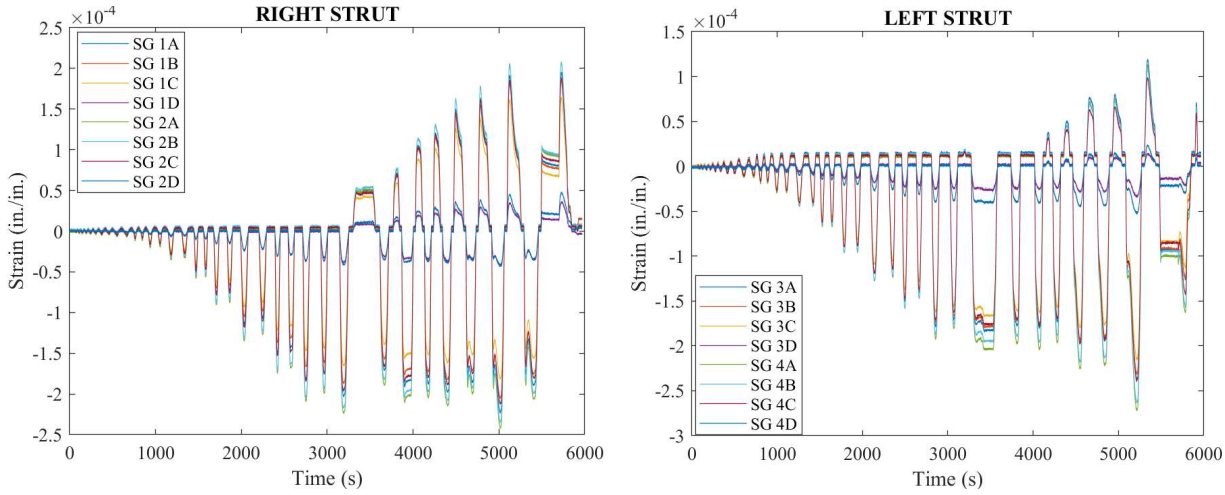

Fig. E18. Raw Strain Gage measurements of Specimen EL3